

**DOCTORAL THESIS**

# Additively Manufactured Advanced Thermal Management Solutions for Electrical Machines

Martin Sarap

TALLINN UNIVERSITY OF TECHNOLOGY  
DOCTORAL THESIS  
54/2025

# **Additively Manufactured Advanced Thermal Management Solutions for Electrical Machines**

MARTIN SARAP



TALLINN UNIVERSITY OF TECHNOLOGY  
School of Engineering  
Department of Electrical Power Engineering and Mechatronics  
This dissertation was accepted for the defence of the degree 26/06/2025

**Supervisor:** Prof. Ants Kallaste  
School of Engineering  
Tallinn University of Technology  
Tallinn, Estonia

**Co-supervisor:** Dr. Payam Shams Ghahfarokhi  
Electrical Engineering  
Tampere University  
Tampere, Finland

**Opponents:** Prof. Roman Pechánek  
Faculty of Electrical Engineering  
University of West Bohemia  
Pilsen, Czech Republic

Prof. Pia Lindh  
School of Energy Systems  
Department Electrical Engineering  
Lappeenranta University of Technology  
Lappeenranta, Finland

**Defence of the thesis:** 22/08/2025, Tallinn

**Declaration:**

Hereby I declare that this doctoral thesis, my original investigation and achievement, submitted for the doctoral degree at Tallinn University of Technology has not been submitted for doctoral or equivalent academic degree.

Martin Sarap



-----  
signature

Copyright: Martin Sarap, 2025  
ISSN 2585-6898 (publication)  
ISBN 978-9916-80-341-7 (publication)  
ISSN 2585-6901 (PDF)  
ISBN 978-9916-80-342-4 (PDF)  
DOI <https://doi.org/10.23658/taltech.54/2025>

Sarap, M. (2025). *Additively Manufactured Advanced Thermal Management Solutions for Electrical Machines* [TalTech Press]. <https://doi.org/10.23658/taltech.54/2025>

TALLINNA TEHNIKAÜLIKOO  
DOKTORITÖÖ  
54/2025

**Kihtlisandusmeetodil valmistatud  
täiustatud jahutuslahendused  
elektrimasinatele**

MARTIN SARAP







# Contents

List of Publications .....	7
Author's Contribution to the Publications .....	8
Introduction .....	9
1.1 Additive Manufacturing for Electrical Machine Thermal Management .....	9
1.2 Hypotheses: .....	11
1.3 Objectives of the Thesis .....	11
1.4 Scientific Contributions of the Thesis.....	12
1.5 Outline of the Thesis .....	12
Abbreviations.....	13
Symbols.....	14
2 State of the Art.....	16
2.1 Additive Manufacturing Methods Used in the Field of Electrical Machine Cooling .	16
2.2 Materials for Additive Manufacturing of Thermal Solutions for Electrical Machines	17
2.2.1 Thermal and Electrical Conductors .....	18
2.2.2 Thermally Conductive Dielectrics.....	18
2.2.3 Magnetic Materials .....	19
2.2.4 Anisotropy in LPBF Materials .....	20
2.3 Additively Manufactured Thermal Management Solutions for Electrical Machines	22
2.3.1 AM for Air-Cooled Electrical Machines .....	24
2.3.2 AM Passive Air-Coolers .....	25
2.3.3 AM Active Air-Coolers .....	25
2.3.4 AM for Liquid- and Direct Conductor Cooling.....	26
3 Advanced Fin Structures for Air-Cooled Electrical Machines Enabled by AM.....	28
3.1 Advanced AM Fin Structures for Passive Heatsinks .....	28
3.1.1 SRM Parameters.....	28
3.1.2 Advanced Fin Designs for Passive Heatsinks.....	30
3.1.3 SRM Thermal Model .....	32
3.1.4 SRM Nonisothermal Fluid Model .....	34
3.1.5 Results and Conclusions of the Passive Heatsink Models .....	37
3.2 Advanced AM Fin Structures for Active Heatsinks.....	38
3.2.1 Axial Flux Switched Reluctance Motor Prototype.....	38
3.2.2 AFSRM Thermal Model .....	40
3.2.3 AFSRM Cooling Fans.....	41
3.2.4 Heatsink Sizing .....	42
3.2.5 Advanced Fin Structures .....	45
3.2.6 Advanced Fin Structure Prototypes and Testing.....	47
3.2.7 Advanced Fin Structure Results .....	48
3.2.8 Evaluation of the Proposed AFSRM Thermal Management Solution .....	50
3.3 Advanced Fin Structures Conclusions and Future Work.....	50
4 Algorithmically Generated Fin Structures .....	52
4.1 Propulsion Drive Parameters .....	52
4.2 Parametric Optimization Model.....	54
4.2.1 Thermal CFD for PO.....	54
4.2.2 Parametric Optimization Model Output .....	56

4.3 Topology Optimization Model .....	57
4.3.1 Density-based Topology Optimization .....	57
4.3.2 Thermal CFD for Density-based TO .....	58
4.3.3 Optimization Process .....	59
4.3.4 TO CFD Model Setup .....	60
4.3.5 TO Model Results .....	61
4.4 Additively Manufactured Prototypes .....	62
4.4.1 Performance Measurements .....	62
4.5 TO Results and Conclusions .....	63
5 Conclusions and Future Work .....	65
References .....	69
Acknowledgements .....	76
Abstract .....	77
Lühikokkuvõte .....	79
Appendix .....	81
Curriculum vitae .....	167
Elulookirjeldus .....	168

## List of Publications

The list of author's publications, on the basis of which the thesis has been prepared:

- I M. Sarap, A. Kallaste, P. Shams Ghahfarokhi, H. Tiismus, and T. Vaimann, "Utilization of Additive Manufacturing in the Thermal Design of Electrical Machines: A Review," *Machines*, vol. 10, no. 4, Art. no. 4, Apr. 2022, doi: 10.3390/machines10040251.
- II M. Sarap, H. Tiismus, A. Kallaste, M. Saarna, M. Kolnes, P. Shams Ghahfarokhi, T. Vaimann, Electrical and Thermal Anisotropy in Additively Manufactured AlSi10Mg and Fe-Si Samples, *Machines* 13 (2025) 1. <https://doi.org/10.3390/machines13010001>.
- III M. Sarap, A. Kallaste, P.S. Ghahfarokhi, T. Vaimann, Analysis of Advanced Passive Heatsinks for Electrical Machines Enabled by Additive Manufacturing, in: 2023 IEEE Workshop Electr. Mach. Des. Control Diagn. WEMDCD, 2023: pp. 1–6. <https://doi.org/10.1109/WEMDCD55819.2023.10110940>.
- IV M. Sarap, S. Singh, A. Kallaste, A. Qureshi, H. Tiismus, T. Vaimann, P.S. Ghahfarokhi, Design of an additively manufactured thermal solution for an axial flux switched reluctance motor, *Case Stud. Therm. Eng.* 66 (2025) 105805. <https://doi.org/10.1016/j.csite.2025.105805>.
- V M. Sarap, S. Singh, A. Kallaste, A. Qureshi, H. Tiismus, T. Vaimann, P.S. Ghahfarokhi, Comparative Study of Advanced Heatsink Structures for Improved Thermal Performance in Axial Flux Motors, *IEEE Access*, doi: 10.1109/ACCESS.2025.3577289.
- VI M. Sarap, A. Kallaste, T. Vaimann, P.S. Ghahfarokhi, Additively Manufactured and Topology Optimized Heatsink for a Propulsion Motor, in: 2024 Int. Conf. Electr. Mach. ICEM, 2024: pp. 1–6. <https://doi.org/10.1109/ICEM60801.2024.10700108>.

## **Author's Contribution to the Publications**

Contribution to the papers in this thesis are:

- I Martin Sarap is the primary author of this article. He conducted the literature overview and wrote the initial draft of the article.
- II Martin Sarap is the primary author of this article. He planned the experiments, designed and built the experimental apparatus, measured the material properties and wrote the initial draft of the paper.
- III Martin Sarap is the primary author of this article. He formulated the problem, designed each of the heatsinks, set up the numerical model and wrote the initial draft of the paper.
- IV Martin Sarap is the primary author of this article. He proposed the design of the thermal solution, designed and built the experimental apparatus, conducted the measurements and wrote the initial draft of the paper.
- V Martin Sarap is the primary author of this article. He designed and modelled each of the heatsinks, conducted the measurements and wrote the initial draft of the paper.
- VI Martin Sarap is the primary author of this article. He formulated the problem, designed the heatsinks, set up the numerical and optimization models, conducted the measurements and wrote the initial draft of the paper.

# Introduction

## 1.1 Additive Manufacturing for Electrical Machine Thermal Management

Colloquially known as 3D printing, additive manufacturing (AM) is an umbrella term covering a range of technologies where physical objects are manufactured through incremental additions of material (as opposed to subtractive manufacturing methods i.e. machining). This form of manufacturing enables practically any geometry that can be represented as a 3D model to be created with a high degree of accuracy. A consequence of the layer-by-layer process is that the cost of producing an object is largely invariant of its geometrical complexity or material selection (other than the cost of the material itself). This design freedom gives engineers the ability to realize optimized geometries without being hindered by the technical or economical limitations of conventional manufacturing methods.

While AM has so far been predominantly a tool for prototyping, it is increasingly being adopted for the production of end-use components, particularly in highly demanding and cost insensitive applications such as aerospace and medical engineering. There, for example, AM is used to manufacture parts with complex internal cavities [1] or individually customized bio-compatible shapes [2]. However, additional benefits such as an incredibly wide material selection ranging from flexible polymers to high-performance metals, supply chain robustness and in-house manufacturing, together with general advancements of AM technologies, have resulted in its growing utilization in many other fields [3–6].

Among these is the field of electrical machines (EM), where applications such as electric aviation demand ever growing power densities. The accompanying increase in phase currents and electrical frequencies inevitably lead to elevated heat generation in the windings and core, while size and weight restrictions limit the available surface area for cooling. At the same time, these same applications require extremely high efficiencies and have strict requirements for reliability. Each of these requirements has its own specifics, however they all share a common connection to temperature through winding resistance, insulation degradation and demagnetization. The universal preference towards lower temperatures in any electrical machine means that effective cooling is crucial to maintain performance, efficiency, and reliability. A solution for these ever-increasing requirements is provided by AM through the ability to realize novel geometries in the pursuit of high-performance cooling solutions. For instance, AM allows the creation of complex cooling structures [7] and optimized thermal paths [8] that can significantly improve the efficiency and power density of motors and generators. Moreover, the ability to integrate multiple components into a single monolithic structure reduces assembly time and potential points of failure, enhancing reliability and ease of maintenance. As AM technologies continue to advance, their integration into the design and manufacturing of electrical machines is expected to drive significant improvements in performance, efficiency, and sustainability.

AM offers a transformation in the technology of EM thermal management by enabling the physical realization of optimized solutions, for which the three most important facets are highlighted in Figure 1.1. By eliminating the roadblocks set by conventional manufacturing, the thermal performance of electrical machines can be improved directly by employing **advanced geometries**, for example by replacing simple heatsink fins with complex structures, improving thermal transfer in the windings through shaped

conductors, or cooling the windings directly through integrated heatsinks. Furthermore, the lack of tooling (e.g. moulds or dies) in AM-based production inherently facilitates **application-specific design** processes. In EM cooling, for example, this can mean components individually shaped according to the specific winding geometry of a motor, or geometrical parameters fine-tuned to a single working point. Finally, even in cases where AM is cost-prohibitive or impractical in terms of final production, its streamlined workflow enables extremely **quick prototyping**, which can be beneficial even in the case of a conventionally mass-manufactured solution.

Currently, the available literature of AM for thermal management is based mainly on the exploration of novel designs for general cooling solutions. The move towards practicality in the form of cooling electrical machines is understandably slow, and optimized solutions with the specific application in mind are even less common in the literature. Air-cooled electrical machines, which are required in many highly demanding applications, are woefully underrepresented in the literature. There is, therefore, a significant gap in the knowledge of applying advanced AM-enabled solutions for the air-cooling of electrical machines.

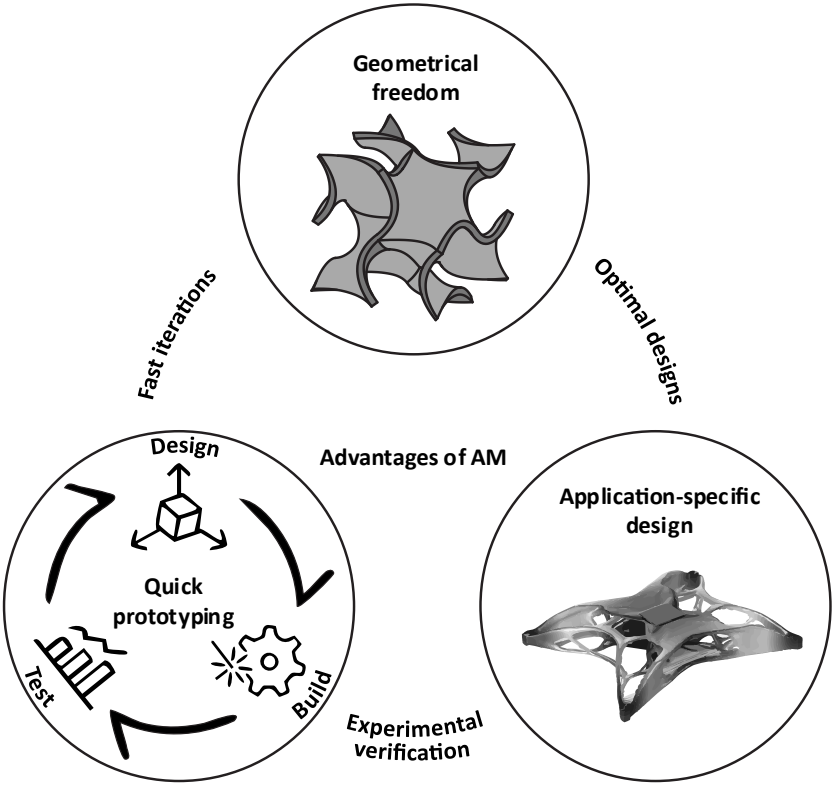


Figure 1.1. Main advantages of additive manufacturing for electrical machine cooling.

## 1.2 Hypotheses

Despite its immense potential for improving thermal performance, research on the utilization of AM in the context of air-cooled electrical machines is currently severely underdeveloped. The inherent design freedom of AM allows advanced fin structures, which improve the efficacy of the heatsink, to be readily fabricated for either prototyping or end use, while its capabilities in mass personalization enable highly customized thermal management solutions that consider the specific requirements and limitations of electrical machines. The following hypotheses are proposed based on the current state of the art in the field:

1. AM can be used to fabricate complex geometries from thermally conductive materials that are suitable for high-performance air-cooling solutions.
2. Advanced fin structures utilizing novel geometries that rely on the capabilities of AM can improve the absolute and relative thermal performance of passively and actively air-cooled electrical machines.
3. Tailor-made solutions that rely on the quick prototyping and application-specific design capabilities of AM enable high-performance thermal management systems for electrical machines.
4. AM enables the effective fabrication of algorithmically optimized geometries for electrical machine cooling.

## 1.3 Objectives of the Thesis

The primary goal of the thesis is to apply the advantages of AM for air-cooled electrical machines through advanced fin structures and customized designs, leading to improved thermal performance. This goal is achieved through methods of material characterization, numerical thermal and fluid modelling, computational optimization, and the experimental verification of physical prototypes. The main goal is achieved via the following objectives:

1. Conduct a literature review of the current state-of-the-art in the relevant AM methods, materials and solutions for electrical machine cooling.
2. Establish a database of the direction-dependent thermal and electrical conductivities of AM aluminium alloy and silicon steel samples, including the effects of heat treatment.
3. Discover and verify novel geometries for passively and actively air-cooled heatsink fin structures that offer improved absolute and/or relative performance over conventional solutions.
4. Utilize AM to design and fabricate a novel thermal management solution for an air-cooled electrical machine to maximize its current-to-weight ratio.
5. Develop a method for the algorithmic generation of optimized fin geometries to maximize the thrust ratio of a propulsion motor and verify the modelled results using physical prototypes.



## 1.4 Scientific Contributions of the Thesis

The thesis presents the following **scientific novelties**:

1. Characterization of anisotropic electrical and thermal conductivities of as-built and thermally treated AlSi10Mg and Fe-Si samples manufactured with laser powder bed fusion.
2. Identification of reduced aerodynamic resistance as the key advantage of advanced structures for absolute thermal performance in AM-based passively and actively air-cooled heatsinks.
3. Recognition of the truss-based rhombi octet lattice structure as a significant improvement over conventional straight fins in terms of gravimetric fin effectiveness for active-air cooling.
4. Development of an application-specific method for the numerical optimization of a propulsion drive motor's heatsink through computational fluid dynamics and Darcy's law.

The thesis presents the following **practical novelties**:

1. Measurements of specific direction-based values for the conductivities of AlSi10Mg and Fe-Si3.7% materials for use in models.
2. Fabrication of advanced fin geometries for passively and actively air-cooled heatsinks together with practical performance measurements.
3. Modelling, fabrication and verification of an integrated mechanical and thermal solution for a yokeless axial flux machine.
4. Utilizing numerical thermal and fluid modelling in conjunction with algorithmic geometry optimization to maximize the thrust ratio of a propulsion motor using an actively air-cooled heatsink.
5. Physical realization of the algorithmically optimized heatsink for gathering measurement results.

## 1.5 Outline of the Thesis

The thesis is divided into four sections that provide an overview of the topic.

**Chapter 2** focuses on the state of the art in additively manufactured thermal solutions in the field of electrical machine cooling. It covers the relevant methods, materials and solutions present in the literature. Furthermore, specific attention is given to the anisotropic qualities of additively manufactured materials.

**Chapter 3** studies AM-enabled advanced fin structures in air-cooled heatsinks. This is done through numerical simulations in the context of a passively cooled radial flux motor, and physical prototypes in the context of an actively cooled axial flux motor.

**Chapter 4** presents an application-specific methodology for the creation of algorithmically optimized actively air-cooled heatsinks. The methodology is utilized in the context of an electric propulsion drive and validated using physical AM prototypes.

**Chapter 5** summarizes the thesis and discusses potentials for future work and improvements in the field.

## Abbreviations

AFSRM	Axial Flux Switcher Reluctance Motor
AM	Additive Manufacturing
BCC	Body-Centred Cubic
BJ	Binder Jetting
CFD	Computational Fluid Dynamics
DCC	Direct Conductor Cooling
EBM	Electron-Beam Melting
EC	Electrical Conductivity
EM	Electrical Machine
FDM	Fused Deposition Modelling
FEM	Finite Element Modelling
HE	Heat Exchanger
IACS	International Annealed Copper Standard
LPBF	Laser Powder Bed Fusion
NACA	National Advisory Committee for Aeronautics
PO	Parametric Optimization
SIMP	Solid Interpolation Material with Penalisation
SLA	Stereolithography
SRM	Switched Reluctance Motor
TC	Thermal Conductivity
TPMS	Triply Periodic Minimal Surface
TO	Topology Optimization

## Symbols

$A_{base}$	Area of the heatsink's base between the fins ( $m^2$ )
$A_{fc}$	Area of the flow channel ( $m^2$ )
$A_{Hs}$	Effective (wetted) area of the heatsink fin structure ( $m^2$ )
$A_s$	Area of the heatsink's inner surface ( $m^2$ )
$Al_{xy}$	AlSi10Mg test sample manufactured perpendicular to the LPBF build direction.
$Al_z$	AlSi10Mg test sample manufactured in the build direction.
$Al_{45^\circ}$	AlSi10Mg test sample manufactured at a $45^\circ$ angle to the LPBF build direction.
$c_p$	Specific heat capacity ( $J/(kg \cdot K)$ )
$f$	Electrical frequency (Hz) / friction factor
$g$	Gravitational acceleration ( $m/s^2$ )
$Fe_{xy}$	Fe-Si3.7% test sample manufactured perpendicular to the LPBF build direction.
$Fe_z$	Fe-Si3.7% test sample manufactured in the build direction.
$h_{bc}$	Contact boundary conductance ( $W/m^2 \cdot K$ )
$h_{conv}$	Convection coefficient ( $W/m^2 \cdot K$ )
$\mathbf{I}$	Identity matrix
$j$	Current density ( $A/mm^2$ )
$j_{\Delta 80^\circ C}$	Current density in the windings at a $80^\circ C$ temperature increase over ambient ( $A/mm^2$ )
$k_j$	Gravimetric current density factor ( $A/(mm^2 \cdot kg)$ )
$k_{ffc}$	Core laminations fill factor
$k_{ffw}$	Winding fill factor
$L_{Fin}$	Length of the heatsink fins (m)
$\mathbf{K}$	Viscous stress tensor (Pa)
$M_{Fe-S}$	Mass of the stator iron (kg)
$M_{Hs}$	Mass of the heatsink sector's fin structure without the base (kg)
$M_\Sigma$	Total mass of the motor/drive (kg)
$n_{Fin}$	Number of heatsink fins
$p$	Heating/loss power density ( $W/m^3$ ) / pressure (Pa)
$p_A$	Absolute pressure (Pa)
$p_{Cu}$	Heating/loss power density in the windings ( $W/m^3$ )
$p_{Fe}$	Heating/loss power density in the core ( $W/m^3$ )
$P_{Cu}$	Copper losses (W)
$P_{Fe}$	Iron losses (W)
$\Delta P_{fan}$	Pressure increase of the cooling fan (Pa)
$\Delta P_{Hs}$	Pressure drop of the heatsink at a given velocity (Pa)
$q$	Heat flux density ( $W/m^2$ )
$Q_{fan}$	Airflow created by the fan ( $m^3/s$ )

$Q_{\Sigma}$	Total heat flux (W)
$R_S$	Specific gas constant
$\mathcal{R}_{Al}$	Thermal resistance of the solid AlSi10Mg (K/W)
$\mathcal{R}_{Cu}$	Thermal resistance of the winding (K/W)
$\mathcal{R}_{C-Cu}$	Thermal resistance of the contact between the winding turns and/or between the winding and the stator (K/W)
$\mathcal{R}_{C-Hs}$	Thermal resistance of the contact with the heatsink (K/W)
$\mathcal{R}_{Conv}$	Thermal resistance associated with convection (K/W)
$\mathcal{R}_{Hs}$	Thermal resistance of the heatsink (K/W)
$\mathcal{R}_{Fe}$	Thermal resistance of the Fe-Si core (K/W)
$\mathcal{R}_0$	Internal thermal resistance (K/W)
$\mathcal{R}_{\Sigma}$	Total thermal resistance of the system (K/W)
$t_{Fin}$	Heatsink fin thickness (m)
$T$	Temperature (°C)
$T_{amb}$	Ambient temperature / 20 °C
$T_{Cu}$	Copper/hotspot temperature (°C)
$T_F$	Average temperature of the heatsink surface (°C)
$\Delta T_{Cu}$	Temperature increase over ambient (°C)
$\mathcal{T}$	Thrust (Nm)
$\mathbf{u}$	Velocity field (m/s)
$v$	Air velocity (m/s)
$V_{Hs}$	Volume of the solid proportion of the sector's fin structure (m <sup>3</sup> )
$V_{FC}$	Volume of the flow channel of the sector's fin structure (m <sup>3</sup> )
$V_{\Omega}$	Volume of the design domain (m <sup>3</sup> )
$w_{ag}$	Equivalent layer of air in terms of thermal resistance (m)
$W$	Weight of the drive (Nm)
$\alpha_p$	Thermal expansion coefficient (1/K)
$\delta$	Boundary layer thickness (m)
$\theta$	Density variable
$\kappa$	Permeability (m <sup>2</sup> )
$\lambda$	Thermal conductivity (W/(m·K))
$\lambda_{Al}$	Thermal conductivity of AlSi10Mg (W/(m·K))
$\lambda_{Fe}$	Thermal conductivity of Fe-Si3.7% (W/(m·K))
$\mu$	Viscosity (Pa·s)
$\rho$	Density (kg/m <sup>3</sup> )
$\rho_E$	Electrical resistivity (Ω·m)
$\rho_{E-Cu}$	Electrical resistivity of copper (Ω·m)
$\sigma$	Ratio of the flow area to the frontal area of the heat sink
$\Omega$	Design domain

## 2 State of the Art

The state of the art is studied to provide up to date information on the methods, materials and existing solutions in the research field of AM thermal solutions for electrical machines. Overall, it is based on the published work I: “Utilization of additive manufacturing in the thermal design of electrical machines: A review”. The initial part of the chapter introduces the reader to the main AM methods used in the field and provides historical context. The specific method of laser powder bed fusion, which is used in the other published works, is specifically highlighted. Afterwards, the relevant materials of the field and their physical properties are described. Special focus is given to the measurement of anisotropic conductivity in the AlSi10Mg and Fe-Si alloys, which are the principal materials used in the published works. A concise summary of the measurement process and results, based on published work II: “Electrical and Thermal Anisotropy in Additively Manufactured AlSi10Mg and Fe-Si Samples”, is provided. Finally, the third part of the chapter describes progress in the field through specific examples from the literature with an emphasis on air-cooling. There, the gaps in the research are identified and the published works III to V are positioned to fill those gaps.

### 2.1 Additive Manufacturing Methods Used in the Field of Electrical Machine Cooling

Various manufacturing methods, with the common property of incremental material addition, fall under AM. While many of them have found a niche in one or more industries, the field of AM electrical machines is mainly concerned with methods capable of producing components from electrically, thermally, and/or magnetically conductive materials. In this regard, the bar is set by conventional manufacturing methods in the form of copper, aluminium and different electrical steel alloys, for which strictly superior alternatives are unavailable outside of specific research contexts [9,10]. Therefore, the necessity of using one of these materials (or alloys thereof) limit AM for EM thermal solutions into three main methods: stereolithography, fused deposition modelling, and laser powder bed fusion.

AM first originated in 1987 [11] with the advent of stereolithography (SLA). This is a method of solidifying thin layers ( $< 100\ \mu\text{m}$ ) of photosensitive liquid polymers using a UV light source. The exposure of light can be precisely controlled using screens, galvanometers or projectors, resulting in highly detailed parts with feature sizes down to tens of micrometres [12]. While only the polymer can be directly hardened, other materials can be added to the liquid polymers as powders to form a composite. Afterwards, the hardened polymer can be removed (e.g. burned or dissolved), leaving behind the added material, albeit significantly shrunk. This allows SLA to be used for manufacturing ceramic and metal parts.

A few years later in 1991, Fused Deposition Modelling (FDM) was commercialized with the launch of the first FDM device by Stratasy. This technology is used to construct individual layers by precisely extruding thermoplastic materials according to the 3D model. In the current consumer space, FDM is by far the most popular AM technology due to low costs and robust devices. The material selection for FDM is extensive, as many thermoplastics, including composites, can be successfully printed. Furthermore, fully metal-based solutions based on rapid melting of aluminium wire have recently become available [13].

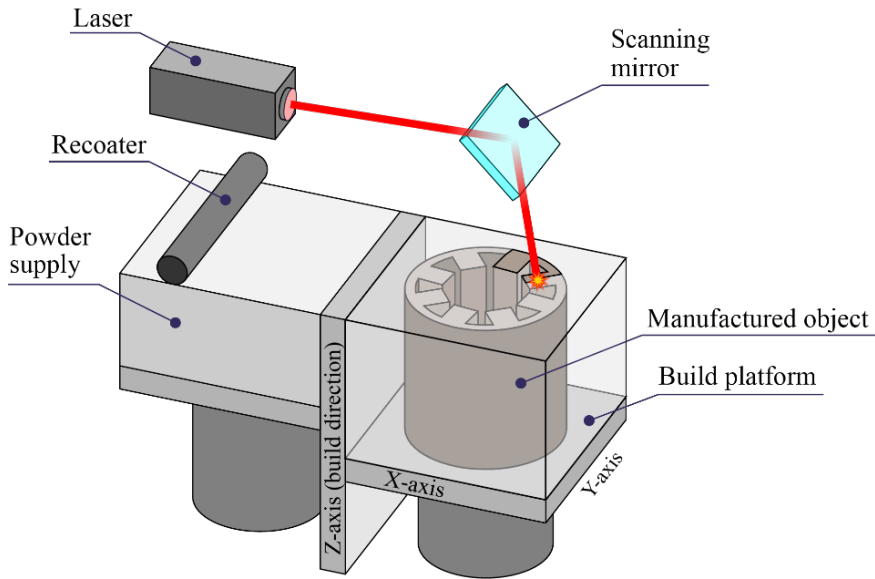


Figure 2.1. LPBF Process [14].

Manufacturing metals directly first became possible in 1995 with the advent of laser powder bed fusion (LPBF). With LPBF, a recoater mechanism is used to deposit thin layers of powder on the build platform, where a laser is used to fully melt cross-sections of the manufactured item. This process, which is illustrated in Figure 2.1, typically results in a homogeneous (although not necessarily isotropic) and virtually non-porous part with thermal, electrical and magnetic properties comparable to the original material. LPBF parts can be highly electrically and thermally conductive with minimum detail sizes of  $\sim 0.1$  mm and densities over 99% [15].

In components for EM thermal solutions, the most important physical property is high thermal conductivity, for which AM methods capable of fabricating metal parts directly are the most suitable. Consequently, by far the largest proportion of literature in the AM EM field is based on LPBF, which is also the method used for the original work presented in this thesis. However, it should be noted that advances in the manufacturing of polymer composite materials are enabling the use of SLA and FDM for thermal management applications.

## 2.2 Materials for Additive Manufacturing of Thermal Solutions for Electrical Machines

For materials used for EM thermal management, higher thermal conductivity (TC) is universally desirable in each component as there's generally no need to restrict heat flow in any way inside an electric machine. However, for electric and magnetic fields, both conductive and nonconductive, and magnetic and nonmagnetic materials can be used to enhance thermal performance. Based on existing materials and their functionality in an electrical machine, three groups can be defined.

### 2.2.1 Thermal and Electrical Conductors

For thermally and electrically conductive non-magnetic materials, AM methods mainly rely on two materials and alloys thereof – copper and aluminium. In their pure forms, both materials are challenging to manufacture directly (i.e. using LPBF) due to high thermal conductivity and reflectivity towards infrared light, resulting in difficulties rapidly heating localized regions of the powder. However, modern devices utilizing shorter wavelengths or electron beams are routinely manufacturing highly conductive copper components [16]. Pure aluminium (or alloys for which conductivity is similarly high), however, is currently not widely used with LPBF for the same reasons, although recent innovations in liquid metal printing could offer new possibilities.

By far the most widely used alternative to pure aluminium and the de facto standard conductive material used in LPBF is the aluminium-silicon alloy AlSi10Mg [17,18]. Originally developed to have a high strength-to-weight ratio, it is significantly less conductive than the best aluminium alloys (~44% IACS vs 61% [19]). However, its popularity in AM solutions stems from its ease of manufacturing with common LPBF devices. This is in a large part due to its lower reflectivity to infrared light, although its improved weldability and powder flowability are important as well. Where higher conductivity is important, pure copper can be replaced with the alloy CuCr1Zr, which is manufacturable with infrared lasers and can achieve conductivity values up to 70% of pure copper [20].

Alternatively, any of the aforementioned materials can be printed indirectly using other AM methods like, SLA, FDM or Binder Jetting (BJ), where the conductive material takes the form of a filler powder inside the primary printed material. In most cases, the primary material is removed in post-processing (through chemical or heat-based methods), although the finalized metal part generally underperforms in terms of conductivity [21].

### 2.2.2 Thermally Conductive Dielectrics

The indirect methods are better suited for thermally conductive dielectric materials. Conventional dielectrics used for insulating windings generally have low thermal conductivities below 1 W/(m·K), significantly reducing the effective conductivity of the winding structure. However, AM can be used to manufacture parts from ceramics like aluminium oxide [22] and alumina nitride [23], which are electrically non-conductive but excellent conductors of heat.

For FDM, two main thermally conductive dielectric material composites are available. First are pastes, in which thermally conductive material is mixed with a viscous paste and then extruded normally. While this makes it simple to create the material, the end result has a relatively low minimum detail size due to inherent inaccuracies in dispensing viscous substances. As an alternative, polymer composite materials formed into standard filament with a TC of up to 6 W/(m·K) are commercially available [24]. The common polymers (such as TPU and PETG) used in these composites mean that the versatility and robustness typical to FDM can be expected, while the end result is more than an order of magnitude more thermally conductive than the pure polymer.

### 2.2.3 Magnetic Materials

Finally, thermal management solutions in electrical machines can involve magnetic materials. Conventionally, these take a passive role as the core is designed with only magnetic performance in mind. However, with the utilization of LPBF, which is capable of producing high-performance magnetic cores [25], cooling solutions such as fluid channels can be integrated directly into the core design (this is already done in laminated cores [26], however AM can increase the effectiveness through optimized geometries). In either case, the TC of the soft-magnetic material is an important part of the thermal system, which is why conductivity measurements of LPBF Fe-Si samples (previously missing from the literature) are included in the third chapter of this work.

Some relevant materials together with the AM method used and the maximum TC achieved are listed in Table 2.1. As a whole, typical cooling elements, such as heatsinks and heat exchangers, where conductivity to mass ratio is highly important, are mostly manufactured from AlSi10Mg with LPBF. This is also the case for the original work presented in this thesis as even less conductive aluminium alloys generally outperform copper in performance-to-weight ratio for air-cooling applications. Other applications, such as AM conductors, where absolute performance is more desirable, typically utilize copper (unless a lower electrical conductivity is actually desirable due to lower AC losses [27]). Finally, thermally conductive ceramics, which can be manufactured indirectly with SLA or FDM, have been proposed for novel cooling solutions [28].

*Table 2.1. Relevant materials in LPBF thermal solutions and the corresponding thermal conductivity values for different manufacturing methods.*

Material	Manufacturing method	Effective thermal conductivity (W/(m·K))
Pure copper	Electrolysis	394
	EBM	390 [29]
	LPBF	317–336
	BJ	245–327 [30]
	Extruded paste	284 [21]
CuCr1Zr	Cast	310–340 [31]
	LPBF	309 [32]
AlSi10Mg	Cast	140-170 [33]
	LPBF	As built: 100-110*
		Heat treated: 150*
Fe-3.7%w.t.Si	LPBF	26*
Aluminium nitride ceramic	Pure	285 [34]
	SLA	> 160 [23]
	BJ	3–4 [35]
Alumina ceramic	SLA	35 [22]

\*Measured as a part of this thesis.



## 2.2.4 Anisotropy in LPBF Materials

While modern LPBF devices can routinely achieve densities exceeding 99% for commonly used materials, the resulting crystal structure of the material can still negatively impact the conductivity of the manufactured object through anisotropy. This is due to the inherent directionality of the LPBF process, which introduces extremely high temperature gradients and directional cooling rates that cause a preferred orientation in the crystal structure [36]. In terms of specific manufacturing parameters, this means that material properties and anisotropy in the part are influenced by build orientation, laser energy density [37], and laser scan speed [38]. As Electrical machines can have relevant heat flux and electrical current through its components in any direction, knowing the conductivities of the materials in all directions is crucial for designing optimized devices. Therefore, the direction-dependent thermal and electrical conductivities of samples made from the two most relevant materials, AlSi10Mg and Fe-Si (specifically a Fe-3.7%w.t.Si alloy), are measured as a part of this thesis. Additionally, as annealing is typically used to improve the properties of LPBF parts, the samples are measured both before and after the heat-treatment process.

### 2.2.4.1 AlSi10Mg and Fe-Si Conductivity Measurements

The anisotropic thermal and electrical conductivity (EC) values of LPBF AlSi10Mg and Fe-Si are measured using cylindrical samples that are manufactured in different orientations as shown in Figure 2.2. For measuring TC, three AlSi10Mg ( $Al_z$ ,  $Al_{45^\circ}$  and  $Al_{xy}$ ) and two silicon steel samples ( $Fe_z$  and  $Fe_{xy}$ ) are fabricated, while EC is measured using z- and xy-direction samples for both materials.

The TC and EC of the samples is measured using the longitudinal heat flow and the four-probe Kelvin methods respectively, for which the results are presented in Table 2.2. Both of these methods are sensitive to anisotropy and suitable for the typical dimensions of LPBF parts. For TC, the parts were measured at two different temperatures in order to detect any temperature-dependent effects, while the EC was measured at a single temperature as it is assumed to have a similar behaviour. Furthermore, after the initial measurements, each sample is subjected to the appropriate thermal treatment in order to study the effects of annealing on the material properties. The heat treatment involved heating the samples a rate of 300 °C/h up to temperatures of 300 °C for AlSi10Mg and 1200 °C for Fe-Si, holding them at these temperatures for two and one hours, respectively, followed by slow furnace cooling.

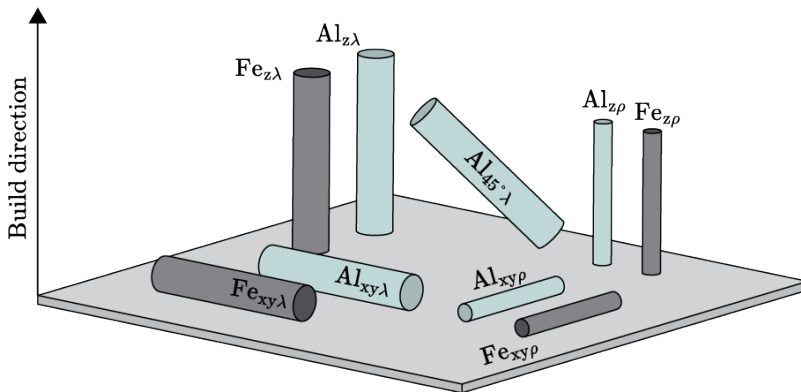


Figure 2.2. LPBF samples for measuring the effect of build orientation on TC and EC [39].

Table 2.2. Results of the conductivity measurements.

Sample	Thermal conductivity at 35° C (W/(m·K))	Thermal conductivity at 70° C (W/(m·K))	Electrical conductivity at 20° C (MS/m)
Al <sub>z</sub> as built	113.3 ± 3.1	116.2 ± 1.8	14.70 ± 0.27
Al <sub>z</sub> annealed	148.2 ± 3.5	149.5 ± 2.3	23.88 ± 0.50
Al <sub>45°</sub> as built	103.0 ± 3.2	106.9 ± 1.7	-
Al <sub>45°</sub> annealed	148.5 ± 3.7	149.9 ± 2.4	-
Al <sub>xy</sub> as built	106.7 ± 3.5	108.0 ± 2.0	13.08 ± 0.36
Al <sub>x</sub> annealed	148.2 ± 3.8	149.8 ± 2.3	24.72 ± 0.86
Fe <sub>z</sub> as built	25.3 ± 0.8	27.0 ± 0.4	1.76 ± 0.03
Fe <sub>z</sub> annealed	25.0 ± 0.7	26.6 ± 0.4	1.78 ± 0.03
Fe <sub>xy</sub> as built	25.4 ± 0.7	26.9 ± 0.4	1.76 ± 0.03
Fe <sub>xy</sub> annealed	24.6 ± 0.8	26.0 ± 0.4	1.77 ± 0.03

Looking at the as-built samples, significant anisotropy can be seen in the AlSi10Mg results, with a 10% higher TC and a 12% higher EC in the z-direction compared to xy (interestingly, the TC of the 45° sample is similar to the xy-sample, suggesting that the anisotropic effects are not a simple function of manufacturing orientation). After annealing, however, the TC and EC of each sample increases significantly (38% and 76% respectively), and the differences effectively disappear. While this clearly demonstrates the importance of heat treatment in the material, the proportionally much higher increase of EC means that heat treatment could be disadvantageous in thermal solutions where eddy currents are a major factor (e.g. direct conductor cooling). In any case, the final conductivities are consistent with known values for the material, meaning that the LPBF prototypes (which are all subjected to heat treatment) created in the subsequent works included in the thesis are assumed to be fully dense and a fixed value of  $\lambda_{Al} = 150 \text{ W/(m·K)}$  is used throughout (the temperature-dependence of the conductivity is too small to justify increasing the complexity of the models).

The silicon steel samples, on the other hand, display consistent conductivity regardless of build direction or heat treatment. This is contrary to its magnetic properties that have been shown to be anisotropic in the literature [40], although this is also alleviated through heat treatment (this is due to grain size being extremely relevant for magnetic properties but not conductivity). In comparison to a commercial 3.0% Si electrical steel (28 W/(m·K) [41]), the measured TC of the AM material is somewhat lower, which is expected due to the larger Si content.

Overall, the results suggest that heat-treatment of the aluminium alloy is important for achieving maximal and isotropic conductivity values. However, if heat-treatment is not available (as would be likely in the case of a multi-material part), the anisotropic material properties must be accounted for in the design process. In terms of Fe-Si, the results mean that the manufacturing direction of LPBF Silicon steel cores should be chosen based on mechanical and post-processing limitations (these become highly relevant when laminated structures are considered).

## 2.3 Additively Manufactured Thermal Management Solutions for Electrical Machines

The goal of an EM thermal management solution is the removal of heat, generated by various losses inside the machine, to the external environment. In the case of more demanding requirements for power density, which is largely a function of maximum current density, the need for more effective cooling quickly increases ( $p = j^2 \rho_E$ ) in order to maintain reliability and efficiency ( $\rho_E \propto T$ ). When modelling electrical machines, the thermal solution is often represented using a lumped parameter network i.e. a thermal circuit, where each of the important elements is represented as either a heat source or a thermal resistance. A typical thermal circuit for an EM is shown in Figure 2.3, where a distinction between internal thermal resistance  $\mathcal{R}_0$  and the heatsink's thermal resistance  $\mathcal{R}_{HS}$  is made.

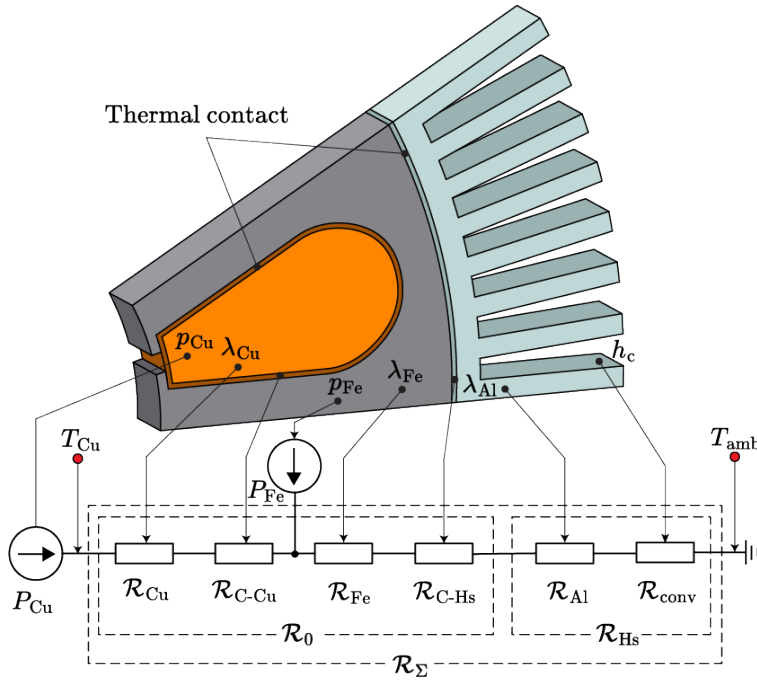


Figure 2.3. Thermal circuit of a conventional electrical machine stator overlaid on the physical geometry.

In any thermal management solution for EM, the heat generated in the machine by various losses is expelled into the surrounding environment through a heat exchanger (HE). By considering the HE as a separate part, the thermal system can be divided into two distinct regions:  $\mathcal{R}_0$  or the solid internal part of the machine where the heat flow is conductive, and  $\mathcal{R}_{HS}$  or the active part of the HE where mainly convection is relevant. While the internal resistance is dependent on the machine's topology and materials, the heatsink's resistance arises mainly from the interaction between its outer surface and the surrounding air. In most electrical motors, air-cooling is used, in which case the HE is directly attached to the stator. When the loss density of the EM surpasses the capabilities of air-cooling, the next solution is liquid-cooling. In that case, heat is transferred from the motor to the HE via a liquid loop, which increases the surface area of the HE

that can be effectively utilized (phase-change methods such as heat pipes achieve the same effect at even higher heat flux densities). Furthermore, as most of the heat in an EM is generated in the windings (which are also the most susceptible to high temperatures due to insulation thermal degradation.), it is useful to define a third category called direct conductor cooling (DCC). In that case, the cooling element, which could utilize either air- or liquid-cooling, is in direct contact with the conductor, effectively bypassing the thermal resistance of the magnetic core and in some cases the electrical insulation.

In the field of AM thermal solutions for EM, the category most represented in the literature is DCC, which is likely due to its potential for achieving the highest current density values. There, the capabilities of AM are generally used to create either components shaped according to the complicated winding geometry or redesign the winding entirely with cooling in mind. Both liquid- and air-cooling, which have gotten significant interest in the *general* AM space, are underrepresented in the EM field. When looking at AM-based air- and liquid-cooling solutions in general, the designs are characterized by complex structures, for which conventional manufacturing is deeply impractical or in some cases impossible. These include algorithmically optimized designs, which can significantly differ from human intuition, or intricate lattice structures, which take full advantage of the design freedom offered by AM through tiny feature sizes and omnidirectional geometries. However, in the specific field of EM cooling, the use of these methods is not fully explored.

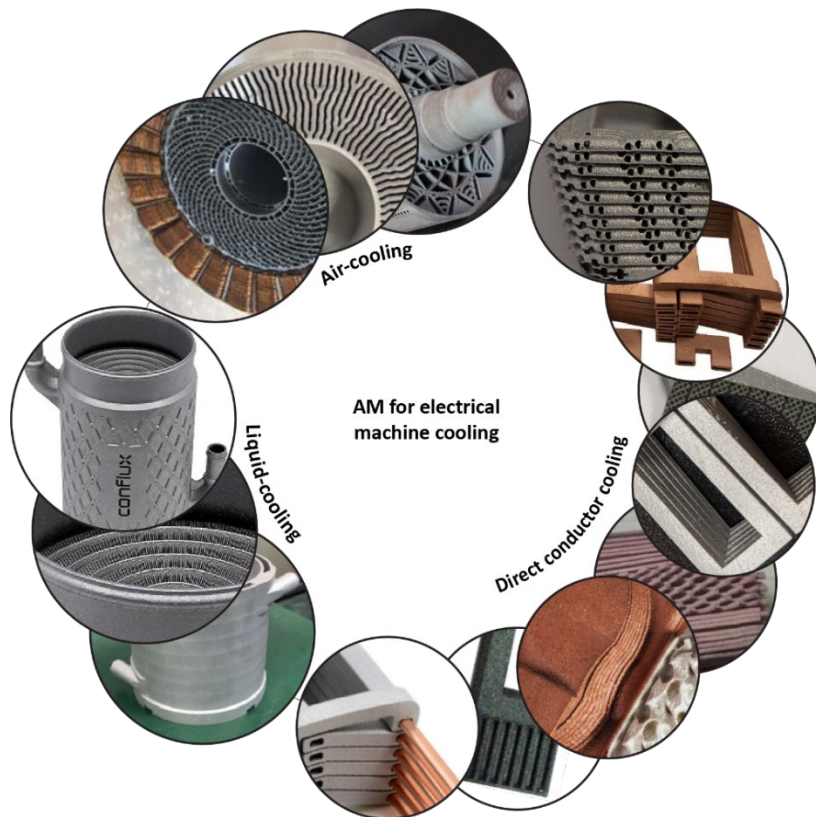


Figure 2.4. Various cooling methods for electrical machines. [42–54]

The three EM cooling categories together with specific AM examples (in cases where literature describing physical prototypes can be found) are illustrated in Figure 2.4. The trend of focusing on DCC is apparent from the high number of works available, while air- and liquid-cooling categories contain only a few examples. The figure also includes the category of geometry generation used in the thermal solution, which is used to illustrate the specific classification of the original work presented in this thesis. While air- and liquid-cooling are both in need of further development, the original work focuses on air-cooling due to its wider applicability in different systems and a lesser reliance on external devices (e.g. water pumps and fluid loops).

### 2.3.1 AM for Air-Cooled Electrical Machines

Air-cooled electrical machines typically cool the stator using a heatsink that expels the generated heat into the external air. Due to the low TC of air, the temperature gradient outside the heatsink's fins is extremely high, meaning that the fin is only effectively expelling heat (through conduction) to a small volume of air called the boundary layer. The key to a heatsink's performance is the minimization of the boundary layer's insulating effect in order to quickly move the warm air away from the fin surface, i.e. creating convective heat flow. This is visualized in Figure 2.5 by modelling convective flux around the fins of two different designs. Conventional heatsink designs (e.g. the straight plate fins shown in (a)), generally aim to create a thinner boundary layer by maximizing flow velocity ( $\delta \propto v^{-1/2}$ ) through relatively open and straightforward structures that promote laminar flow. An added benefit is that typical straight plate fins tend to result in a large effective surface area for heat flux. Alternatively, the boundary layer can also be disrupted directly by encouraging turbulent mixing inside the fin structure. This is typically done by including surfaces with a tangential component in the fin structure (e.g. the pin fin heatsink shown in (b)) that essentially block some of the airflow. This comes at a cost of lower air velocity due to the added drag, which means that the two methods of dealing with the boundary layer are inherently contradictory. Therefore, it can be stated that the optimal fin structure should have a perfect balance between drag and turbulence (while having enough surface area to effectively facilitate heat transfer).

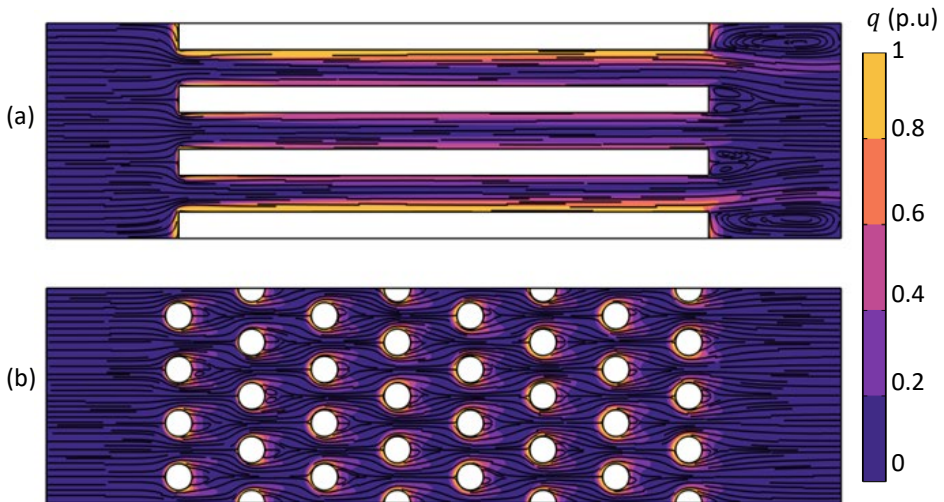


Figure 2.5. 2D illustration of conductive heat flux density around the solid fin structures of a straight finned heatsink (a) and a pin fin heatsink (b). Note the comparatively high amount of turbulence (shown by the black lines) inside the pin fin structure.

Designing air-cooled heatsinks with the freedom of AM in mind means replacing simple structures, which are primarily defined by manufacturing constraints, with advanced geometries that have no such limitations. The advanced structures can improve thermal performance through increased flow velocity, encouraging turbulence (however the literature is heavily skewed towards the latter), or ideally a combination of both. For example, the shape of the fin can be modified to decrease the drag and create a thinner boundary layer through faster flow. In some cases, this can be done without sacrificing conduction in the fin by only removing areas with low heat flux density (e.g. gradually thinning the fins farther from the base). Alternatively, turbulence can be encouraged by designing a fin structure with intricate shapes and flow channels, resulting in complex geometries (e.g. lattice structures) that can practically only be produced by AM.

In terms of creating the necessary airflow through the fin structure, air-cooling is commonly divided into two groups – passive and active cooling. Both are relevant for electrical machines (although active air-cooling is much more prevalent) and can benefit from AM by introducing novel fin structures that improve thermal performance.

### **2.3.2 AM Passive Air-Coolers**

Passive air-coolers represent the simplest cooling method as the entirety of the airflow is created by convective currents, eliminating the need for moving parts. While passive cooling is often used when power density is not a concern, advanced passive cooling solutions become relevant in applications that are restrictive in terms of noise or the number of moving parts. Due to the lack of external pumping power, maximizing thermal performance tends to be much more dependent on minimizing drag rather than promoting turbulence, which is in any case minimal in buoyancy driven flow. Minimizing drag while maximizing heat flux is a heavily geometry-dependent and often non-intuitive task, meaning that conventional design principles based on known empirical correlations are not sufficient for novel AM-based solutions. This forces researchers towards computationally expensive numerical optimization methods. As a result, a large part of the literature for passive cooling solutions for general [55] and specific [56] cases are often based on algorithmic methods of determining optimal material distribution in terms of maximum cooling performance.

However, in the narrow field of EM thermal research, the utilization of AM for passive cooling is underdeveloped, as a review of the literature reveals only a single example [57] based on simulations with a simplified method of average convection coefficients instead of modelling the fluid explicitly. In order to provide preliminary data in this research gap, the published work III “Analysis of Advanced Passive Heatsinks for Electrical Machines Enabled by Additive Manufacturing” is included as a part of this thesis.

### **2.3.3 AM Active Air-Coolers**

Actively air-cooled heatsinks employ a fan to generate airflow in order to increase heat flux from the heatsink surface by approximately an order of magnitude. The higher power density associated with actively cooled heatsinks has generated somewhat more interest in the AM electrical machine community, with three articles based on AM prototypes being available. Two of these describe LPBF AlSi10Mg heatsinks for outer rotor machines. The first one [42] utilizes curved fins connected to each other with lattices. Its final shape is determined with the help of a CFD model, although without a specific optimization method. The second one [43] includes axially straight fins, which are given an organically flowing shape based on parametric optimization in CFD. The third

article [44] introduces a lightweight (inner) rotor for a permanent magnet motor, in which the weight-saving voids act as cooling channels. In this case, a complex triangular geometry, attempting to satisfy mechanical, thermal and electromagnetic requirements is chosen and manufactured from an unspecified steel alloy using LPBF.

The common element in the aforementioned articles is their preliminary nature. While it is shown that AM can be used to produce a working EM thermal solution, the lack of a thorough comparison to a conventional solution means that the advantages of doing so are not sufficiently demonstrated. Therefore, the research field of AM actively air-cooled solutions for EM is advanced further by the published works IV and V “Design of an Additively Manufactured Thermal Solution for an Axial Flux Switched Reluctance Motor” and “Comparative Study of Advanced Heatsink Structures for Improved Thermal Performance in Axial Flux Motors” respectively. In these works, several different fin structures, chosen for either maximizing airflow or encouraging turbulence, are manufactured using LPBF and compared against a thoroughly optimized conventional case. Furthermore, in the published work VI “Additively Manufactured and Topology Optimized Heatsink for a Propulsion Motor”, both performance parameters are optimized simultaneously through topology optimization. This article, which introduces a method of optimizing a heatsink for an electric propulsion drive, is the only example in the literature where a topology optimized actively air-cooled heatsink geometry is verified using a physical prototype.

### **2.3.4 AM for Liquid- and Direct Conductor Cooling**

A similar balance between flow and turbulence exists for liquid cooling as well (both in the cooling block and external heat exchanger), however the generally higher pumping power pushes the optimal design farther in favour of encouraging turbulence. In electrical machines, the typical method of applying liquid cooling is through a cooling jacket mounted on the outside of the motor, similar to an air-cooler. However, while optimized liquid-cooling systems are prevalent in the general AM space, no examples of academic literature exist for AM cooling jackets (or similar solutions) specifically. The lack of interest is likely due the relatively low potential gains available by optimizing the cooling jacket as in that case the internal thermal resistance dominates the thermal circuit. This, however, is solved through direct conductor cooling, which is consequently the most popular cooling method in the AM EM space.

By cooling the conductors directly, the thermal resistance of the core and insulation are partially or entirely mitigated. As a result, exceedingly high current densities of  $> 17$  [48] and  $> 100 \text{ A/mm}^2$  [49] can be sustained if DCC is paired with air- or liquid-cooling respectively. For employing DCC, AM is used in two distinct ways. The first of these is through separate heat exchangers, which are attached on the windings and carry the heat away either through air- or liquid-cooling. In the case where the HEs are manufactured from an electrically conductive material (such as AlSi10Mg), the rapidly changing magnetic field near the windings induce strong eddy currents in the HE material, which can more than offset any gains from cooling [46]. However, AM can be used to create HEs with laminated structures, which effectively reduce eddy current losses without sacrificing much thermal performance. Alternatively, the HE can be manufactured from an electrically non-conductive material such as a polymer [58] or  $\text{Al}_2\text{O}_3$  [28], in which case the HE has no electromagnetic effect. While these solutions achieve substantial performance gains by eliminating the resistance of the core material from the thermal circuit, the low effective thermal conductivity of the winding structure

is still a major limitation. The second way AM can be used to employ DCC is by designing the entire winding with thermal aspects in mind. Either by modifying the geometry so that the heatsink is in direct contact with each winding turn, or alternatively, integrating the cooling element directly into the winding design. In both cases, as an added benefit, the AM winding can be specifically dimensioned according to the geometry of the stator slot in order to achieve a high fill factor.

In summary, AM methods such as LPBF can be used to manufacture materials with high conductivity-to-weight ratios that are perfectly suitable for EM thermal solutions. By applying the inherent design freedom of AM through optimized geometries and novel approaches, the thermal performance of electrical machines can be substantially increased, leading to increased power density, efficiency and reliability. Irrespective of the cooling method used, be it indirect air- or direct conductor cooling, thermal solutions created for specifically AM are characterized by complex geometries, which have hitherto been considered non-viable for conventional manufacturing methods. In the next chapter, the analysis, methods and results concerning the published works III–VI are presented. These articles aim to advance the field of AM for EM cooling further by introducing novel geometries and methods for improved thermal management, together with measurement results based on physical AM prototypes and fair comparisons to conventional solutions.



### 3 Advanced Fin Structures for Air-Cooled Electrical Machines Enabled by AM

The advantages of AM in the context of air-cooled electrical machines are most saliently expressed through advanced fin structures. By expanding the possible solution space beyond simple conventional fins, and considering all three-dimensional shapes, advanced fin structures with improved thermal performance (i.e. reduced  $\mathcal{R}_{\text{Hs}}$ ) can be identified. Currently, the available literature consists of mostly preliminary work looking at (often arbitrarily chosen) shapes such as different lattice structures and airfoils in a general thermal context. While some promising shapes have been identified, the preliminary nature of the work does not allow concrete statements to be made. Therefore, the primary aim of this chapter is to use simulation and measurement results to evaluate the effectiveness of the more promising advanced structures. Crucially, in order to provide relevant conclusions, this work includes fair comparisons to conventional solutions (i.e. straight fins) that have been dimensioned based on comprehensive semi-analytical workflows.

In the first part of the chapter, AM-based design is explored in the context of a passively cooled motor. In this case, a conventional annular heatsink with a design based on a semi analytical model is compared to several different advanced designs, showing that AM can be beneficial both by subtly altering the conventional design or by introducing a significantly altered fin geometry. As passive cooling involves low speed and laminar airflow, accurate comparative results can be obtained through simulations alone. Therefore, the first part of this chapter is fully based on a nonisothermal CFD model and introduces the numerical modelling methods that each of the subsequent works rely on.

The results obtained by modelling the passive heatsink are used in the second part of the chapter to guide the design of a novel thermal solution for an actively air-cooled axial flux motor. In this case, in addition to minimizing  $\mathcal{R}_{\text{Hs}}$  through advanced fin structures, the open nature of the axial flux topology is exploited to also minimize  $\mathcal{R}_0$  by effectively eliminating a part of the thermal circuit. Because the turbulence-based effects associated with active-cooling (especially in the case of advanced structures) and the contact resistances associated with  $\mathcal{R}_0$  are exceedingly difficult to model accurately, this work relies on physical LPBF prototypes to form conclusions.

#### 3.1 Advanced AM Fin Structures for Passive Heatsinks

##### 3.1.1 SRM Parameters

The heatsinks considered in this work are modelled in the context of cooling a small ( $\sim 100$  W nominal power depending on the cooling) 6/4 configuration switched reluctance motor (SRM) with an AM Fe-Si core and hand-wound concentrated windings. The motor shown in Figure 3.1 with the conventional annular heatsink has a stack length of 46 mm and an outer stator diameter of 80 mm. A cylindrical passively cooled heatsink, matching the stack length, is added on stator's outer surface. It consists of a 2 mm thick base and a radial fin structure with an arbitrarily chosen length of 10 mm. These measurements are kept constant between the different fin designs. The other relevant parameters of the SRM prototype are given in Table 3.1.

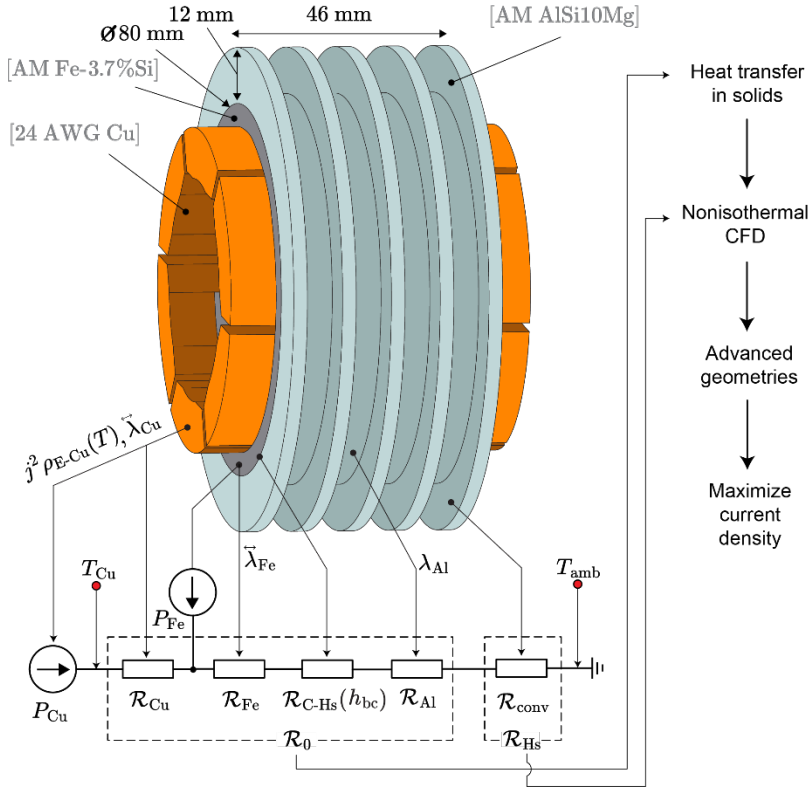


Figure 3.1. 3D model of the SRM stator and the simplified thermal network together with the methods used to find  $\mathcal{R}_0$  and  $\mathcal{R}_{Hs}$ .

Table 3.1. Important parameters of the SRM.

Parameter	Symbol	Value
Stator iron mass	$M_{Fe-S}$	0.51 kg
Iron loss density	$p_{Fe}$	10 W/kg [25]
Winding fill factor	$k_{ffw}$	50%
Core fill factor	$k_{ffc}$	60%
Nominal electrical frequency	$f_E$	50 Hz

The thermal circuit of the SRM is typical for a radial flux machine, where all of the elements have an appreciable effect on the entire system. This work focuses on minimizing  $\mathcal{R}_{Hs}$ , which is the thermal resistance associated specifically with the heat transfer from the outer surface of the heatsink to the surrounding air. As the heatsink is only passively cooled,  $\mathcal{R}_{Hs}$  has a relatively large value, limiting  $j_{Cu}$ . However, in terms of optimization, this provides an excellent opportunity for improvement as even a small relative improvement in  $\mathcal{R}_{Hs}$  will have a considerable effect on  $\mathcal{R}_\Sigma$ .

### 3.1.2 Advanced Fin Designs for Passive Heatsinks

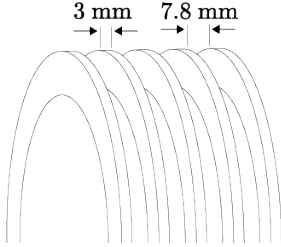
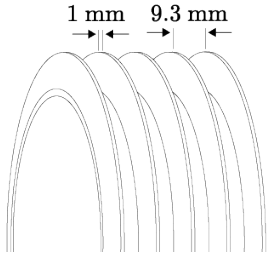
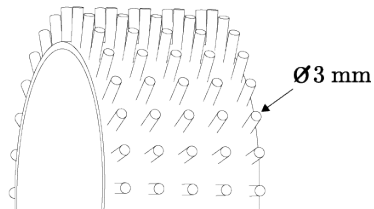
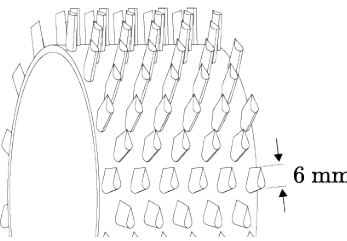
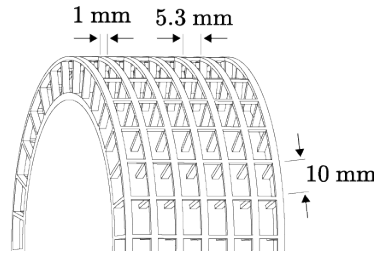
The common element among effective passive heatsinks is a low drag that is achieved through a sparse fin structure. While denser structures offer higher surface area, and intricate designs can encourage boundary layer disruption, the low effective pumping power of buoyancy driven flow is typically unable to take advantage of these effects. The optimization of passively cooled heatsinks is therefore mostly a question of maximizing airflow, even if it means a relatively low fin surface area. This is illustrated well by the conventional solution, which for a passively cooled cylindrical shape is a heatsink with simple annular fins. This type of structure provides minimal drag in the vertical direction, allowing air currents to form around the heatsink. In this study, the design of the annular heatsink is based on a general empirical model by Wang et al [59], resulting in 5 equally spaced fins with a thickness of 4 mm.

For the second solution, a direct improvement on the conventional case is considered in the form of a hyperbolic fin, which is based on the work of Mallick et al [60]. Shaping the fins according to a hyperbolic curve increases the area of the flow channel by gradually reducing the thickness of the fin as the radius increases. As the heat flux density is always lower near the tip of the fin, this does not substantially impede heat flow. However, the wider flow channel near the tip *does* increase total airflow due to viscous shear (faster air on the outside effectively drags the inner air with it), resulting in more effective cooling.

In the third and fourth solutions, the annular fins are segmented into 28 (this value is chosen to create a roughly even spacing in both directions) separate parts, creating a pin fin heatsink structure. Among conventional air-cooled heatsink types, pin fins are often the highest-performing due to increased flow channel area created by the additional gaps. This, understandably, comes at the cost of reduced volume for conductive flux, however, in the case of reasonably conductive materials (e.g. AlSi10Mg), it tends to be a beneficial trade-off. In the third solution, round pins are used, representing the high-end of conventionally manufactured geometries. The fourth solution takes somewhat more advantage of AM by shaping the pins according to NACA 4424 airfoils. The airfoil pin fins, which are inherently designed to be aerodynamic and have proven to be effective for cooling [61], further decrease the total aerodynamic drag of the structure, enabling faster currents to form. As an additional improvement, enabled by the low drag of the pins, the airfoil array is staggered in order to increase the total interaction with the moving air.

Finally, in the fifth solution, a cubic strut-based lattice is used as the fin structure. In this case, aerodynamic drag is substantially increased in favour of promoting direct boundary layer disruption. This lattice structure, which is in general opposed to typical design principles, is representative of the geometries that are popular in the wider AM thermal research space. In this case, its geometrical dimensions are defined in order to roughly match the conventional solution, which results in a relatively sparse lattice (compared to the popular literature). Each of the aforementioned structures are presented in Table 3.2 together with the values for fin area and volume. Note that  $V_{HS}$  consists of only the fin structure and not the cylindrical base of each heatsink to illustrate the difference more clearly.

Table 3.2. Advanced fin structures modelled.

Fin Structure	Geometrical Parameters	Characteristic Geometry
Simple annular fins	$A_{\text{HS}} = 436 \text{ cm}^2$ $V_{\text{HS}} = 44.3 \text{ cm}^3$	
Hyperbolic annular fins	$A_{\text{HS}} = 386 \text{ mm}^2$ $V_{\text{HS}} = 30.4 \text{ cm}^3$	
Round pin fins	$A_{\text{HS}} = 308 \text{ mm}^2$ $V_{\text{HS}} = 11.6 \text{ cm}^3$	
Airfoil pin fins	$A_{\text{HS}} = 352 \text{ mm}^2$ $V_{\text{HS}} = 14.3 \text{ cm}^3$	
Cubic lattice	$A_{\text{HS}} = 548 \text{ mm}^2$ $V_{\text{HS}} = 9.27 \text{ cm}^3$	

### 3.1.3 SRM Thermal Model

In order to accurately model the performance of the proposed heatsinks, and correlate the results to a specific current density, a 3D finite element model (FEM) based on the motor geometry is created. This model includes two parts – heat generation and transfer in the solid materials, used to model  $\mathcal{R}_0$ , and heat transfer and fluid flow around the heatsink, used to model  $\mathcal{R}_{\text{HS}}$ . Since only the steady-state performance of the system is of interest (for a passively cooled motor, the peak loading capabilities are almost entirely dependent on the stator's thermal capacity), all time-dependent effects are disregarded. Similarly, radiative effects, which do not meaningfully differ among the proposed heatsink designs, are disregarded. Finally, throughout the modelling process, the rotor is omitted as its iron losses and the heat transfer across the airgap of the motor is considered negligible.

#### 3.1.3.1 Heat Transfer in Solids

The temperature distribution inside a solid domain is fully defined by the heat equation:

$$\frac{\partial T}{\partial t} = \alpha \nabla^2 T. \quad (3.1)$$

In the case of a stationary problem, terms with time derivatives disappear, and the thermal diffusivity of the material is reduced to only thermal conductivity. For a volume containing heat generation, the problem simplifies into Poisson's equation:

$$\nabla \cdot (-\lambda \nabla T) = p. \quad (3.2)$$

Substituting in Fourier's law ( $\mathbf{q} = -\lambda \nabla T$ ) gives the heat balance equation, which is solved for in the solid domain of the numerical model.

$$\nabla \cdot \mathbf{q} = p. \quad (3.3)$$

In this case, as both the winding and core are thermally anisotropic due to stranded and laminated structures respectively, two thermal conductivity tensors are introduced. The directional TC values for the winding structure are based on its fill factor, in which case the axial component is found simply by multiplying  $k_{\text{ffw}}$  with  $\lambda_{\text{Cu}}$ . The radial components are taken as the effective value for a relatively low fill factor coil at 0.1 W/(m·K) [62]. For the AM Fe-Si core, the in-plane components are defined by the measurements from the previous chapter in conjunction with  $k_{\text{ffc}}$ , and the out-of-plane component at 1 W/(m·K) based on typical laminated cores [63]:

$$\lambda_{\text{Cu}} = \begin{bmatrix} 0.1 & 0 & 0 \\ 0 & 0.1 & 0 \\ 0 & 0 & 200 \end{bmatrix}, \quad \lambda_{\text{Fe}} = \begin{bmatrix} 16 & 0 & 0 \\ 0 & 16 & 0 \\ 0 & 0 & 1 \end{bmatrix}, \quad (3.4)$$

where the z-direction coincides with the motor's axis for the core and the active part of the winding, and perpendicular to the motor's radius and axis in the end-winding region. The winding and core regions (no eddy-current losses are assumed in the heatsink) are further described by heat generation due to Joule heating and hysteresis losses. This is calculated in both regions based on the motor's nominal parameters given in Table 3.1; the core loss density based on average iron losses for the material at the

nominal frequency and magnetic flux density, and copper loss density using temperature-dependent electrical resistivity and the winding fill factor:

$$P_{\text{Cu}} = k_{\text{ffw}} \int_{\text{Cu}} j_{\text{Cu}}^2 \rho_{\text{E}}(T). \quad (3.5)$$

Contact thermal resistance between the stator and heatsink is included in the model (no thermal contact resistance is added between the winding and stator as it is incorporated in the effective TC value of the winding). Numerically, it is modelled through a boundary conductance, the value of which can be in a wide range depending on materials, finishes and tolerances. In this case, a typical value of  $h_{\text{BC}} = 4500 \text{ W(m}^2\text{K)}$  taken from the literature [62] for contact between steel and aluminium is used.

$$\mathbf{n} \cdot \mathbf{q} = h_{\text{BC}}(T_1 - T_2). \quad (3.6)$$

Initially, the model is solved by setting a constant temperature on the outer surface of the heatsink base, in which case  $\mathcal{R}_{\text{HS}} = 0$  and only the internal thermal resistance of the system is present. As the location of the hotspot can be assumed to always be in the windings for typical radial motors, it is not necessary to extract each specific  $\mathcal{R}$  value (which are in any case somewhat arbitrarily defined for complex geometries). Instead, the model is used to simply define an approximate  $\mathcal{R}_0$ , which can be used to correlate a given  $\mathcal{R}_{\text{HS}}$  with a winding current density. Based on the results shown in Figure 3.2, the hotspot temperature increase at a total heat load of 17 W ( $j_{\text{Cu}} = 7.5 \text{ A/mm}^2$ ,  $f = 50 \text{ Hz}$ ) is 38.1 °C, resulting in  $\mathcal{R}_0 = 2.2 \text{ K/W}$ . It should be noted that due to  $\rho_{\text{E-Cu}}(T)$ ,  $\mathcal{R}_0$  will have a slightly different value according to  $j_{\text{Cu}}$ .

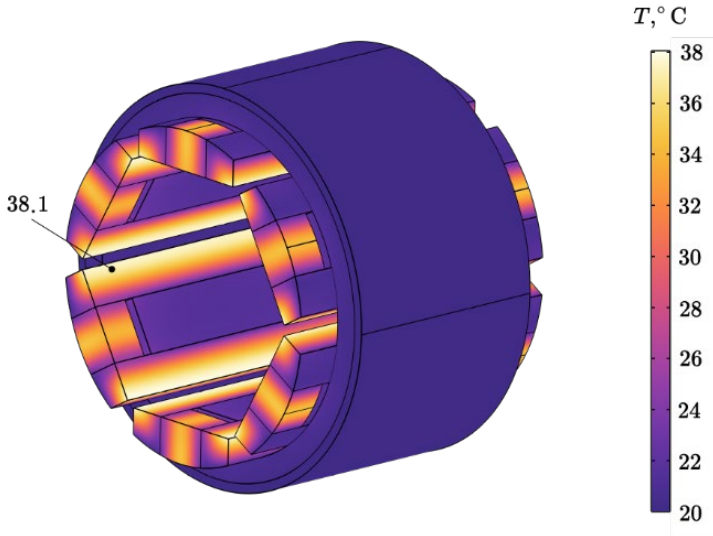


Figure 3.2. Temperature distribution in the SRM stator with only internal thermal resistance present.

### 3.1.3.2 Heat Transfer in Fluids

The  $\mathcal{R}_{\text{Hs}}$  component summarizes the performance of the heatsink fin structure and therefore depends on the surrounding airflow. In the fluid domain of the thermal model, the heat balance equation (3.3) is modified by adding a second term representing the heat flux associated with the moving air. On the right side, as there are no heat sources in the fluid ( $p = 0$ ) and viscous dissipation ( $\mathbf{K} : \nabla \mathbf{u} \approx 0$ ) is disregarded (acceptable for low-velocity airflow [64]), only a term representing the work done by thermal expansion remains.

$$\rho c_p \mathbf{u} \cdot \nabla T + \nabla \cdot \mathbf{q} = \alpha_p T (\mathbf{u} \cdot \nabla p). \quad (3.7)$$

The steady-state velocity field  $\mathbf{u}$  describing the laminar fluid flow is calculated using a standard formulation of Navier-Stokes equations in the case of incompressible flow (in which case  $\nabla \cdot (\rho \mathbf{u}) = 0$ ). The resulting momentum equation is as follows:

$$\rho (\mathbf{u} \cdot \nabla) \mathbf{u} = -\nabla p \mathbf{I} + \nabla \cdot \mathbf{K} + \rho \mathbf{g}, \quad (3.8)$$

where  $\mathbf{K} = \mu (\nabla \mathbf{u} + (\nabla \mathbf{u})^T) - 2/3 \mu (\nabla \cdot \mathbf{u}) \mathbf{I}$  is the viscous stress tensor, and the external force term is defined entirely by gravitational acceleration. Of course, the density of the fluid needs to be defined as a function of temperature in order to create buoyant flow:

$$\rho(T) = \frac{p_A}{R_S T}. \quad (3.9)$$

### 3.1.4 SRM Nonisothermal Fluid Model

Geometrically, the full model, which consists of both the solid and fluid parts, is constructed by adding a large volume of air around the stator, for which the dimensions are shown in Figure 3.3. The sides of the air domain are defined as open boundaries and a constant temperature of 20° C, while the top surface is defined as the outlet ( $p = 1$  atm). In order to model a realistic situation in all directions, a zero-conductivity flat body is added beneath the motor to act as a generic surface. Computational effort is effectively focused by defining a higher mesh density around the heatsink volume where the temperature and pressure gradients are the highest. In total, the model consists of approximately  $10^6$  mesh elements. Finally, the interior of the SRM is separated from the fluid by attaching zero-conductivity endcaps to the stator.

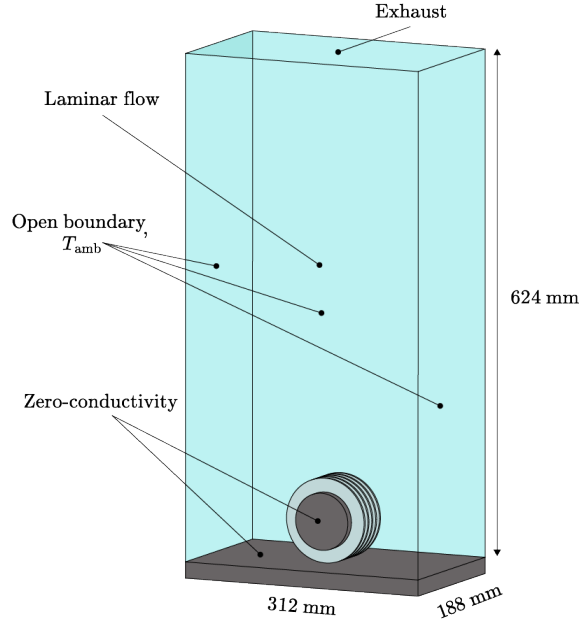


Figure 3.3. Nonisothermal CFD setup of the SRM stator.

Solving the numerical model results in a steady state velocity and temperature fields, the former of which is presented for the simple annular fins in Figure 3.4 together with an illustration of the airflow inside the fin structure, and the latter for each heatsink in Table 3.3. The velocity field, which is plotted on a single  $xz$  plane, is indicative of total airflow and therefore a proxy for performance, although fully relevant only when comparing similar designs. The maximum temperature increase is used to calculate  $\mathcal{R}_\Sigma$ , which determines current density for a given temperature increase (in this case 80 °C is chosen arbitrarily). By subtracting  $\mathcal{R}_0$  from  $\mathcal{R}_\Sigma$ , the performance of the different heatsinks can be compared directly through  $\mathcal{R}_{\text{HS}}$ .

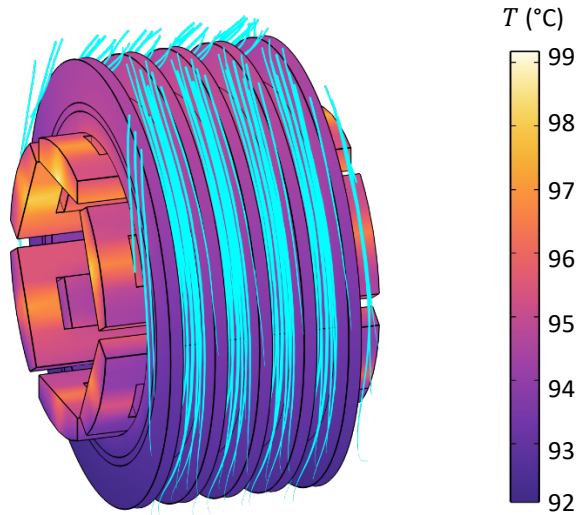
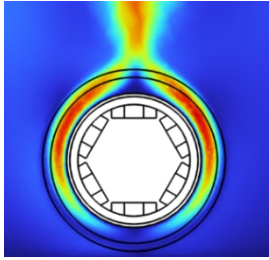
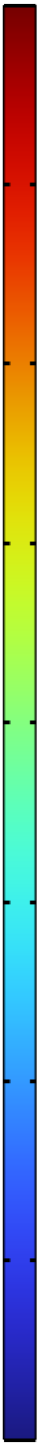
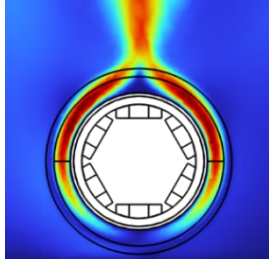
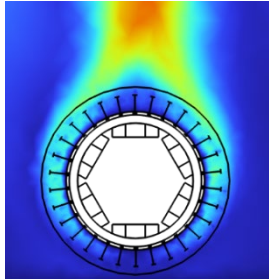
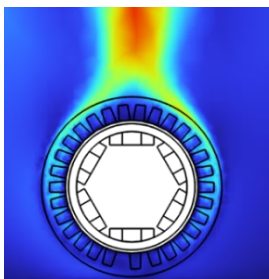
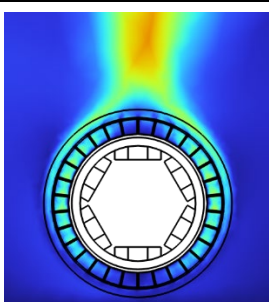


Figure 3.4. Resulting temperature distribution and airflow for the simple annular fins.



Table 3.3. Results of the nonisothermal CFD model [65].

Fin Structure	Resulting values	Velocity distribution	$v$ (m/s)
Simple annular fins	$\Delta T_{Cu} = 90.9\text{ }^{\circ}\text{C}$ $\mathcal{R}_{Hs} = 4.32\text{ K/W}$ $j_{\Delta 80^{\circ}\text{C}} = 6.95\text{ A/mm}^2$		
Hyperbolic annular fins	$\Delta T_{Cu} = 86.9\text{ }^{\circ}\text{C}$ $\mathcal{R}_{Hs} = 4.09\text{ K/W}$ $j_{\Delta 80^{\circ}\text{C}} = 7.15\text{ A/mm}^2$		
Round pin fins	$\Delta T_{Cu} = 86.8\text{ }^{\circ}\text{C}$ $\mathcal{R}_{Hs} = 4.08\text{ K/W}$ $j_{\Delta 80^{\circ}\text{C}} = 7.15\text{ A/mm}^2$		
Airfoil pin fins	$\Delta T_{Cu} = 84.8\text{ }^{\circ}\text{C}$ $\mathcal{R}_{Hs} = 3.97\text{ K/W}$ $j_{\Delta 80^{\circ}\text{C}} = 7.25\text{ A/mm}^2$		
Cubic lattice	$\Delta T_{Cu} = 93.6\text{ }^{\circ}\text{C}$ $\mathcal{R}_{Hs} = 4.48\text{ K/W}$ $j_{\Delta 80^{\circ}\text{C}} = 6.83\text{ A/mm}^2$		

### 3.1.5 Results and Conclusions of the Passive Heatsink Models

Within the results, four important comparisons can be made. First, between the annular fin heatsinks. It is clear from both the velocity distribution and the 4 °C temperature drop that contouring the fins based on a hyperbolic curve is a strict improvement in performance. As the hyperbolic fins have a 31% lower fin mass, the only reason to avoid this design would be mechanical or manufacturing constraints. In the context of the SRM, decreasing  $\mathcal{R}_{\text{Hs}}$  by 5.3% means that the current density in the conductors can be increased by 0.2 A/mm<sup>2</sup>. Secondly, the hyperbolic fins can be compared to the straight round pins. In this case, while a significant amount of material is removed from the fin structure, the thermal performance is effectively unchanged. This illustrates the general effectiveness of pin fin heatsinks, where the added flow channels, perpendicular to the main flow, increase surface interaction with the fluid. It can be assumed, that similarly to the annular fins, contouring the pins in the radial direction would similarly increase performance. Third, comparing the round pins to the airfoil pins, it can be seen that the increased number of pins and staggered formation does not result in significantly reduced airflow. Maintaining a similar airflow while increasing surface area means that the thermal resistance of the heatsink is further reduced by 2.7%, allowing a 0.1 A/mm<sup>2</sup> increase in current density. Finally, the cubic lattice severely underperforms the conventional case with a 3.7% higher  $\mathcal{R}_{\text{Hs}}$ , clearly demonstrating the unsuitability of non-airflow focused designs for passive cooling.

This study serves as an initial exploration of advanced fin structures, which aim to increase thermal performance by utilizing the design freedom of AM. By taking an empirically optimized annular fin heatsink as a starting point, gradual improvements in thermal performance are achieved by modifying the fin structure towards a more complex design. The lowest thermal resistance (8.1% improvement), and therefore the highest current density (4.3% improvement), is achieved using a pin fin heatsink with staggered airfoil-shaped pins. The high performance of the airfoil is due to the combination of a open structure with high airflow (a general property of pin fin heatsinks) and a larger effective surface area (compared to round pins). Although in principle, airfoil pin fins can have turbulence created at the tail-end of each pin, which interacts beneficially with the leading-edge of the next pin, it is unlikely to be relevant at these low velocities. In terms of thermal performance, airfoil pins show significant potential as even a solution with intuitively defined parameters outperformed the conventionally optimized annular fins. Most likely, additional improvement can be expected by optimizing the shape, count and placement of the fins. Additionally, unlike annular fins, pin fin heatsinks are also highly effective in forced-cooling applications, meaning that a similar design could be used in a wider array of applications.

However, when it comes to maximizing power density, the thermal performance of the radial flux SRM is limited on two fronts. First by its relatively high internal thermal resistance, which is an inherent consequence of its topology, and second, by its relatively low performance heatsink, which is a general consequence of passive cooling. Both of these limitations can be substantially mitigated by considering an axial flux topology and an actively air-cooled heatsink, which is the subject of the next part of this chapter.

### 3.2 Advanced AM Fin Structures for Active Heatsinks

Introducing an external airflow source in the form of a cooling fan increases the heat flux from the heatsink's surface by up to an order of magnitude, dramatically reducing  $\mathcal{R}_{HS}$ . Additionally, since the heatsink is no longer responsible for creating the airflow, a denser fin structure becomes more viable in theory. This expands the design space of effective solutions to potentially involve complex and intricate geometries, such as those based on lattice structures. In this work, the actively air-cooled heatsink is implemented on a dual rotor axial flux switched reluctance machine, providing two key benefits compared to a conventional inner rotor radial flux machine. First, in a dual rotor machine, two fans can be used in series, which doubles the pressure increase of a single fan, further increasing the potential of dense AM-based fin structure designs. Second, in the case of an axial flux topology, the heatsink can be mounted directly on the windings without sacrificing electromagnetic performance, effectively eliminating the thermal resistance elements associated with the magnetic core, as seen from the thermal circuit in Figure 3.5. Attaching the heatsink is done through an integrated AM AlSi10Mg frame, which is dimensioned specifically according to the stator core. The integrated frame and heatsink piece, in addition to the two cooling fans comprise the motor's thermal management solution, which is designed to maximize its performance-to-weight ratio.

Maximizing the performance of the thermal management solution is achieved in two distinct parts. Initially, a thorough design process following well-understood analytical and empirical correlations for a conventional finned heatsink is employed to determine the radial length of the cooling system in terms of a maximal gravimetric current density ratio for the motor (in lieu of power density as calculating that requires an entire electromagnetic workflow). The second part involves determining a superior AM-enabled alternative to the conventional fin structure while keeping the outer dimensions invariant. This is achieved by comparing several different fin designs to the optimized conventional solution. In this case, instead of numerical simulations (which become significantly less accurate at higher flow velocities), the performance of each heatsink is evaluated with the help of an AM prototype using a motorette to create the heat load and a pair of cooling fans to generate airflow.

#### 3.2.1 Axial Flux Switched Reluctance Motor Prototype

The proposed solution, designed for an in-house designed and additively manufactured (Fe-Si core) dual-rotor yokeless axial flux switched reluctance motor (AFSRM). The stator of the motor consists of mechanically separate LPBF high-silicon steel core elements wound with round copper wire. The segments are surrounded in the radial direction by the AM AlSi10Mg frame, which provides cooling and structural integrity, and in the axial direction with reinforcing plates. The frame that encloses the wound stator segments is extended radially to form a heatsink, cooling the stator with the help of two fans mounted on the rotors. The resulting exceptionally short thermal path from the winding relies on the unique geometry of axial flux machines and allows for exceptionally high current densities without the need for liquid cooling. By attaching a fan to each rotor, the airflow through the fin structure is provided by two fans in series, which in conjunction with the relatively high operating speed of 6000 rpm creates the potential for a substantial pressure difference. Figure 3.5 presents an exploded view of the machine's components and Table 3.4 lists the important parameters.

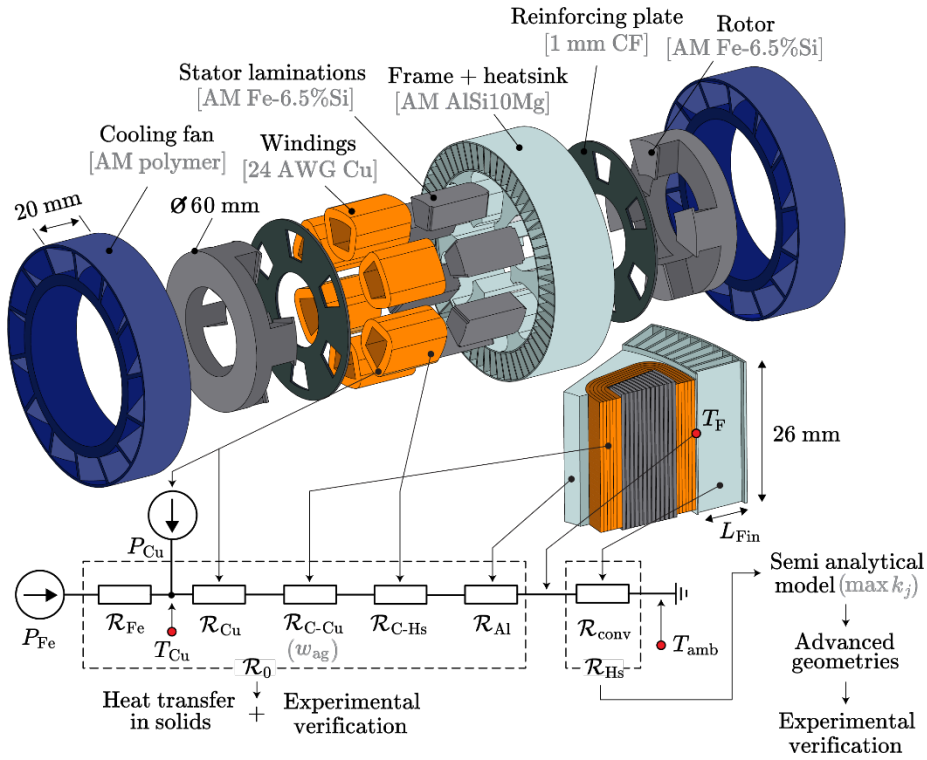


Figure 3.5. Construction of the AFSRM and the corresponding thermal circuit [66].

Table 3.4. Important parameters of the AFSRM.

Parameter	Value
Skit/pole count	6/4
Outer diameter	67.4 mm
Axial length	70.0 mm
Rated speed	6000 rpm
Maximum current density (without heatsink)	$\sim 5 \text{ A/mm}^2 \text{ rms}$
Maximum heat losses (without heatsink)	$\sim 25 \text{ W}$

Experimental data on the cooling solution's performance is gathered using a 1/6 sector of the cooling system, which is fitted over an AM high-silicon steel stator tooth prototype. The tooth is hand-wound with 230 turns of  $0.2 \text{ mm}^2$  copper wire in 6 layers, achieving a fill factor of approximately 64% and an electrical resistance of  $1.20 \Omega$ . Together, these components represent a 1/6 sector of the AFSRM stator assembly. A Pt100 temperature sensor is positioned on the inner radius of the tooth, between the slot liner and the first layer of the winding to measure the temperature  $T_{\text{Cu}}$ . This location is the most thermally isolated from the ambient air, making the sensor's reading indicative of the winding hotspot temperature. Figure 3.6 depicts the 1/6 sector of the stator and frame/heatsink combination, and the stator prototype used for testing the AM heatsink prototypes.

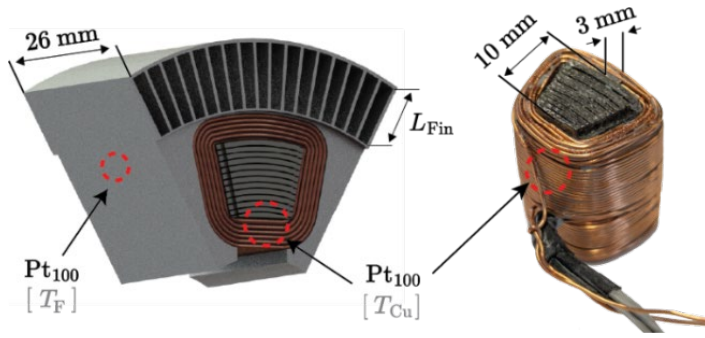


Figure 3.6. The single stator sector and the wound AM stator tooth used for experimental verification. The  $T_F$  temperature sensor is placed inside a shallow hole on the side of the frame and the  $T_{Cu}$  between the innermost winding turn and the slot liner [66].

### 3.2.2 AFSRM Thermal Model

The heat transfer in the solid material is modelled according to equations 3.1, 3.2 and 3.3 to calculate an approximate  $\mathcal{R}_0$  value, which is used to correlate  $\mathcal{R}_{HS}$  with a specific current density. This can be effectively done using a 1/6 symmetrical model of the stator, where any  $\mathcal{R}_{HS}$  can be modelled as a boundary condition on the  $S_F$  surface (acting as an imaginary boundary between the frame and heatsink). Heat flux directed radially from the core is limited by the TC anisotropy of the winding structure. In this case, a complicated TC tensor is avoided by adding a layer conductance at each boundary according to equation (3.5), where the value of  $h_{BC}$  is modelled as an equivalent layer of air with a thickness  $w_{ag}$ . For any novel solution, it is difficult to find a reliable reference value from the literature, meaning that only an approximate value based on past experience can be used, which in this case is  $w_{ag} \approx 10 \mu\text{m}$  (this is not indicating the physical thickness of the contact region but rather the equivalent airgap thickness of the contact thermal resistance). As the boundary resistances create a substantial temperature difference between  $T_{Cu}$  and  $T_F$ , an additional temperature sensor is added on the frame to calculate  $\mathcal{R}_{HS}$  (see published work V for more details).

The heat losses of a single sector are a combination of copper  $P_{Cu}$  and iron losses  $P_{Fe}$ , although to frequencies up to and well beyond the motor's operating point of 400 Hz, the heat generation is dominated by  $P_{Cu}$ . The iron losses at 400 Hz and a core flux density of 1.5 T in high-silicon steel laminations manufactured with LPBF can be estimated based on the available literature to be around 100 W/kg [59]. This results in a  $P_{Fe}$  value of 2.24 W, which is only a fraction of the estimated  $P_{Cu}$  value. Therefore, the iron losses do not significantly impact the temperature *distribution* in the slot and can be simply modelled as an additional source of heat in the thermal circuit. Furthermore, as the frequency dependent losses are relatively small compared to the DC losses, the measurements on the physical prototypes can be carried out using DC current without concern for any AC effects (other than considering the numeric value of  $P_{Fe}$  in the calculations).

Solving the model with these parameters and a current density of 25 A/mm<sup>2</sup> (30.4 W heat load per coil) results in an internal thermal resistance of approximately  $\mathcal{R}_0 = 1 \text{ K/W}$  as seen in Figure 3.7. This value is used in the analytical heatsink design procedure to determine its optimal dimensions in terms of a gravimetric current density ratio. In addition to  $\mathcal{R}_0$ , the design procedure relies on specific airflow parameters, defined by the performance characteristics of the cooling fan pair.

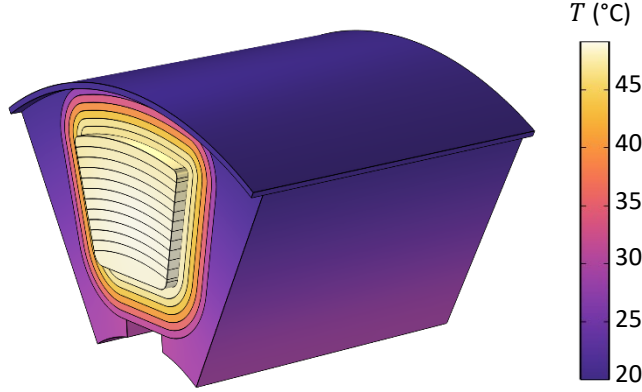


Figure 3.7. Temperature distribution in the AFSRM stator sector with only internal thermal resistance present.

### 3.2.3 AFSRM Cooling Fans

Airflow is created through the heatsink fin structure by two axial fans that are connected directly to the rotors of the machine. The blade length of the fans matches the length of the fins  $L_{Fin}$  to create a consistent outer diameter across the entire length of the motor, and the thickness of the fan is similarly equal to the thickness of the rotor. As the purpose of the fan is only to provide an appropriate amount of airflow (preliminary testing showed that cooling performance is largely invariant of specific blade geometry or number), and not to achieve a specific efficiency or acoustic performance, its 14 fins are designed using a basic curved shape. Performance curves for each blade length (and at the same time each heatsink fin length) are obtained through the measuring of three prototypes (5, 10 and 15 mm) and the interpolation (through fan affinity laws) of the intermediate fin lengths (0.1 mm resolution). The prototypes are additively manufactured from PLA using an FDM process and measured at the extreme values using an in-house flow bench. While only measuring maximum pressure increase at zero flow and maximum flow at zero pressure drop only results in approximated linear curves (Figure 3.8), these two points can be measured significantly easier and more accurately than the intermediate values due to effects of turbulence and helical airflow.

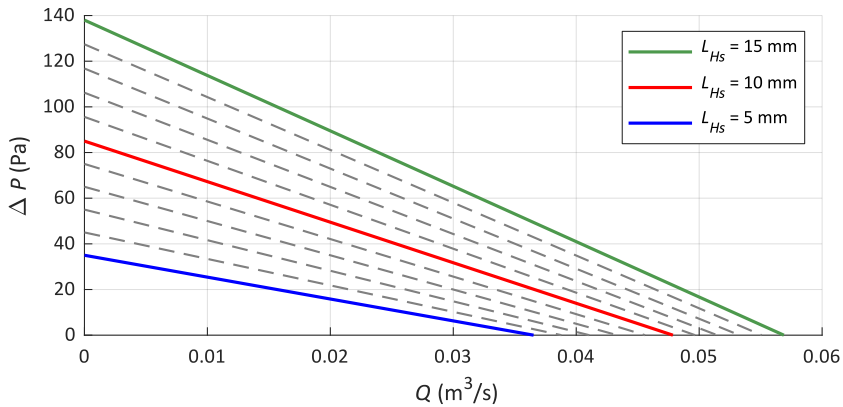


Figure 3.8. Fan pair curves at 6000 rpm and different blade lengths [66].

### 3.2.4 Heatsink Sizing

The end-goal of the cooling solution is to maximize the gravimetric power density of the AFSRM. In this case, instead of calculating the full power density of the motor, which is outside the scope of thermal design, the power-to-weight ratio of the motor is represented by a current density factor:

$$k_j = \frac{j_{Cu}}{M_\Sigma}, \quad (3.10)$$

where equation (3.5) is used to link current density to copper losses, which is itself limited by the performance of the full total thermal system:

$$P_{Cu} = \frac{\Delta T_{Cu}}{\mathcal{R}_0 + \mathcal{R}_{Hs}} - P_{Fe}. \quad (3.11)$$

As  $P_{Fe}$  is effectively constant at a given frequency, and  $\mathcal{R}_0 = 1 \text{ K/W}$  is taken from the thermal model, only  $\mathcal{R}_{Hs}$  is needed to describe  $j_{Cu}$ . Additionally, calculating  $\mathcal{R}_{Hs}$  using the semi analytical model fully determines the heatsink's geometry, which allows the mass of the heatsink to be calculated and therefore  $k_j$  to be fully defined.

#### 3.2.4.1 Analytical Heatsink Model

Initially,  $k_j$  is optimized using a standard semi analytical workflow for a conventional heatsink based on [67] and [68]. This results in straight and open-ended fins as shown in Figure 3.9 (a), however for the purposes of cooling the AFSRM, the final shape is curved, and a top surface is added (b). Since all other dimensions are conveniently defined by the geometry of the axial flux motor, the two design variables to be determined are the length and number of fins (the fin thickness is set at 0.5 mm according to the available LPBF capabilities).

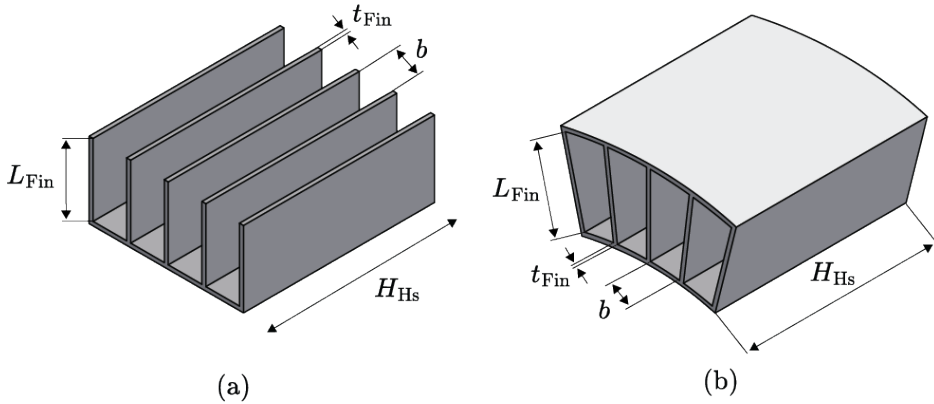


Figure 3.9. The conventional heatsink design considered in the semi analytical model (a) and the modified design used to cool the AFSRM (b) [66].

The design process starts by defining the pressure drop in the flow channel for a given air velocity, which must be a working point of the cooling fan pair:

$$2\Delta P_{\text{Fan}} = \Delta P_{\text{Hs}} = \left(0.42(1 - \sigma^2) + 4f_{\text{app}} \frac{H_{\text{Hs}}}{D_{\text{h}}} + (1 - \sigma^2)^2\right) \rho_{\text{air}} \frac{v^2}{2}, \quad (3.12)$$

where the flow velocity is directly proportional to the flowrate at the operating point:  $v = Q_{\text{Fan}}/A_{\text{fc}}$ .

Naturally,  $\Delta P_{\text{Fan}}$  and  $v$  are inherently linked as the fan pair can only create a certain amount of airflow through a given flow channel area, determined by its performance curve (Figure 3.8). Therefore, the optimization problem involves calculating the flow characteristics of each possible  $L_{\text{Fin}}$  and  $n_{\text{Fin}}$  combination, which are then used to evaluate  $\mathcal{R}_{\text{Hs}}$  and finally  $k_j$ .

The pressure drop in the flow channel for a given velocity is modelled with the use of an apparent friction factor, which is empirically correlated to the flow channel's geometry and the nature of the flow:

$$f_{\text{app}} = \left( \left( \frac{3.44}{\sqrt{\frac{L_{\text{Hs}}}{D_{\text{h}} \cdot Re}}} \right)^2 + (f \cdot Re)^2 \right)^{\frac{1}{2}} \cdot Re^{-1}, \quad (3.13)$$

where  $D_{\text{h}} = 2b$  and the Reynolds number is itself dependent on the geometry, velocity and fluid properties:

$$Re = \frac{\rho_{\text{air}} \cdot v \cdot D_{\text{h}}}{\mu}. \quad (3.14)$$

The apparent friction factor, which is used to model flow in a general flow channel, also contains a term for the friction factor, which is a more specific variable describing a fully developed flow through a uniform channel profile:

$$f = (24 - 32.53k_{\text{a}} + 46.72k_{\text{a}}^2 - 40.83k_{\text{a}}^3 + 22.95k_{\text{a}}^4 - 6.09k_{\text{a}}^5)Re^{-1}, \quad (3.15)$$

where the flow channel aspect ratio is  $k_{\text{a}} = D_{\text{h}}/(2 \cdot L_{\text{Hs}})$ .

While equations (3.12) to (3.15) sufficiently describe the aerodynamics of the heatsink, thermal performance depends on the interaction between the air and the fin surface. This is described using the Nusselt number:

$$Nu = \left( \left( \frac{Re \cdot Pr}{2} \right)^{-3} + \left( 0.664\sqrt{Re} \cdot P_r^{1/3} \sqrt{1 + \frac{3.65}{\sqrt{Re}}} \right)^{-3} \right)^{-1/3}, \quad (3.16)$$

where the modified Reynolds number is  $Re^* = \rho_{\text{air}} \cdot v \cdot b^2/(\mu \cdot L)$  and the convective characteristic of the fluid is explicitly described using the Prandtl number  $Pr = \mu \cdot c_p/\lambda_{\text{air}}$ . Subsequently, the Nusselt number is used to calculate the directly applicable thermal parameters of the average convection coefficient  $h_{\text{conv}} = Nu \cdot \lambda_{\text{air}}/b$  and fin efficiency



$\eta_{fin} = \tanh(m \cdot L_{Hs}) / (m \cdot L_{Hs})$ , where  $m = \sqrt{2 \cdot h_{conv} / (\lambda_{Al} \cdot t_{Fin})}$ . These are then used to find the thermal resistance of a single 1/6 sector (used to clarify the correlation with the thermal model and the physical prototypes) of the heatsink:

$$\mathcal{R}_{Hs} = \frac{6}{h_{conv} \cdot (A_{base} + n_{Fin} \cdot \eta_{Fin} \cdot A_{Fin})}. \quad (3.17)$$

Finally,  $\mathcal{R}_{Hs}$  is correlated with a current density through equations (3.11) and (3.17), and the mass of the heatsink is calculated based on its geometry and the density of AlSi10Mg. Therefore,  $k_j$  can be calculated for each combination of  $L_{Fin}$  and  $n_{Fin}$ . The results are shown in Figure 3.10 at different nominal rotational speeds to illustrate the change in the maximum point. In the figure below, the optimal  $n_{Fin}$  and a hotspot temperature increase of 80 °C are used to construct each curve.

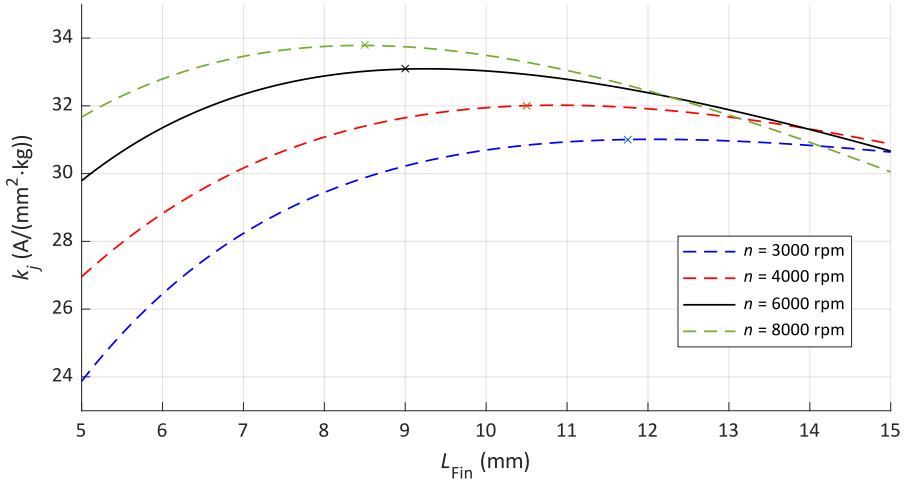


Figure 3.10. Current density factor values at different heatsink fin length fan pair rotational speed values with the maximal values highlighted [66].

At the nominal operating speed of 6000 rpm, the highest  $k_j$  of 33.1 A/(mm<sup>2</sup>·kg) is achieved for a heatsink with 198 fins of a length of 9.0 mm, which results in a total weight of  $M_{\Sigma} = 0.83$  kg and a current density of  $j_{Cu} = 26.8$  A/mm<sup>2</sup>. The thermal resistance of the heatsink sector is  $\mathcal{R}_{Hs} = 0.8$  K/W, which is added to the modelled internal resistance to get a total resistance value of  $\mathcal{R}_{\Sigma} = 1.8$  K/W for the sector.

As the  $k_j$  model is set up in a general manner, it can be used to find the optimal (in terms of  $k_j$ ) geometrical parameters with different inputs. In Figure 3.10, this is done for a range of rotational speeds, showing how the mass-optimized heatsink gets smaller as the available airflow increases. Furthermore, any of the parameters, such as  $\mathcal{R}_0$ ,  $\lambda$  or  $\Delta T_{Cu}$  can be modified to determine the optimal dimensions of the heatsink in a variety of applications. However, in terms of  $\mathcal{R}_{Hs}$ , this model is strictly limited to conventional straight fins, for which accurate analytical and empirical correlations are available. To explore alternative fin structures with potentially higher performance, physical prototypes must be manufactured.

### 3.2.5 Advanced Fin Structures

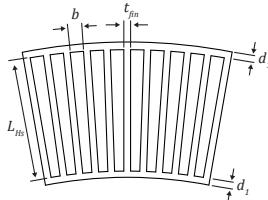
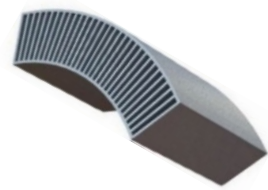
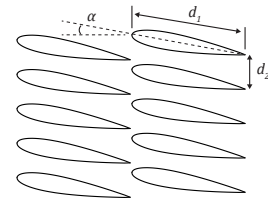
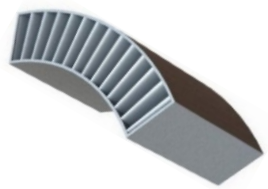
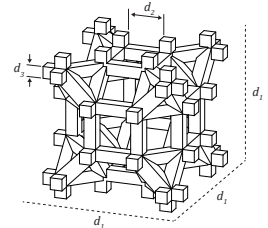
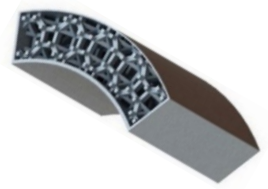
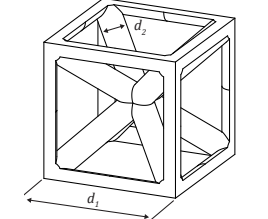
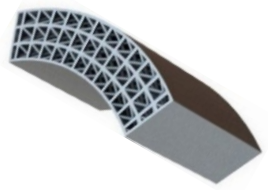
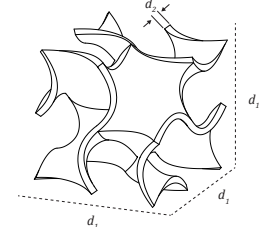

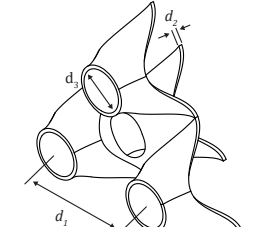

The second part of this work focuses on decreasing  $\mathcal{R}_{\text{HS}}$  through advanced fin structures, for which the general shape and sizing is taken from existing literature. Each advanced design shares the previously found fin length of 9 mm to end up with comparable results. However, other geometrical parameters, such as porosity and cell size are based on a combination of existing results in the literature, and practical manufacturing considerations (e.g. avoiding fractional cells) as accurate analytical and empirical workflows are generally limited to simple fins only.

The first advanced fin design utilizes **airfoil-shaped pins** similarly to the passive heatsink described previously. However, with forced cooling, minimizing drag becomes less important, meaning that a higher fin density and an airfoil angle of attack of  $20^\circ$  (based on the experimental work in [69]) is used. With a significantly lower  $A_{\text{HS}}$  than the conventional case, its performance relies mainly on direct boundary layer disruption at the leading edge (where airflow is effectively tangential to the fin surface), and turbulence on the trailing edge, which is utilized further by using two layers of fins.

The next two advanced designs utilize truss-based lattice structures in order to create an extremely chaotic flow inside the fin structure as a considerable part of the fin surface is tangential to the airflow. The first truss-based solution is a **rhombi octet (RO) lattice** [70–72] with a cell size of 9 mm and a strut thickness of 0.75 mm. This lattice structure, comprised of a rhombicuboctahedron core and octet truss structures in the corners, is characterized by small rectangular details that form cubical cells. In terms of airflow, each cell forms a central path that passes through the entire length of the heatsink, and a large number of parallel paths. The second truss-based design is a combination of a **simple cubic and a body centred cubic (BCC) lattice** [73] with a cell size of 3 mm and 0.6 mm struts. In this case, round struts are placed diagonally in the cuboidal structure, disrupting most of the airflow that would otherwise pass through the heatsink. As a result, an even larger proportion of the airflow is restricted by the fin structure and is forced to move through the parallel paths.

The final two advanced designs are based on mathematically defined triply periodic minimal surfaces (TPMS). Similarly to the previous two cases, these create a large amount of parallel airflow paths, however the discrete trusses are replaced with smooth surfaces. This approach attempts to benefit from the large amount of off-axis airflow without creating unnecessary drag. The first TPMS structure is the **gyroid** [74–76], which is a surface defined as  $\sin(x) \cos(y) + \sin(y) \cos(z) + \sin(z) \cos(x) = 0$ . The gyroid is scaled such that the range  $[0; 2\pi]$  spans a length of 9 mm, and the surface is extended in both directions 1 mm to form a solid body. The resulting fin structure includes two circular channels for each cell that go directly through the entire length, and numerous parallel paths connected by curves. The second TPMS structure is the Schwarz **diamond** [77], which is a surface defined as  $\cos(x) \cos(y) \cos(z) - \sin(x) \sin(y) \sin(z) = 0$ . In this case, the triangular unit cells, are scaled manually in order to avoid disjointed structures. The resulting structure has a wall thickness of approximately 0.5 mm (to avoid geometry clipping) and unlike every other geometry, does not include any flow channels that go straight through the heatsink. Therefore, the entirety of the flow follows the intricate internal structure, which makes it the most extreme case of increasing boundary layer interaction in favour of total airflow. The characteristic geometry, dimensions and visualization of each heatsink design is presented in Table 3.5. In each case,  $A_{\text{HS}}$  and  $V_{\text{FC}}$  are based on the CAD model and  $M_{\text{HS}}$  is based on measurements of the AM prototypes (explaining the apparent discrepancy between  $V_{\text{FC}}$  and  $M_{\text{HS}}$ ).

Table 3.5. Different heatsink designs utilizing advanced fin structures [78].

Fin structure	Geometrical parameters	Characteristic geometry	Heatsink sector model
Straight fins	$L_{\text{Fin}} = 9 \text{ mm}$ $b = 0.8 \text{ mm}$ $N_{\text{Fin}} = 198$ $A_{\text{Hs}} = 151 \text{ cm}^2$ $M_{\text{Hs}} = 13.4 \text{ g}$ $V_{\text{FC}} = 6.04 \text{ cm}^3$		
Airfoil pin fins	$d_1 = 8.7 \text{ mm}$ $d_2 = 2.7 \text{ mm}$ $\alpha = 20^\circ$ $A_{\text{Hs}} = 81.9 \text{ cm}^2$ $M_{\text{Hs}} = 11.4 \text{ g}$ $V_{\text{FC}} = 6.05 \text{ cm}^3$		
Rhombi octet	$d_1 = 9 \text{ mm}$ $d_1 = 2.25 \text{ mm}$ $d_1 = 0.75 \text{ mm}$ $A_{\text{Hs}} = 87.0 \text{ cm}^2$ $M_{\text{Hs}} = 7.80 \text{ g}$ $V_{\text{FC}} = 7.78 \text{ cm}^3$		
Simple cubic + body centred cubic (BCC)	$d_1 = 3 \text{ mm}$ $d_2 = 0.6 \text{ mm}$ $A_{\text{Hs}} = 128 \text{ cm}^2$ $M_{\text{Hs}} = 10.4 \text{ g}$ $V_{\text{FC}} = 7.45 \text{ cm}^3$		
TPMS Gyroid	$d_1 = 9 \text{ mm}$ $d_2 = 1 \text{ mm}$ $A_{\text{Hs}} = 76.4 \text{ cm}^2$ $M_{\text{Hs}} = 10.9 \text{ g}$ $V_{\text{FC}} = 6.39 \text{ cm}^3$		
TPMS Diamond	$d_1 = 6.3 \text{ mm}$ $d_2 = 0.5 \text{ mm}$ $d_3 = 2.3 \text{ mm}$ $A_{\text{Hs}} = 117 \text{ cm}^2$ $M_{\text{Hs}} = 7.10 \text{ g}$ $V_{\text{FC}} = 8.02 \text{ cm}^3$		

### 3.2.6 Advanced Fin Structure Prototypes and Testing

The thermal performance of each of the fin structures is measured through physical prototypes, manufactured via LPBF from AlSi10Mg. The prototypes shown in Figure 3.11 do not contain major manufacturing faults and are dimensionally accurate. The inner surface of the sector, which is in direct contact with the stator winding, is dimensioned specifically according to the exact geometry of the stator winding and polished to minimize  $\mathcal{R}_0$ . The main goal of the measurements is the determination of  $\mathcal{R}_{\text{HS}}$  for each of the fin structures at different fan speeds, which is calculated based on the thermal circuit in Figure 3.5 as the temperature difference between the heatsink surface and the ambient air under a DC heat load:

$$\mathcal{R}_{\text{HS}}(\omega) = \frac{T_{\text{F}} - T_{\text{amb}}}{P_{\text{Cu}}}, \quad (3.18)$$

while the hotspot temperature is kept at a constant  $T_{\text{Cu}} = 100 \text{ }^\circ\text{C}$  during each test to emulate a fixed working point and minimize any temperature dependent effects on  $\mathcal{R}_0$ .

The measurements are performed on a straightforward test bench, where the aluminium alloy frame sector is mounted on a polymer fixture that emulates the full motor as shown in Figure 3.12. Two fans, mounted on both sides of the stator, provide airflow through the heatsink sector and are driven by an external motor with accurate speed control. Measurements of the input heating power (voltage and current) and temperatures are performed with precision multimeters and a data logger respectively.

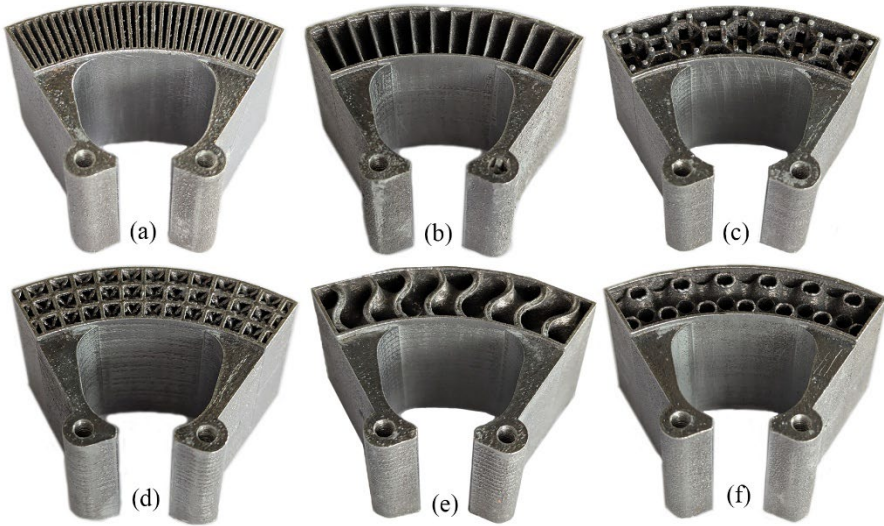


Figure 3.11. LPBF AlSi10Mg heatsink sectors [78].

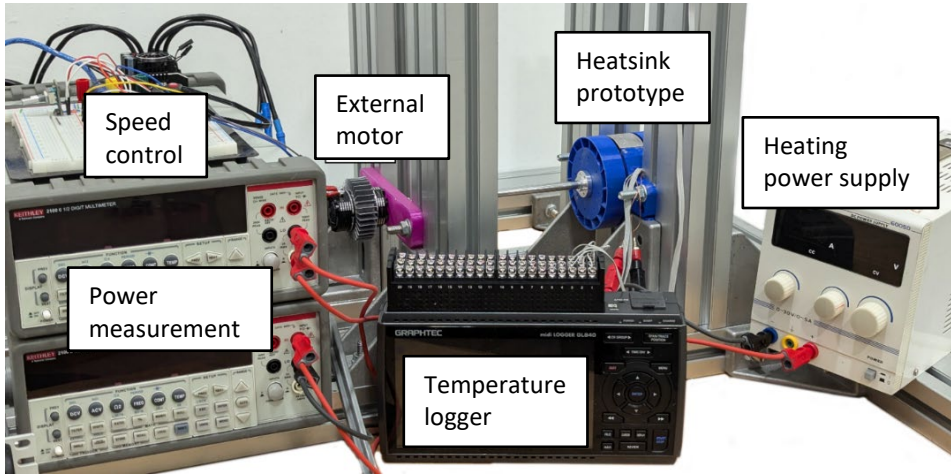


Figure 3.12. Measurement setup [78].

### 3.2.7 Advanced Fin Structure Results

Each frame sector is measured three times to account for a small variance in  $\mathcal{R}_0$  each time the frame is mounted on the stator winding (caused mainly by random variations in the thermal paste application and the positioning of the  $T_F$  sensor). During each of the three test runs, the measured values are used to calculate  $\mathcal{R}_{Hs}$  in the range of 3000 to 6000 rpm. The resulting values are averaged to produce  $\mathcal{R}_{Hs}(\omega)$  curves, which take the form  $y = ae^{bx} + ce^{dx}$ , matching the shape of the analytically calculated values shown in Figure 3.13.

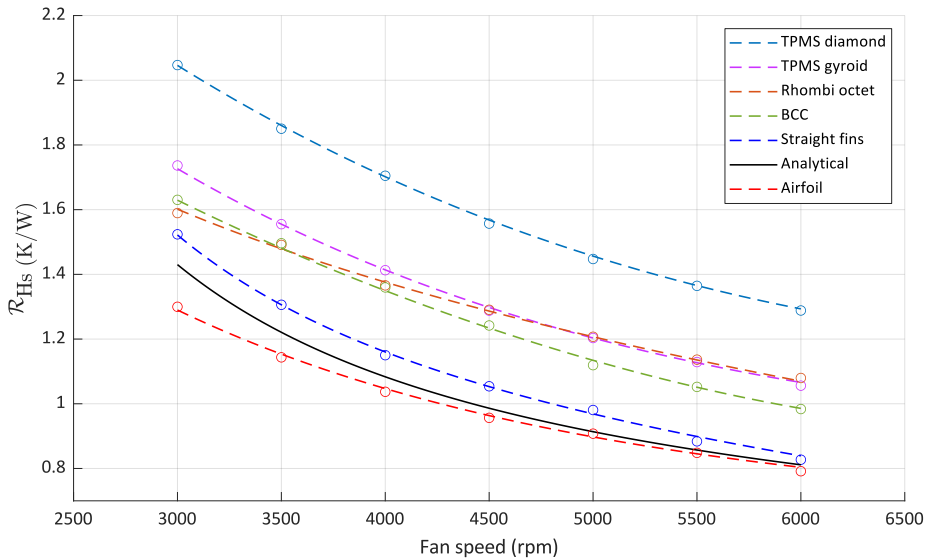


Figure 3.13. Thermal resistances of the different fin structures at a range of fan speeds [78].

The resulting curves are similar to the analytical model, where the performance gains from increasing the fan speed gradually level off. At the nominal operating speed of 6000 rpm the airfoil pin fins have the lowest thermal resistance of 0.8 K/W, which is an approximately 5% improvement over the conventional straight fins. Of the two truss-based designs, the body centered cubic performs the best with a thermal resistance of 0.99 K/W, which is 18% worse than the conventional case. Both TPMS designs have even higher thermal resistances at 1.07 and 1.29 K/W for the gyroid and diamond structures respectively. These results indicate clearly that conventional design principles, which prioritize straightforward flow paths, apply even in the case of the two high-speed fans in series.

As an alternative, as shown in Figure 3.14, the heatsinks can be compared based on mass-based relative performance, in which case each  $\mathcal{R}_{\text{Hs}}$  is multiplied by the fin mass  $M_{\text{Hs}}$ . The resulting value can be imagined as the fin mass required for a thermal resistance of 1 K/W. However, its use should be only limited to specific comparisons as a low relative value does not necessarily mean that an effective heatsink can be constructed.

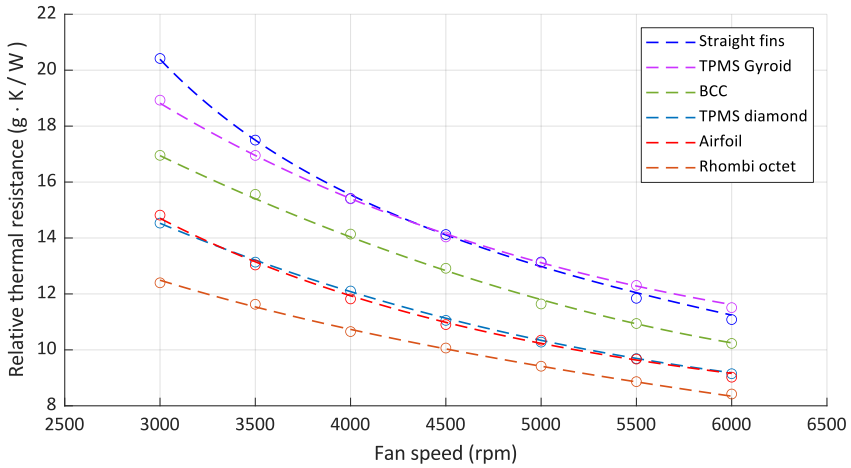


Figure 3.14. Relative thermal resistances of the fin structures at a range of fan speeds [78].

Comparing the relative performance reveals that the rhombi octet structure, while not impressive in terms of absolute performance, achieves a value of 8.34 g · K/W, which is approximately 25% lower than the conventional heatsink. This suggests that the rhombi octet structure is a more efficient use of material terms of thermal performance, however the importance of fin mass compared to absolute thermal resistance is highly application specific. For example, while a 25% reduction in fin mass has only a small effect on the total weight of the AFSRM, applying for a device with a much larger overall loss-density, such as a power transistor, could lead to substantial weight savings. It should be noted that reducing the fin count (using the analytical model) of the conventional heatsink to match the  $M_{\text{Hs}}$  of the rhombi octet does not meaningfully change its relative performance, indicating that this parameter is primarily determined by the geometry type and not specific dimensions. Therefore, instead of focusing on absolute performance, future optimization of the rhombi octet or TPMS structures should focus on relative performance.

### 3.2.8 Evaluation of the Proposed AFSRM Thermal Management Solution

The thermal performance of each heatsink can be linked to a maximum current density in the windings through equations (3.11) and (3.17) by considering the average measured internal thermal resistance of  $\mathcal{R}_0 = 1.14$  K/W (calculated as  $\mathcal{R}_0 = ((T_{Cu} - T_F)) / P_{Cu}$  for each heatsink measurement and averaged across all tests), the approximated  $P_{Fe}(\omega)$  value, and a specified hotspot temperature increase of 80 °C. The results for the most relevant fin structures are shown in Figure 3.15, where the total mass of the drive, consisting of all six stator segments, the full frame, and rotors with the fans, is added to illustrate the relatively small effect of  $M_{Hs}$  in the context of the full motor.

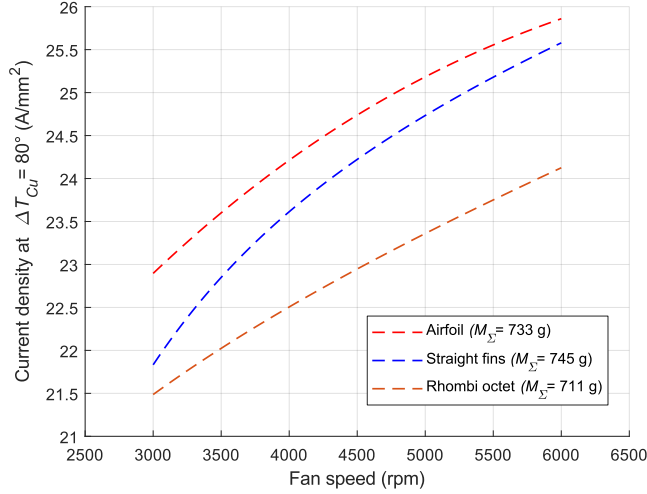


Figure 3.15. Maximum current density values achievable with the different heatsink designs at a hotspot temperature increase of 80 °C.

### 3.3 Advanced Fin Structures Conclusions and Future Work

In this chapter, the potential of AM in EM cooling was explored by focusing on different advanced fin structures with the aim of increasing a motor's maximum current density. The simulated and measured results, for the inner rotor radial flux and dual rotor axial flux reluctance motors respectively, showed the advantage of AM-enabled structures for motor air-cooling applications. The work presents a strong justification for the inclusion of AM in the process of developing EM air-coolers as both absolute and relative thermal performance can be increased through the inclusion of nonconventional structures.

In the case of the passively cooled radial flux machine, advancing the conventional annular fin heatsinks towards novel AM-based geometries provided a clear advantage in absolute and relative thermal performance. While simply altering the shape of the simple fins proved beneficial, the highest performing heatsink, which enables a 1.1% higher current density in the windings at a total weight reduction of 1.6%, is the airfoil pin fin heatsink. This structure, while in principle manufacturable without AM, demonstrates the advantages of moving beyond simple conventional designs and considering novel structures for air-cooling. However, the superior performance of relatively open structures that attempt to maximize natural convection was demonstrated by the disappointing performance of the lattice structure.

After confirming through simulations that AM-enabled advanced structures can be advantageous, focus was directed on physical prototypes and active-air cooling to increase current density further. Additionally, as the internal thermal resistance of the radial flux motor was shown to be a significant limiting factor, an axial flux motor was chosen as the platform. In this case, the segmented nature of the stator allows the heatsink to be placed directly on the windings by utilizing an integrated frame and heatsink combination. When dimensioning the frame, the inherently irregular shape of the wound stator core segments can be effectively dealt with due to the flexibility of AM-based design. This makes the axial flux motor topology an excellent showcase of AM's advantages. Measurement results obtained from the AM prototypes demonstrated the overall effectiveness of the proposed cooling solution and the advantages of advanced fin structures in active air-cooling. The low internal thermal resistance of the system enables a current density of  $> 25 \text{ A/mm}^2$  to be used, which is generally only available with liquid cooling. Therefore, in applications unsuitable for liquid cooling (such as small- and medium-scale electric propulsion), the proposed method for cooling axial flux motors can provide substantial advantages. In terms of advanced fin structures, the lowest thermal resistance was achieved with the airfoil pin fins, which enabled the current density to be increased a further 1.1% while decreasing total weight by 1.6% compared to the conventional straight fins.

Similarly to the passively cooled case, the open structures significantly outperformed the relatively dense structures. Considering the use of two high speed fans in series, a configuration that represents the high-end of the pressure increase achievable with air-cooling, the underperformance of the dense structures in absolute performance should be considered as a basis to disregard similar solutions. This is contrary to much of the previously cited literature, in which dense lattice structures tend to be highly rated, albeit only based on limited comparisons or purely simulation data. Furthermore, it must be noted that the advanced solutions used in this work are unoptimized and only roughly dimensioned based on the literature, while their performance is compared to a thoroughly optimized conventional case. Even so, it is unlikely that optimizing the geometrical parameters of any of the considered lattice structures would propel its performance above the conventional solution.

The tendency of smooth and open structures to outperform intricate lattice structures in air-cooling has resulted in fin structures that, on first impressions, do not necessarily demand AM. However, while the airfoil pin fins and other similar solutions have always been manufacturable, serious work looking into their performance has still only started with the advent of effective AM for conductive materials. There, the extremely fast prototyping capabilities of AM should be considered. By having the option of performing measurements on a physical prototype based on essentially any 3D geometry after only a trivial production time, optimized designs can be evidently discovered and confirmed even if the geometry itself could have been manufactured otherwise. Nevertheless, the main hypothesis of this thesis can be confirmed more convincingly through an improved thermal solution that relies more heavily on the capabilities of AM in terms of realizing complex geometries. Such a solution is introduced in the next chapter through an algorithmically generated fin structure; in which case the resulting geometry is wholly irregular and would prove exceedingly difficult to fabricate without AM.



## 4 Algorithmically Generated Fin Structures

Advances in computational power have enabled a radically different design paradigm by replacing analytical and empirical correlations with the results of a numerical model. In this way, many simplifications of analytical models (e.g. a constant convection coefficient on the entire fin surface) are avoided and the performance of any geometry can be calculated. These results can be used to modify the geometry towards a more effective solution without any prior knowledge of the system's characteristics. In its most basic form, the geometry is modified according to a limited set of design parameters, in which case the overall shape of the result remains predefined. This type of parametric optimization (PO) can be readily used in conjunction with conventional manufacturing techniques, although the result does not generally represent any sort of global optimum. If, however, the manufacturing limitations are relaxed, the limited set of design parameters can be discarded in favour of directly controlling the geometry on the level of individual mesh elements. Such methods, generally called topology optimization (TO), result in fundamentally unique geometries that can reach much closer to a given global optimum and in many cases represent the absolute best performance that is physically possible.

In this chapter, the advantages of combining AM and TO are demonstrated using an electric propulsion drive as the case study. Initially, the numerical model is built and paired with a PO algorithm to produce an optimized conventional heatsink that acts as the initial case. Afterwards, a TO algorithm based on heat transfer and fluid flow in porous media is introduced and used to generate the optimized geometry. Finally, both heatsinks are manufactured from AlSi10Mg using LPBF and measured using the propulsion drive. The resulting TO heatsink, which is not based on any existing geometry or intuitive design, is an excellent expression of the fundamental shift in design methodology that AM represents.

### 4.1 Propulsion Drive Parameters

In the context of an electrical propulsion system, the primary goal of the cooling solution is maximizing thrust-to-weight ratio. The specific drive, consisting of an inner rotor permanent magnet motor and a 12 x 4.5 carbon fibre propeller is illustrated in Figure 4.1. The motor is cooled by a heatsink that covers the entire length of the stator and is in direct contact with the silicon steel laminations. It consists of a 1 mm thick cylindrical base, to which the fins are radially attached. The relevant performance parameters of the drive are shown in Table 4.1.

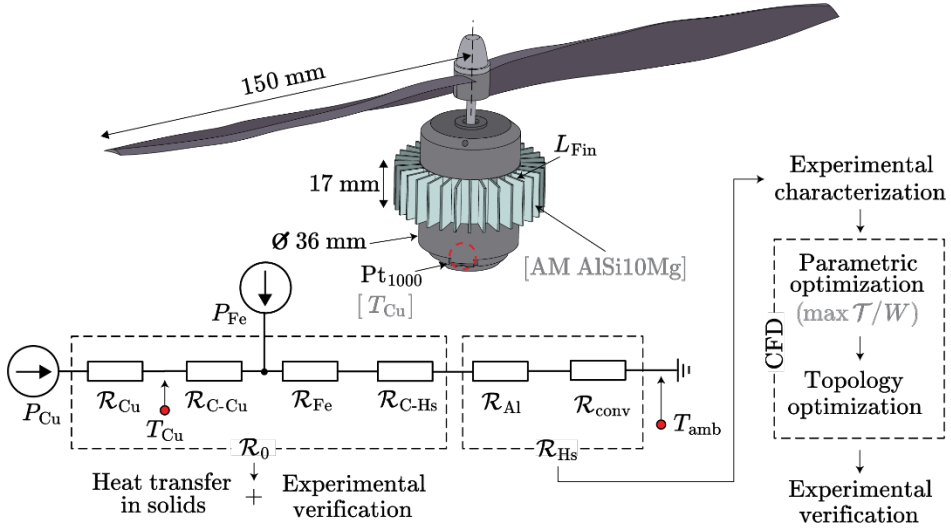


Figure 4.1. Illustration of the proposed propulsion drive and cooling solution [79].

Table 4.1. Important parameters of the drive.

Parameter	Symbol	Value
Number of rotor poles	-	2
Motor outer diameter	-	34.3 mm
Stator stack length	-	17 mm
Drive mass	$M_{\Sigma}$	167 g
Stator iron mass (Estimated)	$M_{Fe}$	100 g
Iron loss density (Estimated)	$p_{Fe}$	10 W/kg (50 Hz)
Phase resistance	$R_{ph}$	4 m $\Omega$ (20 °C)
Propeller radius	$r_{prop}$	154 mm

Before the heatsinks can be modelled, the performance of the drive is measured without any additional cooling. The approximately linear relationship seen in Figure 4.2 means that maximizing thrust can be simply defined as maximizing phase current, which is directly limited by  $\mathcal{R}_{\Sigma}$ . On the other hand, the total weight of the drive depends partly on the volume of the heatsink, meaning that the drive's thrust-to-weight ratio can be represented as the ratio  $\mathcal{T}/W = f(\mathcal{R}_{\Sigma})/f(V_{Hs})$ .

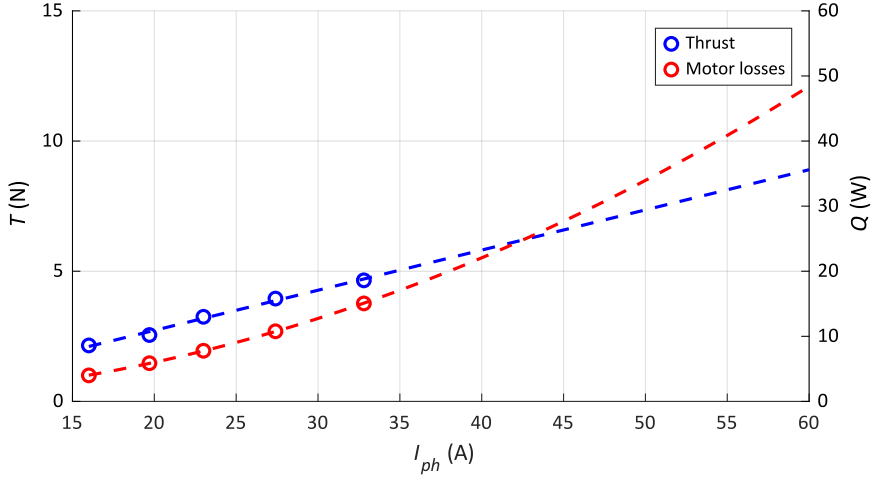


Figure 4.2. Measured thrust, current and calculated copper losses of the drive without a cooling solution implemented [79].

## 4.2 Parametric Optimization Model

Initially, a conventional heatsink with simple straight fins is designed and prototyped in order to provide a point of comparison for the TO results. This design is created by using parametrical optimization in conjugation with a thermal CFD model. The optimization task is described by the following design parameters:

- number of fins  $n_{Fin} \in \{2, 3, \dots, 100\}$ ,
- thickness of the fin  $t_{Fin} \in \{0.50, 0.51, \dots, 2.00\}$  mm,
- length of the fin  $L_{Fin} \in \{2.0, 2.1, \dots, 30.0\}$  mm.

Due to the relatively low number of possible optimization parameter combinations, and a smooth relation to the objective function, the specific choice of the optimization solver is inconsequential. In this case, the Nelder-Mead method implemented in the Comsol Multiphysics software is used. Throughout the iterative optimization process, the CFD model is used to maximize  $\mathcal{T}/W = f(n_{Fin}, t_{Fin}, L_{Fin})$  and finally arrive at the optimal values for the PO variables  $n_{Fin-PO}$ ,  $d_{Fin-PO}$  and  $L_{Fin-PO}$ .

### 4.2.1 Thermal CFD for PO

To maintain equivalence with the TO model (where minimizing computational cost is much more relevant), the fluid is modelled as incompressible and the flow as laminar. Additionally, the momentum equation in (3.8) is further simplified by eliminating the external force (gravity) term, which has a negligible effect in the case of forced cooling. The momentum equation describing the airflow in the PO model is therefore

$$\rho(\mathbf{u} \cdot \nabla)\mathbf{u} = -\nabla p + \nabla \cdot \mathbf{K}, \quad (4.1)$$

where the volumetric strain rate is removed from the viscous stress tensor term in the case of incompressible flow:

$$\mathbf{K} = \mu(\nabla \mathbf{u} + (\nabla \mathbf{u})^T). \quad (4.2)$$

Thermally, the model is similar to the previous case study, where the heat flux is described by Fourier's law, and the heat balance equations (3.3) and (3.7) for the solid and fluid domains respectively. However, in this case, there are no volumes with heat generation ( $p = 0$ ) and the thermal load is defined as a boundary heat flux condition imposed on the heatsink internal surface:

$$-\mathbf{n} \cdot \mathbf{q} = Q_\Sigma / A_S. \quad (4.3)$$

The total amount of heat flux is the sum of copper and iron losses, which are functions of phase current and winding temperature, and electrical frequency respectively:

$$Q_\Sigma = P_{Cu} = 3I_{ph}^2 R_{ph}(T_{Cu}) + M_{Fe} p_{Fe}(f), \quad (4.4)$$

where  $T_{Cu}$  is estimated from modelling the internal resistance as  $\mathcal{R}_0 = 2 \text{ K/W}$  (similarly to the SRM in section 3.1.3.1), and  $f$  is calculated based on the rotational speed of a 2-pole rotor, and  $p_{Fe} \propto f^2$ .

The setup of the CFD model illustrated in Figure 4.3 contains a 45° sector of the full heatsink and the surrounding air. As the drive and heatsink are both fully radially symmetric, appropriate boundary conditions are used to increase the density of the mesh without sacrificing accuracy. The surrounding volume of air is modelled substantially larger than the heatsink to minimize any edge effects that do not appear in reality, and the no-slip condition is applied on all walls.

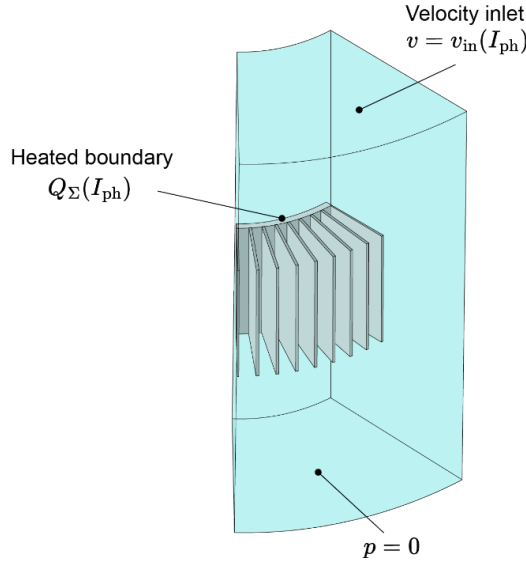


Figure 4.3. Parametric optimization model CFD setup [79].

The airflow created by the propeller is included in the model as a constant velocity inlet with the value  $\mathbf{u} = v_{in}\mathbf{n}$  and an outlet at zero relative pressure ( $(-p\mathbf{I} + \mathbf{K})\mathbf{n} = 0$ ). The value for  $v_{in}$  is the exit velocity of air derived from the propeller thrust equation [80]

in the case of a 0 m/s inlet velocity (meaning that the propeller is stationary relative to the surrounding air). It should be noted that the accuracy of the model could theoretically be increased by calculating  $v_{in}$  as a function of radius (a propeller moves air fastest near the tip) and adding a rotational component to  $\mathbf{u}$ , although reliable data about a realistic velocity distribution at a given distance from the propeller is difficult to obtain.

$$v_{in}(I_{ph}) = \sqrt{\frac{2\mathcal{T}(I_{ph})}{\rho_{air} \cdot \pi r_{prop}^2}} \quad (4.5)$$

During each iteration of the PO algorithm, the mass of the heatsink is calculated and added to the total weight of the drive, while thrust is calculated using  $I_{ph}$  and the correlation from Figure 4.2. The heatsink's thermal performance is defined in the model by the average temperature of the internal cylindrical surface, which is limited to 10 °C in the model in order to avoid unsensible solutions during the optimization process. Even at this modest temperature increase at the heatsink surface, the hotspot temperature in the coils is significantly higher due to a relatively high  $\mathcal{R}_0$ . During the PO process, the phase current is set at  $I_{ph} = 60$  A (an arbitrary value as the exact value of  $\mathcal{R}_0$  is unknown), resulting in a thrust of  $\mathcal{T} = 8.4$  N (Figure 4.2) and an average inlet velocity of  $v_{in} = 13.2$  m/s.

#### 4.2.2 Parametric Optimization Model Output

Running the PO model for a total of 41 iterations results in a heatsink with the following geometrical parameters:  $n_{Fin-PO} = 32$ ,  $t_{Fin-PO} = 0.73$  mm and  $L_{Fin-PO} = 9.6$  mm. The modelled temperature distribution in the PO heatsink at  $I_{ph} = 60$  A is shown in Figure 4.4. The average temperature increase on the heatsink's inner surface is 11.8 °C, which is slightly outside the specified limit. The modelled mass and thermal resistance of the full heatsink are  $M_{Hs-PO} = 16.0$  g and  $\mathcal{R}_{Hs-PO} = 0.24$  K/W respectively.

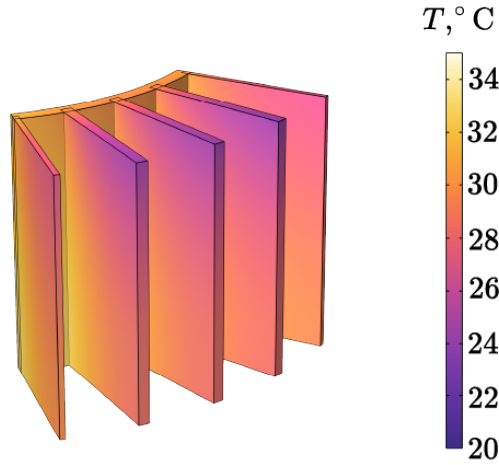


Figure 4.4. PO heatsink temperature distribution [79].

## 4.3 Topology Optimization Model

TO is the general term for computational methods that are used to find the optimal material distribution for a given objective function. These methods are used across many fields, such as aerospace [81], automotive [82], and civil engineering [83]. In thermal engineering, it can be used in conjunction with CFD in order to design high-performance heatsinks with unique geometries [84]. However, with conventional manufacturing methods, the TO algorithm often needs to be a priori limited (such as constraints on minimum corner radii to enable milling), or the results simplified post hoc, in order to end up with a manufacturable geometry. On the other hand, AM methods such as LPBF are capable of directly realizing the complex TO geometries, meaning that the optimized device can be manufactured without compromise. As a result, TO algorithms are rapidly gaining traction in both research and commercial applications.

While various workflows for implementing TO have been developed over the years, the most used workflow for thermal problems is based on three methods.

- Density-based method for defining the physical material properties in terms of a design variable.
- Finite element analysis for calculating the solution variables.
- Gradient-based solver for optimizing the design variable distribution according to an objective function.

### 4.3.1 Density-based Topology Optimization

According to the density-based method of TO, the problem is formulated by defining the design domain  $\Omega$ , which is the volume within which the optimization process occurs. Each mesh element  $e$  inside  $\Omega$  is described by a continuous density variable  $\theta$ , such that

$$0 \leq \theta \leq 1 \quad \forall e \in \Omega. \quad (4.6)$$

This variable describes the proportion of a primary material in terms of a secondary material, in this case AlSi10Mg and air respectively. While  $\theta = 0$  describes a region of air and  $\theta = 1$  aluminium, the intermediate values represent mathematical combinations of the two materials. These allow for smooth transitions between solid and nonsolid regions and are necessary for the numerical model to converge. However, a  $\theta$  value other than 0 or 1 has no physical meaning, making it important to minimize their occurrence in the final solution. This is achieved through methods of penalization, projection and filtering.

While it is possible to correlate  $\theta$  to any physical parameter  $k$  (e.g. thermal conductivity) through a simple linear function, in practice it tends to result in more instances of  $\theta$  with an intermediate value. In order to bias the model towards discrete regions of 0 and 1, **penalization** techniques are used. The most common of these is the Solid Isotropic Material with Penalization (SIMP) method, where a penalty factor  $p_{SIMP}$  is used to discourage intermediate  $\theta$  values using the equation

$$k(\theta) = k_{\min} + \theta^{p_{SIMP}} \cdot (k_{\max} - k_{\min}). \quad (4.7)$$

The degree of penalization is determined by  $p_{SIMP}$ , where a larger value leads to a sharper change in  $k(\theta)$  at  $\theta \rightarrow 1$ . This effectively pushes any element, which “wants” to be solid, quickly towards full density. However, an overly large penalization factor will

also create a dead zone near  $\theta \rightarrow 0$ , where  $k(\theta)$  is nearly constant. As a high sensitivity towards the design variable is generally beneficial for the convergence of any optimization algorithm, it is important to use a balanced value, which in this case is  $p_{\text{SIMP}} = 3$ .

Considering  $\theta$  for each mesh element separately makes the optimization problem entirely dependent on the specific mesh discretization, which tends to result in checkerboard-like structures, impossibly thin lines, and problems with convergence. These issues are mitigated by imposing a minimum length scale  $R_{\min}$  through **filtering**, in which case a filtered density variable  $\theta_F$  is defined based on  $\theta$  and an average of its immediate surroundings. The standard method of Helmholtz filtering is used in this case:

$$\theta_F = R_{\min}^2 \nabla^2 \theta_F + \theta. \quad (4.8)$$

From the definition of  $\nabla^2$ , it's clear that the filtered density variable results in a gradual distribution instead of sharp edges, which again introduces unphysical intermediate density regions. Therefore, **projection** techniques are used to restore the sharp edges, however now without mesh-dependent artefacts. This is commonly done using hyperbolic tangent projection. In this case study, the projection point  $\theta_\beta$  and slope  $\beta$  are defined based on practical experiences as 0.5 and 8 respectively.

$$\theta = \frac{\tanh(\beta(\theta_F - \theta_\beta)) + \tanh(\beta\theta_\beta)}{\tanh(\beta(1 - \theta_\beta)) + \tanh(\beta\theta_\beta)}. \quad (4.9)$$

#### 4.3.2 Thermal CFD for Density-based TO

In order to model physical outcomes in terms of each  $\theta$ , the density variable needs to be linked to one or more physical parameters. In this case, there are three important parameters that depend on  $\theta$  and need to be modelled:

- The mass of the heatsink.
- Heat flux within the design domain.
- Airflow within the design domain.

The first two parameters are solved simply by linking  $\theta$  with the thermal diffusivity ( $k/\rho c_p$ ) of both materials through penalization:

$$\rho(\theta) = \rho_{\text{air}} + \theta^3 \cdot (\rho_{\text{Al}} - \rho_{\text{air}}) \quad (4.10)$$

$$\lambda(\theta) = \lambda_{\text{air}} + \theta^3 \cdot (\lambda_{\text{Al}} - \lambda_{\text{air}}) \quad (4.11)$$

$$c_p(\theta) = c_{p-\text{air}} + \theta^3 \cdot (c_{p-\text{Al}} - c_{p-\text{air}}). \quad (4.12)$$

However, differentiating between a fluid and solid material in terms of flow is somewhat more complicated. While it is possible to link  $\theta$  to either  $\mu$  (modelling the solid as an extremely viscous fluid) or to  $\mathbf{F}$  (modelling the solid as a fictitious force opposing the flow), in practice these solutions tend to be unreliable and create issues with convergence. A more consistent TO model can be defined based on flow in porous media,

where air is modelled as a fluid in approximately fully permeable material, and the heatsink as fluid in an effectively impermeable material, eliminating strictly solid materials from the model entirely. The fluid flow is based on Darcy's law, which sets a linear relationship between the velocity of a fluid and the pressure gradient acting on it through permeability  $\kappa$ :

$$\mathbf{u} = -\frac{\kappa}{\mu} \nabla p. \quad (4.13)$$

Because the intention is to alter the fluid flow inside the design domain according to a single continuous variable  $\theta$ , and not the accurate modelling of a real porous system, porosity of the material can be freely set to 1. Therefore, only permeability needs to be accounted for, although for practical convenience when defining the model, impermeability  $\chi = \kappa^{-1}$  is used instead. Therefore, the final physical parameter is defined as

$$\chi(\theta) = \chi_{\text{air}} + \theta^3 \cdot (\chi_{\text{Al}} - \chi_{\text{air}}). \quad (4.14)$$

As  $\chi$  does not describe the actual impermeability of a real porous system, the values  $\chi_{\text{air}} = 10^7 \text{ m}^{-2}$  and  $\chi_{\text{Al}} = 10^{11} \text{ m}^{-2}$  are chosen fully based on trial and error. Finally, defining the entire model as a fluid means that the heat transfer is modelled in all regions using the heat balance equation given in (3.7).

#### 4.3.3 Optimization Process

Modifying the distribution of  $\theta$  towards a more effective solution requires an **objective function**  $f_o$ . This quantifies the performance being optimized, such as minimizing temperature or maximizing heat flux. While in principle the objective function can have a simple definition (e.g. minimizing the temperature of the heat source), it can be advantageous in terms of sensitivity to small changes, convergence and avoiding local minima to define it based on complementary values (i.e. maximizing the total thermal energy of the outgoing air). In cases where there are multiple optimization criteria, such as achieving maximal thermal transfer while limiting drag,  $f_o$  can end up as a composite function containing several different parameters and weighing constants, for which finding effective values is highly nontrivial. However, in this case, the negative effect of the heatsink on thrust is assumed to be negligible and a simple objective function is defined based on the total heat flux flowing through the solid volume of the heatsink base:

$$f_o = \int_{V_s} \mathbf{q} \cdot dV. \quad (4.15)$$

After solving for a given material distribution, the algorithm performs a sensitivity analysis in order to calculate the effect of each mesh element on the objective function, effectively calculating  $df_o/d\theta$  for  $\forall e \in \Omega$ . In practice, this requires calculating the inverse of a matrix that has a number of elements equal to the square of the design domain's degrees of freedom. The resulting computational cost of TO, almost entirely caused by the sensitivity analysis, is comparable to the cost of solving the physical model itself. Finally, the results of the sensitivity analysis are used to find the next iteration in the optimization process. In density based TO, this is generally done with gradient based solvers. In this case study, the commonly used method of moving asymptotes is utilized. **Constraints** are imposed on the optimization process in order to comply with any given limitation or to reduce the size of the solution space, the latter of which is helpful



for both computational cost and biasing the design towards a certain direction. Most commonly, constraints on the maximum and minimum values for the average volume fraction of the design domain ( $\bar{\theta}_{\min}$  and  $\bar{\theta}_{\max}$ ) are defined, effectively constraining the final mass of the object. In this case study,  $\bar{\theta}_{\min}$  and  $\bar{\theta}_{\max}$  are set at 0.2 and 0.4 respectively, resulting in a single constraint:

$$0.2 \leq \frac{1}{V_{\Omega}} \int_{\Omega} \theta \, dV \leq 0.4 \quad (4.16)$$

#### 4.3.4 TO CFD Model Setup

In principle, it is enough to define an arbitrarily large design domain and a relevant objective function to end up with an optimized geometry. In practice, however, an overly general problem formulation will have difficulties converging into a coherent solution. Therefore, it is useful to start with a vague idea of the desired outcome and bias the TO problem towards that. Therefore, as illustrated in Figure 4.5, the CFD TO model is set up according to the results of the PO model. The design space is defined as a  $1/64$  sector of the heatsink, corresponding to half of a fin in the case of the previously found  $n_{\text{Fin-PO}} = 32$ , with a radius of 9.6 mm, corresponding to  $L_{\text{Fin-PO}}$ . A fixed density of  $\theta = 1$  is imposed on one side boundary, effectively creating the solid core of a fin. Defining  $\Omega$  in this way effectively forces the TO algorithm into a design where  $n_{\text{Fin-TO}} = n_{\text{Fin-PO}}$  and  $L_{\text{Fin-TO}} = L_{\text{Fin-PO}}$ . While this eliminates the possibility of finding a true global optimum, it massively increases the likelihood of converging on an effective solution. Outside the design domain, the TO model setup is similar to the PO case. The internal surface of the heatsink is heated (this time with a fixed boundary temperature instead of heat flux due to a known limitation of the modelling software) and a uniform velocity is imposed on the inlet boundary. The requirement for computational resources is kept to a modest level by limiting the maximum mesh element size to 0.4 mm (ideally this would correspond to at least the minimum feature size of the manufacturing method), which results in an approximately  $10^5$  element mesh. As a result, it is possible to complete the necessary number of iterations ( $\sim 80$ ) and converge on a final solution in approximately 24 h on a modern consumer CPU.

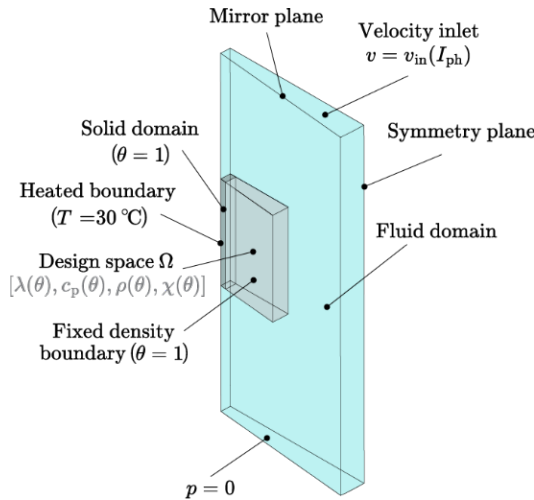


Figure 4.5. TO CFD model setup [79].

### 4.3.5 TO Model Results

The raw output of the TO model shown in Figure 4.6 (a) is the density variable distribution inside the design domain. Whichever strategy for interpolation, filtering and projection is used, in practice, the output will still contain elements with intermediate  $\theta$  values. In a well-converged case, these will form a thin boundary between the solid and nonsolid areas, meaning that the specific cutoff value for  $\theta$  is mostly irrelevant. In other cases, however, the intermediate region is larger, and the cutoff value will have a significant effect on the final geometry. For the purposes of creating a physical prototype in this work, the cutoff value between solid and nonsolid material is defined as  $\theta_{\text{limit}} = 0.4$ . This value is used instead of the typical 0.5 to avoid overly thin structures, which would compromise the mechanical integrity of the heatsink (a consequence of the relatively large intermediate region). In (b), the corresponding fin geometry is modelled as a 45° sector of the heatsink (as in the PO case) with the same electrical parameters of  $I_{\text{ph}} = 60$  A. In this case, the average temperature rise on the internal surface is 7.7 °C, which is 4.1 °C lower than the PO heatsink. This gives it a simulated thermal resistance of  $\mathcal{R}_{\text{HS-TO}} = 0.16$  K/W, however at a mass of  $M_{\text{HS-TO}} = 32$  g, which is two times higher than the PO case. A heatsink with a lower mass (and somewhat higher  $\mathcal{R}_{\text{HS}}$ ) could be created by using a higher  $\theta_{\text{limit}}$  value to reduce the volume of the solid domain, if the intermediate region were smaller (i.e. if the convergence of the model was more effective).

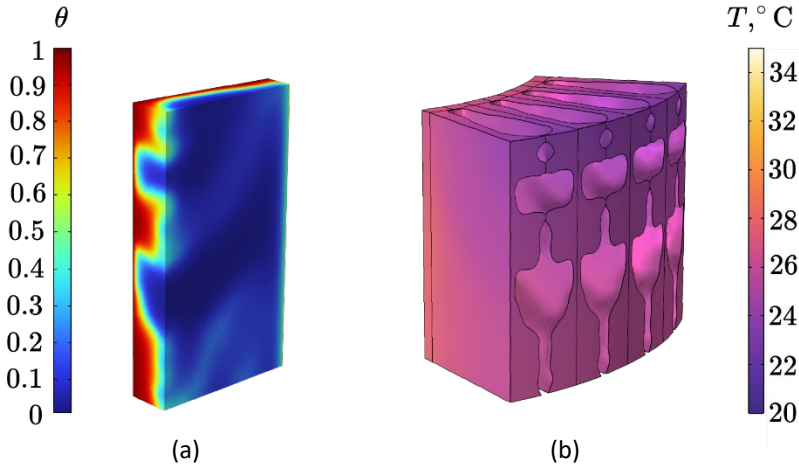


Figure 4.6. Resulting density variable distribution (a) and the temperature distribution in 45° TO heatsink sector if  $\theta > 0.4$  is defined as solid material (b) [79].

The resulting TO fin design is characterized by semi-open channels that redirect some airflow radially away from the heatsink. This is contrary to conventional design, where radial flow is generally not considered. Even though redirecting some of the airflow increases total drag, the increased effective surface area and boundary layer disruption are seemingly beneficial for overall thermal performance. The forming of the channels over the algorithm's iteration are shown in Figure 4.7. Interestingly, similar features appear with different electrical and geometrical parameters, and even different problem formulations (e.g. implementing turbulence). This suggests that the general idea of incorporating radial channels has utility. Therefore, even in cases where TO is not available, adding similar geometrical features in conventional fin designs should be considered.

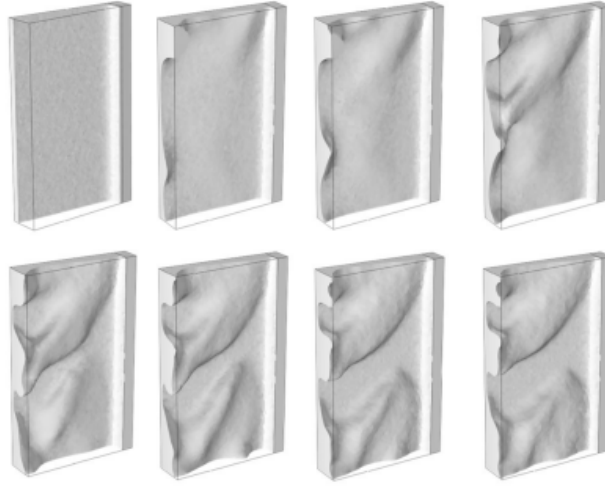


Figure 4.7. Iterative evolution of the TO fin geometry [79].

#### 4.4 Additively Manufactured Prototypes

After the numerical modelling process, AlSi10Mg prototypes of the PO and TO heatsinks are manufactured with LPBF using the SLM Solutions 280 2.0 metal 3D printer, according to the manufacturing and post-processing parameters discussed in the second chapter. The prototypes shown in Figure 4.8 display only minor warping and surface imperfections and can be considered to accurately represent the models. However, subtle dimensional differences result in a weight of 9.5 g for the PO heatsink (compared to 16 g in the model) and 25 g for the TO heatsink (compared to the 32 g in the model), which are added to the mass of the motor (167 g) to get the total weights ( $g = 9.81 \text{ m/s}^2$ ) for both cases of  $W_{\text{PO}} = 1.73 \text{ N}$  and  $W_{\text{TO}} = 1.88 \text{ N}$ . Additionally, as the mounting of the heatsink on the stator has a large effect on  $\mathcal{R}_0$ , care was taken to achieve an identical inner radius and surface finish for both heatsinks.

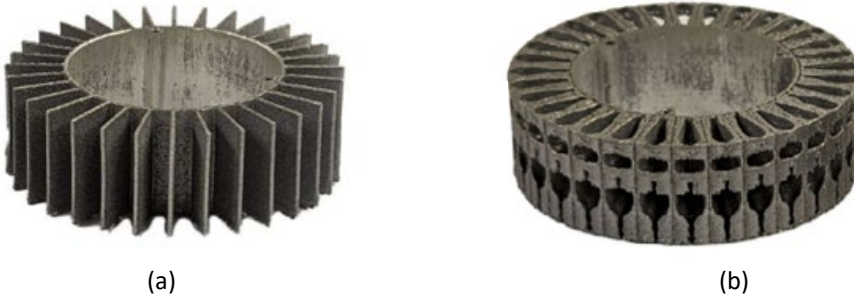


Figure 4.8. AlSi10Mg prototypes of the parametrically optimized (a) and topology optimized (b) heatsinks manufactured with LPBF [79].

##### 4.4.1 Performance Measurements

The performance of the heatsinks is measured by mounting the motor and propeller combination on a thrust stand so that the winding temperature, phase current and thrust can be measured simultaneously. Each phase current value is maintained until a

steady-state temperature is achieved, which is logged using a Pt1000 sensor thermally bonded to the rear end-windings of the motor, covered from direct airflow. This measurement is considered the hotspot temperature and is used to calculate  $\mathcal{R}_\Sigma$  according to the motor's thermal circuit and the total heating power in equation (4.4). The measurement setup, which includes current clamps for measuring  $I_{ph}$  and a precision data logger for measuring  $T_{Cu}$  and  $T_{amb}$ , is presented in Figure 4.9.

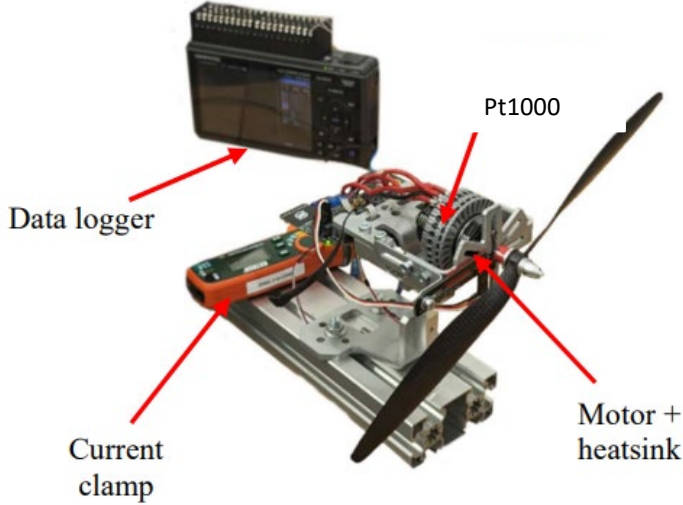


Figure 4.9. Thrust stand setup for measuring the performance of the PO and TO heatsinks [79].

#### 4.5 TO Results and Conclusions

The measurement results for  $\Delta T_{Cu}$  and  $\mathcal{R}_\Sigma$  in Figure 4.10 are shown in terms of phase current, which means that larger values correspond to a higher propeller speed and therefore airflow velocity. Across the measured range, the difference in  $\mathcal{R}_\Sigma$  between the PO and TO heatsinks is consistently around 0.08 K/W, which lines up perfectly with the  $\mathcal{R}_{Hs}$  difference in the numerical models where  $\mathcal{R}_{Hs-PO} = 0.24$  K/W and  $\mathcal{R}_{Hs-TO} = 0.16$  K/W (although some of the difference could potentially be caused by a slightly different  $\mathcal{R}_0$ ). In practice, this leads to a 4 °C drop in end-winding temperature at the target phase current of 60 A.

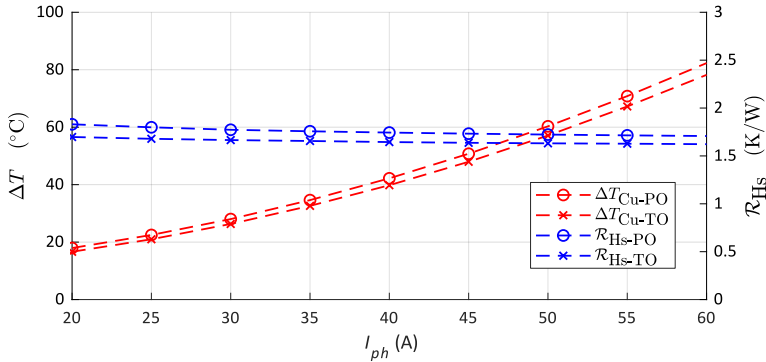


Figure 4.10. Measured temperatures and calculated  $\mathcal{R}_\Sigma$  values at different phase current values for the PO and TO heatsinks [79].

In terms of power, the drive equipped with the TO heatsink is capable of dissipating 1.8 W more heat at a temperature increase of  $\Delta T_{\text{Cu}} = 60^\circ\text{C}$  (chosen arbitrarily for comparison purposes). Defining a  $\Delta T_{\text{Cu}}$  also allows the thrust-to-weight ratio of the drive to be calculated. Interpolating  $I_{\text{ph}}(\Delta T_{\text{Cu}})$  from Figure 4.10, and extrapolating  $\mathcal{T}(I_{\text{ph}})$  from Figure 4.2 (the heatsink has no measurable aerodynamic effect on the thrust generation) gives the following values:  $I_{\text{ph-PO}}(\Delta 60^\circ\text{C}) = 49.8\text{ A}$  and  $\mathcal{T}_{\text{PO}} = 7.2\text{ N}$  for the PO heatsink and  $I_{\text{ph-TO}}(\Delta 60^\circ\text{C}) = 51.4\text{ A}$  and  $\mathcal{T}_{\text{TO}} = 7.4\text{ N}$  for the TO heatsink. Finally, the total weight of the drive in both cases is used to arrive at the thrust-to-weight ratios of 4.16 and 3.94 for the PO and TO heatsinks respectively.

While the thermal performance of the overall motor is dominated by a large  $\mathcal{R}_0$ , which heavily skews the higher thrust-to-weight ratio towards a lightweight heatsink, the main focus of this work is improving the effectiveness of the heatsink itself, i.e. minimizing  $\mathcal{R}_{\text{HS}}$ . In that regard, the TO heatsink performs excellently with a 33% reduction in  $\mathcal{R}_{\text{HS}}$  according to the numerical model, which is verified (albeit not directly) using AM prototypes. The distinctly unique fin geometry of the TO heatsink, which incorporates radially directed semi-open channels between the fins, is an excellent representation of the kinds of novel and unintuitive designs that the combination of TO and AM enables. Furthermore, by basing the optimization model on the specific working conditions of a propulsion drive, the quick prototyping and application-specific design capabilities of AM are fully utilized. Considering the relatively large performance gains in terms of  $\mathcal{R}_{\text{HS}}$  and the low amount of computing resources necessary ( $\sim 24\text{h}$  simulation time on a modern consumer CPU to create the TO heatsink model), topology optimization should certainly be considered as the primary design methodology when supported by the manufacturing method.

In the future, the single-objective model with a restricted solution space used in this work can be improved in several ways. First, fine-tuning the optimization parameters and increasing the available computing power would create a more general model without the predefined  $n_{\text{Fin}}$  and  $L_{\text{Fin}}$  parameters. This will push the final results closer towards a global optimum while simplifying the entire design process by eliminating the PO step. Second, designing the TO heatsink in conjunction with the motor, in which case  $\mathcal{R}_0$  and  $\mathcal{T}/W$  can be accurately modelled for each iteration, will create an application specific problem, resulting in a more desirable outcome in the actual optimization variable (i.e. thrust-to-weight ratio). Another interesting development can be expected in relation to multi-material AM that can potentially enable the concurrent fabrication of copper (conceivably acting as the highly thermally conductive although heavy core of a heatsink) and aluminium. For TO, this creates an interesting challenge as the binary material distribution will evolve into a ternary (or quaternary etc.) problem with potentially additional effects at the material boundaries. Alternatively, ever persistent limitations such as laminated structures for eddy current suppression could offer another path towards complexity with a need to implement various constraints into the TO algorithm. In any case, the advent of AM has allowed physical fabrication capabilities to finally catch up with numerical models, the advancement of which now has strong motivation. The end result being, of course, more effective practical solutions.

## 5 Conclusions and Future Work

This thesis presents a case for adopting additive manufacturing technologies, specifically metal-based LPBF, in the creation of high-performance thermal management solutions for air-cooled electrical machines. Compared to conventional manufacturing solutions, the current capabilities of AM provide three key advantages – geometrical freedom, application-specific design and quick prototyping. While an alternative can be found for each one of these attributes, it is the economically viable combination of all three that establishes AM as a crucial manufacturing technology of the future. In the work presented in this thesis, each of the advantages is utilized to improve the thermal performance of air-cooled electrical machines; the geometrical freedom is considered when design heatsinks with complex fin structures, the highest level of performance is achieved by considering the specific use-case during the design process, and the quick prototyping capabilities are leveraged to facilitate real-world measurements. The results, which include fully integrated solutions and significant improvements thanks to AM-based designs, thoroughly support the hypotheses of the thesis. In the following parts, the conclusions of the work are presented based on the thesis objectives.

A literature survey was conducted on the current state-of-the-art in the relevant AM methods, materials and solutions for electrical machine cooling. First, it revealed that the most suitable AM method for high-performance EM thermal solutions is LPBF due to its capability to work with thermally conductive metals without a noticeable degradation in important physical properties. While LPBF can theoretically be used with pure aluminium and copper (offering high relative and absolute conductivities respectively), practical limitations confine the large majority of existing thermal solutions to the AlSi10Mg alloy that is ~30% less conductive than pure aluminium. However, even though the physical properties of LPBF parts can be approximately equal to conventionally manufactured counterparts, they are still potentially influenced by specific manufacturing and post-processing parameters. For example, both AlSi10Mg and Fe-Si have shown to exhibit anisotropic properties when manufactured with LPBF, in mainly tensile strength and conductivity for the former and magnetic properties for the latter. Therefore, as knowing the TC of both these materials is crucial for accurately modelling the thermal performance of novel AM solutions, the direction-dependent TC and EC of AlSi10Mg and Fe-Si were measured as a part of this work with the following conclusions:

- The as-built AlSi10Mg samples showed significant anisotropy, with the direction coinciding with the manufacturing direction of the layer-by-layer LPBF process displaying a ~10% higher TC (113 vs 103 W/(m·K)) and a 12% higher EC (14.7 vs 13.1 MS/m).
- After heat-treatment, which consisted of heating the samples up to 300 °C, the TC and EC of the AlSi10Mg samples became effectively isotropic and increased to an average value of 150 W/(m·K) (46% increase) and 24 MS/s (83% increase) respectively.
- The as-built Fe-Si samples did not show any anisotropy in either TC or EC, and neither parameter was affected by the heat-treatment process (which has been shown to significantly enhance magnetic performance). Overall, the conductivity of LPBF Fe-Si is in line with commercially available laminations.

The measured TC and EC values confirmed that the available materials and LPBF device are appropriate for use in EM thermal solutions. Due to being isotropic after heat-treatment, a simple numeric value can be used for modelling purposes in the subsequent works. However, in cases where heat-treatment is not available (likely in the case of multi-material AM), the measured direction-dependent values can be used to define accurate TC and EC tensors. Furthermore, due to the much larger relative increase in EC compared to TC with heat treatment, some cooling solutions that are sensitive to eddy currents (e.g. heat guides attached directly to the conductors) could conceivably benefit from a lack of thermal treatment. Future work should look into purposeful reduction of EC in either material through specific manufacturing parameters in order to further reduce eddy current losses. While any such method would likely also reduce TC, depending on the machine topology and application, it can be a beneficial trade off.

Based on the review of the literature, application of AM in the thermal management of electrical machines is currently focused mainly on novel conductor cooling methods, while the research on the improvement of more typical cooling approaches, such as external air-cooled heatsinks, is comparatively lacking. Looking at wider AM-based solutions that could also be suitable for air-cooled EMs, the available literature of general-purpose AM cooling elements is focused on complex and novel structures (such as airfoil-shaped pins or lattice structures), which attempt to increase performance mainly through boundary layer disruption, or algorithmically optimized geometries, which aim to maximize performance through entirely novel structures. Therefore, the main part of this thesis is the investigation of these solutions in the context of air-cooled EMs.

Initially, the performance of various advanced fin structures were modelled numerically using a 3D nonisothermal CFD model. This was done in the context of a passively cooled switched reluctance motor, which resulted in the following main conclusions:

- The performance of conventional annular fins can be significantly improved (5.3% reduction in modelled  $\mathcal{R}_{\text{Hs}}$ ) simply by shaping the fins to be thinner farther away from the heatsink's base. While this geometry does not necessarily require AM for efficient fabrication, it is an excellent example of improving the performance of an established conventional solution through modifying the fin structure towards a more complicated geometry.
- In the case of passive cooling, the modelled results of the AM-based advanced structures showed a definite bias towards relatively open designs that prioritize total airflow over direct boundary layer disruption. The highest thermal performance was observed with the airfoil-shaped pins, which reduced the modelled  $\mathcal{R}_{\text{Hs}}$  by 8.1%
- The only lattice-based fin structure considered in the passive study was the simple cubic lattice. Despite its significantly larger total surface area compared to the conventional annular fins, the fin structure performed the worst out of all the proposed solutions with a 3.7% increase in  $\mathcal{R}_{\text{Hs}}$ , albeit at the lowest total fin volume.

The numerical models show that the thermal performance of heatsink fin structures can be substantially increased by utilizing more complex geometries. However, the fundamental design principles, according to which relatively open structures are favoured in the case of passive cooling, still apply due to the low pumping pressure in the

case of buoyancy driven flow. Therefore, a wider selection of advanced structures was tested in the context of an actively air-cooled AFSRM using an integrated mechanical and thermal solution. In this case, the rapid prototyping capabilities of AM were utilized to create AlSi10Mg frame pieces, which perfectly matched the dimensions of the wound stator core, ensuring a low internal thermal resistance. As a result, in the case of the more effective fin structures, the windings were able to maintain a current density of  $> 25 \text{ A/mm}^2$  at a temperature increase of  $80 \text{ }^\circ\text{C}$ . In conventional machines, this is only achievable using liquid cooling. In terms of comparing the active air-cooling performance of the advanced fin structures, the measurements done on LPBF prototypes gave the following results:

- In the case of active cooling, the airfoil pin fins decreased  $\mathcal{R}_{\text{Hs}}$  by 5% compared to the conventional solution and significantly outperformed each of the lattice structures, none of which managed to match the conventional solution in absolute performance.
- The rhombi octet lattice structure resulted in a 27.8% increase in  $\mathcal{R}_{\text{Hs}}$ , however at a 42% reduced fin mass, which gives it a 25% improved relative performance, making it the most thermally efficient structure in terms of fin mass out of all the studied geometries.

These measurements showed that even in the case of two high speed cooling fans in series, which provide a considerable pressure differential, relatively open fin structures still offer superior cooling, meaning that lattice structures are seemingly suboptimal for absolute thermal performance. However, currently this can only be stated in the context of passive and active air-cooling, while the higher pumping powers associated with liquid cooling could prove beneficial for dense lattice structures. Furthermore, in cases where the mass of the heatsink fins is a larger proportion of the total system mass (e.g. power electronics instead of electrical machines), lattice structures such as the rhombi octet can be favourable even with air-cooling due to higher relative performance compared to the conventional geometry. Nevertheless, in most practical EM-related cases, the best performing predefined fin geometry (that is currently known) can be said to be the airfoil pin fin with a staggered and angled placement.

In the final part of the thesis, to take full advantage of the advantages provided by AM, the common strategy of a predefined fin geometry was (mostly) replaced by an intrinsically novel fin structure using topology optimization. By modelling the heatsink and the surrounding air as a porous fluid based on Darcy's law, an optimization algorithm was used in conjunction with a numerical model to determine the most effective distribution of AlSi10Mg in terms of thermal performance. The TO study, which included measurements done with LPBF prototypes and a comparison to the conventional case, resulted in the following conclusions:

- A numerical optimization method based on fluid heat flow in porous media can be used to effectively optimize the fin geometry of an actively air-cooled heatsink. Compared to a parametrically optimized conventional solution, the topology optimized heatsink resulted in a 33% lower  $\mathcal{R}_{\text{Hs}}$  in the numerical model. The same gain in  $\mathcal{R}_{\text{Hs}}$  was indirectly (measuring  $\mathcal{R}_{\Sigma}$ ) confirmed through physical measurements.



- The resulting geometry of the topology optimization algorithm can be successfully manufactured from AlSi10Mg using LPBF, however the quality of the algorithm's final output can result in difficulties realizing the desired geometry.

For the field of AM-based EM air-cooling (and AM cooling solutions in general), the results of this thesis can be distilled into three important points of knowledge, each of which present a path towards future improvements. First, when absolute thermal performance in with air-cooling is required, which is often the case, fin structures prioritizing total airflow over direct boundary layer disruption are more effective. Currently the highest performing known example of this is the airfoil pin fin heatsink, which comfortably outperforms the commonly researched lattice structures. Consequently, future work should be directed at generalizing the airfoil pin fin heatsink design procedure through analytical and empirical correlations, while also looking into specific modifications of the airfoil shape. However, even higher performance can be achieved by replacing predefined fin structures with novel topology optimized geometries, which can be done at an increasingly affordable computational cost. Considering modern computational resources, it is difficult to argue against prioritizing TO (or other similar computation-based methods) when it comes to designing thermal solutions with AM in mind. The advantages of TO will continue to increase in the future as more detailed models and larger solution spaces become feasible. Finally, the topology of axial flux motors inherently allows effective direct conductor cooling, which can be fully leverage with the use of AM through geometrical freedom, application-specific design and quick prototyping capabilities. As a result, air-cooled motors designed with AM in mind can reach the power density of liquid-cooled motors, creating substantial opportunities for wider applications.

## References

- [1] B. Blakey-Milner, P. Gradl, G. Snedden, M. Brooks, J. Pitot, E. Lopez, M. Leary, F. Berto, A. du Plessis, Metal additive manufacturing in aerospace: A review, *Mater. Des.* 209 (2021) 110008. <https://doi.org/10.1016/j.matdes.2021.110008>.
- [2] A.N. Aufa, M.Z. Hassan, Z. Ismail, F. Ramlie, K.R. Jamaludin, M.Y. Md Daud, J. Ren, Current trends in additive manufacturing of selective laser melting for biomedical implant applications, *J. Mater. Res. Technol.* 31 (2024) 213–243. <https://doi.org/10.1016/j.jmrt.2024.06.041>.
- [3] M.J. Hossain, B.T. Tabatabaei, M. Kiki, J.-W. Choi, Additive Manufacturing of Sensors: A Comprehensive Review, *Int. J. Precis. Eng. Manuf.-Green Technol.* 12 (2025) 277–300. <https://doi.org/10.1007/s40684-024-00629-5>.
- [4] A. Pajonk, A. Prieto, U. Blum, U. Knaack, Multi-material additive manufacturing in architecture and construction: A review, *J. Build. Eng.* 45 (2022) 103603. <https://doi.org/10.1016/j.jobbe.2021.103603>.
- [5] N. Zhao, M. Parthasarathy, S. Patil, D. Coates, K. Myers, H. Zhu, W. Li, Direct additive manufacturing of metal parts for automotive applications, *J. Manuf. Syst.* 68 (2023) 368–375. <https://doi.org/10.1016/j.jmsy.2023.04.008>.
- [6] J.-H. Lee, C.-M. Lee, D.-H. Kim, Repair of damaged parts using wire arc additive manufacturing in machine tools, *J. Mater. Res. Technol.* 16 (2022) 13–24. <https://doi.org/10.1016/j.jmrt.2021.11.156>.
- [7] H. Tan, X. Fan, D. Li, T. Zou, W. Kong, R. Wang, X. Chen, R. Qu, Additively Manufactured Winding Design for Thermal Improvement of an Oil-Cooled Axial Flux Permanent Magnet Machine, *IEEE Trans. Transp. Electrification* 10 (2024) 1911–1922. <https://doi.org/10.1109/TTE.2023.3282213>.
- [8] N. Simpson, G. Yiannakou, H. Felton, J. Robinson, A. Arjunan, P.H. Mellor, Direct Thermal Management of Windings Enabled by Additive Manufacturing, *IEEE Trans. Ind. Appl.* 59 (2023) 1319–1327. <https://doi.org/10.1109/TIA.2022.3209171>.
- [9] A. Hassan, S. Abbas, L. Jie, L. Youming, C. Quanfang, Investigation of the Advanced Novel Carbon Nanotube (CNT) Yarn and Carbon Nanotube Aluminum/Copper Composite Windings for a Single-Phase Induction Motor, *Arab. J. Sci. Eng.* 47 (2022) 14915–14933. <https://doi.org/10.1007/s13369-022-07060-5>.
- [10] S.Q. Jia, F. Yang, High thermal conductive copper/diamond composites: state of the art, *J. Mater. Sci.* 56 (2021) 2241–2274. <https://doi.org/10.1007/s10853-020-05443-3>.
- [11] T. Wohlers, T. Gornet, History of additive manufacturing, (2015).
- [12] A. Husna, S. Ashrafi, A.A. Tomal, N.T. Tuli, A. Bin Rashid, Recent advancements in stereolithography (SLA) and their optimization of process parameters for sustainable manufacturing, *Hybrid Adv.* 7 (2024) 100307. <https://doi.org/10.1016/j.hybadv.2024.100307>.
- [13] J. He, S. Liang, F. Li, Q. Yang, M. Huang, Y. He, X. Fan, M. Wu, Recent Development in Liquid Metal Materials, *ChemistryOpen* 10 (2021) 360–372. <https://doi.org/10.1002/open.202000330>.
- [14] M. Sarap, A. Kallaste, P.S. Ghahfarokhi, H. Tiismus, T. Vaimann, The Effect of Build Direction on the Thermal Conductivity of Additively Manufactured AlSi10Mg and Silicon-steel Samples, in: 2022 Int. Conf. Electr. Mach. ICEM, 2022: pp. 538–543. <https://doi.org/10.1109/ICEM51905.2022.9910944>.

- [15] L. Haferkamp, L. Haudenschild, A. Spierings, K. Wegener, K. Riener, S. Ziegelmeier, G.J. Leichtfried, The Influence of Particle Shape, Powder Flowability, and Powder Layer Density on Part Density in Laser Powder Bed Fusion, *Metals* 11 (2021) 418. <https://doi.org/10.3390/met11030418>.
- [16] K. Morshed-Behbahani, A. Aliyu, D.P. Bishop, A. Nasiri, Additive manufacturing of copper-based alloys for high-temperature aerospace applications: A review, *Mater. Today Commun.* 38 (2024) 108395. <https://doi.org/10.1016/j.mtcomm.2024.108395>.
- [17] N.T. Aboulkhair, M. Simonelli, L. Parry, I. Ashcroft, C. Tuck, R. Hague, 3D printing of Aluminium alloys: Additive Manufacturing of Aluminium alloys using selective laser melting, *Prog. Mater. Sci.* 106 (2019) 100578. <https://doi.org/10.1016/j.pmatsci.2019.100578>.
- [18] M. Laleh, E. Sadeghi, R.I. Revilla, Q. Chao, N. Haghdadi, A.E. Hughes, W. Xu, I. De Graeve, M. Qian, I. Gibson, M.Y. Tan, Heat treatment for metal additive manufacturing, *Prog. Mater. Sci.* 133 (2023) 101051. <https://doi.org/10.1016/j.pmatsci.2022.101051>.
- [19] C. Silbernagel, I. Ashcroft, P. Dickens, M. Galea, Electrical resistivity of additively manufactured AlSi10Mg for use in electric motors, *Addit. Manuf.* 21 (2018) 395–403. <https://doi.org/10.1016/j.addma.2018.03.027>.
- [20] K. Jahns, R. Bappert, P. Böhlke, U. Krupp, Additive manufacturing of CuCr1Zr by development of a gas atomization and laser powder bed fusion routine, *Int. J. Adv. Manuf. Technol.* 107 (2020) 2151–2161. <https://doi.org/10.1007/s00170-020-04941-7>.
- [21] F. Lorenz, J. Rudolph, R. Wemer, Design of 3D Printed High Performance Windings for Switched Reluctance Machines, in: 2018 XIII Int. Conf. Electr. Mach. ICEM, 2018: pp. 2451–2457. <https://doi.org/10.1109/ICELMACH.2018.8506845>.
- [22] W. Sixel, M. Liu, G. Nellis, B. Sarlioglu, Ceramic 3D Printed Direct Winding Heat Exchangers for Improving Electric Machine Thermal Management, in: 2019 IEEE Energy Convers. Congr. Expo. ECCE, 2019: pp. 769–776. <https://doi.org/10.1109/ECCE.2019.8913234>.
- [23] J. Rauchenecker, J. Rabitsch, M. Schwentenwein, T. Konegger, Additive manufacturing of aluminum nitride ceramics with high thermal conductivity via digital light processing, *Open Ceram.* 9 (2022) 100215. <https://doi.org/10.1016/j.oceram.2021.100215>.
- [24] Ice9 TPU - TCPoly - Advanced 3D Printer Materials, (2023). <https://tcpoly.com/flex-ice9/> (accessed May 26, 2025).
- [25] H. Tiismus, A. Kallaste, T. Vaimann, A. Rassõlkin, State of the art of additively manufactured electromagnetic materials for topology optimized electrical machines, *Addit. Manuf.* 55 (2022) 102778. <https://doi.org/10.1016/j.addma.2022.102778>.
- [26] E. Dlala, R.J. Biskup, D. Moseley, A. Bassanese, B. Maniam, J. Mayer, Motor cooling system utilizing axial cooling channels, US10158263B2, 2018. <https://patents.google.com/patent/US10158263B2/en> (accessed May 26, 2025).
- [27] N. Simpson, S.P. Munagala, A. Catania, F. Derguti, P.H. Mellor, Functionally Graded Electrical Windings Enabled by Additive Manufacturing, in: 2022 Int. Conf. Electr. Mach. ICEM, 2022: pp. 1477–1483. <https://doi.org/10.1109/ICEM51905.2022.9910912>.

- [28] W. Sixel, M. Liu, G. Nellis, B. Sarlioglu, Ceramic 3-D Printed Direct Winding Heat Exchangers for Thermal Management of Concentrated Winding Electric Machines, *IEEE Trans. Ind. Appl.* 57 (2021) 5829–5840. <https://doi.org/10.1109/TIA.2021.3104273>.
- [29] P. Frigola, O.A. Harrysson, T.J. Horn, H.A. West, R.L. Aman, J.M. Rigsbee, D.A. Ramirez, L.E. Murr, F. Medina, R.B. Wicker, E. Rodriguez, Fabricating Copper Components with Electron Beam Melting, *AMP Tech. Artic.* 172 (2014) 20–24. <https://doi.org/10.31399/asm.amp.2014-07.p020>.
- [30] A Review on Additive Manufacturing of Pure Copper, (n.d.). <https://www.mdpi.com/2079-6412/11/6/740> (accessed May 26, 2025).
- [31] A. Unterstell, CuCr1Zr, C18150 | Datasheet | METALCOR, (n.d.). <https://www.metalcor.de/en/datenblatt/133/> (accessed May 26, 2025).
- [32] B. Buchmayr, G. Panzl, A. Walzl, C. Wallis, Laser Powder Bed Fusion – Materials Issues and Optimized Processing Parameters for Tool steels, AlSiMg- and CuCrZr-Alloys, *Adv. Eng. Mater.* 19 (2017) 1600667. <https://doi.org/10.1002/adem.201600667>.
- [33] EN 1706:2010 Aluminium and aluminium alloys - Castings - Chemical composition and mechanical properties, (n.d.).
- [34] A. Franco Júnior, D.J. Shanafield, Thermal conductivity of polycrystalline aluminum nitride (AlN) ceramics, *Cerâmica* 50 (2004) 247–253. <https://doi.org/10.1590/S0366-69132004000300012>.
- [35] C.A. Díaz-Moreno, Y. Lin, A. Hurtado-Macías, D. Espalin, C.A. Terrazas, L.E. Murr, R.B. Wicker, Binder jetting additive manufacturing of aluminum nitride components, *Ceram. Int.* 45 (2019) 13620–13627. <https://doi.org/10.1016/j.ceramint.2019.03.187>.
- [36] L. Thijs, K. Kempen, J.-P. Kruth, J. Van Humbeeck, Fine-structured aluminium products with controllable texture by selective laser melting of pre-alloyed AlSi10Mg powder, *Acta Mater.* 61 (2013) 1809–1819. <https://doi.org/10.1016/j.actamat.2012.11.052>.
- [37] D. Wang, Y. Wei, X. Wei, K. Khanlari, Z. Wang, Y. Feng, X. Yang, Selective Laser Melting of Pure Ag and 925Ag Alloy and Their Thermal Conductivity, *Crystals* 12 (2022) 480. <https://doi.org/10.3390/cryst12040480>.
- [38] M.-S. Kim, Effects of Processing Parameters of Selective Laser Melting Process on Thermal Conductivity of AlSi10Mg Alloy, *Materials* 14 (2021) 2410. <https://doi.org/10.3390/ma14092410>.
- [39] M. Sarap, H. Tiismus, A. Kallaste, M. Saarna, M. Kolnes, P. Shams Ghahfarokhi, T. Vaimann, Electrical and Thermal Anisotropy in Additively Manufactured AlSi10Mg and Fe-Si Samples, *Machines* 13 (2025) 1. <https://doi.org/10.3390/machines13010001>.
- [40] M. Garibaldi, I. Ashcroft, J.N. Lemke, M. Simonelli, R. Hague, Effect of annealing on the microstructure and magnetic properties of soft magnetic Fe-Si produced via laser additive manufacturing, *Scr. Mater.* 142 (2018) 121–125. <https://doi.org/10.1016/j.scriptamat.2017.08.042>.
- [41] Electrical Steel Thin Non-Oriented Grades American version, (n.d.). <https://www.polarislaserlaminations.com/Cogent.pdf>.

- [42] R. Wrobel, B. Scholes, A. Hussein, R. Law, A. Mustaffar, D. Reay, A metal additively manufactured (MAM) heat exchanger for electric motor thermal control on a high-altitude solar aircraft – Experimental characterisation, *Therm. Sci. Eng. Prog.* 19 (2020) 100629. <https://doi.org/10.1016/j.tsep.2020.100629>.
- [43] Z. Wang, X. Huang, Design and Preliminary Optimization of a Heat Exchanger Formed by Additive Manufacturing for Outer-Rotor PMSM, *IEEE Trans. Energy Convers.* 39 (2024) 1383–1393. <https://doi.org/10.1109/TEC.2023.3347514>.
- [44] M. Bieber, M. Haase, F. Tasche, A. Zibart, B. Ponick, Additively manufactured air-cooled lightweight rotor for an automotive electric motor, in: 2023 IEEE Int. Electr. Mach. Drives Conf. IEMDC, 2023: pp. i–vii. <https://doi.org/10.1109/IEMDC55163.2023.10238918>.
- [45] H. Tan, X. Fan, D. Li, T. Zou, W. Kong, R. Wang, X. Chen, R. Qu, Additively Manufactured Winding Design for Thermal Improvement of an Oil-Cooled Axial Flux Permanent Magnet Machine, *IEEE Trans. Transp. Electrification* 10 (2024) 1911–1922. <https://doi.org/10.1109/TTE.2023.3282213>.
- [46] R. Wrobel, A. Hussein, A Feasibility Study of Additively Manufactured Heat Guides for Enhanced Heat Transfer in Electrical Machines, *IEEE Trans. Ind. Appl.* 56 (2020) 205–215. <https://doi.org/10.1109/TIA.2019.2949258>.
- [47] T. Chowdhury, S. Koushan, A. Al-Qarni, A. El-Refaie, K. Bennion, E. Cousineau, X. Feng, B. Kekelia, Thermal Management System for an Electric Machine with Additively Manufactured Hollow Conductors with Integrated Heat Pipes, in: 2022 Int. Conf. Electr. Mach. ICEM, 2022: pp. 1920–1926. <https://doi.org/10.1109/ICEM51905.2022.9910918>.
- [48] J. Pecotich, D. Klink, G. Heins, B. Bahrani, Additively Manufactured Electric Machine Conductors with Integrated End Turn Heat Exchangers, in: 2022 Int. Conf. Electr. Mach. ICEM, 2022: pp. 1498–1504. <https://doi.org/10.1109/ICEM51905.2022.9910686>.
- [49] C. Wohlers, P. Juris, S. Kabelac, B. Ponick, Design and direct liquid cooling of tooth-coil windings, *Electr. Eng.* 100 (2018) 2299–2308. <https://doi.org/10.1007/s00202-018-0704-x>.
- [50] Conflux and Donkervoort develop F1-grade additively manufactured air cooler for P24 RS supercar, *Met. Addit. Manuf.* (2025). <https://www.metal-am.com/conflux-and-donkervoort-develop-f1-grade-additively-manufactured-air-cooler-for-p24-rs-supercar/> (accessed May 28, 2025).
- [51] 3D Printed Metal Cooling Jacket Boost the Formula Electric Student Team, *Eplus3D* (n.d.). <https://www.eplus3d.com/3d-printed-metal-cooling-jacket-boost-the-formula-electric-student-team.html> (accessed May 28, 2025).
- [52] F. Wu, A.M. EL-Refaie, A. Al-Qarni, Additively Manufactured Hollow Conductors for High Specific Power Electrical Machines: Aluminum vs Copper, in: 2021 IEEE Energy Convers. Congr. Expo. ECCE, 2021: pp. 4397–4404. <https://doi.org/10.1109/ECCE47101.2021.9595470>.
- [53] N. Simpson, G. Yiannakou, H. Felton, J. Robinson, A. Arjunan, P.H. Mellor, Direct Thermal Management of Windings Enabled by Additive Manufacturing, *IEEE Trans. Ind. Appl.* 59 (2023) 1319–1327. <https://doi.org/10.1109/TIA.2022.3209171>.
- [54] F. Wu, A.M. EL-Refaie, A. Al-Qarni, Additively Manufactured Hollow Conductors Integrated With Heat Pipes: Design Tradeoffs and Hardware Demonstration, *IEEE Trans. Ind. Appl.* 57 (2021) 3632–3642. <https://doi.org/10.1109/TIA.2021.3076423>.

- [55] A.N. Pilagatti, G. Piscopo, E. Atzeni, L. Iuliano, A. Salmi, Design of additive manufactured passive heat sinks for electronics, *J. Manuf. Process.* 64 (2021) 878–888. <https://doi.org/10.1016/j.jmapro.2021.01.035>.
- [56] J. Alexandersen, O. Sigmund, K.E. Meyer, B.S. Lazarov, Design of passive coolers for light-emitting diode lamps using topology optimisation, *Int. J. Heat Mass Transf.* 122 (2018) 138–149. <https://doi.org/10.1016/j.ijheatmasstransfer.2018.01.103>.
- [57] S.U. Hassan, M.H. Shah, P. Gruber, M. Chomat, Triply Periodic Minimal Surfaces Structure for Efficient Heat Dissipation in Motor Housings: A Convective Potential Analysis, in: 2024 Int. Conf. Electr. Mach. ICEM, 2024: pp. 1–7. <https://doi.org/10.1109/ICEM60801.2024.10700091>.
- [58] W. Sixel, M. Liu, G. Nellis, B. Sarlioglu, Cooling of Windings in Electric Machines via 3D Printed Heat Exchanger, in: 2018 IEEE Energy Convers. Congr. Expo. ECCE, 2018: pp. 229–235. <https://doi.org/10.1109/ECCE.2018.8557845>.
- [59] C.-S. Wang, M.M. Yovanovich, J.R. Culham, General Model for Natural Convection: Application to Annular-Fin Heat Sinks, in: Baltimore, Maryland, 1997: pp. 119–128.
- [60] A. Mallick, R. Ranjan, P.K. Sarkar, Effect of heat transfer on thermal stresses in an annular hyperbolic fin: an approximate analytical solution, *J. Theor. Appl. Mech.* 54 (2016) 437–448. <https://doi.org/10.15632/jtam-pl.54.2.437>.
- [61] K.K. Wong, Ho J. Y., Leong, K. C., T.N. and Wong, Fabrication of heat sinks by Selective Laser Melting for convective heat transfer applications, *Virtual Phys. Prototyp.* 11 (2016) 159–165. <https://doi.org/10.1080/17452759.2016.1211849>.
- [62] D. Staton, A. Boglietti, A. Cavagnino, Solving the more difficult aspects of electric motor thermal analysis in small and medium size industrial induction motors, *IEEE Trans. Energy Convers.* 20 (2005) 620–628. <https://doi.org/10.1109/TEC.2005.847979>.
- [63] J.E. Cousineau, K. Bennion, D. DeVoto, S. Narumanchi, Experimental characterization and modeling of thermal resistance of electric machine lamination stacks, *Int. J. Heat Mass Transf.* 129 (2019) 152–159. <https://doi.org/10.1016/j.ijheatmasstransfer.2018.09.051>.
- [64] B. Gebhart, Effects of viscous dissipation in natural convection, *J. Fluid Mech.* 14 (1962) 225–232. <https://doi.org/10.1017/S0022112062001196>.
- [65] M. Sarap, A. Kallaste, P.S. Ghahfarokhi, T. Vaimann, Analysis of Advanced Passive Heatsinks For Electrical Machines Enabled by Additive Manufacturing, in: 2023 IEEE Workshop Electr. Mach. Des. Control Diagn. WEMDCD, 2023: pp. 1–6. <https://doi.org/10.1109/WEMDCD55819.2023.10110940>.
- [66] M. Sarap, S. Singh, A. Kallaste, A. Qureshi, H. Tiismus, T. Vaimann, P.S. Ghahfarokhi, Design of an additively manufactured thermal solution for an axial flux switched reluctance motor, *Case Stud. Therm. Eng.* 66 (2025) 105805. <https://doi.org/10.1016/j.csite.2025.105805>.
- [67] J.R. Culham, Y.S. Muzychka, Optimization of plate fin heat sinks using entropy generation minimization, *IEEE Trans. Compon. Packag. Technol.* 24 (2001) 159–165. <https://doi.org/10.1109/6144.926378>.
- [68] P. Teertstra, M.M. Yovanovich, J.R. Culham, T. Lemczyk, Analytical forced convection modeling of plate fin heat sinks, in: Fifteenth Annu. IEEE Semicond. Therm. Meas. Manag. Symp. Cat No99CH36306, 1999: pp. 34–41. <https://doi.org/10.1109/STHERM.1999.762426>.

- [69] J.Y. Ho, K.K. Wong, K.C. Leong, T.N. Wong, Convective heat transfer performance of airfoil heat sinks fabricated by selective laser melting, *Int. J. Therm. Sci.* 114 (2017) 213–228. <https://doi.org/10.1016/j.ijthermalsci.2016.12.016>.
- [70] J.Y. Ho, K.C. Leong, Cylindrical porous inserts for enhancing the thermal and hydraulic performance of water-cooled cold plates, *Appl. Therm. Eng.* 121 (2017) 863–878. <https://doi.org/10.1016/j.applthermaleng.2017.04.101>.
- [71] J.Y. Ho, K.C. Leong, T.N. Wong, Experimental and numerical investigation of forced convection heat transfer in porous lattice structures produced by selective laser melting, *Int. J. Therm. Sci.* 137 (2019) 276–287. <https://doi.org/10.1016/j.ijthermalsci.2018.11.022>.
- [72] J.Y. Ho, K.C. Leong, T.N. Wong, Additively-manufactured metallic porous lattice heat exchangers for air-side heat transfer enhancement, *Int. J. Heat Mass Transf.* 150 (2020) 119262. <https://doi.org/10.1016/j.jheatmasstransfer.2019.119262>.
- [73] T. Dixit, P. Nithiarasu, S. Kumar, Numerical evaluation of additively manufactured lattice architectures for heat sink applications, *Int. J. Therm. Sci.* 159 (2021) 106607. <https://doi.org/10.1016/j.ijthermalsci.2020.106607>.
- [74] M. Khalil, M.I. Hassan Ali, K.A. Khan, R. Abu Al-Rub, Forced convection heat transfer in heat sinks with topologies based on triply periodic minimal surfaces, *Case Stud. Therm. Eng.* 38 (2022) 102313. <https://doi.org/10.1016/j.csite.2022.102313>.
- [75] D. Mahmoud, S.R.S. Tandel, M. Yakout, M. Elbestawi, F. Mattiello, S. Paradiso, C. Ching, M. Zaher, M. Abdelnabi, Enhancement of heat exchanger performance using additive manufacturing of gyroid lattice structures, *Int. J. Adv. Manuf. Technol.* 126 (2023) 4021–4036. <https://doi.org/10.1007/s00170-023-11362-9>.
- [76] T. Dixit, E. Al-Hajri, M.C. Paul, P. Nithiarasu, S. Kumar, High performance, microarchitected, compact heat exchanger enabled by 3D printing, *Appl. Therm. Eng.* 210 (2022) 118339. <https://doi.org/10.1016/j.applthermaleng.2022.118339>.
- [77] W. Tang, H. Zhou, Y. Zeng, M. Yan, C. Jiang, P. Yang, Q. Li, Z. Li, J. Fu, Y. Huang, Y. Zhao, Analysis on the convective heat transfer process and performance evaluation of Triply Periodic Minimal Surface (TPMS) based on Diamond, Gyroid and Iwp, *Int. J. Heat Mass Transf.* 201 (2023) 123642. <https://doi.org/10.1016/j.jheatmasstransfer.2022.123642>.
- [78] M. Sarap, S. Singh, A. Kallaste, A. Qureshi, H. Tiismus, T. Vaimann, P.S. Ghahfarokhi, Comparative Study of Advanced Heatsink Structures for Improved Thermal Performance in Axial Flux Motors, *IEEE Access* (2025) 1–1. <https://doi.org/10.1109/ACCESS.2025.3577289>.
- [79] M. Sarap, A. Kallaste, T. Vaimann, P.S. Ghahfarokhi, Additively Manufactured and Topology Optimized Heatsink for a Propulsion Motor, in: 2024 Int. Conf. Electr. Mach. ICEM, 2024: pp. 1–6. <https://doi.org/10.1109/ICEM60801.2024.10700108>.
- [80] Propeller Thrust, Glenn Res. Cent. NASA (n.d.). <https://www1.grc.nasa.gov/beginners-guide-to-aeronautics/propeller-thrust/> (accessed May 26, 2025).
- [81] L. Berrocal, R. Fernández, S. González, A. Perifán, S. Tudela, J. Vilanova, L. Rubio, J.M. Martín Márquez, J. Guerrero, F. Lasagni, Topology optimization and additive manufacturing for aerospace components, *Prog. Addit. Manuf.* 4 (2019) 83–95. <https://doi.org/10.1007/s40964-018-0061-3>.

- [82] M. Cavazzuti, A. Baldini, E. Bertocchi, D. Costi, E. Torricelli, P. Moruzzi, High performance automotive chassis design: a topology optimization based approach, *Struct. Multidiscip. Optim.* 44 (2011) 45–56. <https://doi.org/10.1007/s00158-010-0578-7>.
- [83] L. Mei, Q. Wang, Structural Optimization in Civil Engineering: A Literature Review, *Buildings* 11 (2021) 66. <https://doi.org/10.3390/buildings11020066>.
- [84] A. Fawaz, Y. Hua, S. Le Corre, Y. Fan, L. Luo, Topology optimization of heat exchangers: A review, *Energy* 252 (2022) 124053. <https://doi.org/10.1016/j.energy.2022.124053>.



## **Acknowledgements**

I would like to thank my supervisors, co-workers and our wonderful support staff for their support and advice during my PhD studies. This research was financially supported by the Estonian Research Council through the research grant PRG-1827.

## **Abstract**

### **Additively Manufactured Advanced Thermal Management Solutions for Electrical Machines**

This thesis delves into the potential of additive manufacturing, particularly metal-based LPBF, for creating improved thermal management solutions for electrical machines. Increasing demands for electrical machine performance together with constraints on size and weight presents a difficult design challenge for cooling that cannot necessarily be met by conventional manufacturing. This work demonstrates that, through leveraging its unique advantages in geometrical freedom, application-specific design and fast prototyping, significant improvements in thermal performance are available with AM, leading to electrical machines with higher power densities, more efficient operation and increased reliability. Specifically, the work investigates and validates the use of advanced fin structures and algorithmically optimized designs manufactured with LPBF for both passively and actively air-cooled electrical machines. This thesis is based on three main parts.

Initially, a comprehensive literature review of AM methods, materials, and existing solutions in the field of EM thermal management is carried out. In the first part, it highlights the suitability of LPBF for manufacturing thermally conductive materials like AlSi10Mg and magnetic materials like Fe-Si, which are crucial for high-performance EM thermal solutions. However, due to the extreme conditions presented on the materials during the LPBF process, the physical properties of the final object are not necessarily equal to the base material. Therefore, experimental verification of the anisotropic thermal and electrical conductivities of the aforementioned materials is carried out as a necessary step before any novel solutions can be proposed. The results reveal that while the LPBF parts can be suitable for practical applications, it is important to consider the effects of heat treatment and manufacturing direction. The second part of the literature review identifies a research gap specifically in AM-based solutions for air-cooled electrical machines, which have been overshadowed by a plethora of research on direct conductor cooling. While DCC can enable the most power dense EMs to meet extremely strict requirements, the wide applicability and robustness of air-cooling gives means that an AM-based evolution there has perhaps an even larger potential for groundbreaking results. Naturally then, the focus of this thesis was set at advancing the air-cooling of EMs through advanced AM-enabled designs.

After confirming the viability of LPBF and setting a clear focus on air-cooled EMs, the first steps towards improved performance were done in the context of a passively cooled SRM. In the second part of the thesis, through numerical fluid dynamics models, several promising design improvements were studied with encouraging results; advancing conventional designs towards more complicated structures can yield definite improvements. The largest gains were seen with airfoil-shaped pin fins, which most effectively utilize the main working principles of heatsinks through fast-moving airflow and direct interaction with the boundary layer. Emboldened by these results, the thesis continues with the advanced structures, however now in the context of an axial flux machine and with physical AM prototypes. The combination of an axial flux topology with the application-specific design capabilities of AM provides an immediate benefit by implementing the cooling element directly on the heat-producing windings of the machine. Even when paired with a conventional heatsink, this enables current densities

exceeding  $25 \text{ A/mm}^2$ , although its full potential is tapped by again implementing advanced fin structures, namely the airfoil pin fins. Similarly to the simulation results in the passive cooling case, the seemingly unwarrantable complexity of lattice structures does not result in improved absolute performance. However, when it comes to gravimetric relative performance, admittedly rather niche parameter, the strength of lattice structures is revealed with the rhombi octet structure claiming the crown for now. The second part of the thesis clearly demonstrates that when it comes to maximizing thermal performance through a predefined geometry, the airfoil pin fin should be the first choice. Importantly though, this is true when limited only to predefined geometries.

Modern methods have made it possible to replace many established design formulations with computational brute force by creating novel solutions through iterative numerical models. The third part of this thesis introduces this method to the field of EM cooling in the form of a topology optimized heatsink for an electric propulsion drive. For this, a fluid dynamics model based on flow in porous media is constructed. In the model, the distribution of impermeable elements, representing solid conductive material, is iteratively optimized according to an objective function. The resulting heatsink achieves a 33% improvement over a conventional solution through entirely novel features inside the fin structure that are reliant on AM for practically viable fabrication. This gain in performance, which is experimentally verified using LPBF prototypes, conclusively demonstrates the advantages of AM in the thermal management of electrical machines.

## Lühikokkuvõte

### Kihtlisandusmeetodil valmistatud täiustatud jahutuslahendused elektrimasinatele

Käesolev lõputöö uurib kihtlisandusmeetodi rakendamist elektrimasinate jahutuse täiendamisel. Süvenevad nõuded elektrimasinate suutlikkusele ja piirangud mahule ning massile esitavad jahutuse osas väljakutse, millele harilikud tootmismeetodid ei suuda tingimata vastata. Antud töö raames demonstreeritakse, et läbi kihtlisandusmeetodi eeliste, milleks on geomeetriline vabadus, valdkonna-spetsiifiline kujundus ja kiire proovitoote loomine, on võimalik saavutada jahutusvõimekuses märkimisväärsed edusamme. Selle tulemusena on võimalik valmistada võimsustihedamaid, töökindlaid ja kõrgema kasuteguriga elektrimasiinaid. Täpsemalt uurib käesolev töö täiustatud ja algoritmiliselt optimeeritud ribistruktuuride kujundamist, nende tootmist läbi metallide laserpulbersulatus ja kasutamist loomulikult ja sundventileeritud elektrimasinate jahutamisel. Lõputöö koosneb kolmest peamisest osast.

Esiteks viidi läbi põhjalik kirjandusanalüüs, milles uuriti elektrimasinate jahutuse valdkonnas kasutatavaid kihtlisandusmeetodi tehnoloogiaid, materjale ning ka valdkonna teaduskirjanduses olemasolevaid lahendusi. Kirjandusanalüüsi esimeses osas tuuakse välja metallide laserpulbersulatus kui sobivaim tehnoloogia nii soojusjuhtide kui ka magnetiliste materjalide valmistamiseks. Sellegipoolest võib ekstreemsetes tingimustes toimuva protsessi käigus avalduda muutuseid materjalide füüsikalistes omadustes. Seega sooritati muutuste kaardistamiseks enne konkreetsete jahutuslahenduste modelleerimist materjalide anisotroopsete soojus- ja elektrijuhtivuse mõõtmised. Tulemused kinnitasid, et kuigi laserpulbersulatatud detailid sobivad praktiliseks kasutuseks, ei tohi unustada detaili valmistamise suuna ega lõõmutamise mõju. Kirjandusanalüüsi teises osas tuvastati õhkjahutatud mootorite teadusuuringutes suhteline tühimik, mille on tekitanud teadustöö valdav keskendumine mähiste otsejahutusele. Kuigi mähiste otsene jahutus võimaldab suurima võimsustihedusega elektrimasinate loomist, annavad õhkjahutuse laialdasem kasutus ja töökindlus just sellele valdkonnale suurima potentsiaali saavutada kihtlisandusmeetodi najal läbimurdvaid tulemusi. Seega seati lõputöö fookuseks justnimelt õhkjahutatud elektrimasinate arendus läbi kihtlisandusmeetodil põhinevate uudsete lahenduste.

Peale laserpulbersulatus kasulikkuses veendumist ja selge fookuse seadmist tehti esimesed sammud jahutusvõimekuse tõstmise poole passiivselt jahutatud radiaalvoomootori baasil. Lõputöö teises osas uuriti läbi arvutuslike vedelikudünaamika mudelite erinevaid paljulubavaid struktuure ning tulemused olid lootustandvad. Nimelt saavutati tavapäraste kavandite arendamisel keerukamate kujundite suunas selged eelised. Suurim võit modelleeriti tiivaprofiili-kujulise viikribi jahutiga, mis suudab suurendada korraga õhuvoolu kiirust ja otsest piirkihi vastasmõju. Saades tulemustest julgustust, jätkus töö täiustatud struktuuride uurimisega. Seekord aga telgvoomasina ja füüsiliste prototüüpide baasil. Telgwoo topoloogia kombineerimisel kihtlisandusmeetodi võimekusega on võimalik saavutada kohene eelis. Paigutades jahutuselement otse mootori mähiste külge, on isegi tavapärase ribistruktuuriga võimalik saavutada mähistes voolutihedus, mille väärtus ületab  $25 \text{ A/mm}^2$  piiri. Sellegipoolest loodi antud lahenduse täispotentsiaali kasutamiseks täiustatud ribistruktuuridega katsekehad. Sarnaselt eelnevate simulatsioonidega, näitasid mõõtmiste tulemused, et parim absoluutne jahutusvõimekus on võimalik saavutada tiivaprofiili-kujuliste viikribide abil. Samuti ei ole

ka sundventilatsiooni korral kärgstruktuuride keerukus absoluutse jahutusvõimekuse osas põhjendatud, kuid originaalse tulemusena avastati, et nende tugevused peituvad suhtelises jahutusjõudluses. Selle mõnevõrra vähemtähtsa parameetri alusel pakub eelkõige kaheksatahulisel kärgstruktuuril põhinev lahendus parimaid tulemusi. Lõputöö teine osa demonstreerib selgelt, et jahutusvõimekuse parandamisel läbi teadaoleva geomeetria on tiivaprofiili-kujuline viikribi jahuti selge esimene valik. Siiski tuleb meeles pidada, et see väide kehtib vaid teadaoleva geomeetria kasutamise korral.

Moodsate meetodite abil on võimalik paljud olemasolevad lahenduskäigud asendada toore arvutusjõudluse ja iteratiivsete numbriliste mudelitega. Lõputöö kolmandas osas rakendatakse seda protsessi elektrimasinate jahutamiseks läbi topoloogiaoptimeeritud geomeetria. Selle raames luuakse poorsel keskkonnal põhinev vedelikedünaamika mudel, mille abil optimeeritakse iteratiivselt jahuti materjali jaotus ruumis. Mudeli tulemina valminud elektrilise lennumasina ajami jahuti, mida on praktikas võimalik valmistada vaid kihtlisandusmeetodi abil ning mille ribistruktuur põhineb täielikult uudsel geomeetrial, saavutas 33% suuruse edu tavapärase lahenduse üle. See parandus jahutusvõimekuses, mis kinnitati füüsiliste prototüüpide abil, demonstreerib lõplikult kihtlisandusmeetodi eeliseid elektrimasinate jahutuslahedustes.

## Appendix

### Publication I

M. Sarap, A. Kallaste, P. Shams Ghahfarokhi, H. Tiismus, and T. Vaimann, "Utilization of Additive Manufacturing in the Thermal Design of Electrical Machines: A Review," *Machines*, vol. 10, no. 4, Art. no. 4, Apr. 2022, doi: 10.3390/machines10040251.



## Review

# Utilization of Additive Manufacturing in the Thermal Design of Electrical Machines: A Review

Martin Sarap <sup>1,\*</sup>, Ants Kallaste <sup>1</sup>, Payam Shams Ghahfarokhi <sup>1,2</sup>, Hans Tiismus <sup>1</sup> and Toomas Vaimann <sup>1</sup>

<sup>1</sup> Department of Electrical Power Engineering and Mechatronics, Tallinn University of Technology, 19086 Tallinn, Estonia; ants.kallaste@taltech.ee (A.K.); payam.shams@taltech.ee (P.S.G.); hans.tiismus@taltech.ee (H.T.); toomas.vaimann@taltech.ee (T.V.)

<sup>2</sup> Department of Electrical Machines and Apparatus, Riga Technical University, Kalķu iela 1, LV-1658 Riga, Latvia

\* Correspondence: martin.sarap1@taltech.ee

**Abstract:** Additive manufacturing (AM) is a key technology for advancing many fields, including electrical machines. It offers unparalleled design freedom together with low material waste and fast prototyping, which is why it has become to focus of many researchers. For electrical machines, AM allows the production of designs with optimized mechanical, electromagnetic and thermal parameters. This paper attempts to give the reader an overview of the existing research and thermal solutions which have been realized with the use of AM. These include novel heat sink and heat exchanger designs, solutions for cooling the machine windings directly, and additively manufactured hollow windings. Some solutions such as heat pipes, which have been produced with AM but not used to cool electrical machines, are also discussed, as these are used in conventional designs and will certainly be used for additively manufactured electrical machines in the future.

**Keywords:** additive manufacturing; electrical machines; metal 3D-printing; electrical machine cooling



**Citation:** Sarap, M.; Kallaste, A.; Shams Ghahfarokhi, P.; Tiismus, H.; Vaimann, T. Utilization of Additive Manufacturing in the Thermal Design of Electrical Machines: A Review. *Machines* **2022**, *10*, 251. <https://doi.org/10.3390/machines10040251>

Academic Editor: César M. A. Vasques

Received: 1 March 2022

Accepted: 25 March 2022

Published: 31 March 2022

**Publisher's Note:** MDPI stays neutral with regard to jurisdictional claims in published maps and institutional affiliations.



**Copyright:** © 2022 by the authors. Licensee MDPI, Basel, Switzerland. This article is an open access article distributed under the terms and conditions of the Creative Commons Attribution (CC BY) license (<https://creativecommons.org/licenses/by/4.0/>).

## 1. Introduction

The basic design philosophy of electrical machines has remained relatively unchanged for many years, as it has been constrained by the available manufacturing methods. With the rising demand for electric vehicles and green energy, there is a significant push towards higher efficiencies, power densities, lighter weights, and customized solutions for electrical machines, meaning that innovation in the field is required. One technology that might meet those demands is additive manufacturing (AM).

AM, known in the consumer space as 3D printing, is a technology with the ability to manufacture practically any object for which a 3D model can be created, without the complexity and specific geometry of the part significantly impacting the manufacturing costs. This provides huge amounts of design freedom to engineers, who can fully leverage modern computational tools to create truly optimal designs without being constrained by the manufacturing method. Modern AM technologies can utilize many different types of materials, from flexible polymers to high-performance metals, and the local manufacturing nature of AM makes it less reliant on global supply chains. These advantages, in addition to the rapid prototyping and low material waste capabilities, have ensured rapid growth in the field of AM: per the 2021 Wohlers Report, the industry grew by 7.5%, reaching a value of \$12.8 billion in 2020 [1]. The largest shares of that are the medical, dental, and aerospace industries which are forecasted to help the AM market reach a value of \$51 billion by 2030 [2].

With increased power densities and more demanding requirements, the thermal design of machines becomes more important, as larger amounts of heat need to be extracted from smaller-sized machines. AM provides many novel solutions which can be used to enhance the thermal performance of an electrical machine. For air-cooled machines,



traditional radiator fins can be replaced with complex shapes. These can be integrated into the machine to provide structural support while being optimized for minimal weight. For water-cooled machines, the coolant paths can be more complex [3] and brought closer to the heat generation [4].

Therefore, the aim of this paper is to give the reader a summary of the current progress in the utilization of AM in the thermal design of electrical machines. The relevant AM methods, together with their capabilities and limitations, are described to provide an overview of the different technologies and materials used. The paper focuses on different solutions which have taken advantage of the manufacturing freedom offered by AM and can be used to improve the thermal capabilities of existing electrical machines or to manufacture new optimized machines.

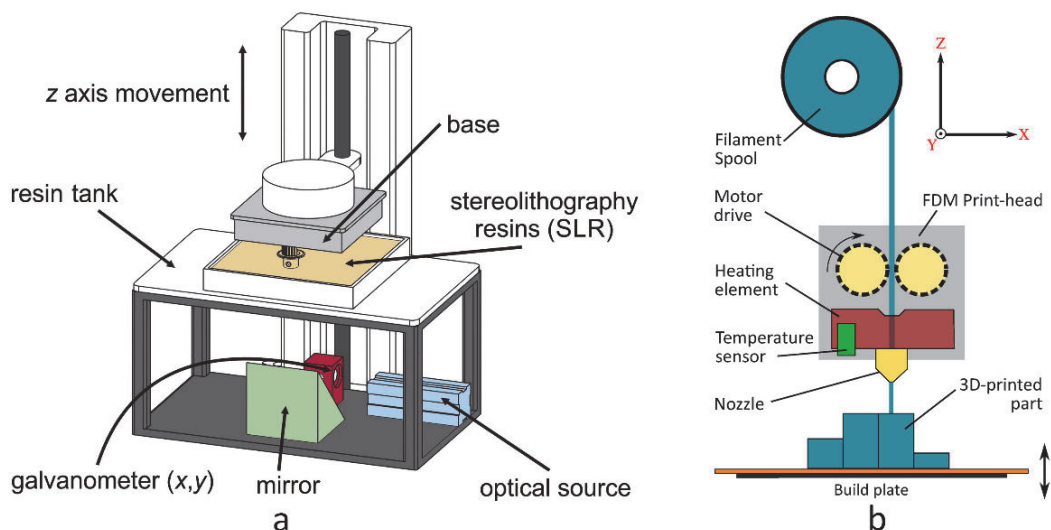
## 2. Additive Manufacturing

Current AM methods can be classified into seven main categories: vat photopolymerization, material extrusion, material jetting, binder jetting, powder bed fusion (PBF), direct energy deposition, and sheet lamination [5,6]. Each method creates the three-dimensional object in a different way and has its own advantages and disadvantages. The biggest differences are in the available materials as photopolymerization and extrusion processes utilize mostly plastic materials, whereas metal objects are most often manufactured with PBF methods.

AM started off in 1987 with the emergence of stereolithography (SLA) [7], which is a vat polymerization technology. This method consists of solidifying thin layers of light-sensitive liquid polymers with a UV light source (Figure 1a), which in the original case was a laser. The position of the laser beam can be accurately controlled using a mirror galvanometer system, resulting in extremely detailed parts. Modern consumer machines often use a UV LED array together with a high-resolution LCD photomask to reduce cost and complexity. This generally produces less detailed parts but has the benefit of being able to print the entire layer at the same time, which significantly improves the printing speed. While only the polymer can be directly hardened, other materials can be added into the liquid polymers as powders. After manufacturing, the hardened polymer can be burned away, leaving only the added material behind, although heavily shrunk compared to the original printed part. This allows SLA to be used for the manufacturing of ceramic and metal parts.

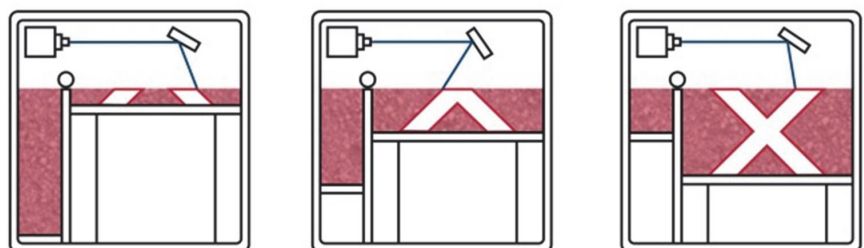
In 1991, fused deposition modeling (FDM) was commercialized with the launch of Stratasys's first FDM printer [8]. With this technology, individual layers are constructed by precisely extruding thermoplastic materials according to a CAD model (Figure 1b). The low costs associated with FDM machines and materials have made it by far the most popular consumer AM technology [9]. The material selection for FDM is wide, as many thermoplastics can be successfully printed, and similarly to SLA, other materials can be used as fillers. Furthermore, fully metal-based solutions based on material extrusion have recently become available [10].

The AM method with the widest material selection is binder jetting (BJ) [11], where an inkjet mechanism is used to selectively deposit a binder material into the powdered material to form layers. BJ can utilize many types of materials, such as ceramics, metals, and polymers. Full-colored prints are also possible due to the inkjet mechanism. The method allows for large build areas, as the binder solidifies at room temperature and does not introduce warping. Depending on the material, the printed parts need to be sintered or infiltrated with a low melting-temperature metal [12]. This produces a part with significant internal porosity, potentially making the method unsuitable for applications where demanding material properties are required.



**Figure 1.** Schematics of (a) SLA reprinted with permission from Ref. [13]. Copyright 2016 Elsevier and (b) FDM [14] processes.

The first powder bed fusion (PBF) method called selective laser sintering (SLS) became available in 1992 [7], although it was patented several years earlier [15]. SLS involves using a powerful laser to selectively fuse powder particles into layers. After each layer, the build platform is lowered, a new coat of powder is applied, and the process repeats until the part is ready. The process of a general laser powder bed fusion (L-PBF) is illustrated in Figure 2. The thickness of each coat of powder defines the layer thickness and determines the Z-axis accuracy of the part. The X- and Y-axis accuracy is determined by the laser assembly and material used. It can be used to manufacture parts from many different types of materials, even metals and ceramics, and can print without the use of support structures, as the part can be supported by the unsintered powder in the build chamber. The technology of selective laser melting (SLM), which was started in 1995 [16], is similar to SLS, as it is also a powder bed process. However, instead of sintering, the (metal) powder is completely melted, leading to a less porous and more homogeneous part with improved thermal, electrical, and magnetic properties. A natural evolution of SLM is the technology of electron beam melting (EBM), where an electron beam is used instead of a laser. This allows for higher energy densities and a wider selection of materials. When printing metals, a dimensional tolerance of  $\pm 0.1$  mm is often cited [17], and with SLM and EBM, densities over 99% can be achieved [18,19].



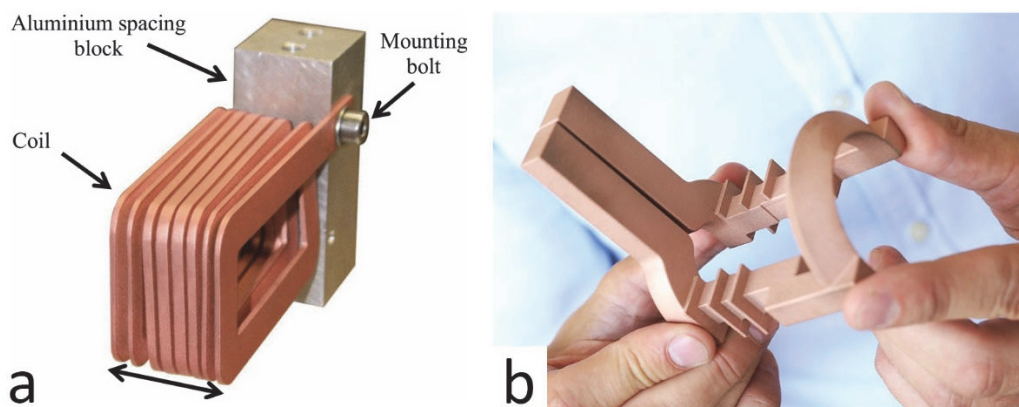
**Figure 2.** Schematic of a laser powder bed fusion process [20].

### 2.1. Materials Used in AM

AM allows many different materials to be used. In the context of thermal solutions for electrical machines, the relevant materials are either good electrical conductors, dielectrics, or have good magnetic properties. These materials are used for different purposes but for all of them, a high value of thermal conductivity is beneficial for increasing the total thermal performance of the machine.

The windings of an electrical machine need to be highly electrically conductive, meaning that copper is an ideal choice. AM allows the shape of the conductors to be optimized for both electrical and thermal purposes. However, a significant challenge in the additive manufacturing of machine windings is the relative difficulty of printing fully dense copper with a PBF based process, as copper reflects up to 98% of the energy applied by an infrared laser beam often used in SLM [21]. This problem can be mitigated by using a green laser [22] or an electron beam [23,24] to achieve virtually fully dense parts with physical properties equivalent to the solid material. Copper can also be printed with other AM methods, such as BJ, SLA, and FDM, but due to the internal porosity of the final part, the thermal conductivity of the resulting object is lower [25,26].

Even though printing copper is less common due to the technological requirements, some impressive results have been achieved. Simpson et al. [27] have used DMLS to create copper alloy windings that are shaped for minimal AC losses (Figure 3a). The experimental results show reduced AC losses, although the electrical conductivity of the sintered material is only 51% IACS. A higher conductivity value of 90% IACS [28] has been achieved by using SLM and a copper alloy (CuCr1Zr) to create an induction heater with integrated water cooling (Figure 3b). The copper alloy CuCr1Zr is noteworthy, as it can be successfully manufactured using SLM with an infrared laser, while still having high thermal (310–340 W/m/K) and electrical ( $\geq 43$  MS/m) conductivity [29,30]. The primary alternative to copper is usually aluminum, with the alloy AlSi10Mg receiving the most attention in AM [31].



**Figure 3.** Additively manufactured (a) copper alloy windings [27] and (b) an induction heater with integrated water cooling [28].

The printing of soft magnetic materials allows for the geometry of the core of an electrical machine to be optimized. This may include liquid cooling channels inside the iron core or cooling fins on the stator surface. The ability to integrate the cooling elements with the machine's core can be beneficial due to the elimination of any contact thermal resistance, even if the thermal conductivity of soft magnetic materials is relatively low. The materials used are typically ferrosilicon alloys, which can be successfully printed using PBF and other AM methods.

The dielectric material needed to insulate the conductive windings is often a large source of thermal resistance in an electrical machine, as the electrically isolating materials used in machines are also poor thermal conductors (values of around 1 W/m/K). This is not the case with some ceramics, which through the use of AM could be utilized in electrical machines as thermally conductive isolation material. Several different AM methods can utilize ceramic materials, including SLA, by suspending the ceramic powder inside a liquid photopolymer [32]. For example, Rauchenecker et al. [33] were able to create complex-shaped alumina nitride ceramic parts with thermal conductivity values over 160 W/m/K. The thermal conductivities of some popular materials manufactured with different AM methods are presented in Table 1.

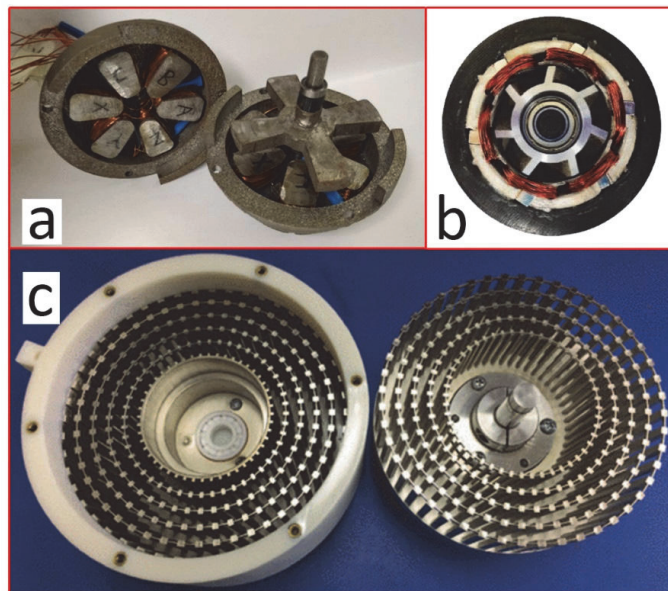
**Table 1.** Thermal conductivities of popular materials used in AM.

Material	Manufacturing Method	Effective Thermal Conductivity (W/m/K)
Pure copper	Electrolysis	394
	EBM	390 [34]
	SLM	317–336 [25]
	BJ	245–327 [25]
	Extruded paste	284 [35]
CuCr1Zr	Cast	310–340 [30]
	SLM	309 [36]
AlSi10Mg	Cast	113 [37]
	SLM	173 [38]
	SLS	100 [39]
Electrical steel	SLM	26 (Fe-3.7 w.t.% Si) [40]
Alumina nitride ceramic	Pure	285 [41]
	SLA	>160 [33]
	BJ	3–4 [42]
Alumina ceramic	SLA	35 [43]

## 2.2. Additively Manufactured Electrical Machines

In the realm of electrical machines, AM is still in the research stage. Individual components of an electrical machine have been successfully manufactured by several groups. Urbanek et al. [44] have designed and manufactured a PMSM rotor from a soft-magnetic ferro-silicon alloy using a laser PBF process. The rotor is designed to utilize the advantages provided by AM by incorporating several design optimizations, including a skewed active part and a hollow shaft. Tseng et al. [45] have used SLM to create a novel SRM rotor that incorporates skewing to reduce cogging torque and plastic ribs to reduce windage losses. Ibrahim et al. [46] have used cold spray AM to create a rotor with alternative PM and soft magnetic composite material layers. The use of AM allowed them to eliminate the bridges and center-posts normally present in PMSM rotors, which limit the motor capabilities.

Some groups have used AM to produce working electrical machines, although not all parts were printed. Tiismus et al. [47] have used SLM to create a working axial-flux switched reluctance motor (Figure 4a). It includes a stator and a rotor which were manufactured from silicon steel. Wu et al. [48] have designed and printed a fan motor that includes a rotor with an integrated impeller to achieve a robust motor with an improved power density (Figure 4b). Ge et al. [49] have used SLA and metal plating to create an electrostatic motor (Figure 4c).



**Figure 4.** Additively manufactured electrical machines: (a) axial flux motor [47], (b) integrated fan motor reprinted with permission from Ref. [48]. Copyright 2021 Elsevier, (c) electrostatic motor [49].

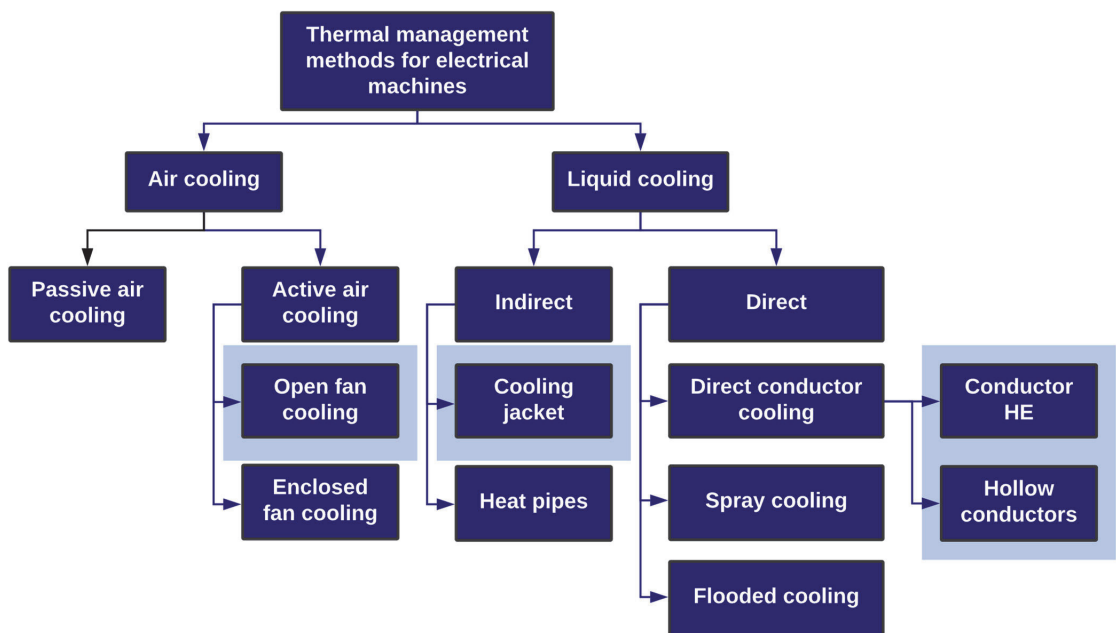
A completely additively manufactured electrical machine, where the windings, insulation, and soft magnetic materials are all printed concurrently, has not yet been achieved, as this would need advances in multi-material printing technologies. Powder bed fusion processes can generally only print a single material, although dual-metal systems do exist [50]. Nonetheless, research in the area is going strong, as additively manufactured electrical machines can have many advantages over traditionally manufactured counterparts [51].

### 3. Additively Manufactured Thermal Management Solutions for Electrical Machines

The thermal management of electrical machines is the main challenge with higher power densities due to the increased heat generated in the windings and core. Higher temperatures are detrimental to the machine's efficiency and reliability, meaning that increases in power density are accompanied by a demand for more powerful cooling. The thermal management methods for electrical machines can be categorized into two main groups—air and liquid cooling (Figure 5). For less power-dense machines, air cooling is often sufficient, and in the case of passive air cooling, the necessary airflow is generated only by natural convection. Liquid cooling is used for more demanding applications and can be further divided into direct and indirect liquid cooling, based on the proximity of the coolant fluid to the source of heat. The most common method of liquid cooling utilizes a cooling jacket, which is a casing with coolant channels that surrounds the machine. Direct liquid cooling methods increase performance by bringing the coolant closer to the source of heat.

Several additively manufactured solutions, which could be used to enhance the performance of most of these methods, have been researched, although only a few examples of AM being used to cool electrical machines specifically currently exist in the literature. This means that there are many opportunities for researchers to utilize existing AM solutions for the cooling of electrical machines. Furthermore, AM can provide novel cooling solutions, which are not practical to manufacture using traditional methods and therefore have previously not received substantial attention.





**Figure 5.** Various cooling methods for electrical machines. The light blue shading indicates that an additively manufactured solution for an electrical machine exists in the literature.

### 3.1. Air Cooling

The simplest way of cooling an electrical machine is through air cooling. The thermal performance of an air cooler depends on its surface area and the velocity of air interacting with that area, with increased surface areas and air speeds resulting in higher cooling capabilities. Air-cooled electrical machines usually incorporate fins on the body to increase the total surface area, which enhances the cooling by increasing the total convective heat transfer rate of the motor body. Using traditional manufacturing techniques (extrusion, skiving, die-casting, and machining) severely limits the shape and dimensions of the cooling fins, as complex shaped fins would be too costly or even impossible to produce. This is not a concern with additive manufacturing, as any shape can be produced, and the cost of a part does not depend on its complexity, meaning that thermally optimal designs can be manufactured.

The simplest air-cooled machines utilize passive cooling, which means that all of the airflow is generated through natural convection. This increases reliability due to a lack of moving parts but creates a complicated design challenge. Simply increasing the cooling surface area can restrict the airflow in the fin structure to the point of lowering total performance. The optimal solution where the surface area and the airflow created by natural convection are both maximized is highly non-trivial and requires advanced methods such as topology optimization (TO).

TO is a mathematical method that spatially optimizes the distribution of material within a defined domain by fulfilling given constraints previously established and minimizing a predefined cost function [52]. For electrical machines, topology optimization has mainly been used to optimize the electromagnetic and mechanical design [53], while thermal optimization has received little attention. The shapes generated by topology optimization with typical thermal constraints are often too complex to produce with traditional methods [54] and thus need additional constraints to produce practical results. However, in the case of AM, these constraints are not required, as practically any shape can be manufac-

tured (although some constraints may still be beneficial for increased printing success [55]). For this reason, topology optimization is widely used in AM [56–59].

Lazarov et al. [60] have used AM to create several different passive heatsinks and have compared different design ideas—TO, lattice structures, and pin fin. The heatsinks were all manufactured from an aluminum alloy, and the designs incorporate the same dimensional limitations. Out of the designs tested, the clear winner was the TO variant, which performed significantly better than any lattice structured design, even though it has a significantly smaller surface area. The difference in performance is explained by the increased airflow that the optimized design can generate through natural convection. The results of the tests are presented in Figure 6. It should be noted that the optimization was performed in a horizontal orientation. The researchers used the TO design to create a simplified and cheap to produce pin fin design, which also performed better than the lattice designs in the horizontal orientation. This research shows the benefits of TO and that simply increasing the surface area with a lattice structure is not necessarily optimal.




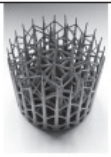
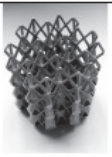

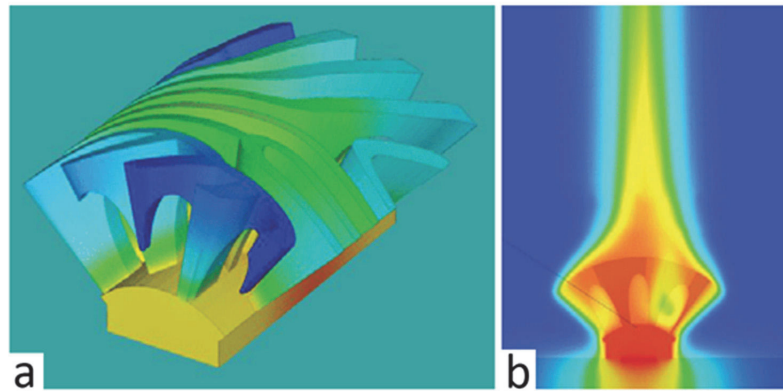
						
	TO	PF	AT	BT	CT	DT
Mass [g]	98	96	119	116	117	205
Volume V [ $\times 10^{-5} \text{m}^3$ ]	3.94	3.53	4.46	4.39	4.46	7.37
Surface A [ $\times 10^{-2} \text{m}^2$ ]	2.36	2.22	2.55	4.19	4.18	10.53
$f = A/V$ [ $\times 10^2 \text{m}^{-1}$ ]	6.00	6.30	5.72	9.55	9.30	14.30
Power	Horizontal orientation $\Delta t$ [ $^{\circ}\text{C}$ ]					
1.09W	5.30	6.45	6.71	6.93	7.38	5.62
2.96W	12.41	15.25	16.16	15.63	16.51	13.23
5.27W	19.59	24.12	25.66	25.02	26.10	21.50
	Vertical orientation $\Delta t$ [ $^{\circ}\text{C}$ ]					
1.09W	5.32	6.69	6.81	6.00	6.60	5.52
2.96W	12.71	16.54	16.32	14.19	14.80	12.33
5.27W	20.62	26.98	25.96	22.09	23.56	19.01

Figure 6. Topology optimized additively manufactured heat sink compared to conventional designs [60].

The advantages of AM for passive air cooling are further demonstrated by Wits et al. [61], who have taken a bio-inspired design approach to create heatsink designs, which are initially based on naturally occurring brain corals (Figure 7a). They have created structures and optimized the design parameters using computational fluid dynamics to manufacture several heatsinks from an aluminum alloy (AlSi10Mg) using SLM. The design succeeds in promoting natural convection (Figure 7b) while still having a high total surface area. Although the authors note that the simulations show decreased surface heat flux in the middle part of the heatsink fins, meaning that the design could be further optimized to increase the effect of natural convection inside the fin structure.

Air-cooled electrical machines with higher power densities require the use of fans as relying only on natural convection is insufficient. While maximizing surface area is still relevant, the goal of aiding natural convection is replaced with the challenge of reducing pressure drop over the fin structure as a higher pressure drop lowers the airflow acting on the fins. A common way of increasing the surface area of an AM heat sink is through the use of lattice structures, which are a form of cellular structure defined as a spacefilling unit cell that can be tessellated along any axis with no gaps between cells [62]. These structures have been traditionally used to reduce weight while retaining necessary mechanical properties.

With the advent of AM, it has become possible to create arbitrary structures from many different materials. Due to this, there has been significant research in the thermal and mechanical properties of additively manufactured lattice structures [63–66].



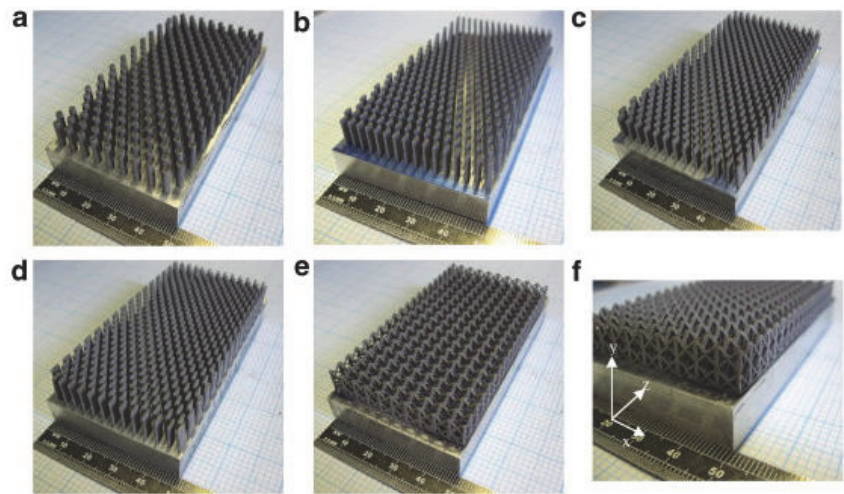
**Figure 7.** Simulated temperature (a) and airflow (b) of the passive heat sink with freeform geometry reprinted with permission from Ref. [61]. Copyright 2018 Elsevier.

For thermal solutions, lattice structures can be used to increase the working surface area of a heatsink while keeping the volume constant. Naively one might create an incredibly dense mesh (lattices with a unit cell size of under 1 mm and a strut diameter of 0.1 mm have been achieved with PBF [67]) and achieve a huge surface area, only to find that such a heatsink does not match expectations, as the increased air resistance created by the dense mesh more than cancels out the effects of the higher surface area. One example of this was observed here [68], as a heatsink with 31% more surface area performed worse than a traditional finned design. Although this does not mean that lattice structures should not be considered for heatsinks. Their ability to provide structural support while having a low weight could outweigh the subpar thermal performance. Furthermore, for electrical machine applications, lattice structures can be beneficial for reducing eddy current losses.

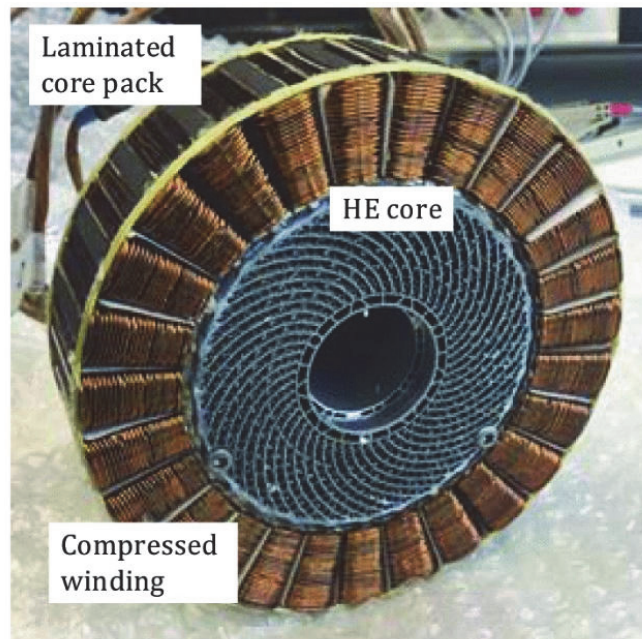
Wong et al. [69] have created several heatsinks from aluminum 6061 using SLM (Figure 8). These include two conventional designs—cylindrical pin (a), rectangular fin (b), and three novel designs—a rectangular fin array with rounded corners (c), a staggered elliptical array (d), and a lattice structure (e and f). The novel heatsink designs are only suitable for AM due to the fine detail and compact spacing of the pin fins, which would make conventional manufacturing prohibitively expensive. They investigated the thermal and fluid flow characteristics of the heatsinks and found that the elliptical pins outperformed their conventional counterparts in both heat extraction and pressure drop, as their shape creates a large surface area while keeping air resistance low. One of the worst performers was the lattice structure, which has a very large surface area but presented too large of a pressure drop to perform effectively. Even though the heatsinks investigated in this study were not fully optimized, they clearly demonstrated the performance enhancements that SLM can provide.

AM also allows designers to utilize fin geometries which can provide structural support while being optimized for lower weight. Wrobel et al. [70] have used AM to create an air-cooled aluminum alloy (AlSi10Mg) heat exchanger (HE) for a propulsion motor in a solar aircraft (Figure 9). The HE needs to cool the motor during take-off, when the losses are the highest, while being lightweight for cruising efficiency and providing structural support to the motor. It is integrated into the motor design, as this allows it to be directly connected to the stator teeth, such that the thermal resistance between the heat generating windings and the HE fins is minimized. The design takes full advantage of AM by utilizing curved fins to maximize the surface area while keeping the weight low.





**Figure 8.** Additively manufactured pin fin heat sinks with different geometries: cylindrical pin (a), rectangular fin (b), rectangular fins with rounded corners (c), staggered elliptical array (d) and a lattice structure (e,f) Reprinted with permission from Ref. [69]. Copyright 2009 Elsevier.

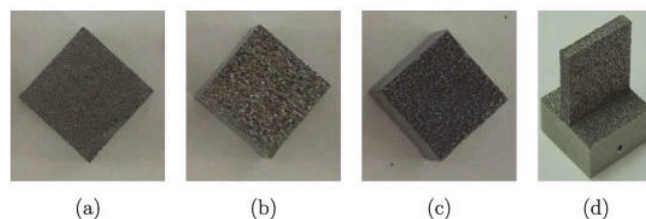


**Figure 9.** Additively manufactured aluminum alloy heat exchanger for a propulsion motor [70].

While traditional heat sink fins are relatively smooth and flat due to the manufacturing methods, a heat sink produced with AM can easily include patterns and shapes on the fin surfaces, which increases cooling performance. Rao et al. [71] have researched heatsink fins with dimpled surfaces, and they calculated that a surface with teardrop dimples shows 1.8 to 2 times better heat-transfer enhancement compared to a flat plate.

Although adding a surface pattern might not be necessary, as the additively manufactured metal has inherently rough surfaces that can be beneficial for cooling (Figure 10).

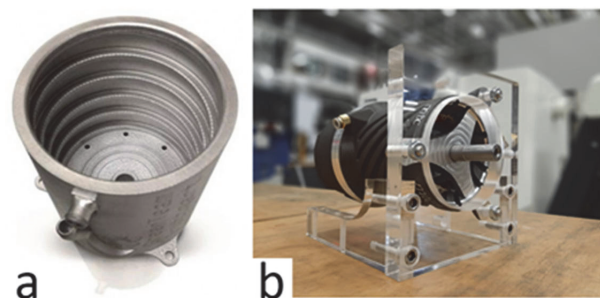
Ventola et al. [72] have measured parts manufactured by direct metal laser sintering and found an up to 73% increase in cooling performance over similar smooth parts. The authors explain that as these results are not explained by the increased surface area due to the roughness, the performance must be caused by turbulent flows created by the multi-scale roughness. They suggest a novel method of modelling this effect, which is in excellent agreement with their measured results. As tools to optimize surface roughness become available, designers of additively manufactured machines may start to use them to vary the printing parameters in certain parts of the machine to achieve optimal cooling performance. The effects of surface roughness were also studied by Kirsch et al. [73], who created several microchannel pin fin arrays using L-PBF. It was found that the surface roughness of pins can be beneficial by exacerbating pin wake interactions. The authors also noted that pin spacing could be increased without sacrificing thermal performance, meaning that the weight and material costs of heat exchangers could be decreased with the use of AM.



**Figure 10.** Aluminum alloy samples manufactured using DMLS with different average surface roughness: 16  $\mu\text{m}$  (a), 24  $\mu\text{m}$  (b), 43  $\mu\text{m}$  (c), 22  $\mu\text{m}$  (d) [72].

### 3.2. Liquid Cooling

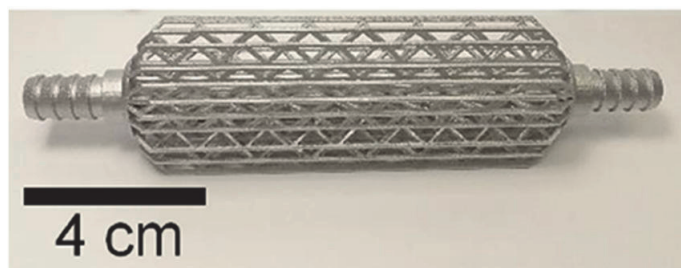
In the case where air cooling is insufficient, liquid cooling can be used to increase the thermal performance of an electrical machine. This is commonly achieved through a water jacket around the machine body, where the heat from the stator is extracted by the coolant. If the cooling jacket is separate from the stator, the contact resistance between the stator surface and the cooling channels significantly reduces thermal performance. The alternative solution is to integrate the cooling channels in the stator design, although this is difficult with conventional manufacturing methods. With an AM motor, optimized coolant paths can be freely integrated into the core, allowing for greatly improved thermal performance. AM can also improve the thermal capabilities of an existing motor by printing a separate cooling jacket with a geometry that is optimized for a specific design. Two examples of this is an aluminum cooling jacket [74] for an electric racing car which increased performance by 37% compared to the previous version (Figure 11a), and a liquid-cooled casing for an electric motor [75] which produced a 10% weight saving and a 30% reduction in size (Figure 11b).



**Figure 11.** Additively manufactured cooling jackets (a) [74] and (b) [75].

The thermal performance of a liquid-cooled electrical machine is heavily dependent on the rate of heat exchange from the machine body to the coolant. Similarly to air cooling, this depends on both the surface area and the pressure drop. Due to the complex nature of fluid dynamics, this optimization is highly non-trivial and often results in solutions that cannot be manufactured using traditional methods. This makes heat exchangers one of the more popular thermal devices to take advantage of the capabilities of metal AM. The ability to produce monolithic parts with high levels of geometric complexity, intricate internal structures, and thin walls lends itself perfectly to creating optimized heat exchangers [76,77].

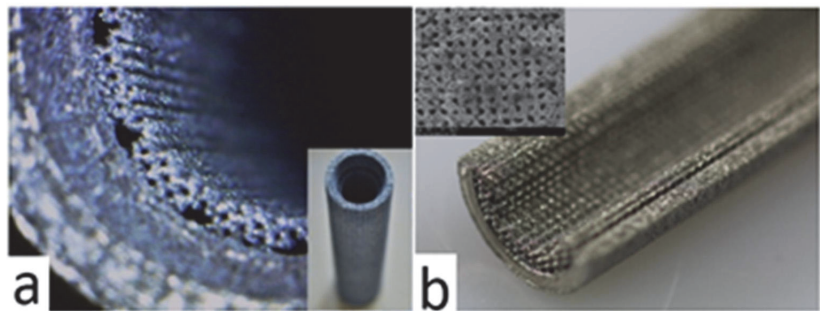
Moon et al. [78] have created an additively manufactured aluminum alloy (AlSi10Mg) HE (Figure 12). The design incorporates a complex fin structure that takes full advantage of AM, achieving a 4X improvement in power density compared to conventional designs. Bernardin et al. [79] have used Direct Metal Laser Sintering (DMLS) to create a stainless-steel twisted tube HE. Utilizing a twisted shape is a known technique for increasing the working surface area and thus the overall heat transfer coefficient of a HE without increasing its size, but the increased manufacturing cost compared to a straight tubed design has suppressed its popularity. For AM, the complexity of the part has little effect on the final cost, meaning that these kinds of optimized designs can be widely used.



**Figure 12.** Additively manufactured heat exchangers: a design with a complex fin structure reprinted with permission from Ref. [78]. Copyright 2020 Elsevier.

### 3.3. Phase Change Cooling

The thermal performance of an electrical machine can also be increased by utilizing heat pipes [80]. These are relatively simple devices that use phase transitions to achieve high values of thermal conductivity [81]. The design of a heat pipe relies on capillary pumping by the wicked interior surface of the device. As it is possible to produce such a surface with AM, there has been significant research in the utilization of different AM methods to produce heat pipes. SLM has been used to create heat pipes from Ti-6Al-4V [82], AISI 316 [83], AlSi12 [84] (Figure 13a,) and laser sintering has been used with stainless steel [85,86]. The heat pipes manufactured with LPBF processes generally perform well, and their effective thermal conductivity is significantly higher than the solid material. The ability to produce heat pipes via AM provides many possibilities for electrical machine cooling, as the designs could be fitted for specific needs, and the materials used can be optimized. For example, utilizing off-the-shelf copper heat pipes can lead to increased eddy current and AC losses [87], whereas heat pipes made from electrical steel and integrated directly into an AM machine could provide a significant increase in thermal capabilities without causing appreciable losses.



**Figure 13.** Additively manufactured heat pipes with an internal wick structure (a) Reprinted with permission from Ref. [84]. Copyright 2013 Elsevier and (b) Reprinted with permission from Ref. [88]. Copyright 2013 Elsevier.

### 3.4. Direct Conductor Cooling

In a typical machine, most of the heat is generated in the conductors due to Joule losses. The conductors are also the most susceptible to high temperatures due to insulation thermal degradation. While copper is highly thermally conductive, the conductivity of the entire winding body is quite low due to the insulation, air bubble and contact resistances present in windings [89]. Furthermore, in a conventionally cooled machine, the heat needs to travel through the core material, which typically has a low value of thermal conductivity. This creates a large thermal resistance between the windings and the surface of the motor, where the heat can be extracted, leading to high temperatures in the windings. The positive correlation of electrical conductivity with temperature is also notable as it reduces the efficiency of the machine when the conductor temperatures are higher. Due to this, the main challenge when cooling electrical machines is removing heat from the windings.

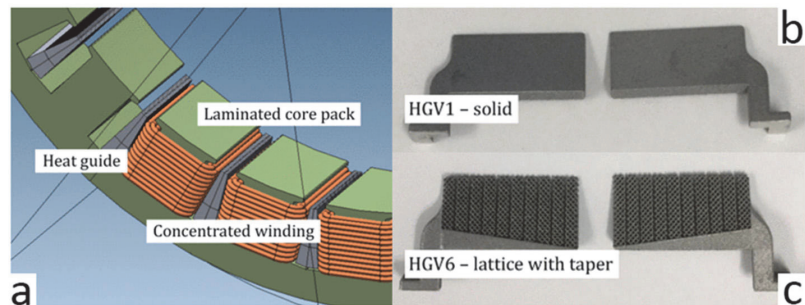
The thermal resistance between the conductors and the cooling medium can be reduced with the use of direct winding heat exchangers. Liquid-cooled heat exchangers that are in direct contact with the windings have been produced with conventional methods and have shown good results [90,91], although these are difficult to implement, and without AM optimized geometries are difficult to achieve.

An additively manufactured solution was proposed by Wrobel et al. [92], who used SLM to create thermally conductive heat guides from an aluminum alloy (AlSi10Mg), which are designed to be placed between the windings of a motor (Figure 14a). As the heat guides are placed near the windings inside the stator slots, they assist in the heat extraction from the active part of the winding, but also contribute to the machine losses due to eddy currents induced by flux leakage. Therefore, a solid heat guide provides negligible performance improvements, but AM enables the production of different lattice structures (Figure 14b,c) which emulate traditional laminations, and thus, it is possible to eliminate most of the extra losses while keeping a high thermal conductivity. Using a heat guide made with lattice structures, they achieved a 55% increased total thermal conductivity from the winding body of a test motorette without significant extra power losses.

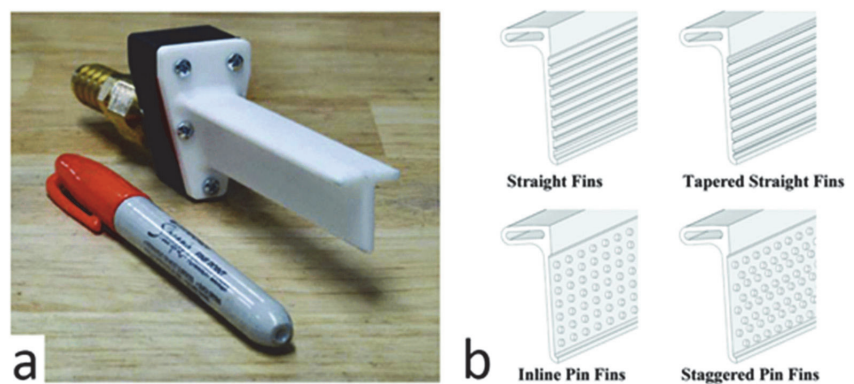
The thermal performance of direct winding heat exchangers can be further increased by utilizing liquid cooling. Sixel et al. [93] created plastic hollow heat exchangers with FDM that allowed for a current density of  $20.5 \text{ A/mm}^2$  in the windings. They later improved the design with a lithography-based method to manufacture heat exchangers from alumina ceramic [43] with a measured thermal conductivity of  $35 \text{ W/m/K}$  (Figure 15a). They achieved a continuous current density of  $30.7 \text{ A/mm}^2$  while keeping the maximum winding temperature below  $132 \text{ C}$ . Using alumina ceramic is noteworthy, as it is both thermally conductive and an electrical insulator, meaning it will not contribute to extra eddy current losses while still not restricting heat flow from the windings to the coolant. To increase the heat transfer from the HE to the liquid coolant, they introduced micro-features on the inside surface of the cooling channel. These increase the total surface area of the HE, albeit



at the cost of increased flow resistance and, therefore, higher pumping power. Of the four different solutions considered (Figure 15b), the straight fin design was chosen for its high performance and easy printability.



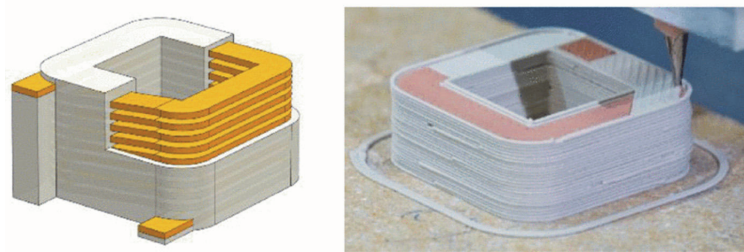
**Figure 14.** Additively manufactured heat guides places between the windings (a), a heat guide with a solid structure (b) and a heat guide utilizing a taper and a lattice structure to reduce eddy current losses (c) Reprinted with permission from Ref. [92]. Copyright 2020 Elsevier.



**Figure 15.** Additively manufactured ceramic heat exchanger for cooling the windings (a) and the different types of internal micro-features tested (b) Reprinted with permission from Ref. [43]. Copyright 2019 Elsevier.

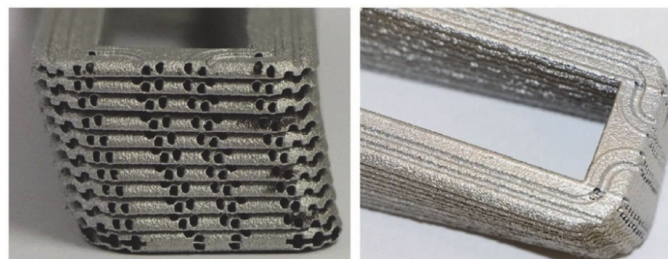
The additive manufacturing of coil windings directly is also possible. Lorenz et al. [35] have used a multi-material extrusion-based method to create high-performance windings for a switched reluctance machine (Figure 16). The process uses metal or ceramic powders mixed with binding agents to create extrudable pastes, which after heat treatment, achieve suitable physical properties. Although the specific electrical conductivity of this coil is lower at 71% (in part due to the 87% density of the printed material), it excels in thermal performance. One of the reasons for this is the higher thermal conductivity of the ceramic compared to conventional dielectric lacquer (3 vs. 1 W/m/K), which significantly reduces the total thermal resistance of the winding. Another advantage comes from the geometry of the conductor, as any part of the copper is separated from the iron core by just one layer of insulation.

Another possibility to further increase current density is to utilize hollow windings and pump coolant directly inside the conductors. Due to the large conductor dimensions and high costs, this is normally only used for large machines in the 100 MW to GW range [94]. Good results have been achieved with conventionally manufactured coolant conduits wrapped in litz wire [95], but AM looks to be the most promising method for achieving effective hollow conductors for smaller machines.



**Figure 16.** Additively manufactured windings with ceramic insulation for a switched reluctance motor. Reprinted with permission from Ref. [35]. Copyright 2018 Elsevier.

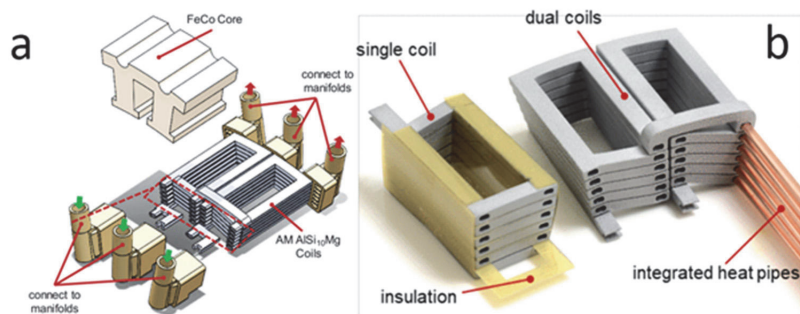
Wohlers et al. [94] have used laser-sintering to create aluminum alloy (AlSi10Mg) fractional-slot concentrated windings, which incorporate a hollow structure for direct liquid cooling of each conductor (Figure 17). In addition to the hollow structure, the rest of the coil geometry is also optimized for minimal losses and maximal cooling. By pumping coolant directly in the conductor, without any interface material (e.g., steel tubes inside the conductors [96]), the thermal resistance between the heat-generating conductors and the coolant is minimized. During testing, the windings were cooled at a constant coolant temperature of 30 °C and achieved a current density of 70 A/mm<sup>2</sup> with a maximum coil temperature of 180 °C. It should be noted that these results are obtained from an aluminum alloy coil and with an identically shaped copper coil, the authors calculate maximum current densities of about 130 A/mm<sup>2</sup>.



**Figure 17.** Additively manufactured aluminum alloy windings with a hollow structure for direct conductor water cooling. Reprinted with permission from Ref. [94]. Copyright 2018 Elsevier.

Wu et al. [4] have modelled a similar design (Figure 18a). It uses additively manufactured aluminum alloy (AlSi10Mg) windings and, due to the direct liquid cooling, can achieve a continuous current density of 20 A<sub>RMS</sub>/mm<sup>2</sup>. Continuing their work with hollow conductors, Wu et al. [97] have used DMLS to integrate copper heat pipes in the hollow aluminum alloy windings (Figure 18b). The shape of the windings was also optimized to maximize the filling factor. Adding copper heat pipes inside the conductors creates additional AC losses, but as most of these losses are concentrated in the first winding layers near the slot opening, the authors of the paper proposed a mixed solution, where some conductors don't have heat pipes. Furthermore, in the future, heat pipes may be printed directly in the structure of the windings, which would eliminate the additional AC losses created due to the copper walls of the heat pipe.

Based on the available research work, direct conductor cooling seems to be the most popular method to utilize AM in the thermal management of electrical machines. Since AM provides virtually complete design freedom, it is logical to apply it to solve thermal problems in the most efficient way possible. Additionally, the small features and complex structures required for optimized conductors make it a perfect challenge for AM. Details about the different AM solutions for direct conductor cooling are presented in Table 2.



**Figure 18.** AM (a) hollow windings [4] and (b) with integrated copper heat pipes reprinted with permission from Ref. [97]. Copyright 2021 Elsevier.

**Table 2.** Comparison of different AM direct conductor cooling solutions.

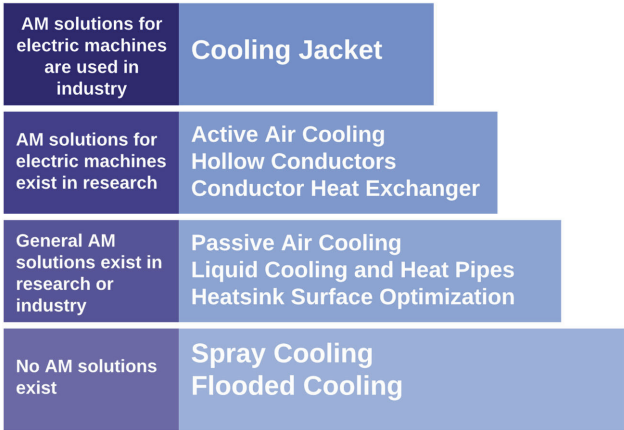
AM Direct Winding Cooling Solutions	Method Used	Material Used	Results
Metal Heat Guides [92]	SLM	AlSi10Mg	40% increased input power at lower and 20% at higher excitation frequencies. 55–85% increase of the winding-to-stator thermal conductance. 5% additional power loss at 1 kHz.
Plastic hollow heat exchangers [93]	FDM	Polycarbonate with aluminum flakes	Current density of 20.5 A/mm <sup>2</sup> with non-encapsulated windings while keeping the hotspot temperature below 150 °C
Ceramic hollow heat exchangers [43]	Lithography	Alumina ceramic	Current density of 30.7 A/mm <sup>2</sup> with encapsulated windings while maintaining the hotspot temperature below 132 °C
Additively manufactured SRM windings with ceramic isolation [35]	Paste extrusion	Copper and ceramic powder suspended in paste	Significantly lower temperatures in the conductors due to superior thermal coupling between the winding and stator. Higher temperature tolerance due to the insulation material.
Liquid cooled tooth coil windings [94]	SLS	AlSi10Mg	Current density of 70 A/mm <sup>2</sup> at 180 °C using aluminum coils and a constant 30 °C coolant
Hollow conductor [4]	DMLS	AlSi10Mg	Current density of 20 A/mm <sup>2</sup> at 1.25 kHz using aluminum coils.
Hollow conductor with integrated heat pipe [97]	DMLS	AlSi10Mg	Current density of 13.9 A/mm <sup>2</sup> at 1.25 kHz and 94.34% total motor efficiency using aluminum coils. 7% higher AC losses in the windings due to the electrically conductive heat pipes.

4. Conclusions

Additive manufacturing is successfully pushing the boundaries of design. It allows the production of shapes and structures which have normally been considered impractical or impossible to create. In the field of electrical machines, AM allows the production of complex optimized geometries, which can offer improved electromagnetic and thermal performance. Furthermore, the cost of a part created with AM is not dependent on its complexity, meaning that designers can utilize optimized shapes without needing to worry about manufacturing costs. Finally, the material selection for AM is incredibly wide, with traditional thermally conductive materials such as copper and aluminum being available and less known ceramic materials being used for novel solutions.

Many different solutions for enhancing thermal capabilities with AM have been researched. One of the most common ideas is to use complex lattice structures to create

mechanically strong but light structures with very high surface area to increase cooling performance. Another popular solution is to utilize topology optimization to create a highly effective heatsink by balancing surface area with airflow. With multi-objective topology optimization, it is also possible to include mechanical strength and weight in the optimization problem to create a purpose-fit design for specific requirements. Further performance increases can be achieved with heat pipes, which possess extremely high thermal conductivity, and with AM could be seamlessly integrated into existing designs. The list of existing additively manufactured thermal solutions is long, although only a few have been used to cool electrical machines specifically, with most of the research currently focused on demonstrating the usefulness of AM by creating general cooling solutions. This is illustrated in Figure 19 with the maturity levels of different AM thermal management technologies in the context of electrical machines. The two exceptions are AM cooling jackets, which have seen use in industry, but no research on the subject exists, and direct conductor cooling, which has received significant interest and is being actively developed for the purpose of cooling electrical machines specifically.



**Figure 19.** The maturity level of different AM thermal management solutions in the context of cooling electrical machines.

In our opinion, the necessary requirement for additively manufactured electrical machines to be competitive is advanced intra-layer multi-material printing. Currently, the state-of-the-art is dual-metal PBF, which is virtually unexplored in the research field and an obvious direction for future work. An example of utilizing a dual-metal system for enhancing the cooling of electrical machines would be a thermally-conductive frame printed directly on the soft magnetic core, which would eliminate the high thermal resistance usually present in machines with aluminum frames. More advanced multi-material printing would allow the manufacturing of a fully functional machine as a single object. This would need the ability to simultaneously print at least three different materials: a soft magnetic material for the core, a highly conductive material for the windings, and an isolating material to separate the two electrically. When taking into account the current growth of AM technology, it seems likely that this technology will be available in the near future. Moreover, considering the myriad of improvements that a fully AM electrical machine could offer, it could even become the norm for high-performance applications.

In conclusion, the market of additive manufacturing is growing with the amount of industrial applications increasing each year. For electrical machines, AM promises higher power densities through optimized shapes, fast prototyping, and simplified supply chains. Currently, AM is used to produce single components with specific optimizations, but in our opinion, it is only a matter of time when fully additively manufactured electrical machines are commercially viable.



**Author Contributions:** Conceptualization, M.S., A.K. and P.S.G.; methodology, M.S. and P.S.G.; validation, M.S., A.K. and P.S.G.; writing—original draft preparation, M.S.; writing—review and editing, P.S.G., A.K., H.T. and T.V.; supervision, A.K. and P.S.G. All authors have read and agreed to the published version of the manuscript.

**Funding:** This research received no external funding.

**Institutional Review Board Statement:** Not applicable.

**Informed Consent Statement:** Not applicable.

**Data Availability Statement:** Not applicable.

**Conflicts of Interest:** The authors declare no conflict of interest.

## References

1. Wohlers Associates. 3D Printing and Additive Manufacturing State of the Industry. 2021. Available online: <https://www.fastenernewsdesk.com/28315/wohlers-report-2021-3d-printing-and-additive-manufacturing-global-state-of-the-industry/> (accessed on 25 March 2022).
2. Lux Research. Will 3D Printing Replace Conventional Manufacturing? 2021. Available online: <https://parametric-architecture.com/will-3d-printing-technology-replace-traditional-manufacturing/> (accessed on 25 March 2022).
3. Ph.D. Student Wins Additive World Design Challenge Award—Campus News. Available online: <https://exchange.nottingham.ac.uk/blog/phd-student-wins-additive-world-design-challenge-award/> (accessed on 21 March 2022).
4. Wu, F.; El-Refaie, A.M. Additively Manufactured Hollow Conductors with Integrated Cooling for High Specific Power Electrical Machines. In Proceedings of the 2020 International Conference on Electrical Machines, ICEM 2020, Gothenburg, Sweden, 23–26 August 2020; pp. 1497–1503. [CrossRef]
5. 3 Additive Manufacturing Technologies to Watch out for in 2017, by 3D Hubs, Xtreme Engineering, Medium. Available online: <https://medium.com/extreme-engineering/3-additive-manufacturing-technologies-to-watch-out-for-in-2017-7226d310ca56> (accessed on 16 November 2021).
6. Calignano, F.; Manfredi, D.; Ambrosio, E.P.; Biamino, S.; Lombardi, M.; Atzeni, E.; Salmi, A.; Minetola, P.; Iuliano, L.; Fino, P. Overview on Additive Manufacturing Technologies. *Proc. IEEE* **2017**, *105*, 593–612. [CrossRef]
7. Wohlers, T.; Gornet, T. History of Additive Manufacturing. *Wohlers Rep.* **2014**, *24*, 118.
8. Twotrees. What Is an FDM 3D Printer? How Do FDM 3D Printers Work? Available online: <https://twotrees3d.com/fdm-3d-printer-how-do-fdm-3d-printers-work/> (accessed on 31 January 2022).
9. All3DP. The Types of 3D Printing Technology of 2021. Available online: <https://all3dp.com/1/types-of-3d-printers-3d-printing-technology/> (accessed on 31 January 2022).
10. 3DPrint.Com. Xerox Unveils ElemX Metal 3D Printer, Collaborates with US Navy. The Voice of 3D Printing/ Additive Manufacturing. Available online: <https://3dprint.com/278710/xerox-unveils-elemx-metal-3d-printer-with-us-navy-as-first-customer/> (accessed on 31 January 2022).
11. Mostafaei, A.; Elliott, A.M.; Barnes, J.E.; Li, F.; Tan, W.; Cramer, C.L.; Nandwana, P.; Chmielus, M. Binder Jet 3D Printing—Process Parameters, Materials, Properties, Modeling, and Challenges. *Prog. Mater. Sci.* **2021**, *119*, 100707. [CrossRef]
12. Introduction to Binder Jetting 3D Printing, Hubs. Available online: <https://www.hubs.com/knowledge-base/introduction-binder-jetting-3d-printing/#what> (accessed on 13 February 2022).
13. Weng, Z.; Zhou, Y.; Lin, W.; Senthil, T.; Wu, L. Structure-Property Relationship of Nano Enhanced Stereolithography Resin for Desktop SLA 3D Printer. *Compos. Part A Appl. Sci. Manuf.* **2016**, *88*, 234–242. [CrossRef]
14. Khatri, B.; Lappe, K.; Habedank, M.; Mueller, T.; Megnin, C.; Hanemann, T. Fused Deposition Modeling of ABS-Barium Titanate Composites: A Simple Route towards Tailored Dielectric Devices. *Polymers* **2018**, *10*, 666. [CrossRef] [PubMed]
15. Deckard, C. Method and Apparatus for Producing Parts by Selective Sintering. U.S. Patent 4,863,538A, 17 October 1986.
16. Meiners, W.; Wissenbach, K.; Gasser, A. Shaped Body Especially Prototype or Replacement Part Production. Ger. Patent DE19649865C1, 2 December 1996.
17. Dimensional Accuracy of 3D Printed Parts, Hubs. Available online: <https://www.hubs.com/knowledge-base/dimensional-accuracy-3d-printed-parts/#metal> (accessed on 16 November 2021).
18. Gong, G.; Ye, J.; Chi, Y.; Zhao, Z.; Wang, Z.; Xia, G.; Du, X.; Tian, H.; Yu, H.; Chen, C. Research Status of Laser Additive Manufacturing for Metal: A Review. *J. Mater. Res. Technol.* **2021**, *15*, 855–884. [CrossRef]
19. Zhang, M.; Zhou, X.; Wang, D.; He, L.; Ye, X.; Zhang, W. Additive Manufacturing of In-Situ Strengthened Dual-Phase AlCoCuFeNi High-Entropy Alloy by Selective Electron Beam Melting. *J. Alloys Compd.* **2022**, *893*, 162259. [CrossRef]
20. McDonough, J.R. A Perspective on the Current and Future Roles of Additive Manufacturing in Process Engineering, with an Emphasis on Heat Transfer. *Therm. Sci. Eng. Prog.* **2020**, *19*, 100594. [CrossRef]
21. Guschlbauer, R.; Burkhardt, A.K.; Fu, Z.; Körner, C. Effect of the Oxygen Content of Pure Copper Powder on Selective Electron Beam Melting. *Mater. Sci. Eng. A* **2020**, *779*, 139106. [CrossRef]

22. Siva Prasad, H.; Brueckner, F.; Volpp, J.; Kaplan, A.F.H. Laser Metal Deposition of Copper on Diverse Metals Using Green Laser Sources. *Int. J. Adv. Manuf. Technol.* **2020**, *107*, 1559–1568. [CrossRef]
23. Ramirez, D.A.; Murr, L.E.; Martinez, E.; Hernandez, D.H.; Martinez, J.L.; MacHado, B.I.; Medina, F.; Frigola, P.; Wicker, R.B. Novel Precipitate–Microstructural Architecture Developed in the Fabrication of Solid Copper Components by Additive Manufacturing Using Electron Beam Melting. *Acta Mater.* **2011**, *59*, 4088–4099. [CrossRef]
24. Guschlbauer, R.; Momeni, S.; Osmanlic, F.; Körner, C. Process Development of 99.95% Pure Copper Processed via Selective Electron Beam Melting and Its Mechanical and Physical Properties. *Mater. Charact.* **2018**, *143*, 163–170. [CrossRef]
25. Jiang, Q.; Zhang, P.; Yu, Z.; Shi, H.; Wu, D.; Yan, H.; Ye, X.; Lu, Q.; Tian, Y. A Review on Additive Manufacturing of Pure Copper. *Coatings* **2021**, *11*, 740. [CrossRef]
26. Ebrahimi, N.D.; Ju, Y.S. Thermal Conductivity of Sintered Copper Samples Prepared Using 3D Printing-Compatible Polymer Composite Filaments. *Addit. Manuf.* **2018**, *24*, 479–485. [CrossRef]
27. Simpson, N.; Mellor, P.H. Additive Manufacturing of Shaped Profile Windings for Minimal AC Loss in Gapped Inductors. In Proceedings of the 2017 IEEE International Electric Machines and Drives Conference, IEMDC 2017, Miami, FL, USA, 21–24 May 2017. [CrossRef]
28. How 3D Printing Is Redefining Inductor Coil Production, GKN Additive. Available online: <https://www.gknpm.com/en/our-businesses/gkn-additive/how-3d-printing-is-redefining-inductor-coil-production/> (accessed on 24 January 2022).
29. Wegener, T.; Koopmann, J.; Richter, J.; Krooß, P.; Niendorf, T. CuCrZr Processed by Laser Powder Bed Fusion—Processability and Influence of Heat Treatment on Electrical Conductivity, Microstructure and Mechanical Properties. *Fatigue Fract. Eng. Mater. Struct.* **2021**, *44*, 2570–2590. [CrossRef]
30. METALCOR. CuCr1Zr, C18150, Datasheet. Available online: <http://www.metalcor.de/en/datenblatt/133/> (accessed on 24 January 2022).
31. Aboulkhair, N.T.; Simonelli, M.; Parry, L.; Ashcroft, I.; Tuck, C.; Hague, R. 3D Printing of Aluminium Alloys: Additive Manufacturing of Aluminium Alloys Using Selective Laser Melting. *Prog. Mater. Sci.* **2019**, *106*, 100578. [CrossRef]
32. Chen, Z.; Li, Z.; Li, J.; Liu, C.; Lao, C.; Fu, Y.; Liu, C.; Li, Y.; Wang, P.; He, Y. 3D Printing of Ceramics: A Review. *J. Eur. Ceram. Soc.* **2019**, *39*, 661–687. [CrossRef]
33. Rauchenecker, J.; Rabitsch, J.; Schwentenwein, M.; Konegger, T. Additive Manufacturing of Aluminum Nitride Ceramics with High Thermal Conductivity via Digital Light Processing. *Open Ceram.* **2022**, *9*, 100215. [CrossRef]
34. Frigola, P.; Harrysson, O.A.; Horn, T.J.; West, H.A.; Aman, R.L.; Rigsbee, J.M.; Ramirez, D.A.; Murr, L.E.; Medina, F.; Wicker, R.B.; et al. Fabricating Copper Components with Electron Beam Melting. *Adv. Mater. Processes* **2014**, *172*, 20–24.
35. Lorenz, F.; Rudolph, J.; Wemer, R. Design of 3D Printed High Performance Windings for Switched Reluctance Machines. In Proceedings of the 2018 23rd International Conference on Electrical Machines, ICEM 2018, Alexandroupoli, Greece, 3–6 September 2018; pp. 2451–2457. [CrossRef]
36. Buchmayr, B.; Panzl, G.; Walzl, A.; Wallis, C. Laser Powder Bed Fusion—Materials Issues and Optimized Processing Parameters for Tool Steels, AlSiMg- and CuCrZr-Alloys. *Adv. Eng. Mater.* **2017**, *19*, 1600667. [CrossRef]
37. Aluminum 360.0-F Die Casting Alloy. Available online: <http://www.matweb.com/search/DataSheet.aspx?MatGUID=46cc3a20683748718693cbb6039bec68> (accessed on 31 January 2022).
38. Sélo, R.R.J.; Catchpole-Smith, S.; Maskery, I.; Ashcroft, I.; Tuck, C. On the Thermal Conductivity of AlSi10Mg and Lattice Structures Made by Laser Powder Bed Fusion. *Addit. Manuf.* **2020**, *34*, 101214. [CrossRef]
39. Krishnan, M.; Atzeni, E.; Canali, R.; Calignano, F.; Manfredi, D.; Ambrosio, E.P.; Iuliano, L. On the Effect of Process Parameters on Properties of AlSi10Mg Parts Produced by DMLS. *Rapid Prototyp. J.* **2014**, *20*, 449–458. [CrossRef]
40. Sarap, M.; Kallaste, A.; Ghahfarokhi, P.S.; Tiismus, H.; Vaimann, T. Determining the Thermal Conductivity of Additively Manufactured Metal Specimens. In Proceedings of the 2022 29th International Workshop on Electric Drives: Advances in Power Electronics for Electric Drives (IWED), Moscow, Russia, 26–29 January 2022.
41. Franco Júnior, A.; Shanafield, D.J. Thermal Conductivity of Polycrystalline Aluminum Nitride (AlN) Ceramics. *Cerâmica* **2004**, *50*, 247–253. [CrossRef]
42. Díaz-Moreno, C.A.; Lin, Y.; Hurtado-Macías, A.; Espalin, D.; Terrazas, C.A.; Murr, L.E.; Wicker, R.B. Binder Jetting Additive Manufacturing of Aluminum Nitride Components. *Ceram. Int.* **2019**, *45*, 13620–13627. [CrossRef]
43. Sixel, W.; Liu, M.; Nellis, G.; Sarlioglu, B. Ceramic 3D Printed Direct Winding Heat Exchangers for Improving Electric Machine Thermal Management. In Proceedings of the 2019 IEEE Energy Conversion Congress and Exposition, ECCE 2019, Baltimore, MD, USA, 29 September–3 October 2019; pp. 769–776. [CrossRef]
44. Urbanek, S.; Frey, P.; Magerkohl, S.; Zimmer, D.; Tasche, L.; Schaper, M.; Ponick, B. Design and Experimental Investigation of an Additively Manufactured PMSM Rotor. In Proceedings of the 2021 IEEE International Electric Machines and Drives Conference, IEMDC 2021, Hartford, CT, USA, 17–20 May 2021. [CrossRef]
45. Application of Additive Manufacturing for Low Torque Ripple of 6/4 Switched Reluctance Motor, IEEE Conference Publication, IEEE Xplore. Available online: <https://ieeexplore.ieee.org/document/7837094> (accessed on 16 November 2021).
46. Ibrahim, M.; Bernier, F.; Lamarre, J.M. Novel Multi-Layer Design and Additive Manufacturing Fabrication of a High Power Density and Efficiency Interior PM Motor. In Proceedings of the ECCE 2020—IEEE Energy Conversion Congress and Exposition, Detroit, MI, USA, 11–15 October 2020; pp. 3601–3606. [CrossRef]

47. Tiismus, H.; Kallaste, A.; Vaimann, T.; Rassolkin, A.; Belahcen, A. Additive Manufacturing of Prototype Axial Flux Switched Reluctance Electrical Machine. In Proceedings of the 2021 28th International Workshop on Electric Drives: Improving Reliability of Electric Drives, IWED 2021, Moscow, Russia, 27–29 January 2021. [\[CrossRef\]](#)
48. Wu, S.T.; Huang, P.W.; Chang, T.W.; Jiang, I.H.; Tsai, M.C. Application of Magnetic Metal 3-D Printing on the Integration of Axial-Flow Impeller Fan Motor Design. *IEEE Trans. Magn.* **2021**, *57*, 8201205. [\[CrossRef\]](#)
49. Ge, B.; Ludois, D.C.; Ghule, A.N. A 3D Printed Fluid Filled Variable Elastance Electrostatic Machine Optimized with Conformal Mapping. In Proceedings of the ECCE 2016—IEEE Energy Conversion Congress and Exposition, Milwaukee, WI, USA, 18–22 September 2016. [\[CrossRef\]](#)
50. Aconity MIDI+, Aconity3D. Available online: <https://aconity3d.com/products/acinity-midi-plus/> (accessed on 16 November 2021).
51. Abdalmagid, M.; Sayed, E.; Bakr, M.; Emadi, A. Additive Design Possibilities of Electrical Machines. In Proceedings of the 2018 IEEE 59th Annual International Scientific Conference on Power and Electrical Engineering of Riga Technical University, RTUCON 2018, Riga, Latvia, 12–13 November 2018. [\[CrossRef\]](#)
52. Topology Optimization—An Overview, ScienceDirect Topics. Available online: <https://www.sciencedirect.com/topics/computer-science/topology-optimization> (accessed on 17 November 2021).
53. Abdalmagid, M.; Sayed, E.; Bakr, M.; Emadi, A. Geometry and Topology Optimization of Switched Reluctance Machines: A Review. *IEEE Access* **2022**, *10*, 5141–5170. [\[CrossRef\]](#)
54. Zhu, J.; Zhou, H.; Wang, C.; Zhou, L.; Yuan, S.; Zhang, W. A Review of Topology Optimization for Additive Manufacturing: Status and Challenges. *Chin. J. Aeronaut.* **2021**, *34*, 91–110. [\[CrossRef\]](#)
55. Misiun, G.; van de Ven, E.; Langelaar, M.; Geijselaers, H.; van Keulen, F.; van den Boogaard, T.; Ayas, C. Topology Optimization for Additive Manufacturing with Distortion Constraints. *Comput. Methods Appl. Mech. Eng.* **2021**, *386*, 114095. [\[CrossRef\]](#)
56. Topology Optimization for 3D Printing—3Dnatives. Available online: <https://www.3dnatives.com/en/topology-optimisation140820184/> (accessed on 17 November 2021).
57. Langelaar, M. Topology Optimization of 3D Self-Supporting Structures for Additive Manufacturing. *Addit. Manuf.* **2016**, *12*, 60–70. [\[CrossRef\]](#)
58. Walton, D.; Moztarzadeh, H. Design and Development of an Additive Manufactured Component by Topology Optimisation. *Procedia CIRP* **2017**, *60*, 205–210. [\[CrossRef\]](#)
59. Gaynor, A.T.; Meisel, N.A.; Williams, C.B.; Guest, J.K. Multiple-Material Topology Optimization of Compliant Mechanisms Created Via PolyJet Three-Dimensional Printing. *J. Manuf. Sci. Eng.* **2014**, *136*, 061015. [\[CrossRef\]](#)
60. Lazarov, B.S.; Sigmund, O.; Meyer, K.E.; Alexandersen, J. Experimental Validation of Additively Manufactured Optimized Shapes for Passive Cooling. *Appl. Energy* **2018**, *226*, 330–339. [\[CrossRef\]](#)
61. Wits, W.W.; Jafari, D.; Jeggels, Y.; van de Velde, S.; Jeggels, D.; Engelberts, N. Freeform-Optimized Shapes for Natural-Convection Cooling. In Proceedings of the Thermo 2018—24th International Workshop on Thermal Investigations of ICs and Systems, Stockholm, Sweden, 26–28 September 2018. [\[CrossRef\]](#)
62. Helou, M.; Kara, S. Design, Analysis and Manufacturing of Lattice Structures: An Overview. *Int. J. Comput. Integr. Manuf.* **2017**, *31*, 243–261. [\[CrossRef\]](#)
63. Kovalevsky, A.; Mats, A.; Shmurak, M.; Fleisher, A. Experimental Study of Aluminum Foams Thermal Conductivity. Prospects of Additive Manufacturing for Novel Heat Exchangers Production. In Proceedings of the 2020 IEEE 10th International Conference on Nanomaterials: Applications and Properties, NAP 2020, Sumy, Ukraine, 9–13 November 2020. [\[CrossRef\]](#)
64. Wang, N.; Kaur, I.; Singh, P.; Li, L. Prediction of Effective Thermal Conductivity of Porous Lattice Structures and Validation with Additively Manufactured Metal Foams. *Appl. Therm. Eng.* **2021**, *187*, 116558. [\[CrossRef\]](#)
65. Takezawa, A.; Zhang, X.; Kitamura, M. Optimization of an Additively Manufactured Functionally Graded Lattice Structure with Liquid Cooling Considering Structural Performances. *Int. J. Heat Mass Transf.* **2019**, *143*, 118564. [\[CrossRef\]](#)
66. Yang, L.; Mertens, R.; Ferrucci, M.; Yan, C.; Shi, Y.; Yang, S. Continuous Graded Gyroid Cellular Structures Fabricated by Selective Laser Melting: Design, Manufacturing and Mechanical Properties. *Mater. Des.* **2019**, *162*, 394–404. [\[CrossRef\]](#)
67. Kaur, I.; Singh, P. Critical Evaluation of Additively Manufactured Metal Lattices for Viability in Advanced Heat Exchangers. *Int. J. Heat Mass Transf.* **2021**, *168*, 120858. [\[CrossRef\]](#)
68. Smith, R. *Thermal Testing of a 3D Printed Super Dense Mesh Heatsink against State-of-The-Art Finned Geometry*; Qualified Rapid Products: West Jordan, UT, USA, 2015.
69. Wong, M.; Owen, I.; Sutcliffe, C.J.; Puri, A. Convective Heat Transfer and Pressure Losses across Novel Heat Sinks Fabricated by Selective Laser Melting. *Int. J. Heat Mass Transf.* **2009**, *52*, 281–288. [\[CrossRef\]](#)
70. Wrobel, R.; Scholes, B.; Mustaffer, A.; Ullah, S.; Reay, D.; Mecrow, B.; Hussein, A. Design and Experimental Characterisation of an Additively Manufactured Heat Exchanger for the Electric Propulsion Unit of a High-Altitude Solar Aircraft. In Proceedings of the 2019 IEEE Energy Conversion Congress and Exposition, ECCE 2019, Baltimore, MD, USA, 29 September–3 October 2019; pp. 753–760. [\[CrossRef\]](#)
71. Rao, Y.; Li, B.; Feng, Y. Heat Transfer of Turbulent Flow over Surfaces with Spherical Dimples and Teardrop Dimples. *Exp. Therm. Fluid Sci.* **2015**, *61*, 201–209. [\[CrossRef\]](#)
72. Ventola, L.; Robotti, F.; Dialameh, M.; Calignano, F.; Manfredi, D.; Chiavazzo, E.; Asinari, P. Rough Surfaces with Enhanced Heat Transfer for Electronics Cooling by Direct Metal Laser Sintering. *Int. J. Heat Mass Transf.* **2014**, *75*, 58–74. [\[CrossRef\]](#)

73. Kirsch, K.L.; Thole, K.A. Pressure Loss and Heat Transfer Performance for Additively and Conventionally Manufactured Pin Fin Arrays. *Int. J. Heat Mass Transf.* **2017**, *108*, 2502–2513. [\[CrossRef\]](#)
74. European Powder Metallurgy Association (EPMA). Cooling Jacket with Internal Helix Structure. Available online: <https://www.epma.com/spotlight-on-pm/cooling-jacket-with-internal-helix-structure> (accessed on 10 February 2022).
75. Additive Manufactured Electric Motor. Available online: <https://ncam.the-mtc.org/case-studies/additive-manufactured-electric-motor/> (accessed on 11 February 2022).
76. Kim, J.; Yoo, D.J. 3D Printed Compact Heat Exchangers with Mathematically Defined Core Structures. *J. Comput. Des. Eng.* **2020**, *7*, 527–550. [\[CrossRef\]](#)
77. Kaur, I.; Singh, P. State-of-the-Art in Heat Exchanger Additive Manufacturing. *Int. J. Heat Mass Transf.* **2021**, *178*, 121600. [\[CrossRef\]](#)
78. Moon, H.; Miljkovic, N.; King, W.P. High Power Density Thermal Energy Storage Using Additively Manufactured Heat Exchangers and Phase Change Material. *Int. J. Heat Mass Transf.* **2020**, *153*, 119591. [\[CrossRef\]](#)
79. Bernardin, J.D.; Ferguson, K.; Sattler, D. The Testing and Model Validation of an Additively Manufactured Twisted Tube Heat Exchanger. In Proceedings of the ASME 2019 13th International Conference on Energy Sustainability, Collocated with the ASME 2019 Heat Transfer Summer Conference, Bellevue, WA, USA, 14–17 July 2019. [\[CrossRef\]](#)
80. Putra, N.; Ariantara, B. Electric Motor Thermal Management System Using L-Shaped Flat Heat Pipes. *Appl. Therm. Eng.* **2017**, *126*, 1156–1163. [\[CrossRef\]](#)
81. Chaudhry, H.N.; Hughes, B.R.; Ghani, S.A. A Review of Heat Pipe Systems for Heat Recovery and Renewable Energy Applications. *Renew. Sustain. Energy Rev.* **2012**, *16*, 2249–2259. [\[CrossRef\]](#)
82. Thompson, S.M.; Aspin, Z.S.; Shamsaei, N.; Elwany, A.; Bian, L. Additive Manufacturing of Heat Exchangers: A Case Study on a Multi-Layered Ti–6Al–4V Oscillating Heat Pipe. *Addit. Manuf.* **2015**, *8*, 163–174. [\[CrossRef\]](#)
83. Esarte, J.; Blanco, J.M.; Bernardini, A.; San-José, J.T. Optimizing the Design of a Two-Phase Cooling System Loop Heat Pipe: Wick Manufacturing with the 3D Selective Laser Melting Printing Technique and Prototype Testing. *Appl. Therm. Eng.* **2017**, *111*, 407–419. [\[CrossRef\]](#)
84. Ameli, M.; Agnew, B.; Leung, P.S.; Ng, B.; Sutcliffe, C.J.; Singh, J.; McGlen, R. A Novel Method for Manufacturing Sintered Aluminium Heat Pipes (SAHP). *Appl. Therm. Eng.* **2013**, *52*, 498–504. [\[CrossRef\]](#)
85. Ozguc, S.; Pai, S.; Pan, L.; Geoghegan, P.J.; Weibel, J.A. Experimental Demonstration of an Additively Manufactured Vapor Chamber Heat Spreader. In Proceedings of the 18th InterSociety Conference on Thermal and Thermomechanical Phenomena in Electronic Systems, ITherm 2019, Las Vegas, NV, USA, 28–31 May 2019; pp. 416–422. [\[CrossRef\]](#)
86. Richard, B.; Pellicone, D.; Anderson, W.G. Loop Heat Pipe Wick Fabrication via Additive Manufacturing. In Proceedings of the 47th International Conference on Environmental Systems, Charleston, SC, USA, 16–20 July 2017.
87. Wrobel, R.; Reay, D. A Feasibility Study of Heat Pipes for Thermal Management of Electrical Machines. In Proceedings of the ECCE 2020—IEEE Energy Conversion Congress and Exposition, Detroit, MI, USA, 11–15 October 2020; pp. 4230–4237. [\[CrossRef\]](#)
88. McGlen, R.J. An Introduction to Additive Manufactured Heat Pipe Technology and Advanced Thermal Management Products. *Therm. Sci. Eng. Prog.* **2021**, *25*, 100941. [\[CrossRef\]](#)
89. Chong, Y.C.; Staton, D.; Gai, Y.; Adam, H.; Popescu, M. Review of Advanced Cooling Systems of Modern Electric Machines for Embodiment Application. In Proceedings of the 2021 IEEE Workshop on Electrical Machines Design, Control and Diagnosis, WEMDCD 2021, Modena, Italy, 8–9 April 2021; pp. 149–154. [\[CrossRef\]](#)
90. Semidey, S.A.; Mayor, J.R. Experimentation of an Electric Machine Technology Demonstrator Incorporating Direct Winding Heat Exchangers. *IEEE Trans. Ind. Electron.* **2014**, *61*, 5771–5778. [\[CrossRef\]](#)
91. Schiefer, M.; Doppelbauer, M. Indirect Slot Cooling for High-Power-Density Machines with Concentrated Winding. In Proceedings of the 2015 IEEE International Electric Machines and Drives Conference, IEMDC 2015, Coeur d’Alene, ID, USA, 10–13 May 2015; pp. 1820–1825. [\[CrossRef\]](#)
92. Wrobel, R.; Hussein, A. A Feasibility Study of Additively Manufactured Heat Guides for Enhanced Heat Transfer in Electrical Machines. *IEEE Trans. Ind. Appl.* **2020**, *56*, 205–215. [\[CrossRef\]](#)
93. Sixel, W.; Liu, M.; Nellis, G.; Sarlioglu, B. Cooling of Windings in Electric Machines via 3-D Printed Heat Exchanger. *IEEE Trans. Ind. Appl.* **2020**, *56*, 4718–4726. [\[CrossRef\]](#)
94. Wohlers, C.; Juris, P.; Kabelac, S.; Ponick, B. Design and Direct Liquid Cooling of Tooth-Coil Windings. *Electr. Eng.* **2018**, *100*, 2299–2308. [\[CrossRef\]](#)
95. Lindh, P.; Petrov, I.; Jaatinen-Varri, A.; Gronman, A.; Martinez-Iturralde, M.; Satrustegui, M.; Pyrhonen, J. Direct Liquid Cooling Method Verified with an Axial-Flux Permanent-Magnet Traction Machine Prototype. *IEEE Trans. Ind. Electron.* **2017**, *64*, 6086–6095. [\[CrossRef\]](#)
96. Polikarpova, M.; Ponomarev, P.; Røytta, P.; Semken, S.; Alexandrova, Y.; Pyrhönen, J. Direct Liquid Cooling for an Outer-Rotor Direct-drive Permanent-Magnet Synchronous Generator for Wind Farm Applications. *IET Electr. Power Appl.* **2015**, *9*, 523–532. [\[CrossRef\]](#)
97. Wu, F.; El-Refaie, A.; Al-Qarni, A. Additively Manufactured Hollow Conductors Integrated with Heat Pipes: Design Tradeoffs and Hardware Demonstration. *IEEE Trans. Ind. Appl.* **2021**, *57*, 3632–3642. [\[CrossRef\]](#)



**Publication II**

M. Sarap, H. Tiismus, A. Kallaste, M. Saarna, M. Kolnes, P. Shams Ghahfarokhi, T. Vaimann, Electrical and Thermal Anisotropy in Additively Manufactured AlSi10Mg and Fe-Si Samples, *Machines* 13 (2025) 1. <https://doi.org/10.3390/machines13010001>.





## Article

# Electrical and Thermal Anisotropy in Additively Manufactured AlSi10Mg and Fe-Si Samples <sup>†</sup>

Martin Sarap <sup>1,\*</sup>, Hans Tiismus <sup>1</sup>, Ants Kallaste <sup>1</sup>, Mart Saarna <sup>2</sup>, Märt Kolnes <sup>2</sup>,  
Payam Shams Ghahfarokhi <sup>3</sup> and Toomas Vaimann <sup>1</sup>

<sup>1</sup> Department of Electrical Power Engineering and Mechatronics, Tallinn University of Technology, 19086 Tallinn, Estonia; ants.kallaste@taltech.ee (A.K.); toomas.vaimann@taltech.ee (T.V.)

<sup>2</sup> Department of Mechanical and Industrial Engineering, Tallinn University of Technology, 19086 Tallinn, Estonia; mart.saarna@taltech.ee (M.S.); mart.kolnes1@taltech.ee (M.K.)

<sup>3</sup> Electrical Engineering Unit, Tampere University, P.O. Box 692, FI-33014 Tampere, Finland; payam.shamsghahfarokhi@tuni.fi

\* Correspondence: martin.sarap1@taltech.ee

<sup>†</sup> This paper is an extended version of our paper published in 2022 International Conference on Electrical Machines (ICEM), Valencia, Spain, 5–8 September 2022.

**Abstract:** In the context of rising power densities in electrical machines, additive manufacturing presents an opportunity to develop more powerful thermal solutions. However, the physical properties of objects manufactured using this process remain unclear. This research examines the directional thermal and electrical conductivities of aluminum alloy (AlSi10Mg) and silicon steel (Fe-3.7%wt. Si) samples produced via laser powder bed fusion (LPBF), both prior to and following heat treatment. The findings indicate that the as-built aluminum samples exhibit higher conductivities in the orientation parallel to the LPBF build direction, while annealing results in higher conductivities overall and an absence of anisotropy. On the other hand, the silicon steel samples show constant conductivities and lack of anisotropy both before and after heat treatment. These results have practical applications in the design of additively manufactured electrical machines, where the thermal and electrical resistance of the materials have a major impact on thermal and electromagnetic performance.

**Keywords:** electrical machines; thermal conductivity; additive manufacturing



Academic Editor: Ibrahim Tansel

Received: 26 November 2024

Revised: 13 December 2024

Accepted: 21 December 2024

Published: 24 December 2024

**Citation:** Sarap, M.; Tiismus, H.; Kallaste, A.; Saarna, M.; Kolnes, M.; Shams Ghahfarokhi, P.; Vaimann, T. Electrical and Thermal Anisotropy in Additively Manufactured AlSi10Mg and Fe-Si Samples. *Machines* **2025**, *13*, 1. <https://doi.org/10.3390/machines13010001>

**Copyright:** © 2024 by the authors. Licensee MDPI, Basel, Switzerland. This article is an open access article distributed under the terms and conditions of the Creative Commons Attribution (CC BY) license (<https://creativecommons.org/licenses/by/4.0/>).

## 1. Introduction

Additive manufacturing (AM) offers unparalleled design freedom in many fields, including electrical machines, where laser powder bed fusion (LPBF) can be used to manufacture all parts of the machine. Currently, commercial use of LPBF is limited to highly demanding applications such as aerospace, meaning that AM electrical machines are currently in the research phase. However, ongoing trends in the wider adoption of AM and more cost- and time-efficient machines (e.g., multi-laser systems) ensure that the technology is becoming prevalent in other fields as well.

While AM can be used with a wide selection of materials to manufacture parts with high complexity (the cost of manufacturing is only weakly dependent on part complexity), the physical properties of the final parts are not always the same as the base material and can be anisotropic [1]. This includes the material's thermal conductivity (TC) and electrical conductivity (EC), which can depend on several manufacturing parameters, such as the build orientation, laser energy density [2], and laser scan speed [3]. The main effects that influence the physical properties of the final AM part are porosity and crystal structure.



The effects of porosity have become less relevant, as relative densities well above 99% are routinely achieved with LPBF [4]. Therefore, the often anisotropic crystal structure resulting from the LPBF process, which involves high-temperature gradients [5] and rapid directional cooling rates [6], is the main contributor to changes in the physical properties of the final part.

The two most relevant materials in the field of AM electrical machines are silicon steel as the soft-magnetic material [7] and the aluminum alloy AlSi10Mg as the electrically and thermally conductive material [8]. Electrical machines can have relevant heat flux and electrical current through both of these materials in any direction, meaning that knowing the TC and EC in each axis is needed to create optimal designs.

The crystal structure of high-silicon steel (6.9%wt. Si) manufactured via LPBF was analyzed by Garibaldi et al., who found columnar grains oriented towards the build direction, which depended on the laser energy [9]. Kang et al. [10] measured the magnetic properties of LPBF Fe-Ni-Si samples and found a more favorable hysteresis loop when magnetizing the part in the build direction, which they attributed to the columnar grain structure. Therefore, while the magnetic properties of silicon steel manufactured with LPBF have been shown to be anisotropic, its thermal conductivity has not been thoroughly researched.

The physical and mechanical properties of the aluminum alloy AlSi10Mg have been previously studied and are known to be anisotropic. Mfusi et al. [11] manufactured AlSi10Mg samples with different build orientations and found higher ultimate tensile strength in the build direction. Anisotropic thermal conductivities in AlSi10Mg samples have been measured by several groups [12,13], with around 10% higher TC in the build direction and a reduction in anisotropy with heat treatment being the common result.

Knowing the thermal properties of the relevant materials is essential when designing optimized electrical machines. In the case of additive manufacturing, this extends to a need to know the properties in the case of the specific manufacturing method. This article is an extension of our previously published conference paper [1], in which the direction-dependent TC of silicon steel (3.7%wt. Si) and AlSi10Mg samples manufactured via LPBF are determined. As an extension of that work, we have measured the electrical conductivity of the materials. Furthermore, we have utilized optical and electron microscopy for visualizing the crystal structure of the materials, in order to give an explanation for the measurement results.

## 2. Methodology

### 2.1. Sample Preparation

All the samples measured in this paper were manufactured using LPBF, of which a simplified illustration is provided in Figure 1. This is an AM method, where thin layers of powder are melted with one or more lasers to form a three-dimensional object. Modern LPBF devices are capable of manufacturing single parts with outer dimensions in excess of  $1 \times 1 \times 1$  m and without any degradation in mechanical properties throughout the part. However, the inherent directionality of heat flux during the LPBF process and the rapid cooling rates involved can create anisotropy in the part, which can have significant effects on physical properties such as thermal and electrical conductivity. It should be noted that in principle, the location of the object on the build platform changes the direction of heat flux in both heating and cooling. Therefore, it can have an appreciable effect on its physical parameters. However, in this article, each sample is printed near the center of the platform, meaning that any effects of part location are not observed.

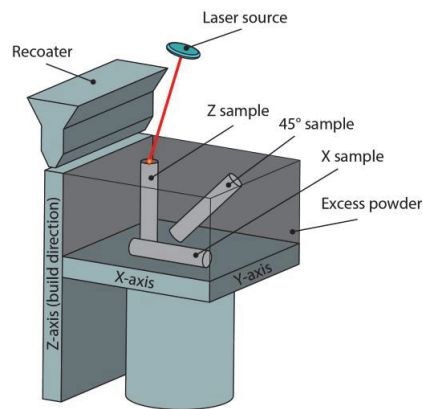


Figure 1. Illustration of the LPBF process with the directional thermal conductivity samples shown.

A number of AlSi10Mg and Fe-Si (3.7%wt. Si) samples were built using LPBF in different orientations, to study the effects of manufacturing direction on the thermal and electrical conductivities of LPBF samples. Table 1 includes a list of the samples used in this paper. The designators Z, X, and 45° correspond to a manufacturing orientation that is parallel, perpendicular, and at a 45° angle to the LPBF build direction, respectively.

Table 1. List of created samples.

Measured Property	Material	Manufacturing Orientation	No. of Samples Created
Thermal conductivity	AlSi10Mg	Z	1
		45°	1
		X	1
	FeSi (3.7%wt. Si)	Z	1
		X	1
Electrical conductivity	AlSi10Mg	Z	2
		X	2
	FeSi (3.7%wt. Si)	Z	2
		X	2

The physical and mechanical properties of objects manufactured via LPBF depend on the specific manufacturing parameters; however, the exact details of the causes are not always known. Generally, the variations in properties are explained through variations in energy density when heating the material. For example, laser energy density (directly defined by laser power) and part porosity are highly correlated [14,15], with low energies and high energies both resulting in increased porosity through partial melting and melt pool instabilities, respectively. The effective power density of the heating is also dependent on the path of the laser, which is in part defined by hatch spacing (the distance between adjacent scan tracks of the laser). It is known that layer thickness, laser power, and scanning velocity can affect the relative density and hardness of the LPBF part [16]. The scan strategy, which describes the exact pattern of the laser beam during the manufacturing process, can affect the object’s crystallographic texture and therefore create anisotropy in the final part [17]. Therefore, when describing the material properties of LPBF parts, knowing the specific manufacturing parameters is crucial in order to reproduce the results and apply the knowledge in practical designs. Table 2 presents the parameters used for manufacturing the samples in this article. These can be considered typical values, which have an excellent

success rate and result in effectively non-porous parts with mechanical properties equal to the base material.

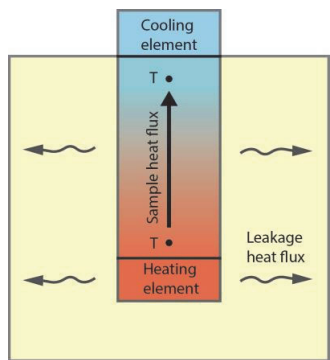
**Table 2.** Important manufacturing parameters [1].

Parameter	Value (Aluminum)	Value (Steel)
Layer thickness	50 $\mu\text{m}$	50 $\mu\text{m}$
Hatch distance	170 $\mu\text{m}$	120 $\mu\text{m}$
Laser power	350 W	250 W
Scanning velocity	1.15 m/s	0.5 m/s
Scan strategy	Stripes	Stripes
Environment	Nitrogen	Nitrogen
Oxygen content	$\sim 0.1\%$	$\sim 0.1\%$

Metal parts produced through additive manufacturing are often subjected to annealing to improve their properties through enhanced crystallographic texture and reduced anisotropy. The process involves heating the part above its recrystallization temperature for some duration, followed by cooling. The crystal structure of the material can be altered in a desirable manner by precisely controlling the temperature of the processed part over the duration of the process. For the samples used in this paper, post-manufacturing thermal treatments were performed in a graphite chamber Webb-107 vacuum furnace. The samples were heated in a  $\sim 0.1$  mbar vacuum environment, with a heating rate of  $300\text{ }^{\circ}\text{C/h}$  up to the target temperature, then held for the desired duration, which was followed by slow furnace cooling. The target temperature and annealing duration were  $1200\text{ }^{\circ}\text{C}$  and 1 h for the silicon steel and  $300\text{ }^{\circ}\text{C}$  and 2 h for the aluminum.

2.2. Measuring Thermal Conductivity

The thermal conductivity of solid materials can be measured in different ways. The most common is laser flash analysis (LFA), which is frequently used in the literature for measuring LPBF samples. However, it is only applicable for fully dense and homogeneous materials [18], making it potentially inaccurate when measuring AM samples. Therefore, the TC of the samples is measured using the longitudinal heat flow method. This method consists of heating the sample from one end and cooling it from the other end, while measuring the temperature difference over a specified length when a steady state has been reached. As the total input power can be accurately measured, the TC of the material can be derived from Fourier’s law. The measurement schematic is presented in Figure 2.



**Figure 2.** Illustration of the technique used to measure the TC of the samples with T showing the location of the temperature sensors used to determine the temperature drop across a known length.

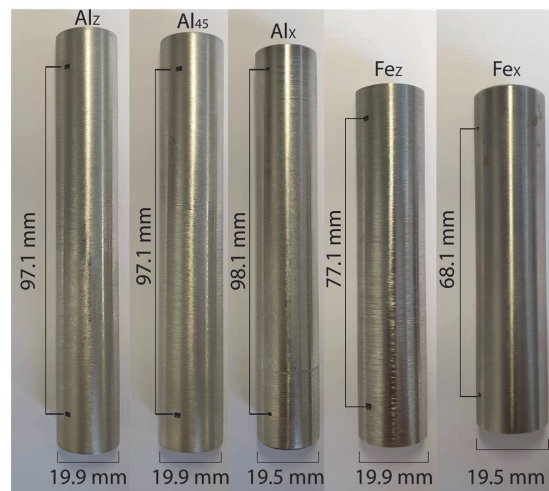
The specific method used in this paper omits the direct measurement of heat flux through the sample, which is normally achieved through two reference standards with known conductivity at the ends of the sample. By measuring this flux directly, any leakage heat flow through the insulation is effectively made irrelevant. However, using reference standards introduces additional uncertainties, such as in the value of their TC, additional temperature sensors (uncertainties in both positioning and readings) and added surfaces with thermal contact resistances.

Instead, in the method used in this paper, the flux is calculated numerically using a simple 3D model with inputs for the temperatures of the heatsink and the surface of the insulation. As long as the sample is properly insulated, the leakage heat flow through the insulation is several orders of magnitude lower than the total power input. In this case, considering the simplicity of the geometry, it is reasonable to claim that calculating the leakage flow results in a high degree of certainty in addition to a simpler testing setup.

Three AlSi10Mg samples were manufactured to measure the effect of build orientation on the TC of the parts. According to the manufacturer, the TC of this material is 130–150 W/m/K at 20 °C after annealing [19]. Another manufacturer of the same alloy [20] gives the as-built TC as 100–110 W/m/K.

Two samples ( $\text{Fe}_z$  and  $\text{Fe}_x$ ) were manufactured from silicon steel (3.7%wt. Si), which is a material widely used for AM soft-magnetic applications. The composition and magnetic properties of this specific material have been measured previously in [21]. As the thermal properties of AM silicon steel are not well known, a commercially available material (3.0%wt. Si) with a thermal conductivity of 28 W/m/K [22] is used as a comparison.

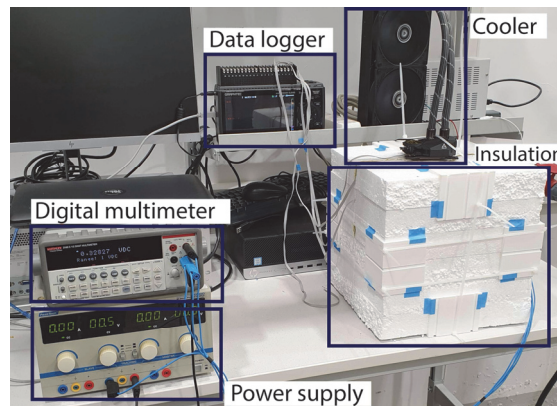
Each sample includes small rectangular holes for the PT100 temperature sensors, which allow the location of the sensors, and therefore the active length of the samples, to be accurately known, reducing one of the main sources of uncertainty normally present in TC measurements. After the AM process, the samples received post-processing to achieve a uniform diameter and smooth finish on all surfaces. The ends of the samples were polished for reduced thermal resistance. The samples together with the relevant dimensions are presented in Figure 3.



**Figure 3.** The LPBF aluminum alloy and silicon steel samples for measuring thermal conductivity with the distance between the temperature sensor openings shown [1].

The TC measurements were performed in a thermally stable room with no appreciable airflow affecting the cooler and the insulation around the test samples. Several different

values for the input power were used to measure the TC of the samples at different temperatures. For each separate measurement, the system was given several hours to reach a steady state to eliminate any transient effects caused by thermal capacitance. A TO-220 power resistor screwed to the bottom of the sample was used to provide the input heat through a very low thermal resistance, while allowing the total electrical input power to be accurately measured. The cold side of the sample was cooled by a water-cooling unit to create a large temperature gradient over the length of the sample. The performance of the cooling is important, as it helps decrease the overall thermal resistance of the sample stack and therefore reduces the unwanted heat flow through the insulation. The measurement setup is presented in Figure 4.



**Figure 4.** Thermal conductivity measurement setup [1].

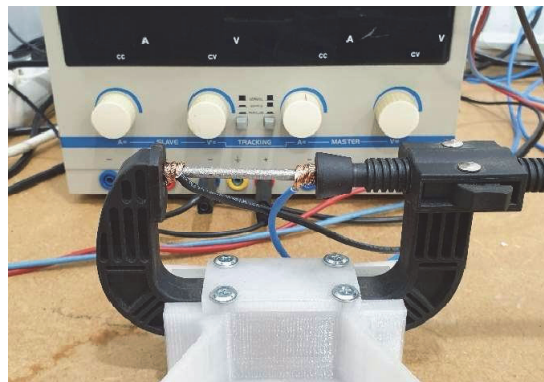
The uncertainties of the TC measurements are calculated by using the maximum and minimum possible values based on the uncertainty of each individual measurement. The largest source of uncertainty comes from the accuracy of the temperature sensors, which is specified as  $\pm 0.1 + 0.00017 |T|$ . Another contributing factor is the measurement error of the physical dimensions of the samples, particularly the distance between the temperature sensors, which was measured via digital calipers with an accuracy of 0.01 mm. The approximation of insulation losses through the use of a numerical model is also a contributor, with a relative uncertainty of the effective heat flow estimated to be around 0.5–1%, depending on the conductivity of the sample. Other smaller sources of uncertainty, such as measuring the electrical input power, were also considered. The resulting relative errors for the TC measurements fell between 3% and 5%. It is worth mentioning that the uncertainty is mostly relevant when considering absolute values, and the method can be used to compare different samples with very high consistency.

### 2.3. Measuring Electrical Conductivity

Additional cylindrical test samples were manufactured from both materials using LPBF for measuring the electrical conductivity. The measurements were performed using the four-probe Kelvin method. The sample measurements were verified with a digital caliper. A current of up to 3 A was passed through the sample, and the voltage drop over a set distance was measured at a temperature of 20 °C. Each sample was measured three times with results averaged and the corresponding measurement uncertainty was calculated similarly to the TC samples. The electrical measurements were performed using Keithley 2100 6-digit multimeters. The electrical conductivity test samples were printed both in parallel (Z) and perpendicular (X) to the build direction, similar to the TC samples. The aluminum samples had an average cross-section area of 15.5 mm<sup>2</sup> and the voltage drop



was measured over an average length of 35.6 mm. The silicon steel samples had an average cross-section area of  $9.0 \text{ mm}^2$ , and the voltage drop was measured over an average length of 40.2 mm. The electrical conductivity measurement setup with an AlSi10Mg sample is presented in Figure 5.



**Figure 5.** The experimental setup for measuring the electrical conductivity.

#### 2.4. Microstructure Imaging

Test cubes ( $10 \times 10 \times 10 \text{ mm}$ ) for both materials were manufactured for microstructure analysis. It was conducted through standard metallographic practices of polishing, etching, and optical/electron microscopy, involving SEM-EDS ZEISS Ultra 55 (for scanning electron micrography, Oberkochen, Germany) and Zeiss Axiovert 25 (for light optical micrography, Oberkochen, Germany). Etching of the silicon steel samples was conducted after polishing the surfaces up to  $0.05 \mu\text{m}$  and treating the surface for 15 s using Nital 5.0%. For AlSi10Mg samples,  $\text{NaOH} + \text{C}_6\text{FeK}_3\text{N}_6$  treatment for two 15 s steps was used with  $0.05 \mu\text{m}$  polishing between the etching steps. The grain structure was evaluated according to the mean value intercepted method.

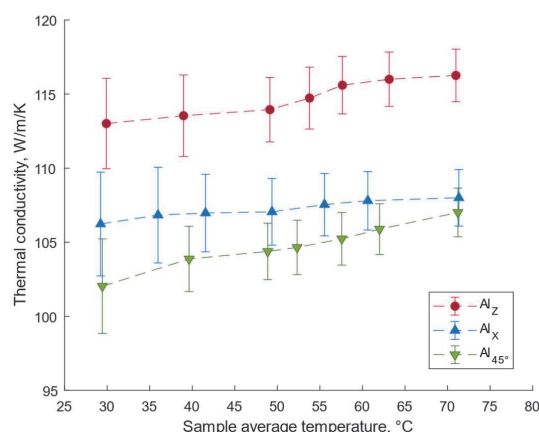
### 3. Results and Discussion

#### 3.1. Thermal Conductivity Results

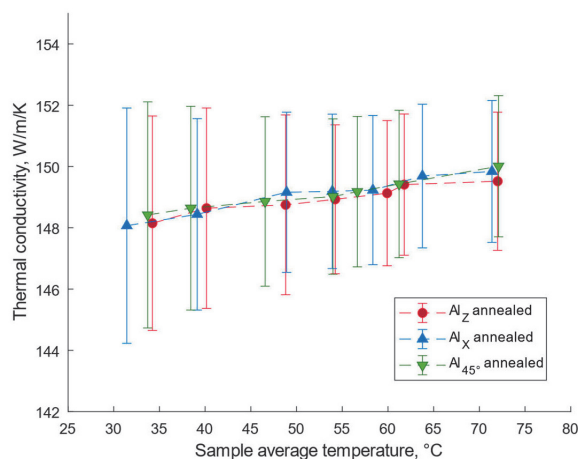
The graph in Figure 6 displays the results of the TC measurements for the as-built aluminum samples along with the calculated uncertainties. The measurement conducted on the pre-annealed samples showed a 10% rise in TC in the Z-direction, roughly  $115 \text{ W/m/K}$  compared to the approximately  $105 \text{ W/m/K}$  in the X-direction. For each sample, it was observed that there was a roughly linear correlation between TC and temperature, which is a common characteristic of this alloy at the measured temperature range [12].

The increased TC in the Z-direction is generally explained in the literature by a preferred grain orientation in the material, which is formed during the LPBF process [23]. Additionally, the bulk TC of the material can be affected by the presence of Si in the crystal structure [24]. It is interesting to note that the measured conductivity of the Al45 sample is slightly lower than that of the AlX sample, suggesting that the correlation between TC and build direction is not simply linear.

The measurement results for the annealed samples are displayed in Figure 7. The values are consistently high, ranging from  $148$  to  $150 \text{ W/m/K}$ . The results clearly show that annealing eliminates any manufacturing orientation effects, as no significant anisotropy was observed. However, the TC of the samples is still correlated with temperature.



**Figure 6.** Thermal conductivity measurement results for the as-built aluminum samples [1].



**Figure 7.** Results of the TC measurements for the aluminum samples [1].

The results of the silicon steel samples are presented in Figure 8. The measured values, which range from 24.43 to 27.47 W/m/K, are nearly the same for each sample, indicating no noticeable influence of either manufacturing orientation or heat treatment on the TC of the material. The TC of the samples increases with increasing temperature, which is typical for steel at this temperature range [25]. In comparison to a commercial 3.0% Si electrical steel, the measured TC of the AM material is somewhat lower. This is an expected result, as the comparatively lower TC of silicon has a larger effect at higher concentrations. Therefore, it can be said based on the measurement results that the LPBF process does not negatively impact the TC of silicon steel.

The measurements indicate no difference in the TC between the as-built and annealed samples. This is different from the magnetic properties of LPBF silicon steel, which have been shown to be anisotropic. Additionally, heat treatment has been shown to affect the properties of LPBF silicon steel, as Garibaldi et al. [26] measured the impact of heat treatment on the magnetic properties of Fe-6.9%wt. Si samples. They noted a decrease of roughly 50% in power losses after annealing the sample at 1150 °C for 1 h, which they attributed to the increase in grain size within the steel. Thus, while it seems that the LPBF process can produce some anisotropy in silicon steel, the material's TC is not significantly affected. Table 3 provides a summary of the measurements. The values for

specific temperatures are interpolated, and the uncertainty of the measurement at the nearest lower temperature is used.

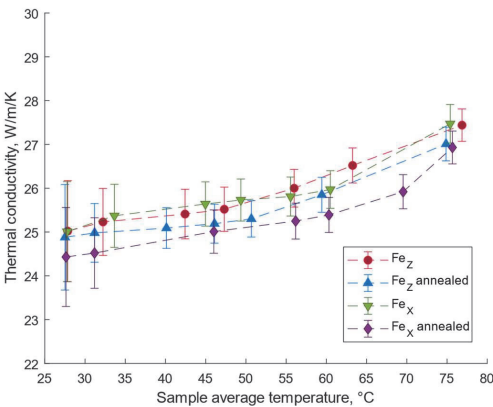


Figure 8. Measured thermal conductivity values for the as-built and annealed silicon steel samples [1].

Table 3. Measurement results for the thermal conductivities of the as-built and annealed samples [1].

Sample	Thermal Conductivity at 35 °C (W/m/K)	Thermal Conductivity at 70 °C (W/m/K)
Al <sub>Z</sub> as-built	113.3 ± 3.1	116.2 ± 1.8
Al <sub>Z</sub> annealed	148.2 ± 3.5	149.5 ± 2.3
Al <sub>45</sub> as-built	103.0 ± 3.2	106.9 ± 1.7
Al <sub>45</sub> annealed	148.5 ± 3.7	149.9 ± 2.4
Al <sub>X</sub> as-built	106.7 ± 3.5	108.0 ± 2.0
Al <sub>X</sub> annealed	148.2 ± 3.8	149.8 ± 2.3
Fe <sub>Z</sub> as-built	25.3 ± 0.8	27.0 ± 0.4
Fe <sub>Z</sub> annealed	25.0 ± 0.7	26.6 ± 0.4
Fe <sub>X</sub> as-built	25.4 ± 0.7	26.9 ± 0.4
Fe <sub>X</sub> annealed	24.6 ± 0.8	26.0 ± 0.4

3.2. Electrical Conductivity Results

The results of the electrical conductivity for the as-built and annealed samples are presented in Table 4. The measured values are similar to the TC, as the aluminum samples manufactured parallel to the build direction show notably higher electrical conductivity. The increase in electrical conductivity with the annealing process for the aluminum sample is comparatively high but in line with other measurements of the same alloy. The Fe-Si samples similarly did not show any deviation from the characteristics of the thermal results, with the electrical conductivity of the samples being invariant of manufacturing orientation and heat treatment.

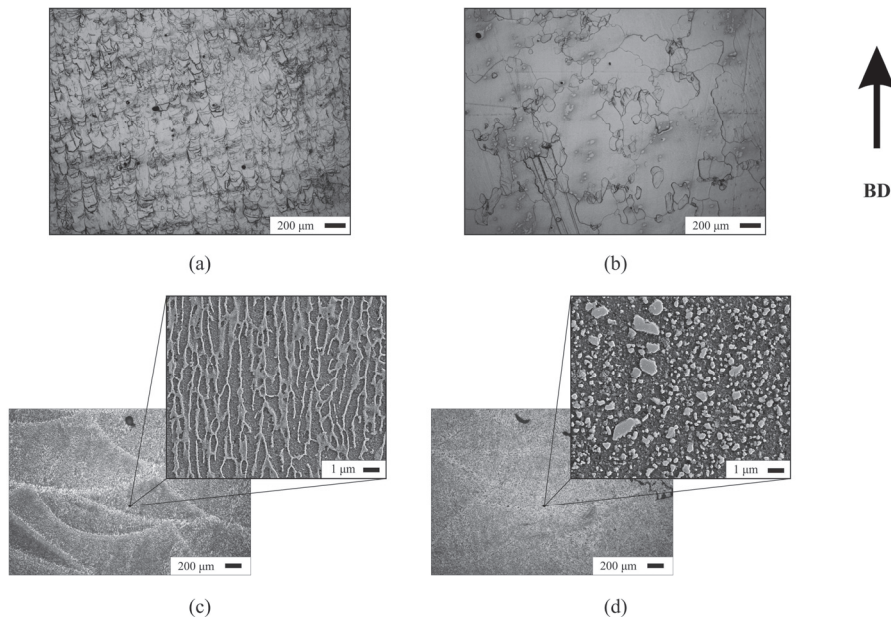
Table 4. Measured electrical conductivities of the samples.

Sample	Electrical Conductivity at 20 °C (MS/m)
Al <sub>Z</sub> as-built	14.70 ± 0.27
Al <sub>Z</sub> /annealed	23.88 ± 0.50
Al <sub>X</sub> as-built	13.08 ± 0.36
Al <sub>X</sub> /annealed	24.72 ± 0.86
Fe <sub>Z</sub> as-built	1.76 ± 0.03
Fe <sub>Z</sub> /annealed	1.78 ± 0.03
Fe <sub>X</sub> as-built	1.76 ± 0.03
Fe <sub>X</sub> /annealed	1.77 ± 0.03



### 3.3. Microstructure Analysis

The microstructural imaging results are presented in Figure 9, with the build direction (Z-axis) of the process indicated.



**Figure 9.** Annealing induced microstructure evolution of the printed material. Grain growth in silicon steel: (a) as-built state and (b) post-annealing. Breakdown of lamellar Si microstructures: (c) as-built state and (d) post-annealing.

The as-built microstructure of the unannealed XZ plane samples shows typical columnar structures with an oriented growth in the build direction. This can be related to rapid solidification (103–106 K/s) and vertical directionality of the manufacturing process: from the bottom to top, inducing a characteristic solidification along the build direction. The fused microstructures of the two materials did exhibit significant differences.

The as-built silicon steel samples showed a uniform, relatively fine crystallographic structure in the range of 18–140 μm, with an average grain size of 65 μm. The structure coarsened substantially after the thermal treatment, up to approximately 195 μm. Post-annealing, the range of the crystallographic grains varied significantly, ranging from 40 to 600 μm.

Compared to the uniformly fused structure of the Fe-Si, the structure of both as-built and heat-treated AlSi10Mg exhibited Si-phase depositions within the Al matrix. In this case, the EN ISO 643:2020 standard was not applicable for grain size evaluation. It could be verified, however, that the α-Al features within the silicon-rich matrix were in the range of 0.5–1 μm. It was also evident that the annealing process changed the Si distribution of the eutectic microstructure and created coarser Si particles within the Al matrix instead of the initial eutectic lamellar Si microstructure. A similar breakdown of the silicon-rich areas into smaller roughly spherical agglomerations has been documented in other works as well [27].

This change in the material microstructure is responsible for the effect of annealing on the thermal and electrical conductivity of the AlSi10Mg samples. The anisotropic boundaries of Si segregating the elongated α-Al structures act as additional resistance for any electrical charge attempting to pass the material. After the heat treatment, these

boundaries are broken and a lower resistance path for the electrical charge is created. When considering the transmission of thermal energy, the mechanism is similar: This is because both thermal and electrical conductivity are strongly dependent on the inherent electron mobility within the material. As the AM silicon steel exhibited a largely uniform microstructure, the obtained properties were also isotropic. Unlike magnetic properties, thermal and electrical conductivities are considered mostly invariant of grain size [7], and thus, significant changes in the conductive behavior of silicon steel were not observed post-annealing.

#### 4. Conclusions

The thermal and electrical conductivities of AlSi10Mg and Fe-Si samples manufactured using laser powder bed fusion were measured using longitudinal heat flow and 4-probe Kelvin measurements, respectively.

The as-built AlSi10Mg samples exhibited marked anisotropy, with higher thermal and electrical conductivities in the orientation parallel to the LPBF build direction. This anisotropy disappeared after annealing, which also enhanced the overall conductivities. This suggests that post-processing treatments are crucial for optimizing the material properties of AlSi10Mg for applications requiring high thermal and electrical performance. On the other hand, if heat treatment is not possible for any reason, it means that the anisotropy must be accounted for during the design phase. Furthermore, as the annealing process seems to have a larger impact on TC than EC, in some electrical machine applications, such as heat exchangers for direct-conductor cooling, forgoing heat treatment can be beneficial for reducing AC losses in aluminum without sacrificing too much thermal performance.

On the other hand, the silicon steel samples showed uniform thermal and electrical conductivities, with no significant anisotropy regardless of the build direction or heat treatment. This is somewhat different from the magnetic properties, which have shown some anisotropy in the literature. However, this uniformity indicates that Fe-Si is a reliable material for applications where isotropic properties are essential. In practice, it means that when manufacturing a silicon steel core with LPBF, the build direction can be freely chosen based on magnetic, mechanical (this is especially relevant when manufacturing laminated structures), and post-processing limitations. Future work should look into non-standard manufacturing parameters in order to purposefully reduce the electrical conductivity of silicon steel, which in turn would help reduce eddy currents. This would likely also decrease thermal conductivity; however, depending on the machine topology and cooling method, the TC of the soft magnetic material can be insignificant in terms of overall thermal performance.

The microstructure analysis performed on the samples using LOM and SEM imaging was in line with the measurement results and provided extra context for the measured results. The AlSi10Mg samples showed a breakdown of the initial eutectic lamellar Si microstructure into coarser Si particles after annealing, which contributed to the improved conductivities. The Fe-Si samples, however, maintained a uniform microstructure, explaining the consistent conductivity values.

In conclusion, this study underscores the importance of considering both the manufacturing process and post-processing treatments in the design and application of additively manufactured materials. The insights gained here will aid in the development of more efficient and reliable electrical machines, paving the way for advancements in additive manufacturing technologies.

**Author Contributions:** Conceptualization, M.S. (Martin Sarap); methodology, M.S. (Martin Sarap), H.T. and M.S. (Mart Saarna); validation, M.S. (Martin Sarap) and M.S. (Mart Saarna); writing—original draft preparation, M.S. (Martin Sarap), H.T. and M.S. (Märt Saarna); writing—review

and editing, A.K., M.K. and P.S.G.; visualization, M.S. (Martin Sarap); supervision, A.K. and P.S.G.; project administration, A.K.; funding acquisition, A.K. and T.V. All authors have read and agreed to the published version of the manuscript.

**Funding:** This research was funded by the Estonian Research Council grant PRG-1827.

**Data Availability Statement:** Data are contained within the article.

**Conflicts of Interest:** The authors declare no conflicts of interest.

## References

1. Sarap, M.; Kallaste, A.; Ghahfarokhi, P.S.; Tiismus, H.; Vaimann, T. The Effect of Build Direction on the Thermal Conductivity of Additively Manufactured AlSi10Mg and Silicon-steel Samples. In Proceedings of the 2022 International Conference on Electrical Machines (ICEM), Valencia, Spain, 5–8 September 2022; pp. 538–543. [CrossRef]
2. Wang, D.; Wei, Y.; Wei, X.; Khanlari, K.; Wang, Z.; Feng, Y.; Yang, X. Selective Laser Melting of Pure Ag and 925Ag Alloy and Their Thermal Conductivity. *Crystals* **2022**, *12*, 480. [CrossRef]
3. Kim, M.S. Effects of Processing Parameters of Selective Laser Melting Process on Thermal Conductivity of AlSi10Mg Alloy. *Materials* **2021**, *14*, 2410. [CrossRef] [PubMed]
4. Attar, H.; Calin, M.; Zhang, L.C.; Scudino, S.; Eckert, J. Manufacture by selective laser melting and mechanical behavior of commercially pure titanium. *Mater. Sci. Eng. A* **2014**, *593*, 170–177. [CrossRef]
5. Barba, D.; Alabort, C.; Tang, Y.T.; Viscasillas, M.J.; Reed, R.C.; Alabort, E. On the size and orientation effect in additive manufactured Ti-6Al-4V. *Mater. Des.* **2020**, *186*, 108235. [CrossRef]
6. Rosenthal, I.; Stern, A.; Frage, N. Microstructure and Mechanical Properties of AlSi10Mg Parts Produced by the Laser Beam Additive Manufacturing (AM) Technology. *Metallogr. Microstruct. Anal.* **2014**, *3*, 448–453. [CrossRef]
7. Tiismus, H.; Kallaste, A.; Vaimann, T.; Lind, L.; Virro, I.; Rassõlkin, A.; Dedova, T. Laser Additively Manufactured Magnetic Core Design and Process for Electrical Machine Applications. *Energies* **2022**, *15*, 3665. [CrossRef]
8. Wohlers, C.; Juris, P.; Kabelac, S.; Ponick, B. Design and direct liquid cooling of tooth-coil windings. *Electr. Eng.* **2018**, *100*, 2299–2308. [CrossRef]
9. Garibaldi, M.; Ashcroft, I.; Simonelli, M.; Hague, R. Metallurgy of high-silicon steel parts produced using Selective Laser Melting. *Acta Mater.* **2016**, *110*, 207–216. [CrossRef]
10. Kang, N.; El Mansori, M.; Guittoneau, F.; Liao, H.; Fu, Y.; Aubry, E. Controllable mesostructure, magnetic properties of soft magnetic Fe-Ni-Si by using selective laser melting from nickel coated high silicon steel powder. *Appl. Surf. Sci.* **2018**, *455*, 736–741. [CrossRef]
11. Mfusi, B.J.; Tshabalala, L.C.; Popoola, A.P.I.; Mathe, N.R. The effect of selective laser melting build orientation on the mechanical properties of AlSi10Mg parts. *IOP Conf. Ser. Mater. Sci. Eng.* **2018**, *430*, 012028. [CrossRef]
12. Strumza, E.; Yeheskel, O.; Hayun, S. The effect of texture on the anisotropy of thermophysical properties of additively manufactured AlSi10Mg. *Addit. Manuf.* **2019**, *29*, 100762. [CrossRef]
13. Yang, P.; Deibler, L.A.; Bradley, D.R.; Stefan, D.K.; Carroll, J.D. Microstructure evolution and thermal properties of an additively manufactured, solution treatable AlSi10Mg part. *J. Mater. Res.* **2018**, *33*, 4040–4052. [CrossRef]
14. Kim, W.R.; Bang, G.B.; Kwon, O.; Jung, K.H.; Park, H.K.; Kim, G.H.; Jeong, H.T.; Kim, H.G. Fabrication of porous pure titanium via selective laser melting under low-energy-density process conditions. *Mater. Des.* **2020**, *195*, 109035. [CrossRef]
15. Peng, T.; Chen, C. Influence of energy density on energy demand and porosity of 316L stainless steel fabricated by selective laser melting. *Int. J. Precis. Eng. Manuf.—Green Technol.* **2018**, *5*, 55–62. [CrossRef]
16. Greco, S.; Gutzeit, K.; Hotz, H.; Kirsch, B.; Aurich, J.C. Selective laser melting (SLM) of AISI 316L—Impact of laser power, layer thickness, and hatch spacing on roughness, density, and microhardness at constant input energy density. *Int. J. Adv. Manuf. Technol.* **2020**, *108*, 1551–1562. [CrossRef]
17. Thijs, L.; Kempen, K.; Kruth, J.P.; van Humbeeck, J. Fine-structured aluminium products with controllable texture by selective laser melting of pre-alloyed AlSi10Mg powder. *Acta Mater.* **2013**, *61*, 1809–1819. [CrossRef]
18. ASTM E1461; Standard Test Method for Thermal Diffusivity by the Flash Method. ASTM: West Conshohocken, PA, USA, 2013.
19. SLM Solutions, Material Data Sheet Al-Alloy AlSi10Mg/EN AC-4300/EN AC-AlSi10Mg. Available online: [https://www.slm-solutions.com/fileadmin/Content/Powder/MDS/nw/2024/MDS\\_AlSi10Mg\\_2024-04.1\\_EN.pdf](https://www.slm-solutions.com/fileadmin/Content/Powder/MDS/nw/2024/MDS_AlSi10Mg_2024-04.1_EN.pdf) (accessed on 23 December 2024).
20. EOS Aluminium AlSi10Mg Material Data Sheet Metal Solutions. Available online: [https://www.eos.info/var/assets/03\\_system-related-assets/material-related-contents/metal-materials-and-examples/metal-material-datasheet/aluminium/material\\_datasheet\\_eos\\_aluminium-alsi10mg\\_en\\_web.pdf](https://www.eos.info/var/assets/03_system-related-assets/material-related-contents/metal-materials-and-examples/metal-material-datasheet/aluminium/material_datasheet_eos_aluminium-alsi10mg_en_web.pdf) (accessed on 23 December 2024).
21. Tiismus, H.; Kallaste, A.; Belahcen, A.; Tarraste, M.; Vaimann, T.; Rassõlkin, A.; Asad, B.; Shams Ghahfarokhi, P. AC Magnetic Loss Reduction of SLM Processed Fe-Si for Additive Manufacturing of Electrical Machines. *Energies* **2021**, *14*, 1241. [CrossRef]

22. Si 3 and, A. 0.4%, Chemical Composition, Typical Electrical Steel, Thin Non-Oriented Grades Coating SURALAC® 7000. Available online: <https://www.polarislaserlaminations.com/Cogent.pdf> (accessed on 23 December 2024).
23. Silbernagel, C.; Ashcroft, I.; Dickens, P.; Galea, M. Electrical resistivity of additively manufactured AlSi10Mg for use in electric motors. *Addit. Manuf.* **2018**, *21*, 395–403. [[CrossRef](#)]
24. Kimura, T.; Nakamoto, T.; Mizuno, M.; Araki, H. Effect of silicon content on densification, mechanical and thermal properties of Al-xSi binary alloys fabricated using selective laser melting. *Mater. Sci. Eng. A* **2017**, *682*, 593–602. [[CrossRef](#)]
25. Xing, Y.; Wang, W.; Al-azzani, H. Assessment of thermal properties of various types of high-strength steels at elevated temperatures. *Fire Saf. J.* **2021**, *122*, 103348. [[CrossRef](#)]
26. Garibaldi, M.; Ashcroft, I.; Lemke, J.N.; Simonelli, M.; Hague, R. Effect of annealing on the microstructure and magnetic properties of soft magnetic Fe-Si produced via laser additive manufacturing. *Scr. Mater.* **2018**, *142*, 121–125. [[CrossRef](#)]
27. Takata, N.; Kodaira, H.; Sekizawa, K.; Suzuki, A.; Kobashi, M. Change in microstructure of selectively laser melted AlSi10Mg alloy with heat treatments. *Mater. Sci. Eng. A* **2017**, *704*, 218–228. [[CrossRef](#)]

**Disclaimer/Publisher’s Note:** The statements, opinions and data contained in all publications are solely those of the individual author(s) and contributor(s) and not of MDPI and/or the editor(s). MDPI and/or the editor(s) disclaim responsibility for any injury to people or property resulting from any ideas, methods, instructions or products referred to in the content.



**Publication III**

M. Sarap, A. Kallaste, P.S. Ghahfarokhi, T. Vaimann, Analysis of Advanced Passive Heatsinks for Electrical Machines Enabled by Additive Manufacturing, in: 2023 IEEE Workshop Electr. Mach. Des. Control Diagn. WEMDCD, 2023: pp. 1–6. <https://doi.org/10.1109/WEMDCD55819.2023.10110940>.



# Analysis of Advanced Passive Heatsinks For Electrical Machines Enabled by Additive Manufacturing

Martin Sarap

Department of Electrical Power  
Engineering and Mechatronics  
Tallinn University of Technology  
Tallinn, Estonia  
martin.sarap1@taltech.ee

Ants Kallaste

Department of Electrical Power  
Engineering and Mechatronics  
Tallinn University of Technology  
Tallinn, Estonia  
ants.kallaste@taltech.ee

Payam Shams Ghahfarokhi

Department of Electrical Power  
Engineering and Mechatronics  
Tallinn University of Technology  
Tallinn, Estonia  
payam.shams@ttu.ee

Toomas Vaimann

Department of Electrical Power  
Engineering and Mechatronics  
Tallinn University of Technology  
Tallinn, Estonia  
toomas.vaimann@taltech.ee

**Abstract**— This paper presents numerical models of several different natural convection based heatsink designs for an additively manufactured switched reluctance machine. The proposed heatsink designs incorporate geometries that have improved thermal performance but are difficult to produce with conventional methods, making them ideal options for additive manufacturing. The heatsinks are compared to a traditional longitudinal plate fin heatsink model with a heat transfer coefficient of 0.159 W/K. The highest performing proposed heatsink model achieves a heat transfer coefficient of 0.184 W/K, showing that additively manufactured passive heatsinks can provide significantly improved cooling for totally enclosed non-ventilated machines.

**Keywords**—Additive manufacturing, Switched reluctance machine, Passive heatsinks.

## I. INTRODUCTION

Additive manufacturing (AM) is advancing electrical machine technologies by offering unparalleled design freedom. As a result, a substantial amount of work has been published both for utilizing AM to improve the electromagnetic [1], [2] and thermal [3] design of electrical machines. In the case of thermal design, a large amount of focus has been put on direct conductor cooling, as the largest gains can be seen there. However, the most common way of cooling an electrical machine utilizes a finned heatsink mounted around the stator, which is cooled either by active ventilation or natural convection. In the latter case, no moving parts are required as all of the airflow is driven by the buoyancy differences of the non-isothermal air around the heatsink. Although, this limits the performance of the heatsink as the heat transfer coefficient of the heatsink surfaces is around 2.5 – 25 W/(m<sup>2</sup>·K) compared to the 10 – 500 W/(m<sup>2</sup>·K) of actively air-cooled surfaces [4].

The performance of general purpose additively manufactured passive heatsinks has been researched to some degree. Lazarov et al [5] created AM passive heatsinks for LED lights utilizing different lattice structures and topology

optimization. The optimized device showed clearly higher performance, although the lattice structure designs were comparable to a conventional pin-fin heatsink utilizing a much simpler design. Pilagatti et al [6] found similar results with a topology optimized heatsink performing comparatively well. Wits et al [7] took a bio-inspired approach and modelled a passive heatsink based on the intricate geometry of the surface of a brain coral. The heatsink was successful in creating airflow throughout the fin structure, although a direct comparison with a conventional design was not given.

In this paper, different passive heatsinks are analyzed in the context of cooling additively manufactured electrical machines. For this, an AM switched reluctance machine (SRM) is used as the heat source, although the results are relevant for any radial flux inner-rotor machine that is cooled by a heatsink on the stator surface. The paper looks at several different heatsink designs that include AM specific solutions and improvements to existing methods that take advantage of the design freedom provided by AM. The inclusion of improved versions of conventional designs serves to create a better demonstration of AM's advantages in thermal design, as these are directly comparable to existing solutions. The data gathered from these models will be used in future works for manufacturing the heatsinks using selective laser melting (SLM).

## II. METHODOLOGY

### A. Physical Model

The heatsink models presented in this paper are designed for cooling a small additively manufactured SRM with a 6/4 configuration and an estimated nominal power of about 50 W. The machine's stator is additively manufactured from silicon steel (3.7%wt.Si) using SLM and has an outer diameter of 80 mm, a length of 46 mm and a total iron mass of 0.51 kg. The electromagnetic and thermal parameters of this material have been measured in previous works [8]. The construction of the core includes airgaps that mimic traditional steel laminations for suppressing eddy currents. The machine's rotor is omitted from the model as it would have no appreciable effect on the steady state performance of the heatsink, while adding to the computational complexity.

---

This work was supported by the Estonian Research Council grant (PRG-1827).



The heatsink of the machine is added around the outer surface of the stator and spans the entire stack length. The heatsink model consists of a solid base with a thickness of 2 mm and an active area with a radial height of 10 mm. The length of the active area is used as a size constraint for all of the different heatsinks presented in this paper. As the heatsink is modelled in the context of additive manufacturing, the aluminum alloy AlSi10Mg is used as the material. This is a common alloy used in AM thermal solutions due to good physical and mechanical properties in addition to excellent manufacturability [9]. Furthermore, the model contains endcaps with low thermal conductivity that provide no cooling but affect the airflow around the machine to achieve more realistic results. The cross-section of the motor including a conventional straight finned heatsink is presented in Fig. 1.

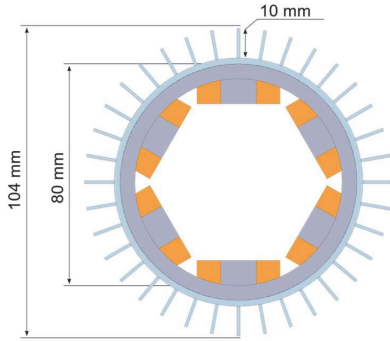


Fig. 1. Cross-section of the switched reluctance machine with an axial straight fin heatsink.

### B. Thermal Model

The heat generated in machine consists of both copper and iron losses. The copper losses are calculated using an average current density of 7.5 A/mm<sup>2</sup> in each stator slot giving a total copper loss of 11.9 W in the machine. The iron losses are calculated using an average flux density of 1 T in the core at a frequency of 50 Hz. The iron losses at these parameters for a similar SLM core of the same material were measured to be 10 W/kg, meaning that the stator iron losses of the modeled SRM are 5.1 W and the total losses add up to 17 W. The proportion of iron losses is significantly higher compared to a conventional machine due to the limited capability of the AM core to suppress eddy currents.

The thermal conductivity of the aluminum alloy manufactured by SLM was previously measured at 150 W/m/K [10]. The thermal conductivity of the AM core material has previously been measured at around 27 W/(m·K) [10] for a solid part. The fill factor of the AM stator is around 60 % due to the lamination structure, resulting in an effective thermal conductivity of 16 W/(m·K) in the X and Y planes. The conductivity in the Z direction is decreased significantly by the airgaps and a typical value for electrical steel laminations of 1 W/(m·K) is used [11].

The windings are modelled in two pieces – axial and end-winding parts. The thermal conductivity of the windings is similarly different from the base material due to a fill factor and insulation material between the copper strands. In this model, a fill factor of 50 % is used, giving the TC in the direction of the strands a value of 200 W/(m·K). The TC in

both orthogonal directions is taken from literature as roughly 0.1 W/(m·K) [12].

### C. Modelling Parameters

The modelling of the heatsinks was done in COMSOL Multiphysics using the computational fluid dynamics module. To ensure a realistic airflow, the motor was placed inside a container of air with a height, length and width that are 6, 2 and 3 times than the motor dimensions respectively. The top of the container was modelled as an exhaust at a pressure of 1 atm. The sides have the no-slip condition at an ambient temperature of 20 °C. A flat body with a low thermal conductivity of 0.3 W/(m·K) was added 10mm below the motor to simulate a general surface the motor would be placed on. The floor surface does not contain appreciable heat flow but impedes with the airflow of the motor heatsink in a realistic manner.

The results of the simulation are calculated for steady state and a fully developed flow is achieved. The airflow was modelled as laminar and weakly compressible with included gravity to enable buoyancy driven flow. The air adjacent to the heatsink is modelled with an extra dense mesh to improve accuracy and help the model converge. The inside of the motor was described as a void; therefore, all the inside surfaces are thermally isolated. Any effects of radiative cooling are ignored. The conjugate heat transfer model is illustrated in Fig. 2.

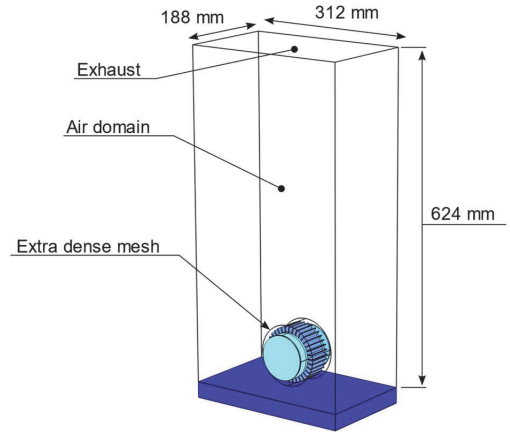


Fig. 2. Conjugate heat transfer model of the SRM.

## III. RESULTS AND DISCUSSION

Four different main heatsink designs were analyzed: longitudinal fin, annular fin, pin-fin, and lattice structure. The first two types are common solutions for different types of commercially available machines, with the annular fin design being specialized for motors cooled by natural convection. Pin-fin heatsinks generally perform better under natural convection than conventional plate finned heatsinks and are widely used in electronics, automotive and other applications. However, they are more difficult to manufacture and are not as robust in their construction, which is why they are generally not used for cooling electrical machines. Lattice structure based heatsinks are novel methods that are mostly enabled by AM and are popular in the research community.

The performance of the different heatsink designs is defined by their heat transfer coefficients. This is calculated

for each heatsink design using the temperature difference of the stator outer surface and ambient. As the total heat flux through the stator surface is known, the coefficient demonstrates the total cooling ability of the heatsink. The average convection coefficient of the entire outer surface of the heatsink is also calculated to provide comparable results to other passive heatsinks.

### A. Longitudinal Fin Heatsink

The base case of the longitudinal fin heatsink is representative of the most common heatsink geometry for electrical machines. Although the shape is better suited for active cooling with an axial airflow path, it is still reasonably effective as a passive cooler. The parameters of the heatsink used in this paper are based on work done Kim et al [13] on similarly sized cylindrical heatsinks with longitudinal plate fins. Using this data, the heatsink for the SRM was designed with 36 fins that are 1 mm thick and equally spaced radially around the motor. The resulting airflow for the basic longitudinal fin heatsink is illustrated in Fig. 3.

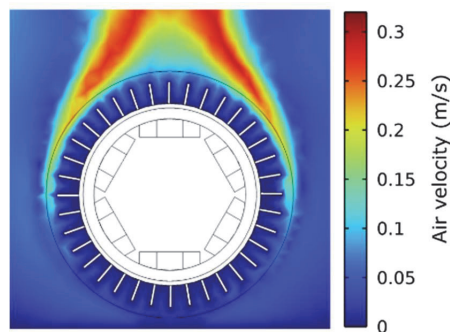


Fig. 3. Resulting temperature distribution for the base longitudinal fin heatsink.

The hottest spot of the motor occurred expectedly in the end-winding region and reached a value of 106.7 °C, giving the heatsink a heat transfer coefficient of 0.159 W/K and an average convection coefficient of 4.40 W/(m²·K)

It is evident from the resulting airflow distribution that the performance of this heatsink is limited in the case of natural convection due the orientation of the fins being orthogonal to the airflow direction, which significantly limits the airflow in the grooves between the fins. This means that even though the total surface area of the fins is high, only a part of it is in direct contact with cooling medium, resulting in a low effective surface area. Therefore, improvements to the design are considered. Primarily, the airflow is increased by cutting radial slits in the fins that allow air to flow across the heatsink. Several different parameters for the added slits were tried, with three 3 mm wide slits proving to be the most effective.

A second way to potentially increase the performance of this type of heatsink is to introduce a sinusoidal curve in the fins that increases the active surface area without significantly limiting the airflow. This “wavy fin” method would drastically increase the cost of manufacturing the heatsink with traditional means, making it perfect for demonstrating the value of the design freedom offered by AM. The results for the heatsink with added slits, axial curvature, and radial curvature are presented in Fig. 4 and Table I. The airflow is measured at the axial midplane of the motor, which

corresponds to the middle of the central slit. On this plane, the intra-fin airflow created by the slits is clearly visible.

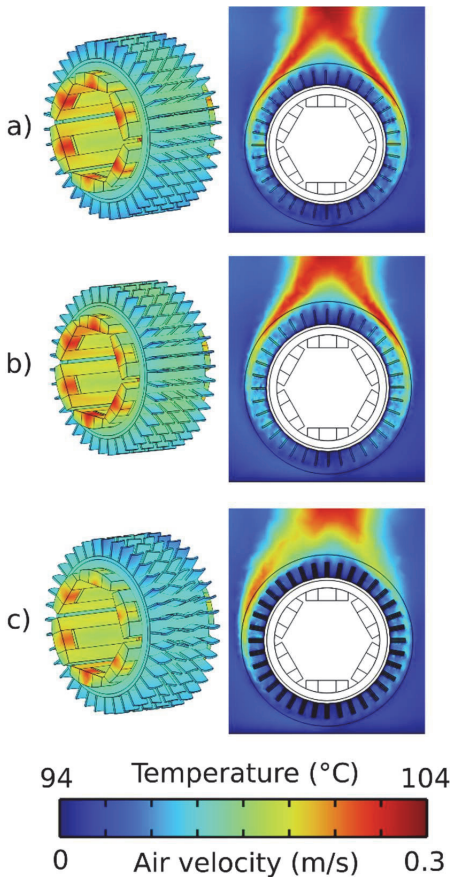


Fig. 4. Resulting temperature distribution and airflow for the longitudinal fin heatsink with a) slits, b) radially curved fins, and c) axially curved

TABLE I. RESULTS FOR THE LONGITUDINAL FIN HEATSINKS

Heatsink type	Winding hot-spot temperature (°C)	Heat transfer coefficient (W/K)	Average convection coefficient (W/m²·K)
Base longitudinal fin	106.7	0.159	4.40
Longitudinal fin with slits	103.4	0.164	5.05
Longitudinal fins with radial curvature	103.3	0.165	5.03
Longitudinal fins with axial curvature	102.2	0.166	5.00

The resulting images show increased airflow inside the heatsink area, which is caused by adding the slits in the fins. The added airflow is significant enough that the performance of the heatsink is substantially higher even though the total active area of the heatsink is reduced. While the radial wave has no effect on performance, the axially waved fins provide a slight improvement, as the curvature increases the fin surface area and helps guide the airflow. The results for the axially waved fins are shown in the case where the phase of

the wave is opposite on the left and right side of the heatsink. This results in a significantly asymmetric airflow path and a roughly 1.5 °C difference in temperature between the sides, suggesting that the phase of the sinusoidal wave has an appreciable effect on cooling performance.

### B. Annular Fin Heatsink

The annular fin heatsink utilizes circular fins around the cylindrical base to increase the cooling surface area without impeding the vertical airflow path created by natural convection. Due to its simple construction and comparatively high performance, it is used in commercially available passively cooled machines. The base case annular fin heatsink is designed based on the method described by Wang et al [14]. By following their analytical model, the annular heatsink was designed with 5 equally spaced circular fins that are each 4 mm thick.

As is the case with the longitudinal fin design, the performance of an annular fin heatsink can be improved with AM by introducing more complex geometries. Mallick et al [15] studied annular hyperbolic fins for reducing the effect of thermal stress and found improvements in thermal transfer with their analytical model. Another general idea of increasing the performance of this type of heatsink is by adding smaller branching fins on the fin tips that increase the active surface area. Both of these design ideas are modelled and the resulting temperature distributions for the annular heatsinks are presented in Fig. 5 and Table II.

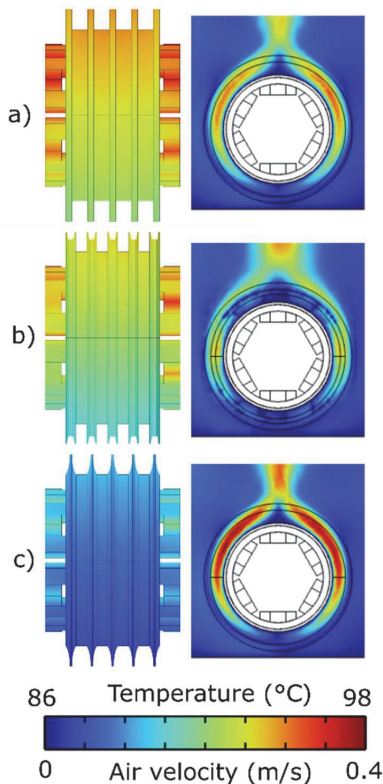


Fig. 5. Characteristic geometry and resulting temperature distribution for the a) base annular fin, b) branched annular fin, and c) hyperbolic annular fin heatsinks.

TABLE II. RESULTS FOR THE ANNULAR FIN HEATSINKS

Heatsink type	Winding hot-spot temperature (°C)	Heat transfer coefficient (W/K)	Average convection coefficient (W/m²·K)
Annular fin	99.0	0.172	5.30
Branched annular fin	97.8	0.174	4.34
Hyperbolic annular fin	94.3	0.180	6.42

The results of the simulation show a significant increase in performance as compared to the longitudinal fin heatsink. Even though the total surface area of the annular fins is lower, the proportion of the area that is in contact with the cooling medium is high, resulting in a large effective surface area. Furthermore, the vertical orientation of the fins ensures high air velocity around the heatsink.

The hyperbolic shaped annular fins offer comparatively the highest cooling performance, as the extra space between the fin tips results in higher air velocity inside the heatsink active area. Additionally, the hyperbolic shape of the fin increases its total surface area by reducing thickness at the end of the fin, where extra material is not needed due to a low heat flux. The branched fins, however, failed to create significant secondary airflow in the branch structure due to the comparatively small size of the geometry, resulting in similar performance to the base case. The results of the annular fin heatsinks confirm the basic design ideology of passive heatsinks, where increasing surface area at the cost of flow resistance is generally detrimental.

### C. Pin-Fin Heatsinks

Conventional pin-fin heatsinks utilize a large number of circular pins that are evenly placed on the heatsink base. This method achieves a very low flow resistance throughout the heatsink structure and therefore generally provides excellent performance with natural convection. The base pin-fin heatsink presented in this paper incorporates a total of 150 circular pins with a diameter of 3 mm that are mounted on the base plate as a 3 by 30 in-line array. These parameters are found by taking the annular fin heatsink geometry as a starting point and adjusting based on preliminary simulation results.

A modified version of the pin-fin heatsink is also modelled. Several papers [16], [17] have presented the advantages of using rounded rectangle and airfoil shaped pins in actively cooled heatsink, as this helps decrease the overall pressure drop created by the heatsink. This also applies in the case of natural convection, as the shaped pins help decrease the flow resistance in the direction naturally created by the rising hot air. Furthermore, Park et al [18] have showed that placing the pins as a staggered (in the direction of the airflow) array further increases performance. Therefore, a modified airfoil pin-fin heatsink incorporating both of these improvements is also modelled. The results for the pin-fin heatsinks are presented in Fig. 6 and Table III.



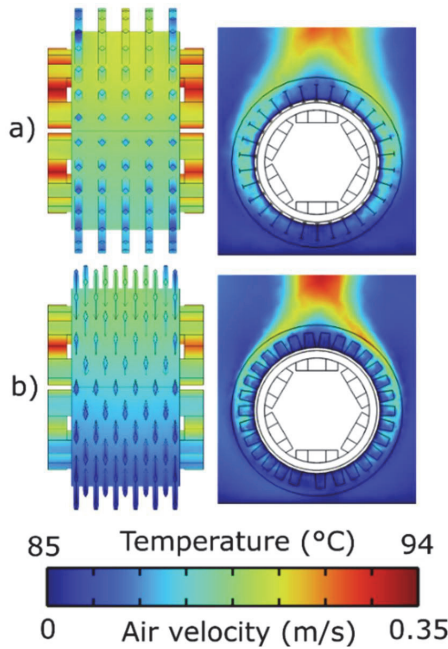


Fig. 6. Resulting temperature and airflow distribution for the a) round and b) airfoil pin-fin heatsinks.

TABLE III. RESULTS FOR THE PIN-FIN HEATSINKS

Heatsink type	Winding hot-spot temperature (°C)	Heat transfer coefficient (W/K)	Average convection coefficient (W/m <sup>2</sup> ·K)
Round pin-fin	94.2	0.180	7.97
Airfoil pin-fin	92.2	0.184	7.21

The pin-fin heatsinks provide extremely good performance due to a combination of low flow resistance and a high effective surface area. While the in-line array of pins creates a high flow in the fin structure, there is little air movement radially between neighboring pins, depriving much of the pin surface area of airflow. This problem is almost completely alleviated by the staggered array, as this allows the entire pin surface to be in contact with the cooling medium. Furthermore, the aerodynamic shape of the pin reduces the overall flow resistance of the heatsink.

#### D. Lattice Structure Heatsinks

Generally, the highest surface areas can be achieved by utilizing lattice structures. These are mesh-like structures comprising of periodic unit cells that are widely used in the AM space. By manipulating the density of the mesh, one can design a heatsink with an arbitrarily high surface area, although the increased air resistance of such structures normally results in significantly reduced performance even with active cooling. In this paper, two types of 3D lattice structures were used: a simple-cubic truss, and simple-cubic plate. Both of these structures are based on work done by Dixit et al [19]. The resulting temperature distribution and airflow for the lattice structure heatsinks is presented in Fig. 7 and Table IV.

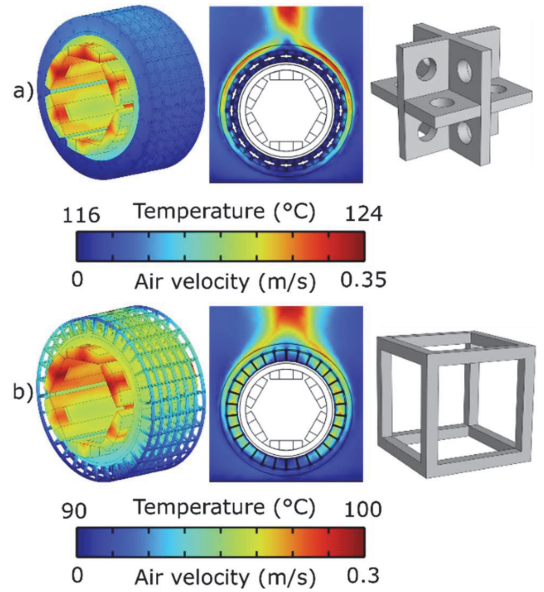


Fig. 7. Resulting temperature and airflow distribution as well as the characteristic geometry for the a) simple-cubic plate, and b) simple-cubic truss lattice structure heatsinks.

TABLE IV. RESULTS FOR THE LATTICE STRUCTURE HEATSINKS

Heatsink type	Winding hot-spot temperature (°C)	Heat transfer coefficient (W/K)	Average convection coefficient (W/m <sup>2</sup> ·K)
Simple-cubic plate	123.8	0.137	1.70
Simple-cubic truss	100.2	0.169	4.19

The results of simple-cubic plate heatsink show exceptionally poor performance, as the radial plate around the middle of the heatsink blocked almost all airflow, essentially reducing the effective height of the heatsink in half. However, the simple-cubic truss showed cooling performance on-par with the base annular fin heatsink. In a similar fashion to the pin-fin examples, the truss heatsink provides low air resistance and a high effective surface area. Although the added radial trusses decrease performance when compared to the pin-fin heatsink, these substantially increase the mechanical strength of the device, which is a common tradeoff with lattice structure heatsinks.

#### E. Discussion

Finally, the performance of the different heatsink designs is compared. The simulated heat transfer coefficients of the heatsinks in Fig. 9 are plotted in an ascending order, with a larger value signifying a higher performing device. Overall, the presented simulation results successfully demonstrate the advantages of non-conventional passive coolers for electrical machines. Compared to the widely used and commercially available longitudinal fins, the airfoil shaped pins are able to reduce the hot-spot temperature of the AM SRM by 14.5 °C, which is a 16% gain in the thermal performance.

When analyzing the different passive heatsink designs modelled in this paper, it becomes evident that optimizing for buoyancy driven flow is primarily a question of maximizing

airflow. While the design freedom offered by additive manufacturing makes it tempting to create intricately structured heatsinks with extremely high surface areas, the sensible approach seems to be focusing on optimizing the geometries for maximal airflow and ensuring that the full surface of the heatsink is in contact with the fast-moving cooling medium.

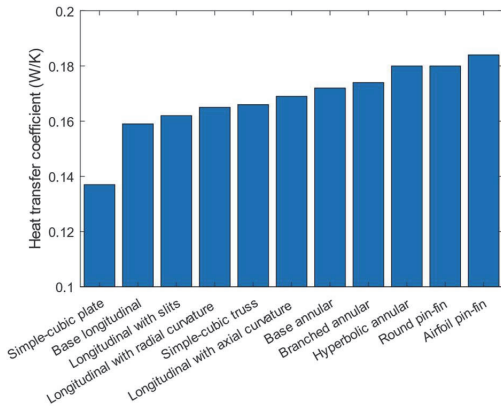


Fig. 9. Comparison of the heat transfer coefficients for all the heatsink designs.

With the possible exception for the lattice-structure based designs, the heatsinks proposed in this paper can be manufactured using conventional methods. However, the results for the initial designs presented in this paper show that adding design complexity can increase thermal performance, suggesting that further optimized designs would only be manufacturable using AM methods. Furthermore, AM enables the creation of highly customized heatsinks that are optimized for specific applications and have significantly shorter development times, therefore leading to higher performing devices in practice.

#### IV. CONCLUSION

This paper investigated the performance of different passive heatsinks for an additively manufactured switched reluctance motor through numerical modelling. Results were gathered for several different heatsinks that incorporate advanced design elements, which can benefit from the unique opportunities and design freedom offered by metal AM. The results of the simulations showed clear advantages for complex geometries, therefore demonstrating the benefits of AM for cooling electrical machines. The most promising design ideas will be pursued more thoroughly in future works and the heatsinks will be further optimized and additively manufactured using selective laser melting to validate the models using real-world measurements.

#### REFERENCES

- [1] M. U. Naseer, A. Kallaste, B. Asad, T. Vaimann, and A. Rassölkin, "A Review on Additive Manufacturing Possibilities for Electrical Machines," *Energies* 2021, Vol. 14, Page 1940, vol. 14, no. 7, p. 1940, Mar. 2021, doi: 10.3390/EN14071940.
- [2] H. Tiismus, A. Kallaste, T. Vaimann, and A. Rassölkin, "State of the art of additively manufactured electromagnetic materials for topology optimized electrical machines," *Addit Manuf*, vol. 55, p. 102778, Jul. 2022, doi: 10.1016/J.ADDMA.2022.102778.
- [3] M. Sarap, A. Kallaste, P. S. Ghahfarokhi, H. Tiismus, and T. Vaimann, "Utilization of Additive Manufacturing in the Thermal Design of Electrical Machines: A Review," *Machines* 2022, Vol. 10, Page 251, vol. 10, no. 4, p. 251, Mar. 2022, doi: 10.3390/MACHINES10040251.
- [4] R. B. W. K. and G. W. Philip Kosky, *Exploring Engineering: An Introduction to Engineering and Design (Fourth Edition) - 978-0-12-801242-0*, vol. 11, no. 6. 2015. Accessed: Jan. 31, 2023. [Online]. Available: <http://www.sciencedirect.com:5070/book/9780124158917/exploring-engineering?via=ihub>
- [5] B. S. Lazarov, O. Sigmund, K. E. Meyer, and J. Alexandersen, "Experimental validation of additively manufactured optimized shapes for passive cooling," *Appl Energy*, vol. 226, pp. 330–339, Sep. 2018, doi: 10.1016/J.APENERGY.2018.05.106.
- [6] A. N. Pilagatti, G. Piscopo, E. Atzeni, L. Iuliano, and A. Salmi, "Design of additively manufactured passive heat sinks for electronics," *J Manuf Process*, vol. 64, pp. 878–888, Apr. 2021, doi: 10.1016/J.JMAPRO.2021.01.035.
- [7] W. W. Wits, D. Jafari, Y. Jeggels, S. van de Velde, D. Jeggels, and N. Engelberts, "Freeform-Optimized Shapes for Natural-Convection Cooling," *THERMINIC 2018 - 24th International Workshop on Thermal Investigations of ICs and Systems, Proceedings*, Dec. 2018, doi: 10.1109/THERMINIC.2018.8593305.
- [8] H. Tiismus *et al.*, "Laser Additively Manufactured Magnetic Core Design and Process for Electrical Machine Applications," *Energies* 2022, Vol. 15, Page 3665, vol. 15, no. 10, p. 3665, May 2022, doi: 10.3390/EN15103665.
- [9] N. T. Aboulkhair, M. Simonelli, L. Parry, I. Ashcroft, C. Tuck, and R. Hague, "3D printing of Aluminium alloys: Additive Manufacturing of Aluminium alloys using selective laser melting," *Prog Mater Sci*, vol. 106, p. 100578, Dec. 2019, doi: 10.1016/J.PMATSCI.2019.100578.
- [10] M. Sarap, A. Kallaste, P. S. Ghahfarokhi, H. Tiismus, and T. Vaimann, "The Effect of Build Direction on the Thermal Conductivity of Additively Manufactured AlSi10Mg and Silicon-steel Samples," *2022 International Conference on Electrical Machines, ICEM 2022*, pp. 538–543, 2022, doi: 10.1109/ICEM51905.2022.9910944.
- [11] J. E. Cousineau, K. Bennion, D. DeVoto, and S. Narumanchi, "Experimental characterization and modeling of thermal resistance of electric machine lamination stacks," *Int J Heat Mass Transf*, vol. 129, pp. 152–159, Feb. 2019, doi: 10.1016/J.IJHEATMASSTRANSFER.2018.09.051.
- [12] D. Staton, A. Boglietti, and A. Cavagnino, "Solving the More Difficult Aspects of Electric Motor Thermal Analysis in Small and Medium Size Industrial Induction Motors," *IEEE TRANSACTIONS ON ENERGY CONVERSION*, vol. 20, no. 3, 2005, doi: 10.1109/TEC.2005.8477979.
- [13] H. J. Kim, B. H. An, J. Park, and D. K. Kim, "Experimental study on natural convection heat transfer from horizontal cylinders with longitudinal plate fins," *Journal of Mechanical Science and Technology*, vol. 27, no. 2, pp. 593–599, Feb. 2013, doi: 10.1007/S12206-012-1236-3/METRCS.
- [14] C.-S. Wang, M. Yovanovich, and J. R. Culham, "General Model for Natural Convection: Application to Annular-Fin Heat Sinks," in *ASME National Heat Transfer Conference*, 1997, pp. 119–128.
- [15] A. Mallick, R. Ranjan, and P. K. Sarkar, "Effect of heat transfer on thermal stresses in an annular hyperbolic fin: an approximate analytical solution," *Journal of Theoretical and Applied Mechanics*, vol. 54, no. 2, pp. 437–448, Apr. 2016, doi: 10.15632/JTAM-PL.54.2.437.
- [16] K. K. Wong, J. Y. Ho, K. C. Leong, and T. N. Wong, "Fabrication of heat sinks by Selective Laser Melting for convective heat transfer applications," <https://doi.org/10.1080/17452759.2016.1211849>, vol. 11, no. 3, pp. 159–165, Jul. 2016, doi: 10.1080/17452759.2016.1211849.
- [17] G. S. Sodhi, C. Botting, E. Lau, M. Palanisamy, M. Rouhani, and M. Bahrami, "Hybrid heat sinks for thermal management of passively cooled battery chargers," *Int J Energy Res*, vol. 45, no. 4, pp. 6333–6349, Mar. 2021, doi: 10.1002/ER.6260.
- [18] S. J. Park, D. Jang, S. J. Yook, and K. S. Lee, "Optimization of a staggered pin-fin for a radial heat sink under free convection," *Int J Heat Mass Transf*, vol. 87, pp. 184–188, Aug. 2015, doi: 10.1016/J.IJHEATMASSTRANSFER.2015.03.089.
- [19] T. Dixit, P. Nithiarasu, and S. Kumar, "Numerical evaluation of additively manufactured lattice architectures for heat sink applications," *International Journal of Thermal Sciences*, vol. 159, Jan. 2021, doi: 10.1016/J.IJTHEMALSCI.2020.106607.

**Publication IV**

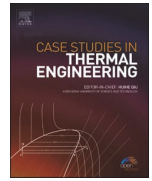
M. Sarap, S. Singh, A. Kallaste, A. Qureshi, H. Tiismus, T. Vaimann, P.S. Ghahfarokhi, Design of an additively manufactured thermal solution for an axial flux switched reluctance motor, Case Stud. Therm. Eng. 66 (2025) 105805. <https://doi.org/10.1016/j.csite.2025.105805>.





Contents lists available at ScienceDirect

## Case Studies in Thermal Engineering

journal homepage: [www.elsevier.com/locate/csite](http://www.elsevier.com/locate/csite)

## Design of an additively manufactured thermal solution for an axial flux switched reluctance motor

Martin Sarap<sup>a,\*</sup>, Shalini Singh<sup>b</sup>, Ants Kallaste<sup>a</sup>, Ahmed Qureshi<sup>b</sup>, Hans Tiismus<sup>a</sup>, Toomas Vaimann<sup>a</sup>, Payam Shams Ghahfarokhi<sup>c</sup><sup>a</sup> Department of Electrical Power Engineering and Mechatronics, Tallinn University of Technology, 19086, Tallinn, Estonia<sup>b</sup> Additive Design and Manufacturing Systems Lab, Department of Mechanical Engineering, Faculty of Engineering, University of Alberta, Edmonton, Canada<sup>c</sup> Electrical Engineering Unit, Tampere University, FI-33014, Tampere, Finland

## ARTICLE INFO

## Keywords:

Additive manufacturing  
Electrical machines  
Thermal solutions  
Switched reluctance motor

## ABSTRACT

This study presents the design and evaluation of an additively manufactured thermal solution for an axial flux switched reluctance motor, aimed at enhancing its applicability in light unmanned aircraft propulsion. The primary objective is to optimize the motor's power-to-weight ratio by improving its thermal management through innovative heatsink designs. The methodology involves a comprehensive design procedure to dimension a conventional finned heatsink. The performance of the heatsink is experimentally tested under practical conditions using a motorette setup and cooling fans. Key findings indicate that the proposed thermal solution can enable very high current densities for an air-cooled electrical machine.

## 1. Introduction

Additive manufacturing (AM) methods, such as laser powder bed fusion (LPBF) are used in the field of electrical machines to manufacture soft-magnetic components with optimized structures [1], conductors with improved electrical [2] and thermal [3] performance, and advanced thermal solutions utilizing novel geometries [4]. A number of researchers are focusing on AM reluctance motors [5,6], as the single-material construction of the rotor lends itself to current LPBF manufacturing capabilities, and a more sustainable machine [7]. However, when compared to permanent magnet motors, the power density of reluctance machines is limited, making high current densities, and therefore increased thermal capabilities necessary for demanding applications such as propulsion [8], where high power density and efficiency are crucial [9].

Among the different topologies available for reluctance motors, the axial-flux configuration is well suited for effective cooling due to the accessibility of the stator conductors, which enables direct cooling of the winding structure. A survey of the literature reveals several solutions based on liquid-cooling, which can support current densities up to 20 A/mm<sup>2</sup> [10,11] with indirect cooling and over 100 A/mm<sup>2</sup> with direct conductor cooling [12]. Air-cooling based solutions, which can be preferable in propulsion applications, are somewhat less common in literature [13–15]. Relevant to this paper is the work of Berndt et al. [16], who achieved a current density of >10 A/mm<sup>2</sup> with the use of an integrated rotor fan and cooling channels in the stator, and the work of Mohamed et al. [17], who introduced a laminated aluminum housing around the windings and showed that a current density of >14 A/mm<sup>2</sup> is possible. Still,

\* Corresponding author.

E-mail address: [martin.sarap1@taltech.ee](mailto:martin.sarap1@taltech.ee) (M. Sarap).<https://doi.org/10.1016/j.csite.2025.105805>

Received 19 November 2024; Received in revised form 8 January 2025; Accepted 18 January 2025

Available online 20 January 2025

2214-157X/© 2025 The Authors. Published by Elsevier Ltd. This is an open access article under the CC BY license (<http://creativecommons.org/licenses/by/4.0/>).



## Nomenclature

### Latin symbols

$A_{base}$	heatsink base surface area [m <sup>2</sup> ]
$A_{Cu}$	conductor surface area [m <sup>2</sup> ]
$A_{fin}$	total surface area of a heatsink fin [m <sup>2</sup> ]
$b$	heatsink fin spacing [m]
$B_{ag}$	average airgap flux density [T]
$c_p$	specific heat of air [J/g K]
$D_i$	stator iron inner diameter [m]
$D_o$	stator iron outer diameter [m]
$D_h$	fin channel hydraulic diameter [m]
$f$	friction factor
$f_{app}$	apparent friction factor
$f_{el}$	electrical frequency [Hz]
$h_{conv}$	convection coefficient [W/(m <sup>2</sup> •K)]
$H_{HS}$	height of the heatsink [m]
$I$	current in a single stator coil [A]
$j_{max}$	maximum current density [A/mm <sup>2</sup> ]
$k_a$	flow channel aspect ratio
$k_{SRM}$	motor design constant
$k_j$	current density constant [A/(mm <sup>2</sup> •kg)]
$L_{fan}$	fan blade length [m]
$L_{HS}$	heatsink active length [m]
$m$	fin coefficient
$M_{\Sigma}$	total mass of the motor [kg]
$n$	rotational speed [rpm]
$N_{Cu}$	number of winding layers
$N_{fin}$	number of fins in the heatsink
$N_u$	Nusselt number
$P_{Cu}$	copper losses in a stator segment [W]
$P_{Fe}$	iron losses in a stator segment [W]
$P_{out}$	motor output power [W]
$P_r$	Prandtl number
$P_{\Sigma}$	total losses in a stator segment [W]
$\Delta P$	pressure increase [Pa]
$\Delta P_{fan}$	pressure increase at a chosen operating point [Pa]
$\Delta P_{HS}$	pressure drop in the heatsink for a given flow [Pa]
$Q$	airflow created by the fan [m <sup>3</sup> /h]
$Q_{fan}$	airflow at a fan operating point [m <sup>3</sup> /h]
$r_{Cu}$	winding resistance [ $\Omega$ ]
$Re$	Reynolds number
$Re^*$	modified Reynolds number
$R_{HS}$	thermal resistance of the heatsink sector [K/W]
$R_0$	internal thermal resistance of the frame sector [K/W]
$R_{\Sigma}$	total thermal resistance of a single sector of the cooling solution [K/W]
$S_F$	imaginary surface differentiating the frame and the heatsink
$t_{fin}$	thickness of a single fin [m]
$T_{amb}$	ambient temperature [°C]
$T_{Cu}$	winding hotspot temperature [°C]
$T_{SF}$	average temperature of the $S_F$ surface [°C]
$T'_{SF}$	measured temperature of the $S_F$ surface
$\Delta T_{Cu}$	measured temperature increase of the winding hotspot [°C]
$\Delta T'_{SF}$	measured temperature increase of the $S_F$ surface [°C]
$v$	air velocity in the heatsink [m/s]
$w_{air}$	equivalent airgap thickness [m]

### Greek symbols

$\sigma$	ratio of the flow channel area compared to the full area of the heatsink
----------	--

$\eta_{fin}$	fin efficiency
$\lambda_{air}$	thermal conductivity of air [W/(m•K)]
$\lambda_{Al}$	thermal conductivity of AlSi10Mg [W/(m•K)]
$\mu$	dynamic viscosity of air [kg/(m•s)]
$\rho_{air}$	density of air [kg/m <sup>3</sup> ]

further increases in current density, in addition to a reduction in weight, are necessary to increase the viability of reluctance motors in electric propulsion.

This article presents a novel additively manufactured cooling solution for a dual rotor yokeless axial flux switched reluctance motor (AFSRM), with the goal of enabling the motor to be used in light aircraft propulsion applications. The cooling solution consists of an aluminum alloy frame that surrounds the wound stator segments and provides direct conductor cooling with its integrated heatsink and two cooling fans attached to the rotors. This novel cooling method, uniquely suitable for axial flux machines, enables very high current densities without liquid cooling. A comprehensive design procedure is used for selecting the design and dimensions of the cooling solution to ensure a maximum current density to weight ratio. The performance characteristics of the cooling solution are measured under practical conditions, for which an AM motorette is built for providing the heat load and a pair of cooling fans is used to provide the airflow. The goal of the tests is finding out the thermal resistance of the cooling solution, which is by far the most important thermal parameter when evaluating the maximum current density of an electrical machine in practice.

## 2. Design procedure

### 2.1. Axial flux reluctance motor cooling

Fig. 1 illustrates the 6-slot 4-pole configuration AFSRM with the proposed thermal solution, consisting of a frame and two cooling fans. This motor's intended application is for small aircraft propulsion, which limits the thermal solution to air-cooling and creates a need for maximal power density in terms of weight at an operating speed of up to 6000 rpm. The symmetrical nature of the machine lends itself to using two axial cooling fans in series. At high speeds, the fans can create a large amount of airflow through the heatsink fins, effectively cooling the windings. Both the soft-magnetic and thermal components of the AFSRM are additively manufactured using LPBF; the former from high silicon-steel (Fe<sub>6.5%</sub>Si) and the latter from AlSi10Mg.

The motor utilizes a dual-rotor topology, in which the stator yoke is substituted for a second rotor, eliminating stator yoke losses and simplifying the manufacturing of the stator laminations with LPBF. Structural integrity of the stator is achieved by incorporating an aluminum frame that surrounds the windings, and a 1 mm thick reinforcing plate that supports the stator teeth without putting pressure on the delicate winding structure. As the frame is in direct contact with the winding, it is extended radially to act as a heatsink. The resulting short thermal path from the winding to the heatsink leads to efficient heat extraction, which facilitates high current density capabilities in the coils. Since all other dimensions are conveniently defined by the geometry of the motor, the main design variable is the length of the heatsink fins  $L_{HS}$ .

Experimental results for the performance of the cooling solution are obtained with the use of an additively manufactured 1/6 sector of the cooling solution. This is inserted over an AM high-silicon steel stator tooth prototype. The tooth is surrounded by a conventional winding consisting of 230 turns of 0.2 mm<sup>2</sup> copper wire hand wound on the core in 6 layers, resulting in a fill factor of roughly 64 % and an electrical resistance of 1.20  $\Omega$  for the segment. These components together represent a 1/6 sector of the AFSRM stator assembly. A Pt100 temperature sensor (IEC 1/10 class) is placed on the inner radius of the tooth, between the slot liner and the first layer of the

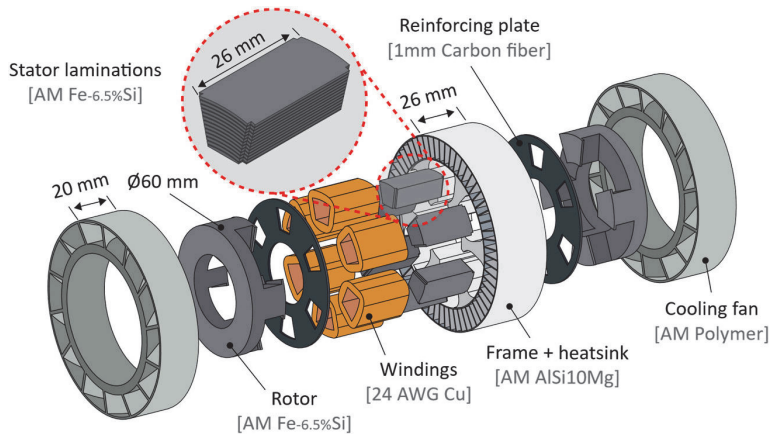


Fig. 1. Exploded view of the main AF-SRM components and the materials used.

winding, in order to measure the temperature  $T_{Cu}$ . This location is thermally most separated from the ambient air, meaning that the reading from this sensor is considered as the winding hotspot temperature. Fig. 2 (a) illustrates a 1/6 sector of the stator, which is used for testing the AM heatsink prototype. The AM high silicon steel stator core prototype with the winding and integrated Pt100 temperature sensor is shown in (b).

The purpose of the thermal solution is to increase the power-to-weight ratio of the motor through increased current density. The maximum mechanical output power of an AFSRM can be given as:

$$P_{out} = k_{SRM} \bullet B_{ag} \bullet j_{max} \bullet A_{Cu} \bullet (D_o^2 - D_i^2) \bullet n \quad (1)$$

It should be noted that in practice, increasing  $j_{max}$  will result in a different optimal geometry for the motor, as the ratio between tooth and winding area is generally dependent on it. However, defining  $P_{out}$  strictly as a function of  $j_{max}$  requires the parametrization of the entire AFSRM design procedure, which is outside the scope of this paper. Instead, it is considered that  $P_{out} \propto j_{max}$  and the output power of the motor is expressed simply through  $j_{max}$ . This allows the proposed thermal solution to be directly compared to other cooling methods, and its potential benefits can be directly considered for other motor types (i.e. permanent magnet axial-flux motors).

## 2.2. Electro-thermal model

A 3D electro-thermal model is built to evaluate the effect of the cooling solution on eddy current losses and estimate the internal thermal resistance of the system. Finding the eddy current losses in the frame involves modelling the entire motor at the nominal electrical frequency of 400 Hz (corresponding to a rotational speed of 6000 rpm for a 6/4 SRM) and an airgap flux density of 1 T. It is found that a solid AlSi10Mg (with an electrical conductivity of  $5.94 \cdot 10^{-8} \Omega \text{ m}$  [18]) frame covering the entire winding results in unacceptably large eddy currents. The concentration of eddy current losses in the solid frame is shown in Fig. 3 (a). This is fixed by adding a gap to its inner radial face, which breaks the contour without sacrificing much thermal contact resulting in acceptable losses, as shown in (b). The frame eddy current losses as a proportion of copper losses at this operating point are plotted in Fig. 4.

On the thermal side, the radial symmetry of the AFSRM and heatsink allows the system to be accurately modelled as a single 1/6 stator segment. Fig. 5 (a) presents a simplified thermal network of the sector and (b) shows a 2D view of the numerical model. Of particular importance is  $S_F$ , which is the imaginary surface separating the frame's internal thermal resistance from the resistance of the heatsink, allowing the total thermal resistance to be modelled as the sum of internal thermal resistance  $R_0$  and the heatsink thermal resistance  $R_{HS}$ .  $R_0$  itself consists of the thermal resistance associated with the winding and the aluminum frame. The average temperature of the  $S_F$  surface  $T_{SF}$  is estimated with the temperature measurement  $T'_{SF}$ .

The total losses associated with a single motor sector  $P_\Sigma$  are a combination of iron losses  $P_{Fe}$  and DC copper losses  $P_{Cu}$ . Based on the available literature [19], the iron losses of AM high-silicon steel laminations at 400 Hz and 1.5 T can be estimated to be around  $\sim 100$  W/kg, resulting in an  $P_{Fe}$  value of 2.24 W in a single stator segment. This is significantly lower than the estimated  $P_{Cu}$ , meaning that the effects of  $P_{Fe}$  on the temperature distribution are negligible and a DC measurement is sufficient to analyze the performance of the physical prototype.  $P_{Cu}$  is calculated by using the RMS current in the coil and the electrical resistance of the coil. The latter is calculated separately for each coil layer  $N_{Cu}$  according to its modelled average temperature at a given  $T_{Cu}$  value.

$$P_{Cu} = \sum_{i=1}^{N_{Cu}} I^2 \frac{r_{Cu}(T)}{N_{Cu}} \quad (2)$$

Anisotropy in the winding structure is achieved by adding contact resistances between the winding and frame boundaries. Physically, this is caused by a combination of insulating material and air inside the winding structure, although it can be modelled as an equivalent layer of air with a thickness  $w_{air}$ . Adding contact resistances between the relevant surfaces will result in a substantial temperature difference between the hotspot and the  $S_F$  surface, defining the internal thermal resistance of the sector  $R_0$ . The

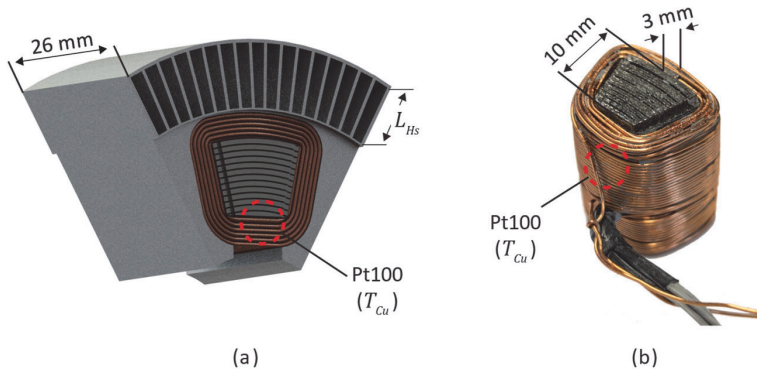


Fig. 2. Model of a single stator sector with the aluminum alloy frame and heatsink (a), and the physical prototype of a single high silicon steel wound stator core segment (b).

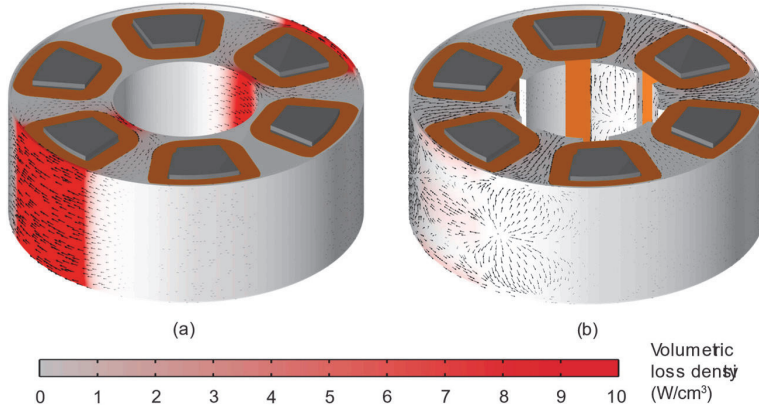


Fig. 3. Eddy current distribution and loss density in the (a) solid and (b) gapped AlSi10Mg frames.

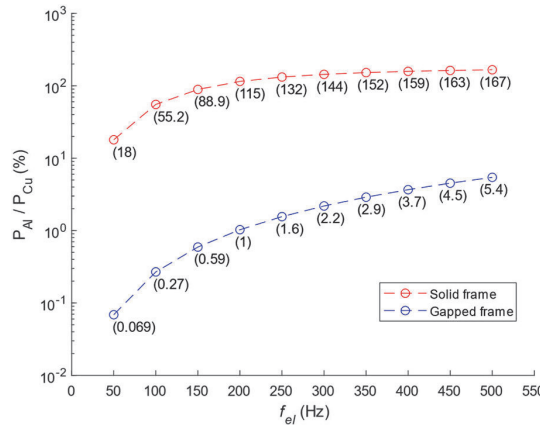


Fig. 4. Total eddy current losses as a percentage of copper losses in the frames at different electrical frequencies at an airgap flux density of 1 T and a rotor angle of 0°.

relationship between  $w_{air}$  and  $R_0$  is shown in Fig. 6 (a) where the linear increase demonstrates that the thermal resistance of the solid conductive materials is a negligible part of  $R_0$ .

The total thermal resistance of the cooling solution  $R_\Sigma$  is the sum of  $R_0$  and the thermal resistance of the heatsink  $R_{Hs}$ . It is expressed as the temperature difference between the hotspot and ambient at a given total heat load.

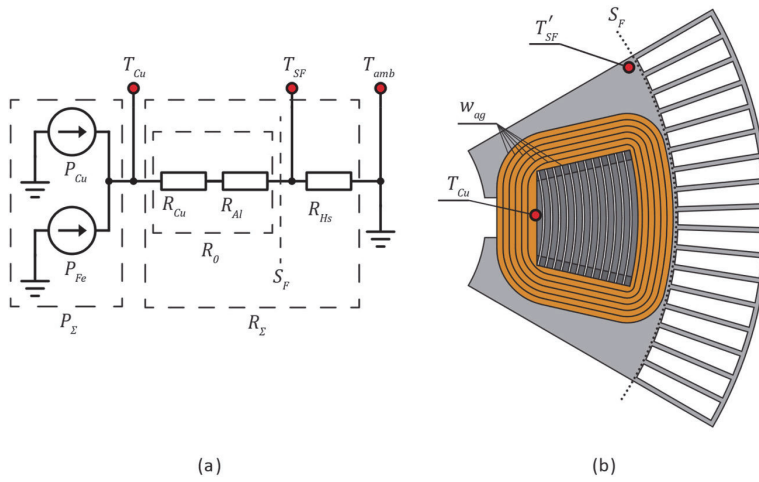
$$R_\Sigma = \frac{T_{Cu} - T_{amb}}{P_\Sigma} \quad (3)$$

Each of the elements in eq. (3) can be measured accurately and consistently over multiple measurements, therefore resulting in an accurate value for  $R_\Sigma$ . However, to analyze the performance closer, it is necessary to know the value of  $R_{Hs}$  separately, which is defined by the temperature difference between the  $S_F$  surface and ambient.

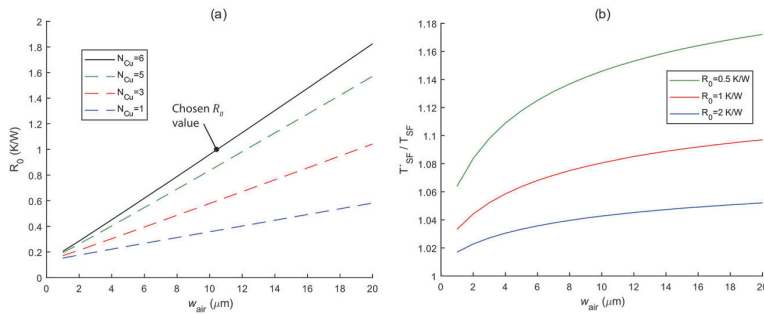
$$R_{Hs} = R_\Sigma - R_0 = \frac{T_{SF} - T_{amb}}{P_\Sigma} \quad (4)$$

$R_{Hs}$  (along with  $R_0$ ) can only be calculated by knowing  $T_{SF}$ , as then the frame can be effectively modelled as a single thermal resistance with  $P_\Sigma$  passing it. Therefore, a temperature sensor  $T'_{SF}$  is placed near  $S_F$  with the goal of estimating  $T_{SF}$ . The effectiveness of using  $T'_{SF}$  to estimate  $T_{SF}$  can be evaluated by modelling the ratio  $T'_{SF}/T_{SF}$  at different  $w_{air}$  and  $R_{Hs}$  values (as both  $R_0$  and  $R_{Hs}$  vary between individual tests,  $T'_{SF}/T_{SF}$  needs to be insensitive to these changes). This is presented across a range of  $w_{air}$  and  $R_{Hs}$  in Fig. 5 b), showing that the sensor reading  $T'_{SF}$  can be used to estimate  $T_{SF}$ .

As a specific value for  $R_0$  is necessary for determining the optimal value for  $L_{Hs}$ , a value for  $w_{air}$  needs to be chosen. For a non-conventional solution, such as the one introduced in this paper, it is difficult to find a reference value in literature, meaning that



**Fig. 5.** Thermal models of a single stator sector. (a) Simplified LPTN model; (b) 2D view of the numerical model. The locations of the temperature sensors are shown in red.

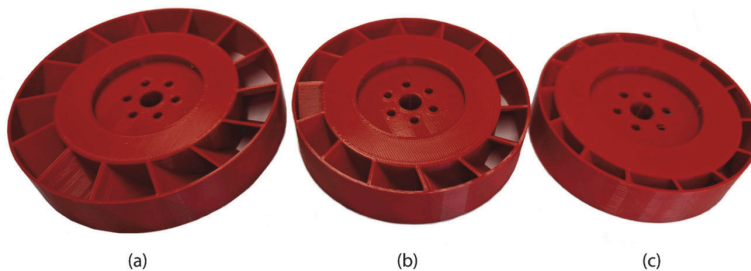


**Fig. 6.** Effect of the equivalent airgap thickness  $w_{air}$  on the (a) internal thermal resistance and (b) accuracy of the  $T'_{SF}$  measurement. Different winding layer counts are shown to illustrate its effect on  $R_0$ .

the chosen value must be based on previous experience with similar solutions. Therefore, a value of  $w_{air} \approx 10 \mu m$  is used, which results in a modelled internal resistance of  $R_0 = 1 \text{ K/W}$ .

### 2.3. Cooling fans

Airflow through the heatsink is created by a pair of axial fans connected to the rotors of the machine. The length of the blades matches the heatsink ( $L_{fan} = L_{Hs}$ ) and a simple geometry is used, as initial prototypes showed that as long as the outer dimensions are



**Fig. 7.** Fan prototypes at (a)  $L_{Hs} = 15 \text{ mm}$ , (b)  $L_{Hs} = 10 \text{ mm}$  and (c)  $L_{Hs} = 5 \text{ mm}$ .

fixed, the specific fan geometry has negligible effects on its performance curve. The height of the fan is equal to the total height of the rotor and the number of blades of 14 is chosen based on initial testing. Physical prototypes at the values of  $L_{Hs} = (5, 10, 15)$  mm shown in Fig. 7 are additively manufactured from PLA and tested at a range of rotational speeds. The intermediate solutions, which are used to select the optimal  $L_{Hs}$  value, are interpolated with a 0.1 mm step.

The aerodynamic performance is measured with a conventional flow bench at the two extremes; maximum static pressure in the case of  $Q = 0$ , and free flow in the case of  $\Delta P = 0$ . The curves are assumed to be linear. The resulting curves at the rated operating speed of 6000 rpm together with the interpolated values are presented in Fig. 8. The performance of the fans can be extrapolated to any rotational speed based on the fan affinity laws, where  $Q \propto n$  and  $\Delta P \propto n^2$ .

## 2.4. Analytical model

The analytical model is used to find the optimal value of  $L_{Hs}$  at a given  $n$  by calculating the  $R_{Hs}$  for conventional finned heatsinks with various  $L_{Hs}$  values using the design procedure described in Refs. [20,21]. Naturally, the maximum allowable current density in the windings can be increased up to a value limited by  $R_0$  by using an arbitrarily large heatsink (i.e.  $L_{Hs} > D_0$ ). This, however, disproportionately adds to the total weight of the motor  $M_\Sigma$ , reducing specific power. Therefore, a current density factor  $k_j$  is used to determine an optimal  $L_{Hs}$ :

$$k_j = \frac{j_{max}}{M_\Sigma} \quad (5)$$

Finding the  $L_{Hs}$  corresponding to the highest  $k_j$  includes finding the optimal  $n_{fan}$  and the corresponding  $\Delta P_{fan}$  and  $Q_{fan}$  for each case, which then define  $R_{Hs}$ . Based on this, the value of  $j_{max}$  is found according to the maximum allowed hotspot temperature and  $k_j$  can be calculated, considering the total mass of the motor in each case. The design procedure considers a straight heatsink with a single bottom plate as shown in Fig. 9 (a), although the resulting dimensions are used to produce a curved model with an additional top surface reinforcing the fins (b).

The analytical models begins by calculating the pressure drop of the heatsink  $\Delta P_{Hs}$ , which is equal to the pressure increase of the fan pair at a given working point:

$$2 \bullet \Delta P_{fan} = \Delta P_{Hs} = \left( 0.42 \bullet (1 - \sigma^2) + 4 \bullet f_{app} \bullet \frac{H_{Hs}}{D_h} + (1 - \sigma^2)^2 \right) \bullet \rho_{air} \frac{v^2}{2} \quad (6)$$

where  $D_h = 2 \bullet b$  is the approximate hydraulic diameter of the flow channel defined as two times the gap between the fins, and  $v$  is the average velocity of the flow through the channels, calculated by dividing the flow rate at the operating point  $Q_{fan}$  by the total area of the flow channels.

The apparent friction factor of the flow  $f_{app}$  depends on the friction factor  $f$  and Reynolds number  $Re$ :

$$f_{app} = \left( \left( \frac{3.44}{\sqrt{\frac{L_{Hs}}{D_h \bullet Re}}} \right)^2 + (f \bullet Re)^2 \right)^{\frac{1}{2}} \bullet Re^{-1} \quad (7)$$

$Re$  is calculated using the dynamic viscosity of air  $\mu$ :

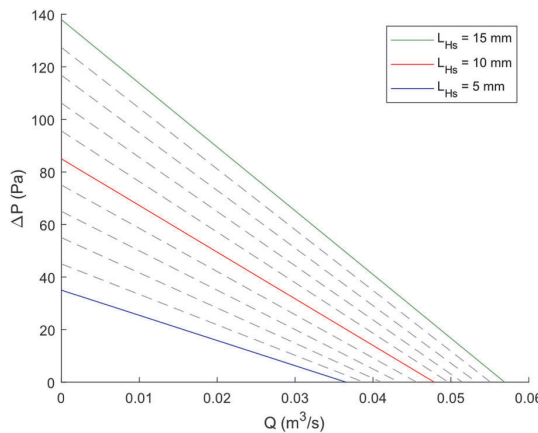


Fig. 8. Resulting linearized fan curves together with the interpolated values at 1 mm steps.



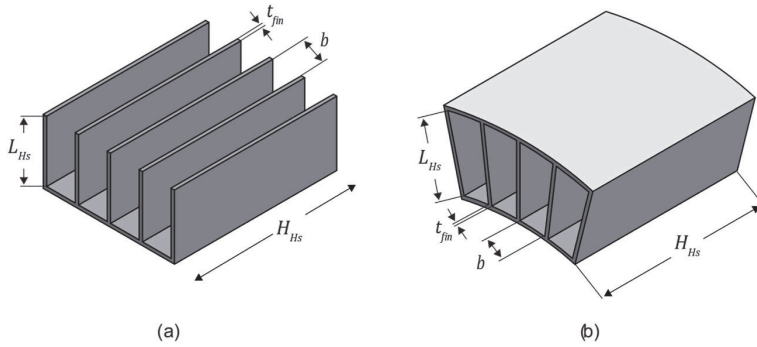


Fig. 9. The heatsink geometry considered in the analytical model a) and the curved shape of the heatsink used in the proposed cooling solution b).

$$R_e = \frac{\rho_{air} \cdot v \cdot D_h}{\mu} \quad (8)$$

and the friction factor is a function containing the flow channel's aspect ratio  $k_a = D_h / (2 \cdot L_{Hs})$  and  $R_e$ :

$$f = (24 - 32.527 \cdot k_a + 46.721 \cdot k_a^2 - 40.829 \cdot k_a^3 + 22.954 \cdot k_a^4 - 6.089 \cdot k_a^5) / R_e \quad (9)$$

The geometry of the flow channels and the pressure drop created by the heatsink for a given  $Q_{fin}$  is determined by the number of fins  $N_{fin}$ . Therefore, each possible value of  $N_{fin}$  is matched with an operating point of the cooling fan pair, and the best performing case is chosen for each  $L_{Hs}$  value. The thickness of the heatsink fin is fixed at  $t_{fin} = 0.5$  mm to ensure it is manufacturable with AM. The thermal resistance of a 1/6 sector of the heatsink  $R_{Hs}$  is calculated:

$$R_{Hs} = \frac{6}{h_{conv} \cdot (A_{base} + N_{fin} \cdot \eta_{fin} \cdot A_{fin})} \quad (10)$$

The average convection coefficient acting on the fin surface calculated by using the Nusselt number and the thermal conductivity of air:

$$h_{conv} = \frac{N_u \cdot \lambda_{air}}{b} \quad (11)$$

$N_u$  is calculated using a modified Reynolds number  $R_e^*$  and the Prandtl number  $P_r$ :

$$N_u = \left( \left( \frac{R_e \cdot P_r}{2} \right)^{-3} + \left( 0.664 \sqrt{R_e} \cdot P_r^{1/3} \sqrt{1 + \frac{3.65}{\sqrt{R_e}}} \right)^{-3} \right)^{-1/3} \quad (12)$$

where  $R_e^* = \rho_{air} \cdot v \cdot b^2 / (\mu \cdot L)$  and  $P_r$  is defined by fluid:

$$P_r = \frac{\mu \cdot c_p}{\lambda_{air}} \quad (13)$$

The efficiency of the fin is calculated using the coefficient  $m = \sqrt{2 \cdot h_{conv} / (\lambda_{Al} \cdot t_{fin})}$ , which includes the thermal conductivity of the solid material.

$$\eta_{fin} = \frac{\tanh(m \cdot L_{Hs})}{m \cdot L_{Hs}} \quad (14)$$

The maximum heat load in the sector for a given hotspot temperature rise  $\Delta T_{Cu}$  can be calculated by adding together the internal thermal resistance of the frame and the resistance of the heatsink:

$$P_\Sigma = \frac{\Delta T_{Cu}}{R_0 + R_{Hs}} \quad (15)$$

The maximum current density of the windings is found through Joule's law by subtracting the iron losses from the maximum heat load and dividing by the conductor surface area:

$$j_{max} = \frac{\sqrt{(P_\Sigma - P_{fe}) / r_{Cu}}}{A_{turn}} \quad (16)$$

It is considered that the electric resistance of the coil  $r_{Cu}$  depends on the average temperature of the winding layers, which is found at the defined hotspot temperature using the numerical thermal model. The volume of the heatsink is used to calculate its mass based on the density of the solid material, which in the case of AlSi10Mg is  $2.58 \text{ g/cm}^3$  [22]. The mass of the heatsink and frame can be added to the electromagnetic mass to calculate the total mass of the motor for each case of  $L_{Hs}$ . The current density factor can then be calculated using the following equation:

$$k_j = \frac{j_{max}(L_{Hs})}{M_{\Sigma}(L_{Hs})} \quad (17)$$

Limiting the hotspot temperature to  $100^\circ\text{C}$  and running the model in the range of  $L_{Hs} = 5 \dots 15 \text{ mm}$  results in the  $k_j$  values for each configuration presented in Fig. 10. At a rotating speed of 6000 rpm, the highest value of  $33.1 \text{ A/(mm}^2 \cdot \text{kg)}$  is achieved in the case of  $L_{Hs} = 9.0 \text{ mm}$ . In this case, the calculated values for  $j_{max}$  and  $M_{\Sigma}$  are  $26.8 \text{ A/mm}^2$  and  $0.83 \text{ kg}$  respectively, and the operating point of the fan pair is defined as  $\Delta P_{fan} = 114.7 \text{ Pa}$  and  $Q_{fan} = 41.0 \text{ m}^3/\text{h}$ . The resulting heatsink consists of 198 fins and the calculated total thermal resistance of the 1/6 sector is  $R_{Hs} = 1.8 \text{ K/W}$  ( $R_0 = 1 \text{ K/W}$  is taken from the thermal model).

### 3. Experimental setup

#### 3.1. Additively manufactured heatsink sample

The heatsink sector prototype is manufactured for the aluminum alloy AlSi10Mg on the Coherent Creator SLM device. After manufacturing, the sample was heat-treated at  $300^\circ\text{C}$  for 2 h to increase the thermal conductivity of the material and remove any anisotropy left from the manufacturing process [23]. The physical prototype is shown in Fig. 11.

The physical prototype is dimensionally accurate and does not display any manufacturing faults. The geometry of the frame is dimensioned for the specific shape of the stator winding, displaying the advantages of AM in personalized design. Matching the shape of the frame to the winding is crucial for ensuring a minimal  $R_0$ . This is lowered further by polishing the internal surface and applying thermal paste.

#### 3.2. Performance measurements

The temperatures  $T_{Cu}$ ,  $T_{SF}$  and  $T_{amb}$  are measured in a practical setup, where the entire airflow is provided by the cooling fan pair. The measurements are performed at a range of rotational speeds of 3000–6000 rpm, with an appropriate current used for each test, such that a hotspot temperature close to the defined operating point of  $100^\circ\text{C}$  is achieved. The heatsink is measured three times with the tooth being removed from the frame each time. This is done to ensure more accurate results and to demonstrate the validity of the  $T_{SF}$  measurement (the calculated  $R_{Hs}$  of each run should be close to identical, even though  $R_0$  and  $R_{\Sigma}$  are varying).

During the measurement process, the rotational speed of the fans is controlled by an external motor (with a sensor for accurate speed control), while the stator is excited with a DC current at a steady value to produce the heat load, which is calculated simply as the product of the measured current and voltage drop across the coil. The use of DC instead of AC has a negligible effect on the thermal performance, as at any non-trivial current density  $P_{Cu} \gg P_{Fe}$ . The test setup is presented in Fig. 12.

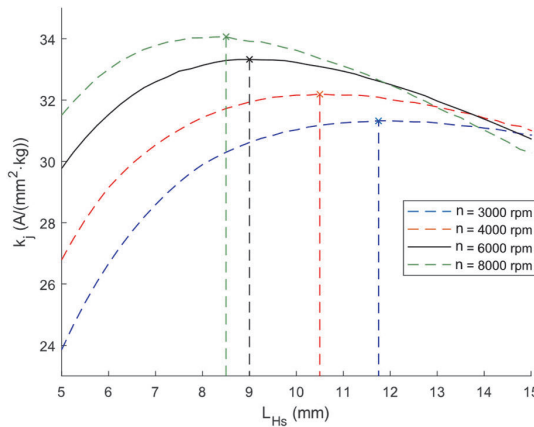


Fig. 10. Calculated  $k_j$  at different  $L_{Hs}$  and  $n$  values.



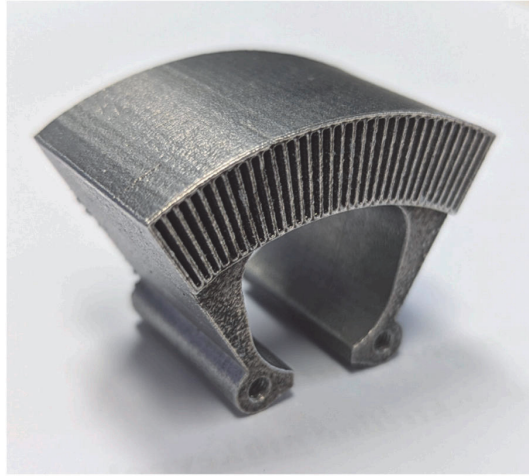


Fig. 11. Physical prototype of the heatsink sector manufactured from AlSi10Mg with LPBF.

## 4. Results and discussion

### 4.1. Verification of the frame average temperature measurement

The prototype was used to conduct three initial tests, where the contact was significantly altered by varying the thermal paste application, as this is a convenient way to control  $R_0$ . The cases high  $R_0$ , average  $R_0$  and low  $R_0$  correspond to no thermal paste being used, insufficient thermal paste and sufficient thermal paste respectively. In Fig. 13, the measured temperature increases  $\Delta T_{Cu}$  and  $\Delta T_{SF}$  values for each case are plotted across the rotational speed range at a constant heat load of  $P_{Cu} = 15$  W.

Expectedly, each case resulted in a significantly different  $\Delta T_{Cu}$ , showing the effect of  $R_0$  on the total cooling performance. However, the temperature increase of the aluminum frame (which is defined only by  $R_{HS}$ ) is essentially constant across the runs, demonstrating that the approximate measurement of the average temperature of the frame is valid in a wide range.

### 4.2. Heatsink thermal resistances

The subsequent measurements are similarly performed in three independent runs, although this time good thermal contact is ensured for each run to minimize variation in  $R_0$ , which was in the range of 1.15–1.26 K/W with an average value of 1.19 K/W, corresponding to a 12  $\mu$ m equivalent airgap thermal resistance. This is close to the estimated value of 1 K/W used in the analytical model, meaning that the optimized  $L_{HS}$  value can be considered valid. The  $R_{HS}$  values presented in Fig. 14 are taken as the average of the three runs and fitted to a logarithmic curve. The analytically calculated  $R_{HS}$  at each  $n$ , which is based on the measured fan performance curve, is added for comparison purposes.

The measured average curve matches the shape and approximate value of the analytical model, with the measured  $R_{HS}$  decreasing from a maximum value of 1.52 K/W at 3000 rpm to a minimum of 0.85 K/W at 6000 rpm. A small difference between the analytical and experimental results is expected due to the curved geometry with an added outer surface used in the physical model. Some differences also arrive from the non-ideal airflow in the practical case, as some of it is lost from the airgap in the radial direction. Interestingly, adding a flow guide to block the radial leakage path during testing slightly decreases the performance of the heatsink.

The measured thermal resistance can be used to calculate the maximum allowable steady state current density for the cooling solution (Fig. 15) with the added heat load of the iron losses ( $P_{Fe} \propto f^2$  and  $P_{Fe400Hz} = 2.24$  W) and a defined hotspot temperature of  $T_{max} = 100$  °C. The average measured contact resistance value of  $R_0 = 1.19$  K/W is added to the previously graphed  $R_{HS}$  values to find  $R_{\Sigma}$ , which is used to calculate  $j_{max}$  based on eq. (16). The temperature-based electrical resistance of the coil is calculated using the numerical model.

Across the measured rotational speeds of 3000–6000 rpm,  $R_{\Sigma}$  is in the range of 2.71 to 2.04 K/W, which limits the maximum heat load to 30.0 and 37.0 W respectively. After subtracting  $P_{Fe}$ , the maximum calculated current density is in the range of 22.3–25.2 A/mm<sup>2</sup>.

The maximum current density of >25 A/mm<sup>2</sup> achieved in this work is a value that is generally reserved for liquid-cooled machines [24] or novel unconventional winding structures [25], which are often limited to a low amount of turns. Achieving it with conventional windings composed of 230 turns, and forced-air cooling is mainly a consequence of the structure of the axial flux machine, which inherently makes it possible to cool the conductors directly, substantially reducing  $R_0$ . This is opposed to conventional air-cooled radial motors, which are characterized by a relatively large  $R_0$ , making the role of the heatsink less important. The AFSRM described in this paper includes approximately equal  $R_0$  and  $R_{HS}$  values, meaning that minimizing  $R_{HS}$  is important. The yokeless axial

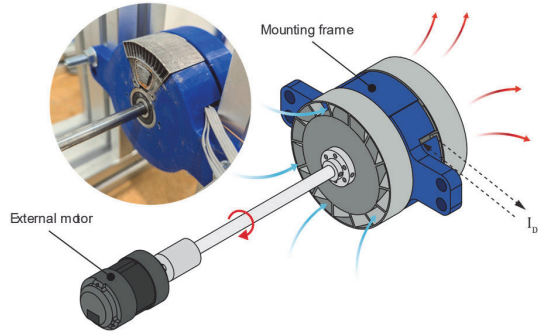


Fig. 12. Experimental measurement setup for the heatsink sector.

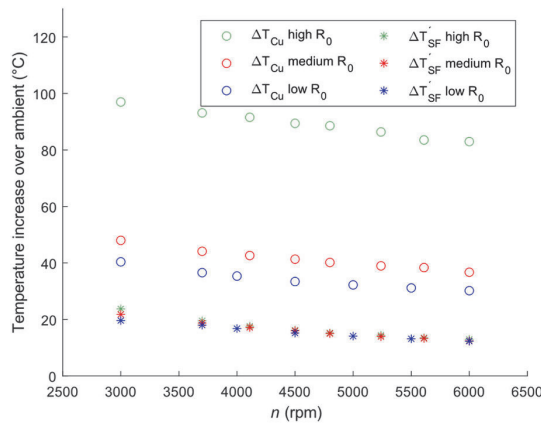


Fig. 13. Hotspot and frame temperature increase for the three cases: high  $R_0$  (no thermal paste), medium  $R_0$  (insufficient thermal paste) and low  $R_0$  (sufficient thermal paste).

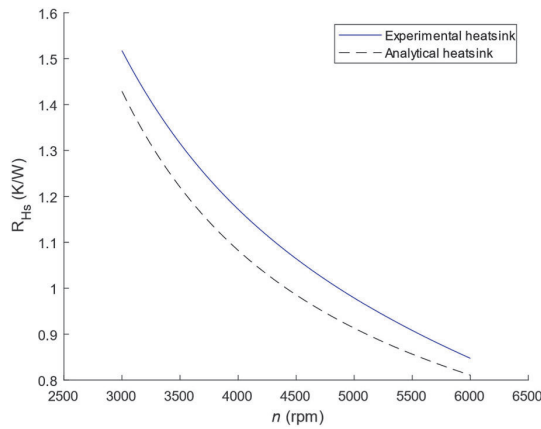


Fig. 14. Thermal resistances of the heatsinks at different fan speeds.

flux structure is also conducive to a low  $R_{Hs}$  due to the ample available space for a heatsink and the inherent possibility of utilizing two cooling fans in series.

Looking at the total thermal resistance as a sum of  $R_0$  and  $R_{Hs}$  clearly shows a path to improving performance further. The obvious

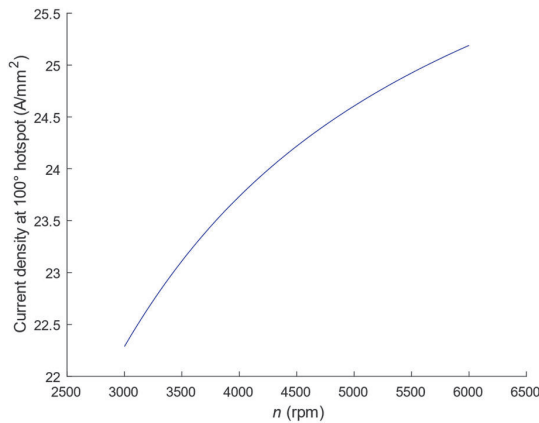


Fig. 15. Maximum steady state current density at  $T_{Cu} = 100\text{ }^{\circ}\text{C}$ .

choice is reducing  $R_0$ , which is most effectively done by reducing the number of layers in the windings. If this is taken to the extreme and only a single layer is used (as is often done with AM windings [26]),  $R_0$  can theoretically be reduced to 0.38 K/W as per Fig. 5 a). Subsequently, this would result in a new optimal  $L_{HS}$  and a heatsink with an analytically calculated  $R_{HS}$  of 0.59 K/W. Altogether, this results in a theoretical maximum current density to 37 A/mm<sup>2</sup> at 6000 rpm.

## 5. Conclusion

A novel additively manufactured cooling solution for a dual rotor yokeless axial flux switched reluctance machine was designed to increase its power-to-weight ratio and improve its viability for light unmanned aircraft propulsion applications. It consists of an aluminum alloy frame, which surrounds the windings and extends radially to form a conventional finned heatsink. Axial cooling fans connected to the two rotors provide airflow through the heatsink, effectively cooling the windings and therefore substantially increasing the maximum available current density in the conductors.

Firstly, the effects of the cooling solution on the AC losses of the machines were evaluated with a numerical electromagnetic model. After the viability of the initial design was confirmed, a thermal model was used to estimate the thermal characteristics of the system, including its internal thermal resistance. Based on the thermal model and experimentally obtained performance curves of cooling fans, an analytical design process was followed to determine the geometry of the heatsink, which is defined by the length and number of heatsink fins. The analytical model concluded with a heatsink geometry, which maximizes the ratio of current density to total motor weight.

The resulting geometry was additively manufactured from the aluminum alloy AlSi10Mg using LPBF and used to construct a motorette prototype. Its thermal performance was validated in practical measurements, where the winding were heated with DC current, and airflow was created by the cooling fan pair. The measurements validated the models and demonstrated that the proposed cooling solution is capable of achieving a maximum current density of >25 A/mm<sup>2</sup> at a rotational speed of 6000 rpm, while keeping the hotspot temperature increase under 80 °C. These results suggest that the proposed thermal solution can significantly enhance the viability of axial flux switched reluctance motors for power-dense electric propulsion systems.

Future work will focus on two key aspects of the proposed thermal solution. Firstly, reducing the system's internal thermal resistance, which is mainly created by the winding structure, will enable even higher current densities to be used. Here, large gains can be made with AM conductors by eliminating some of the contact resistance present in the conventional winding. This also opens up the possibility for aluminum conductors, which can potentially offer improved power density at higher speeds. Secondly, the performance of the heatsink could likely be further increased by optimizing the heatsink geometry and applying surface elements, which are uniquely available to AM heatsinks. Alternatively, redesigning the with the use of topology optimization could provide even higher performance. Finally, redesigning and manufacturing the AFSRM based on the substantially higher current density will make it possible to directly illustrate the effect of the cooling solution on the power density of the machine.

## CRedit authorship contribution statement

**Martin Sarap:** Writing – original draft, Methodology, Formal analysis, Conceptualization. **Shalini Singh:** Resources, Methodology. **Ants Kallaste:** Writing – review & editing, Supervision, Resources, Funding acquisition. **Ahmed Qureshi:** Supervision, Resources. **Hans Tiismus:** Methodology. **Toomas Vaimann:** Funding acquisition. **Payam Shams Ghahfarokhi:** Writing – review & editing.

## Declaration of competing interest

The authors declare that they have no known competing financial interests or personal relationships that could have appeared to influence the work reported in this paper.

## Acknowledgements

This work was supported by the Estonian Research Council grant PRG-1827. The authors are grateful to The University of Alberta for manufacturing the physical samples.

## Data availability

Data will be made available on request.

## References

- [1] M.U. Naseer, A. Kallaste, B. Asad, T. Vaimann, A. Rassõlkin, A review on additive manufacturing possibilities for electrical machines, *Energies* 14 (7) (Jan. 2021), <https://doi.org/10.3390/en14071940>, 7.
- [2] N. Simpson, D.J. North, S.M. Collins, P.H. Mellor, Additive manufacturing of shaped profile windings for minimal AC loss in electrical machines, *IEEE Trans. Ind. Appl.* 56 (3) (May 2020) 2510–2519, <https://doi.org/10.1109/TIA.2020.2975763>.
- [3] H. Tan, et al., Additively manufactured winding design for thermal improvement of an oil-cooled axial flux permanent magnet machine, *IEEE Trans. Transp. Electrification* (2023), <https://doi.org/10.1109/TTE.2023.3282213>, 1–1.
- [4] R. Wrobel, B. Scholes, A. Hussein, R. Law, A. Mustaffar, D. Reay, A metal additively manufactured (MAM) heat exchanger for electric motor thermal control on a high-altitude solar aircraft – experimental characterisation, *Therm. Sci. Eng. Prog.* 19 (Oct. 2020) 100629, <https://doi.org/10.1016/j.tsep.2020.100629>.
- [5] L. Gargalis, et al., Additive manufacturing and testing of a soft magnetic rotor for a switched reluctance motor, *IEEE Access* 8 (2020) 206982–206991, <https://doi.org/10.1109/ACCESS.2020.3037190>.
- [6] T. Huguet, J. Saffa, C. Nadal, F. Vêlé, M. Ackermann, C. Henaux, Performances evaluation of a 3D printed rotor for a synchronous reluctance machine, in: 2021 IEEE International Workshop of Electronics, Control, Measurement, Signals and Their Application to Mechatronics (ECMSM), Jun. 2021, pp. 1–8, <https://doi.org/10.1109/ECMSM51310.2021.9468847>.
- [7] J.D. Widmer, R. Martin, M. Kimiabeigi, Electric vehicle traction motors without rare earth magnets, *Sustain. Mater. Technol.* 3 (Apr. 2015) 7–13, <https://doi.org/10.1016/j.susmat.2015.02.001>.
- [8] E. Bostanci, M. Moallem, A. Parsapour, B. Fahimi, Opportunities and challenges of switched reluctance motor drives for electric propulsion: a comparative study, *IEEE Trans. Transp. Electrification* 3 (1) (Mar. 2017) 58–75, <https://doi.org/10.1109/TTE.2017.2649883>.
- [9] Z. Song, C. Liu, Energy efficient design and implementation of electric machines in air transport propulsion system, *Appl. Energy* 322 (Sep. 2022) 119472, <https://doi.org/10.1016/j.apenergy.2022.119472>.
- [10] P. Lindh, et al., Direct liquid cooling method verified with an axial-flux permanent-magnet traction machine prototype, *IEEE Trans. Ind. Electron.* 64 (8) (Aug. 2017) 6086–6095, <https://doi.org/10.1109/TIE.2017.2681975>.
- [11] Y. Wang, T. Zhu, W. Geng, J. Guo, Y. Sun, Cooling system analysis of an enclosed yokeless stator for high-power axial flux PM motor with distributed winding, *IEEE Trans. Ind. Electron.* 71 (3) (Mar. 2024) 2789–2799, <https://doi.org/10.1109/TIE.2023.3270540>.
- [12] C. Jenkins, et al., Innovations in axial flux permanent magnet motor thermal management for high power density applications, *IEEE Trans. Transp. Electrification* 9 (3) (Sep. 2023) 4380–4405, <https://doi.org/10.1109/TTE.2023.3242698>.
- [13] A.S. Fawzal, R.M. Cirstea, T.J. Woolmer, M. Dickison, M. Blundell, K.N. Gyftakis, Air inlet/outlet arrangement for rotor cooling application of axial flux PM machines, *Appl. Therm. Eng.* 130 (Feb. 2018) 1520–1529, <https://doi.org/10.1016/j.applthermaleng.2017.11.121>.
- [14] P.S. Nasab, R. Perini, A. Di Gerlando, G.M. Foglia, M. Moallem, Analytical thermal model of natural-convection cooling in axial flux machines, *IEEE Trans. Ind. Electron.* 67 (4) (Apr. 2020) 2711–2721, <https://doi.org/10.1109/TIE.2019.2913811>.
- [15] W. Geng, Y. Zhang, S. Ge, J. Guo, Q. Li, Z. Zhang, 3-D thermal network modeling and thermal analysis of an air-cooled yokeless stator axial flux PM motor with heat pipes, *IEEE Trans. Transp. Electrification* (2024), <https://doi.org/10.1109/TTE.2024.3395655>, 1–1.
- [16] S. Berndt, A. Kleimaier, Encapsulated air cooling system for scalable axial flux motors, in: 2021 International Conference on Electrical Drives & Power Electronics (EDPE), Sep. 2021, pp. 43–49, <https://doi.org/10.1109/EDPE53134.2021.9604050>.
- [17] A.H. Mohamed, A. Hemeida, A. Rasekh, H. Vansompel, A. Arkkio, P. Sergeant, A 3D dynamic lumped parameter thermal network of air-cooled YASA axial flux permanent magnet synchronous machine, *Energies* 11 (4) (Apr. 2018), <https://doi.org/10.3390/en11040774>, 4.
- [18] C. Silbernagel, I. Ashcroft, P. Dickens, M. Galea, Electrical resistivity of additively manufactured AISi10Mg for use in electric motors, *Addit. Manuf.* 21 (May 2018) 395–403, <https://doi.org/10.1016/j.addma.2018.03.027>.
- [19] A. Plotkowski, et al., Design and performance of an additively manufactured high-Si transformer core, *Mater. Des.* 194 (Sep. 2020) 108894, <https://doi.org/10.1016/j.matdes.2020.108894>.
- [20] J.R. Culham, Y.S. Muzychka, Optimization of plate fin heat sinks using entropy generation minimization, *IEEE Trans. Compon. Packag. Technol.* 24 (2) (Jun. 2001) 159–165, <https://doi.org/10.1109/6144.926378>.
- [21] P. Teertstra, M.M. Yovanovich, J.R. Culham, T. Lemczyk, Analytical forced convection modeling of plate fin heat sinks, in: Fifteenth Annual IEEE Semiconductor Thermal Measurement and Management Symposium (Cat. No.99CH36306), IEEE, San Diego, CA, USA, 1999, pp. 34–41, <https://doi.org/10.1109/STHERM.1999.762426>.
- [22] L. Wang, S. Wang, J. Wu, Experimental investigation on densification behavior and surface roughness of AISi10Mg powders produced by selective laser melting, *Opt. Laser. Technol.* 96 (Nov. 2017) 88–96, <https://doi.org/10.1016/j.optlastec.2017.05.006>.
- [23] M. Sarap, A. Kallaste, P.S. Ghahfarokhi, H. Tiismus, T. Vaimann, The effect of build direction on the thermal conductivity of additively manufactured AISi10Mg and silicon-steel samples, in: 2022 International Conference on Electrical Machines (ICEM), Sep. 2022, pp. 538–543, <https://doi.org/10.1109/ICEM51905.2022.9910944>.
- [24] Y. Gai, et al., Cooling of automotive traction motors: schemes, examples, and computation methods, *IEEE Trans. Ind. Electron.* 66 (3) (Mar. 2019) 1681–1692, <https://doi.org/10.1109/TIE.2018.2835397>.
- [25] A. Reinap, F.J. Márquez-Fernández, R. Andersson, C. Högmark, M. Alaküla, A. Göransson, Heat transfer analysis of a traction machine with directly cooled laminated windings, in: 2014 4th International Electric Drives Production Conference (EDPC), Sep. 2014, pp. 1–7, <https://doi.org/10.1109/EDPC.2014.6984395>.
- [26] A. Selema, J. Van den Abbeele, M.N. Ibrahim, P. Sergeant, Innovative 3-D printed coil and cooling designs for weight-sensitive energy-saving electrical machine, *IEEE Trans. Transp. Electrification* 10 (3) (Sep. 2024) 5282–5293, <https://doi.org/10.1109/TTE.2023.3322522>.



**Publication V**

M. Sarap, S. Singh, A. Kallaste, A. Qureshi, H. Tiismus, T. Vaimann, P.S. Ghahfarokhi, Comparative Study of Advanced Heatsink Structures for Improved Thermal Performance in Axial Flux Motors, IEEE Access, doi: 10.1109/ACCESS.2025.3577289.



Received 23 May 2025, accepted 1 June 2025, date of publication 6 June 2025, date of current version 16 June 2025.

Digital Object Identifier 10.1109/ACCESS.2025.3577289

## RESEARCH ARTICLE

# Comparative Study of Advanced Heatsink Structures for Improved Thermal Performance in Axial Flux Motors

MARTIN SARAP<sup>1</sup>, (Graduate Student Member, IEEE), SHALINI SINGH<sup>2</sup>,  
ANTS KALLASTE<sup>1</sup>, (Senior Member, IEEE), AHMED JAWAD QURESHI<sup>2</sup>,  
HANS TIISMUS<sup>1</sup>, TOOMAS VAIMANN<sup>1</sup>, (Senior Member, IEEE),  
AND PAYAM SHAMS GHAHFAROKHI<sup>3</sup>, (Senior Member, IEEE)

<sup>1</sup>Department of Electrical Power Engineering and Mechatronics, Tallinn University of Technology, 19086 Tallinn, Estonia

<sup>2</sup>Additive Design and Manufacturing Systems Laboratory, Department of Mechanical Engineering, Faculty of Engineering, University of Alberta, Edmonton, AB T6G 2R3, Canada

<sup>3</sup>Electrical Engineering Unit, Tampere University, 33014 Tampere, Finland

Corresponding author: Martin Sarap (martin.sarap1@taltech.ee)

This work was supported by the Estonian Research Council under Grant PRG-1827.

**ABSTRACT** Additive manufacturing has enabled the use of advanced geometries such as lattice-structures in heatsinks. This study investigates the thermal performance of various advanced heatsink designs in the context of cooling the windings of an axial flux motor using active air cooling. Physical samples of the heatsinks are additively manufactured from an aluminum alloy and tested under realistic airflow conditions. The heatsink designs are compared against an optimized conventional finned geometry based on the measured thermal resistance at a given fan speed. This ensures that the results are representative of real-world use cases and applicable in practical solutions. The results indicate that airfoil-shaped pins can slightly outperform conventional straight fins in thermal resistance while weighing less. In terms of mass-based relative performance, the rhombi octet lattice structure outperformed the other prototypes. These findings reinforce conventional design principles in terms of absolute performance while suggesting that lattice structures can provide higher relative performance in certain weight sensitive applications.

**INDEX TERMS** Heat sinks, three-dimensional printing, switched reluctance motors.

## I. INTRODUCTION

Increasing demands for power density in all types of electrical devices are often accompanied by correspondingly increased demands for cooling performance. This is also the case for electrical machines, where applications such as aircraft propulsion demand exceedingly higher thermal performance. One way that researchers are attempting to meet those demands is by incorporating various advanced geometries in the design of air-cooled heatsinks, which has resulted in a plethora of literature concerning various advanced fin designs. While many of these are based on simulations, metal additive manufacturing (AM) methods

such as laser powder bed fusion (LPBF) have made it possible to manufacture physical prototypes for performing practical measurements [1], [2], [3], [4], [5]. However, despite the prevalence of research in the field, straightforward comparisons with conventional solutions under appropriate conditions are often missing, meaning that the utility of these advanced solutions in real-world cooling applications is still unclear.

For example, Ho et al. [6] manufactured different pin-fin heatsinks with a focus on airfoil-shaped pins. They found that in a certain range of Reynolds number values correctly placed airfoil pins outperformed simple circular and rounded rectangular pins in terms of Nusselt number. However, the method of choosing the main geometrical parameters for the variants (i.e. fin count and spacing) is seemingly arbitrary, meaning

The associate editor coordinating the review of this manuscript and approving it for publication was Eric Li.



that it is difficult to evaluate the significance of the performance difference in a practical context. Other works, such as the one by Khalil et al. [7] compare different variations of gyroid structures and while the results are useful for choosing a specific gyroid geometry, the work provides no context for the absolute performance of the heatsinks. This is representative of the relevant literature in general as comparisons are made either in a narrow context between similar solutions, or against non-optimized conventional solutions, which do not provide useful information in the context of practical use cases, where a thoroughly optimized conventional solution can be expected to be available.

Therefore, the purpose of this study is to investigate the thermal performance of a selection of advanced heatsink designs, which have shown potential in literature, but for which direct comparisons against optimized conventional solutions are not available. This is done in the context of an actively air-cooled electrical motor, for which power-to-weight ratio is prioritized and directly dependent on the performance of the cooling solution. By evaluating the thermal performance of the advanced fin structures in a practical case, where an analytically optimized conventional solution is included in the comparison, relevant claims can be made about the real-world viability of these structures for forced-air cooling. The article starts with a general introduction of the cooling solution, for which the initial conventional heatsink was designed in our previous paper [8]. Afterwards, the advanced fin structures are described, followed by the test results of the AM prototypes are presented and analyzed.

II. HEATSINK DESIGN AND MODELING

A. AXIAL FLUX RELUCTANCE MOTOR COOLING

The advanced fin structures investigated in this work are implemented for the heatsink of a dual-rotor axial flux switched reluctance motor (AFSRM), for which the main parameters are presented in Table 1. This motor topology is uniquely suitable for advanced air-cooled solutions for two reasons. First, the heatsink can be mounted directly on the windings to eliminate a majority of the internal thermal resistance typically present in radial flux machines. As a result, the thermal resistance associated with the heatsink fins compose a much larger proportion of the overall thermal system, making the choice of the specific fin geometry much more relevant. Second, the dual-rotor topology inherently enables the use of two cooling fans in series without increasing the axial length of the motor, creating a large potential for heat extraction using only air-cooling.

The construction of the motor with the initial thermal solution incorporating conventional straight fins is shown in Figure 1. The separate stator segments are held together by an AM aluminum alloy (AlSi10Mg) frame, which includes an integrated heatsink for cooling the coils. This alloy is used instead of pure aluminum (which has a substantially higher thermal conductivity and a similar density) due to practical limitations when using LPBF. Axial cooling fans, with an

TABLE 1. Main parameters of the reluctance motor.

Parameter	Value
Slot/pole count	6/4
Outer diameter	67.4 mm
Axial length	70.0 mm
Rated speed	6000 rpm
Maximum current density	25 A/mm <sup>2</sup> rms
Maximum heat losses	>200 W

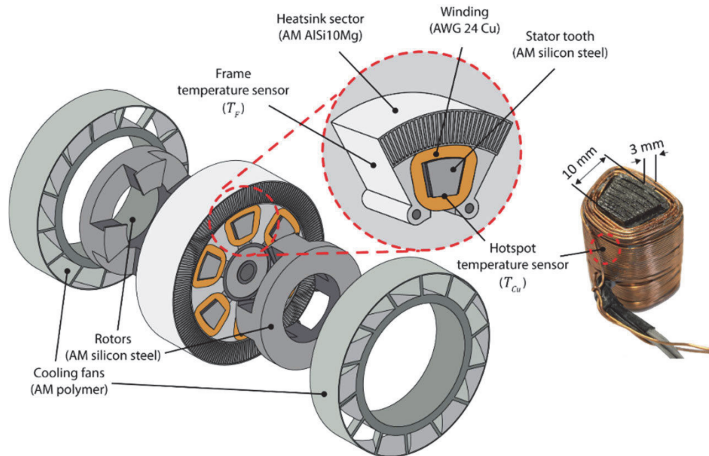
outer diameter matching the heatsink and a thickness matching the rotor, are attached to both rotors and provide airflow through the heatsink. The total heat load in the motor is a combination of copper, iron and mechanical losses, of which the copper losses are a large majority due to the high current density used in the windings.

A single stator slot of the machine and a corresponding 1/6 sector of the heatsink and frame combination is prototyped for measuring the performance of the various advanced fin structures. The stator tooth consists of a high silicon steel laminated stator tooth produced with LPBF, around which a coil consisting of 230 turns of a 0.2 mm<sup>2</sup> wire is wound. The hotspot temperature of the stator is measured with a Pt100 sensor placed between the inner coil layer and the steel tooth. An additional Pt100 sensor is placed inside the AlSi10Mg frame in order to differentiate between the total thermal resistance of the system and the thermal resistance of the heatsink.

B. HEATSINK DESIGN

Making useful claims about the applicability of novel fin designs requires a comparison to an optimized conventional solution. For this reason, an initial conventional heatsink with simple straight fins is prototyped and its performance is used as a benchmark for the advanced fin structures. The number of fins and length of the fin are optimized based on maximum power density of the motor through an analytical design process, which is described in detail in our previous paper [8], resulting in a heatsink with 198 fins with a length of 9 mm (the thickness of the fin is fixed at 0.5 mm in order to ensure manufacturability with LPBF). This is done according to the performance curve of the fan pair at 6000 rpm.

The effectiveness of an air-cooled heatsink is mainly determined by the interaction between the fin surface area and the passing airflow. In the case of a conventional heatsink, the straightforward airflow path ensures that sufficient airflow passes the relatively large surface area. However, this type of steady flow also results in a comparatively thick boundary layer, which is the slow-moving layer of insulating air that forms near the surface of the heatsink. Due to this, many alternatives for the conventional design have been proposed with the justification of minimizing the insulating effect of the boundary layer, mainly by introducing turbulence. However, modifying the fin geometry this way tends to increase the total aerodynamic drag of the system, which reduces total



**FIGURE 1.** Exploded view of the thermal system used to cool the axial flux motor showing the 1/6 sector used for practical measurements.

airflow and potential for heat transfer. Therefore, an effective fin geometry needs to find a balance between total airflow, fin surface area and turbulence.

### C. ADVANCED FIN DESIGNS

The advanced fin designs tested in this study are based on novel geometries that are promising candidates for air-cooling applications, although for which reliable comparisons to relevant alternatives are lacking. The novelty of these solutions precludes detailed analytical or empirical workflows, and the complicated nature of the structures means that numerical models cannot be relied upon. Therefore, reliable performance data can only be obtained through physical prototypes, while the specific geometrical parameters of each prototype must rely on initial findings from literature. However, to create a fair comparison, some of the geometrical dimensions are altered in this work to fit the use-case (e.g. avoiding fractional cells and imposing a fin length of 9 mm based on the optimized conventional design).

The first advanced fin design shown in Table 2 is a pin fin heatsink with airfoil-shaped pins. Pin fins are widely used in conventional solutions as they provide excellent cooling performance even with simple round or rectangular pins. The effectiveness of the pin array lies in the turbulence around the pins that disrupts the boundary layer. Novel pin designs, which can potentially provide improved performance, have gotten some attention in the AM space [9], [10], [11], [12]. The pins modelled for this prototype are based on the work of Ho et al. [6], who compared circular, rounded rectangular and airfoil-shaped pins under turbulent airflow conditions. Looking at different pin arrays and angles of attack, the best experimental results were achieved with a staggered array of NACA 0024 airfoil pins at an angle of attack of 20°.

The second advanced design is based on the work of Ho et al. [13], [14], [15] and utilizes a rhombi octet lattice

structure, which includes a rhombicuboctahedron core and truss structures in the corners. In this case, a high proportion of the fin surface is perpendicular to the airflow, resulting in significant turbulence. In [13] AM samples with different cell sizes were measured under forced air-cooling, showing that smaller cells resulted in larger Nusselt numbers at a cost of higher pressure drops. In [14] they show that the structure can provide higher heat flux density than a conventional fin-tube heat exchanger, although the pressure drop associated with the structure is high. For the purposes of our study, a cell size of 9 mm was chosen to avoid a fractional cell count.

Other truss-based structures are also actively researched. Combinations of cubic and truss-based lattices were numerically modelled in [16] under laminar flow. Out of the different lattices, the simple-cubic combined with a body centered cubic lattice (BCC) at a cell size of 3.5 mm had the best overall thermal performance. The BCC geometry is similar to the rhombi octet, however replacing the smaller rectangular struts with larger round pins increases the fin surface area and could lead to a smoother flow path. In our case, the cell size is changed to 3.0 mm in order to fit three full cells in the fin length.

The final types of structures investigated in this study are based on triply periodic minimal surfaces (TPMS). These have mainly been considered in liquid-based heat exchangers where both the gyroid and diamond structures have outperformed conventionally designed counterparts [17], [18], [19]. Additionally, the gyroid has been tested in forced-air cooling applications by Khalil et al. [7], who manufactured different variations and found the G-sheet with a porosity of 0.8 to have the lowest thermal resistance. The gyroid and diamond structures achieve a complex flow path using only smooth surfaces, potentially offering an effective balance between flowrate and boundary layer disruption. Uniquely, the diamond does not include any direct path through the fin

TABLE 2. Different heatsink designs.

Fin Structure	Geometrical Parameters	Characteristic Geometry	Heatsink Sector Model
Straight fins initial case	$L_{HS} = 9\text{ mm}$ $t_{fin} = 0.5\text{ mm}$ $b = 0.8\text{ mm}$ $d_1 = 0.5\text{ mm}$ $N_{fin} = 198$ $A_{HS} = 151\text{ cm}^2$ $M_{HS} = 13.4\text{ g}$ $V_{FC} = 6.04\text{ cm}^3$		
Airfoil pin fins	$d_1 = 8.7\text{ mm}$ $d_2 = 2.7\text{ mm}$ $\alpha = 20^\circ$ $A_{HS} = 81.9\text{ cm}^2$ $M_{HS} = 11.4\text{ g}$ $V_{FC} = 6.05\text{ cm}^3$		
Rhombi octet	$d_1 = 9\text{ mm}$ $d_2 = 2.25\text{ mm}$ $d_3 = 0.75\text{ mm}$ $A_{HS} = 87.0\text{ cm}^2$ $M_{HS} = 7.80\text{ g}$ $V_{FC} = 7.78\text{ cm}^3$		
Simple cubic + body centered cubic (BCC)	$d_1 = 3\text{ mm}$ $d_2 = 0.6\text{ mm}$ $A_{HS} = 128\text{ cm}^2$ $M_{HS} = 10.4\text{ g}$ $V_{FC} = 7.45\text{ cm}^3$		
TPMS Gyroid	$d_1 = 9\text{ mm}$ $d_2 = 1\text{ mm}$ $A_{HS} = 76.4\text{ cm}^2$ $M_{HS} = 10.9\text{ g}$ $V_{FC} = 6.39\text{ cm}^3$		
TPMS Diamond	$d_1 = 6.3\text{ mm}$ $d_2 = 0.5\text{ mm}$ $d_3 = 2.3\text{ mm}$ $A_{HS} = 117\text{ cm}^2$ $M_{HS} = 7.10\text{ g}$ $V_{FC} = 8.02\text{ cm}^3$		

structure, meaning that the entirety of the flow must follow the intricate internal structure. This makes it the most extreme case of sacrificing flowrate in favor of turbulence. In our prototypes, the gyroid is dimensioned with a porosity of 0.8 and a cell size of 9 mm, while the diamond, for which the unit cell is irregularly shaped, is scaled manually to avoid disjointed structures in the final geometry.

Table 2 contains the characteristic dimensions of each design and includes a rendering of the final fin structure. The value of  $A_{Hs}$  is taken from the CAD model and represents the wetted surface of the heatsink sector.  $M_{fins}$  is the total mass of the fins together with curved top and bottom surfaces. This value is later confirmed by weighing the manufactured prototypes.  $V_{FC}$  is the volume of the flow channel, taken from the model and used for calculating the Nusselt number.

#### D. THERMAL MODEL

When comparing different heatsink designs, care must be taken to separate the thermal resistance of the heatsink  $R_{Hs}$  (K/W) from the internal thermal resistance of the system  $R_0$ . As shown in Figure 2, this includes the resistance of the copper winding turns  $R_{Cu}$ , the contact resistance between the coil and frame  $R_C$ , and the resistance of the aluminum frame itself  $R_{Al}$ .

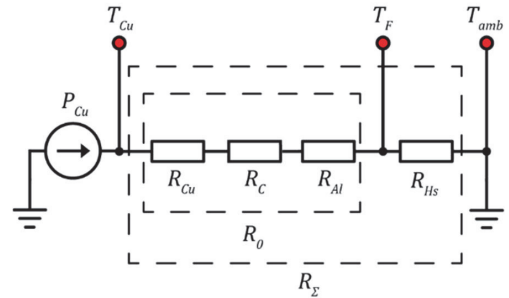
Among the different resistances, accounting for  $R_C$  is the most challenging, as it depends on the mechanical fit of the frame and varies each time the frame is mounted on the coil. This variation is minimized by having nearly identical dimensions and surface finishes for each heatsink prototype, together with the use of thermal paste, although it cannot be fully eliminated. Therefore, an additional temperature sensor is added on the frame-heatsink boundary, which allows the thermal resistance of the heatsink to be measured using eq. 1.

$$R_{Hs} = \frac{T_F - T_{amb}}{P_{Cu}} \quad (1)$$

where  $T_F$  is the frame temperature,  $T_{amb}$  is the ambient temperature and  $P_{Cu}$  (W) is the total heat load generated in the stator tooth.

This formulation assumes that the measured frame temperature  $T_F$  is equal to the average temperature of the heatsink base as there is no way to measure the latter directly without significantly altering the heat flow. A detailed description of measuring the frame temperature is discussed in our previous paper [8], in which the measured  $T_F$  is slightly modified depending on the total thermal resistance of the system.

Knowing the value for  $R_{Hs}$  is useful for calculating the temperature rise for a given heat load, however the performance of a heatsink can be further analyzed through the convection coefficient  $h_c$  (W/(m<sup>2</sup>·K)), which describes heat flow from the heatsink surface to the ambient air. In the case of air cooling, the total heat flow is low enough that the temperature gradient in the solid material is negligible, meaning that the average convection coefficient can be expressed as a simple division:  $h_c = R_{Hs}/A_{Hs}$ .



**FIGURE 2.** Lumped parameter thermal model of the motor sector showing the distinction between internal thermal resistance  $R_0$  and the resistance of the heatsink fins  $R_{Hs}$ .

Additionally, the average convection coefficient can be used to calculate the Nusselt number  $N_u$  of a heatsink, which is a dimensionless number describing the ratio between total and conductive heat transfer. Generally, a high  $N_u$  is desirable, as it indicates a more effective geometry for dissipating heat into the ambient environment. The Nusselt number for internal flow is defined as  $N_u = (h_c \cdot D_h)/\lambda_{air}$ , where  $D_h$  (m) is the hydraulic diameter of the flow channel and  $\lambda_{air}$  (W/(m·K)) is the thermal conductivity of the fluid. Due to the significantly different geometries of the designs, the hydraulic diameter is defined in the most general form as  $D_h = 4V_{FC}/A_{Hs}$ , where  $V_{FC}$  (m<sup>3</sup>) is the total volume of the flow channel.

#### E. AIRFLOW MODEL

The airflow characteristics of each heatsink are measured in addition to thermal performance to provide a more thorough analysis of the results. This is done by channeling the airflow exiting the heatsink through a flow bench, which allows the volumetric airflow through the heatsink to be measured and the working point of the fan pair to be found. The pair of axial fans used to provide airflow through the fins utilize a simple blade geometry consisting of 14 blades and are dimensioned according to the heatsink, so that the outer diameter of the motor is consistent. The use of appropriately sized (both in terms of geometry and pumping power) fans ensures that the heatsinks are tested under airflow conditions that correspond to a practical use case.

The performance of the fan pair is measured in the two extreme operating conditions with an in-house flow bench. First, the airflow is measured without any added drag, resulting in the maximum airflow value at a given fan speed. Second, the maximum pressure generated by the fan pair is measured by fully blocking the airflow. The results of measuring the two extreme working points at different speeds are presented in Figure 3. In Figure 4, these values are used to define linear fan curves that approximate the performance of the fan pair at each operating point. Therefore, the working point of each fan speed and heatsink combination can be



evaluated only by measuring the volumetric airflow through the heatsink.

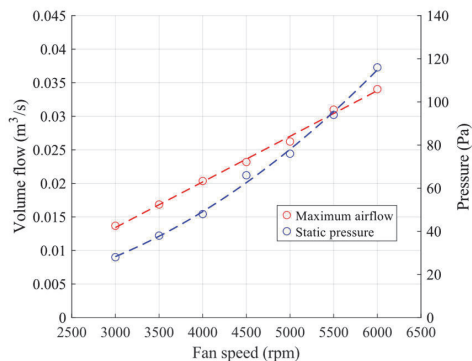


FIGURE 3. Measured free airflow and maximum static pressure of the cooling fan pair at different rotational speeds.

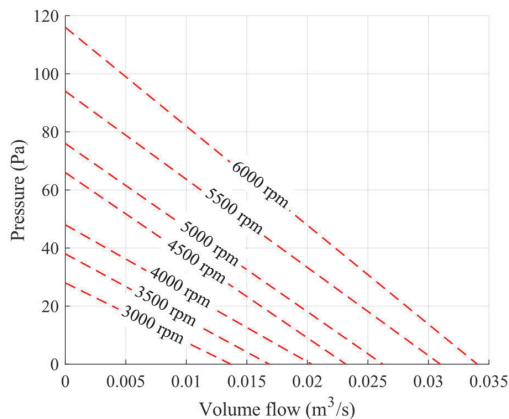


FIGURE 4. Linearized fan curves at different rotational speeds.

III. EXPERIMENTAL SETUP

A. ADDITIVELY MANUFACTURED PROTOTYPES

The experimental measurements are carried out on frame sector prototypes, which are additively manufactured from the aluminum alloy AISi10Mg using the Coherent Creator LPBF device. The relevant process parameters are presented in Table 3. After the manufacturing process, the samples were subjected to heat-treatment at 300 °C for 2 hours, which is necessary to achieve an isotropic thermal conductivity value of approximately 148 W/(m· K) [20].

The physical prototypes shown in Figure 5 are dimensionally accurate and do not display any major manufacturing faults. The internal surfaces of the frame, which are in direct contact with the coil, are carefully polished to an identical surface finish. After the polishing process, no appreciable differences in the dimensions of the stator slot opening

TABLE 3. Printing parameters utilized for manufacturing the AISi10Mg prototypes.

Parameter	Value
Layer height	30 μm
Laser power	230 W
Scanning velocity	500 mm/s
Hatching distance	40 μm
Scanning strategy	Stripes
Environment	Argon
Oxygen content	<0.1 %

are present. The internal thermal resistance of the cooling solution, which is a large contributor to the overall thermal performance, is minimized by tailoring the slot opening specifically to the shape of the wound coil so that there would be no thermally insulating gaps between the coil and frame. The contact resistance is lowered further by applying thermal paste on the mating surfaces.

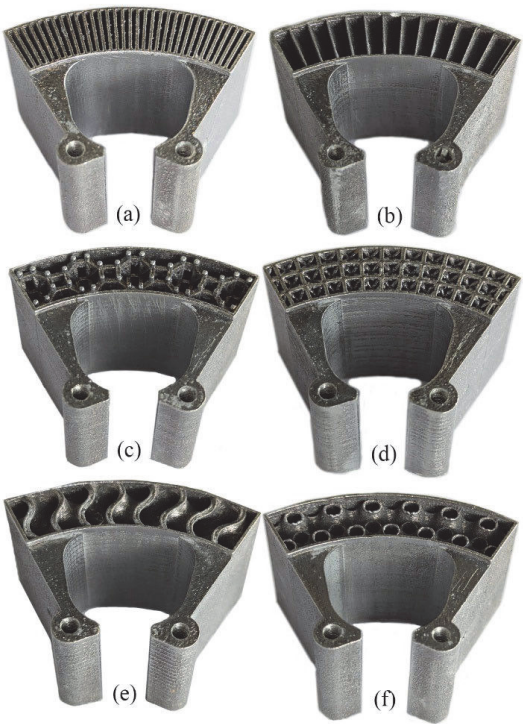
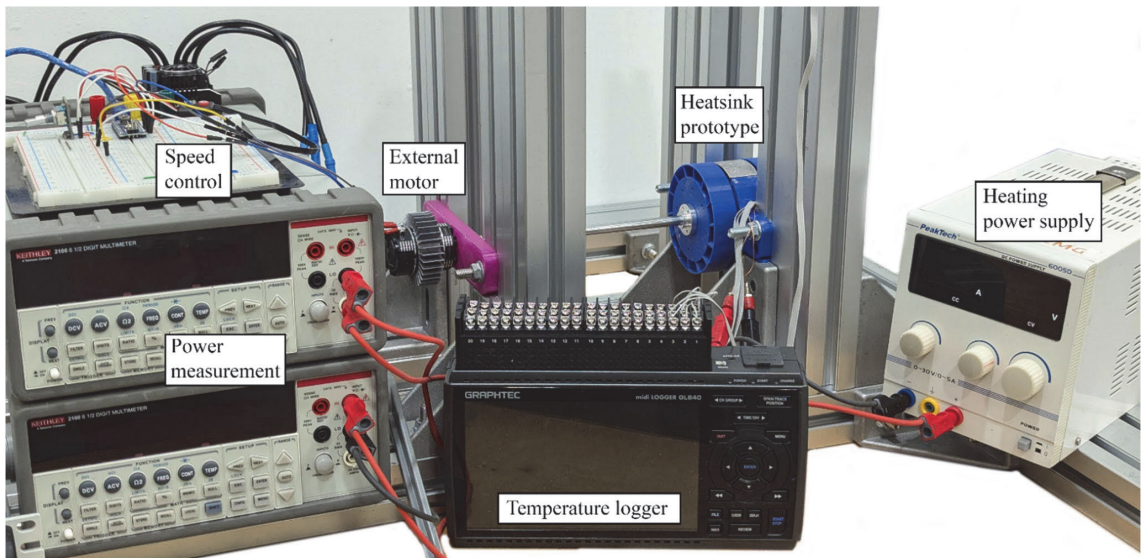


FIGURE 5. AM heatsink sectors: a) conventional straight fins, b) airfoil pin fins, c) rhombi octet, d) BCC e) TPMS gyroid, f) TPMS diamond.

B. PERFORMANCE MEASUREMENTS

The thermal performance of each prototype is determined by measuring the temperature difference between the base of the heatsink and the ambient air while heating the coil under a DC load. The input heating power, calculated by



**FIGURE 6.** Experimental setup for measuring the temperatures at different fan speeds. A commercial electronic drive is used to run the fans at different rotational speeds. A DC power supply is used to provide the heat load in the coils, which is measured using two precision multimeters. The temperatures are monitored throughout the measurement process using a high-accuracy logging device.

multiplying the current and voltage, is controlled in order to achieve a steady-state hotspot temperature of 100 °C, emulating a fixed working point of the motor and avoiding any temperature-dependent variances in the internal thermal resistance (e.g. thermal expansion of the coil changing the value of  $R_C$ ). During testing, the entire heat load is generated in the windings through Joule heating, as the iron losses, which are present during normal operation, do not have a meaningful effect on the temperature distribution and therefore the performance of the heatsink. Airflow through the heatsink is created by running the fans at a range of rotational speeds (using an external motor). The measurement setup is presented in Figure 6. When measuring the aerodynamic performance, the airflow exiting the heatsink is directed into the flow bench so that the operating point of the fan pair can be determined (this is avoided during thermal testing so as not to introduce additional drag). As a linear performance curve for the fan pair is known at each speed, the operating point for each heatsink can be approximated simply by measuring the total amount of outflowing air.

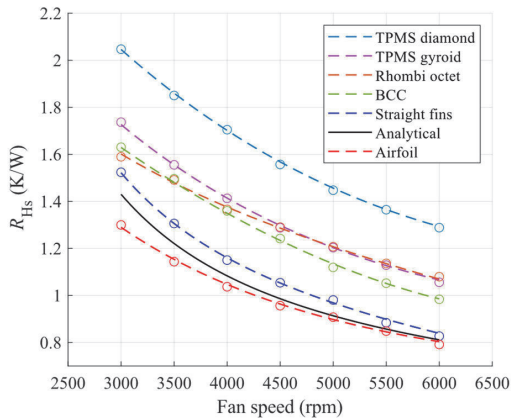
Measuring the temperatures is done in three separate runs to account for the small run-to-run variation in the internal thermal resistance of the system. This is mainly caused by the quality of the mechanical fit between the frame and winding, placement of the frame temperature sensor and the uncertainty of the sensor reading. For each run, the frame and ambient temperatures are used to calculate each  $R_{Hs}$  based on equation 1. The  $R_{Hs}$  values from the three runs are averaged to produce the resulting exponential curves in the form  $y = ae^{bx}ce^{dx}$ , matching the analytically calculated curve.

## IV. RESULTS AND DISCUSSION

### A. ABSOLUTE THERMAL RESISTANCE

The resulting thermal resistance curves shown in Figure 7 are compared to the analytically calculated performance curve of the conventional finned heatsink (based on the workflows from [21] and [22] and presented in detail in our previous paper [8]) by using the fan performance curve. The measured values generally match the shape of the analytical model, where performance gains due to a higher fan speed gradually level off, although slight differences in the shape of the curves can be observed. At the operating speed of 6000 rpm, the airfoil pin fin heatsink performs the best with a  $R_{Hs}$  value of 0.80 K/W, which is 5% lower than the conventional straight fins at 0.84 K/W. The best performing lattice-based heatsink is the body-centered cubic at 0.99 K/W, which is 18% higher than the conventional case. Both TPMS heatsinks perform the worst, with the gyroid and diamond achieving a minimum thermal resistance of 1.07 and 1.29 K/W respectively. The resulting  $R_{Hs}$  values reinforce conventional design principles by showing significantly better performance for the designs with a straightforward airflow path, as only the airfoil pin fin heatsink outperformed the conventional straight fins in absolute thermal performance. The other geometries, which create a much more complicated airflow path, all result in a significantly higher  $R_{Hs}$ . This would suggest that when the goal is minimizing thermal resistance, lattice-structures are ineffective and more conventional fin structures should be considered. It is considered that the current comparison is between an optimized conventional case and non-optimized advanced geometries, however, the

magnitude of the difference is enough to clearly see the disadvantage of the lattice-based designs in absolute performance.



**FIGURE 7.** Thermal resistances of the different heatsinks at a range of fan speeds.

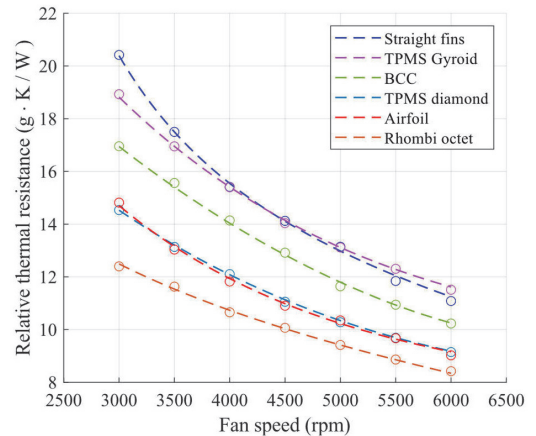
### B. RELATIVE THERMAL RESISTANCE

Alternatively, the performance of the heatsinks can be compared according to their relative thermal. This is shown in Figure 8, where the relative values are calculated by multiplying the  $R_{Hs}$  value with the fin mass of the heatsink. The results show the rhombi octet performing the best at a relative thermal resistance of 8.34 g · K/W (for a rough comparison, this unit can be thought of as the fin mass needed to achieve a 1 K/W thermal resistance, however in reality the relationship between fin mass and thermal resistance is highly non-linear) This is significantly lower than the conventional heatsink at 11.2 g · K/W, suggesting that the rhombi octet geometry is a more efficient use of material in terms of thermal resistance. However, while a lower relative value means that less material is needed for the measured  $R_{Hs}$ , it does not mean an arbitrary resistance can be achieved by using more material.

It should also be noted that the relevance of relative thermal resistance is heavily application specific as in most practical cases the fin mass of the heatsink is only a small part of the total mass of the device. For example, if the electromagnetic mass of the axial flux stator segment together with the mass of the aluminum frame totaling 59 grams is added to the fin mass, the denser but higher performing conventional and airfoil heatsinks result in a more power-dense motor. If, however, the heat-generating device is relatively small (e.g. a single transistor), the higher relative performance of the Rhombi octet could prove useful.

Interestingly, according to the analytical model, reducing the fin count of the conventional heatsink to 102 (from 198) in order to match the fin mass of the rhombi octet, results in a roughly unchanged relative performance of 11.3 g · K/W. This indicates that the relative performance is more so a function of geometry type rather than specific dimensions. Therefore,

while it seems unlikely that the rhombi octet or TPMS diamond could be used to increase absolute performance, further optimizing the designs in terms of performance-per-weight would be a worthwhile goal.



**FIGURE 8.** Relative thermal resistances of the prototypes based on fin mass.

### C. AIRFLOW

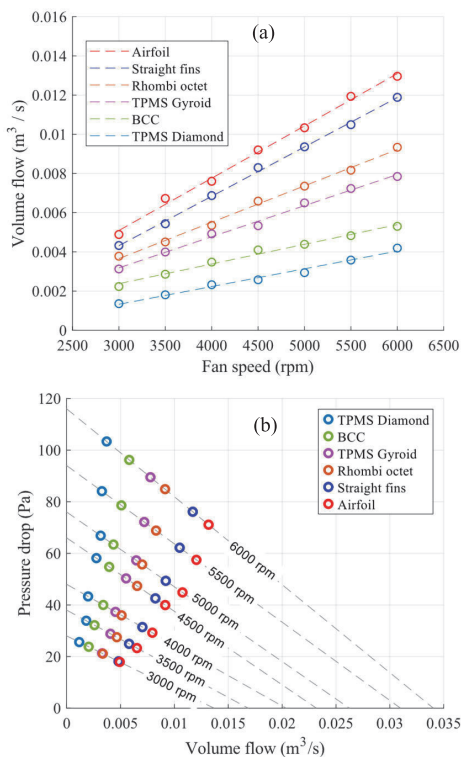
While the  $R_{Hs}$  values are sufficient to meaningfully describe the thermal performance of each fin structure, a justification for the results can be given through aerodynamic performance measurements. For this, the volumetric airflow through the sectors is measured and multiplied by six in order to represent the flow through the entire heatsink, for which the resulting values are presented in Figure 9 (a). In (b), these values are placed on the linear performance curves in order to define the approximate operating points.

The comparison between flow rates generally correlates with the thermal performance, further demonstrating that simple flow paths with low drag outperform complicated designs. Assuming that the analytically optimized conventional heatsink occupies the performance “sweet spot” on the fan pair performance curve, it can be stated that the lattice-based structures are overly dense. However, decreasing drag without changing their fundamental structure would decrease the fin surface area as well, meaning it would not necessarily improve performance. Therefore, it is reasonable to assume that the underperforming lattice structures are altogether suboptimal for active-air cooling. On the other hand, the comparatively high flow through the airfoil pin fin structure indicates that its performance could be improved by increasing either fin size or density to match the pressure drop of the conventional heatsink.

### D. DERIVED PERFORMANCE PARAMETERS

Derived parameters such as the heatsink’s average convection coefficient and Nusselt number, which combine both geometrical and performance parameters describe the general efficiency of the heatsink. While the absolute values of these



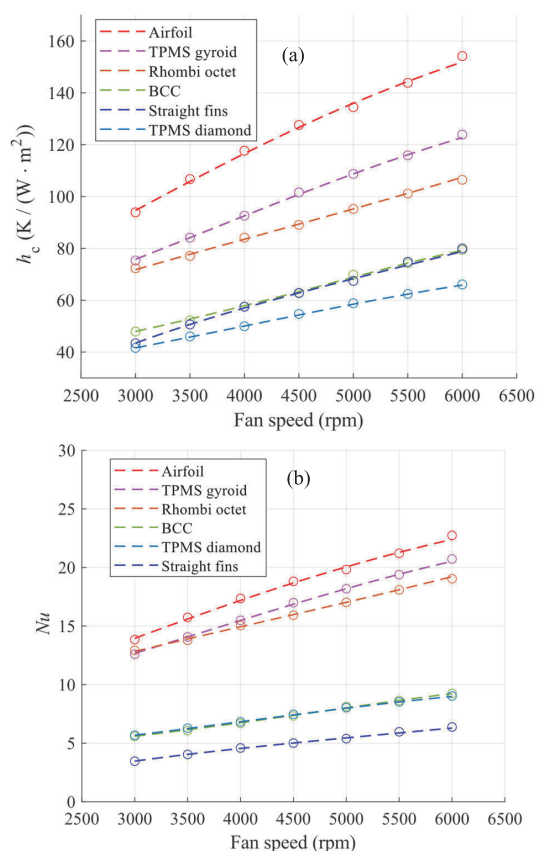


**FIGURE 9.** Measured airflow through the heatsink (a) and the corresponding approximated fan pair operating point at 6000 rpm (b).

parameters are not overly important in terms of cooling performance, comparing the results across different structures can provide additional reasoning for the measurement results and guidance for future improvements.

In Figure 10 (a), the effectiveness of the fin surface area is evaluated using the average convection coefficient  $h_c$  of each design. In this case, the airfoil fins achieve a maximum  $h_c$  value of  $153 \text{ K}/(\text{W} \cdot \text{m}^2)$ , while the value for the conventional solution is significantly lower at  $79 \text{ K}/(\text{W} \cdot \text{m}^2)$ . Notably, the TPMS gyroid, which underperforms in terms of thermal resistance, achieves a value of  $123 \text{ K}/(\text{W} \cdot \text{m}^2)$ . In Figure 10 (b), similar results are shown in terms of Nusselt number, where the airfoil pins achieve the largest result with a maximum value of 22.5, while the conventional heatsink reaches a value of 6.3.

While comparisons based on  $h_c$  and Nusselt numbers generally favor structures with a lower fin area, they can nonetheless offer insights into the effectiveness of the designs. In the case of the conventional straight fins, both derived values indicate that the structure is not particularly efficient, however its performance is simply a consequence of having the highest total fin area. For the airfoil pin fin heatsink, the comparatively high  $h_c$  value shows that the structure is extremely effective in terms of fin area, which is further confirmed by the high Nusselt number. This is



**FIGURE 10.** Average convection coefficient of the total fin surface area (a) and the Nusselt number (b) for each design.

likely a result of a large amount of direct boundary layer disruption due to the angled placements of the airfoils, and the turbulence created in the leading- and tail-edge of each airfoil, which is further amplified by the staggered pin placement. However, it must be understood that these advantages are highly reliant on total airflow, meaning that additional testing with various airfoil geometries and placements is needed to find the optimal configuration.

The rhombi octet and TPMS gyroid fin structures similarly achieve relatively high  $h_c$  values, although at a much lower volumetric airflow than the airfoil pins. This confirms the common belief that the intricate flow paths can create a large amount of boundary layer disruption, although this comes at the expense of significantly reduced airflow. While it can be hypothesized that increasing the cell size could improve performance, considering the large gap in  $R_{Hs}$ , it is unlikely that the absolute performance of the gyroid and rhombi octet could match the airfoils. However, the high relative performance of the rhombi octet is certainly deserving of further study and experimentation with different design parameters. Finally, the BCC and TPMS diamond structures



underperform in every way, which is likely due to the structures being far too dense to allow for effective airflow, and a generally ineffective geometry for boundary layer disruption.

## V. CONCLUSION

In this article, several different heatsink prototypes implementing advanced structures were additively manufactured from AlSi10Mg and tested under real-world conditions by cooling an electrical motor coil. The prototypes are mainly compared based on their absolute and relative thermal resistance, as these parameters directly limit the power-to-weight ratio of the motor. Based on the measurement results, the following conclusions can be drawn:

- Among all the prototyped designs, the airfoil pin fin heatsink resulted in the lowest thermal resistance and therefore allows for the highest current in the motor coils. Notably, this is the case with a non-optimized case where the geometrical parameters were chosen based on literature and not tailored to the specific use-case. Furthermore, the increase in performance was achieved at a 15% lower fin mass compared to the conventional geometry.

- The best relative performance is achieved with the heatsink utilizing a rhombi-octet lattice-structure. However, this is in the case where only the fin mass of the heatsink is considered, meaning that the real performance depends heavily on the specific application.

- Heatsinks utilizing lattice structures all perform significantly worse than the conventional case in absolute thermal performance. At a fan speed of 6000 rpm, the best performing lattice was the rhombi-octet, which resulted in an 18% higher thermal resistance than the conventional fins.

- Of the two triply periodic minimal surfaces tested here, the Gyroid significantly outperformed the Diamond, while still resulting in a 27% higher thermal resistance than the conventional case at a fan speed of 6000 rpm. The TPMS Diamond, which is the only studied geometry where there are no airflow paths going straight through the heatsink, performed the worst out of all the prototypes with a thermal resistance 54% higher than the conventional case

## REFERENCES

- [1] B. M. Nafis, R. Whitt, A.-C. Iradukunda, and D. Huitink, "Additive manufacturing for enhancing thermal dissipation in heat sink implementation: A review," *Heat Transf. Eng.*, vol. 42, no. 12, pp. 967–984, Jul. 2021, doi: [10.1080/01457632.2020.1766246](#).
- [2] I. Kaur and P. Singh, "State-of-the-art in heat exchanger additive manufacturing," *Int. J. Heat Mass Transf.*, vol. 178, Oct. 2021, Art. no. 121600, doi: [10.1016/j.ijheatmasstransfer.2021.121600](#).
- [3] Y. S. See, J. Y. Ho, K. C. Leong, and T. N. Wong, "Experimental investigation of a topology-optimized phase change heat sink optimized for natural convection," *Appl. Energy*, vol. 314, May 2022, Art. no. 118984, doi: [10.1016/j.apenergy.2022.118984](#).
- [4] F. Careri, R. H. U. Khan, C. Todd, and M. M. Attallah, "Additive manufacturing of heat exchangers in aerospace applications: A review," *Appl. Thermal Eng.*, vol. 235, Nov. 2023, Art. no. 121387, doi: [10.1016/j.applthermaleng.2023.121387](#).
- [5] L. Y. X. Lum, T. N. Wong, J. Y. Ho, and K. C. Leong, "Three-dimensional topology-optimized structures for enhanced low-temperature thermal energy storage," *Appl. Energy*, vol. 362, May 2024, Art. no. 123001, doi: [10.1016/j.apenergy.2024.123001](#).
- [6] J. Y. Ho, K. K. Wong, K. C. Leong, and T. N. Wong, "Convective heat transfer performance of airfoil heat sinks fabricated by selective laser melting," *Int. J. Thermal Sci.*, vol. 114, pp. 213–228, Apr. 2017, doi: [10.1016/j.ijthermalsci.2016.12.016](#).
- [7] M. Khalil, M. I. H. Ali, K. A. Khan, and R. A. Al-Rub, "Forced convection heat transfer in heat sinks with topologies based on triply periodic minimal surfaces," *Case Stud. Thermal Eng.*, vol. 38, Oct. 2022, Art. no. 102313, doi: [10.1016/j.csite.2022.102313](#).
- [8] M. Sarap, S. Singh, A. Kallaste, A. Qureshi, H. Tiismus, T. Vaimann, and P. S. Ghahfarokhi, "Design of an additively manufactured thermal solution for an axial flux switched reluctance motor," *Case Stud. Thermal Eng.*, vol. 66, Feb. 2025, Art. no. 105805, doi: [10.1016/j.csite.2025.105805](#).
- [9] T. Menrath, A. Rosskopf, F. B. Simon, M. Groccia, and S. Schuster, "Shape optimization of a pin fin heat sink," in *Proc. 36th Semicond. Thermal Meas., Model. Manage. Symp. (SEMI-THERM)*, Mar. 2020, pp. 10–16, doi: [10.23919/SEMI-THERM50369.2020.9142830](#).
- [10] E. M. Dede, S. N. Joshi, and F. Zhou, "Topology optimization, additive layer manufacturing, and experimental testing of an air-cooled heat sink," *J. Mech. Design*, vol. 137, no. 11, pp. 1–15, Nov. 2015, doi: [10.1115/1.4030989](#).
- [11] N. P. Nguyen, E. Maghsoudi, S. N. Roberts, D. C. Hofmann, and B. Kwon, "Understanding heat transfer and flow characteristics of additively manufactured pin fin arrays through laser-induced fluorescence and particle image velocimetry," *Int. J. Heat Mass Transf.*, vol. 222, May 2024, Art. no. 125198, doi: [10.1016/j.ijheatmasstransfer.2024.125198](#).
- [12] M. R. Haque, R. R. Redu, M. A.-A. Rafi, M. M. Haque, and M. Z. Rahman, "Numerical investigation of heat transfer performance for rectangular, elliptical, and airfoil shaped pin fin heatsinks through the novel combination of perforation and bulge inserts," *Int. Commun. Heat Mass Transf.*, vol. 138, Nov. 2022, Art. no. 106352, doi: [10.1016/j.icheatmasstransfer.2022.106352](#).
- [13] J. Y. Ho, K. C. Leong, and T. N. Wong, "Experimental and numerical investigation of forced convection heat transfer in porous lattice structures produced by selective laser melting," *Int. J. Thermal Sci.*, vol. 137, pp. 276–287, Mar. 2019, doi: [10.1016/j.ijthermalsci.2018.11.022](#).
- [14] J. Y. Ho, K. C. Leong, and T. N. Wong, "Additively-manufactured metallic porous lattice heat exchangers for air-side heat transfer enhancement," *Int. J. Heat Mass Transf.*, vol. 150, Apr. 2020, Art. no. 119262, doi: [10.1016/j.ijheatmasstransfer.2019.119262](#).
- [15] J. Y. Ho and K. C. Leong, "Cylindrical porous inserts for enhancing the thermal and hydraulic performance of water-cooled cold plates," *Appl. Thermal Eng.*, vol. 121, pp. 863–878, Jul. 2017, doi: [10.1016/j.applthermaleng.2017.04.101](#).
- [16] T. Dixit, P. Nithiarasu, and S. Kumar, "Numerical evaluation of additively manufactured lattice architectures for heat sink applications," *Int. J. Thermal Sci.*, vol. 159, Jan. 2021, Art. no. 106607, doi: [10.1016/j.ijthermalsci.2020.106607](#).
- [17] D. Mahmoud, S. R. S. Tandel, M. Yakout, M. Elbestawi, F. Mattiello, S. Paradiso, C. Ching, M. Zaher, and M. Abdelnabi, "Enhancement of heat exchanger performance using additive manufacturing of gyroid lattice structures," *Int. J. Adv. Manuf. Technol.*, vol. 126, nos. 9–10, pp. 4021–4036, Jun. 2023, doi: [10.1007/s00170-023-11362-9](#).
- [18] T. Dixit, E. Al-Hajri, M. C. Paul, P. Nithiarasu, and S. Kumar, "High performance, microarchitected, compact heat exchanger enabled by 3D printing," *Appl. Thermal Eng.*, vol. 210, Jun. 2022, Art. no. 118339, doi: [10.1016/j.applthermaleng.2022.118339](#).
- [19] W. Tang, H. Zhou, Y. Zeng, M. Yan, C. Jiang, P. Yang, Q. Li, Z. Li, J. Fu, Y. Huang, and Y. Zhao, "Analysis on the convective heat transfer process and performance evaluation of triply periodic minimal surface (TPMS) based on diamond, gyroid and twp," *Int. J. Heat Mass Transf.*, vol. 201, Feb. 2023, Art. no. 123642, doi: [10.1016/j.ijheatmasstransfer.2022.123642](#).
- [20] M. Sarap, H. Tiismus, A. Kallaste, M. Saarna, M. Kolnes, P. Shams Ghahfarokhi, and T. Vaimann, "Electrical and thermal anisotropy in additively manufactured AlSi10Mg and Fe-Si samples," *Machines*, vol. 13, no. 1, p. 1, Dec. 2024, doi: [10.3390/machines13010001](#).
- [21] J. R. Culham and Y. S. Muzychka, "Optimization of plate fin heat sinks using entropy generation minimization," *IEEE Trans. Compon. Packag. Technol.*, vol. 24, no. 2, pp. 159–165, Jun. 2001, doi: [10.1109/6144.926378](#).

- [22] P. Teertstra, M. M. Yovanovich, J. R. Culham, and T. Lenczyk, "Analytical forced convection modeling of plate fin heat sinks," in *Proc. 15th Annu. IEEE Semicond. Thermal Meas. Manage. Symp.*, San Diego, CA, USA, Jul. 1999, pp. 34–41, doi: [10.1109/STHERM.1999.762426](https://doi.org/10.1109/STHERM.1999.762426).



**MARTIN SARAP** (Graduate Student Member, IEEE) received the B.Sc. and M.Sc. degrees in electrical power engineering from Tallinn University of Technology, Estonia, in 2018 and 2021, respectively, where he is currently pursuing the Ph.D. degree with the Department of Electrical Power Engineering and Mechatronics. He is an early-stage Researcher with the Department of Electrical Power Engineering and Mechatronics, Tallinn University of Technology. His main

research interests include thermal solutions for additively manufactured electrical machines.



**SHALINI SINGH** received the B.Tech. degree from AKGEC, India, and the M.Tech. and Ph.D. degrees in mechanical engineering from IIT Indore, in 2023. She is currently a Postdoctoral Research Fellow with the University of Alberta, specializing in metal additive manufacturing, smart materials, and material characterization. She has published extensively and serves as a reviewer for several leading materials science journals. Her research interests include process

optimization, integration of shape memory alloys, and real-time monitoring in additive manufacturing.



**ANTS KALLASTE** (Senior Member, IEEE) was born in Pärnu, Estonia, in 1980. He received the B.Sc., M.Sc., and Ph.D. degrees in electrical engineering from Tallinn University of Technology, Tallinn, Estonia, in 2004, 2006, and 2013, respectively. He is currently a Professor of electrical machines with the Department of Electrical Power Engineering and Mechatronics, Tallinn University of Technology. In addition, he is holding the position of the Head of the Chair of Electrical

Machines Research Group. He is a member of the Estonian Society of Moritz Hermann Jacobi.



**AHMED JAWAD QURESHI** is currently a Professor and the Engineering Research Chair of the Advanced Manufacturing Processes and Automation, Department of Mechanical Engineering, University of Alberta. He specializes in additive manufacturing, robust and transdisciplinary engineering design, and process automation. He is recognized for bridging academic research with industrial innovation to advance next-generation manufacturing solutions. His current research

interests include robotic wire-based AM, plasma-transferred arc technologies for oil sands, geometric deviation modeling, ferromagnetic 3D printing, and advanced polymer-metal composite materials.



**HANS TIISMUS** received the B.Sc. and M.Sc. degrees in applied physics from Tallinn University of Technology (TalTech), Estonia, in 2011 and 2013, respectively, and the Ph.D. degree from the Electrical Machine Research Group (EMG), Department of Electrical Power Engineering and Mechatronics, TalTech, in 2022. He is currently a full-time Researcher with TalTech. His research activities (which have culminated with more than 30 publications) have been focused on additive manufacturing (AM) of electromagnetic materials and electrical machinery. In 2022, he received the Estonian National Research Award in technical sciences for the research cycle "Additively Manufactured Electrical Machines."



**TOOMAS VAIMANN** (Senior Member, IEEE) was born in Pärnu, Estonia, in 1984. He received the B.Sc., M.Sc., and Ph.D. degrees in electrical engineering from Tallinn University of Technology, Tallinn, Estonia, in 2007, 2009, and 2014, respectively. He is currently a Senior Researcher with the Department of Electrical Power Engineering and Mechatronics, Tallinn University of Technology. Internationally, he has been a Postdoctoral Researcher with the Department of Electrical Engineering and Automation, Aalto University, Espoo, Finland, and works as a Visiting Professor with the Faculty of Control Systems and Robotics, ITMO University, St. Petersburg, Russia. He has been working in several companies as an Electrical Engineer. His main research interest includes the diagnostics of electrical machines. He is a member of the Estonian Society of Moritz Hermann Jacobi and the Estonian Society for Electrical Power Engineering.



**PAYAM SHAMS GHAIFAROKHI** (Senior Member, IEEE) was born in Iran, in 1986. He received the B.Sc. degree in electrical power engineering from Islamic Azad University Najafabad Branch (IAUN), Najafabad, Iran, in 2010, the M.Sc. degree in electrical power engineering from Newcastle University, Newcastle upon Tyne, U.K., in 2011, and the Ph.D. degree in electrical engineering and machines from Tallinn University of Technology, Tallinn, Estonia, in 2019. He pursued

a postdoctoral research from Riga Technical University, Riga, Latvia, and the CISE—Electromechatronic Systems Research Centre, Covilhã, Portugal. He currently holds positions as an Academy Research Fellow and a Senior Researcher with the Faculty of Information Technology and Communication Sciences, Electrical Engineering Unit, Tampere University, Tampere, Finland. His primary research interests include the electromagnetic design and thermal management of electric motors for traction applications.

...



**Publication VI**

M. Sarap, A. Kallaste, T. Vaimann, P.S. Ghahfarokhi, Additively Manufactured and Topology Optimized Heatsink for a Propulsion Motor, in: 2024 Int. Conf. Electr. Mach. ICEM, 2024: pp. 1–6. <https://doi.org/10.1109/ICEM60801.2024.10700108>.



# Additively Manufactured and Topology Optimized Heatsink for a Propulsion Motor

Martin Sarap,  
Department of Electrical Power  
Engineering and Mechatronics  
Tallinn University of Technology  
Tallinn, Estonia  
[martin.sarap1@taltech.ee](mailto:martin.sarap1@taltech.ee)

Ants Kallaste, Toomas Vaimann  
Department of Electrical Power  
Engineering and Mechatronics  
Tallinn University of Technology  
Tallinn, Estonia

Payam Shams Ghahfarokhi  
Faculty of Information Technology and  
Communication Sciences  
Tampere University  
Tampere, Finland

**Abstract**— Additive manufacturing, used in conjunction with topology optimization, allows the realization of complex algorithmically generated geometries with improved physical characteristics. In this paper, these methods are used to enhance the performance of an electrical propulsion drive via improved cooling capabilities. An air-cooled heatsink is modelled, optimized, and additively manufactured, after which practical measurements are performed. Finally, comparisons to a similarly sized conventional heatsink are used to demonstrate the benefits and potential limitations of topology optimization and additive manufacturing in the field of electrical machines.

**Keywords**—3D printing, topology optimization, electrical machines.

## I. INTRODUCTION

The ongoing electrification of aviation highlights the strive towards more power-dense and efficient propulsion drives [1]. In achieving these goals, the limitations are often thermal, meaning that the technologies used for cooling the motors must evolve to manage the ever-increasing requirements. Among the methods of advanced thermal management, a noteworthy technology is topology optimization (TO), which is used to produce various solutions with optimized geometries. However, it has not yet seen wide use in the field of electrical machines.

Topology optimization, an algorithmic way of distributing material in a defined design space through successive iterations, is a powerful tool for creating optimized geometries for a number of applications. In electromagnetic design, TO has been used to successfully improve the design rotors [2], [3], magnets [4] and stators [5]. It is, however, more widely used in thermal engineering, where a multitude of [6], [7], [8] solutions can be found in the literature. As a rule, these employ complex geometries, which are infeasible in the context of conventional manufacturing methods. Therefore, more versatile methods, such as metal additive manufacturing (AM), must be used for realizing these types of optimized geometries.

The synergy between AM and TO is evident in the scientific literature, where the physical prototypes of different kinds of TO solutions are seldom built with anything other than AM. In the field of electrical machines, metal-based AM methods, such as selective laser melting (SLM), are used for creating soft [9] and hard [10] magnetic components, different types of conductors [11], and various thermal solutions [12]. Often the main point of interest in this research is the realization of complex geometries, made possible by the inherent design freedom offered by AM. Creating physical

prototypes of TO thermal solutions for cooling electrical machines is therefore a natural step forward.

Propulsion drives for electric aircraft provide an excellent opportunity for the synergistic implementation of TO and AM. In a typical aircraft, the shaft of the motor is directly attached to the propeller, which, in the process of producing lift, moves a large amount of air in the direction of the motor. The resulting high-velocity airflow can be effectively utilized for cooling the motor by implementing a heatsink on the stator. In the case of propulsion, where maximal thrust-to-weight ratio is desirable, the mass of the drive must also be considered. This creates a well-defined optimization problem for an actively air-cooled heatsink, where the gains in thermal performance must be balanced with keeping the mass of the heatsink low.

In this paper, a topology optimized actively air-cooled heatsink prototype for an electric propulsion drive is modelled using non-isothermal computational fluid dynamics (CFD), and the resulting geometry is additively manufactured from the aluminum alloy AlSi10Mg. The cooling solution is implemented on a commercially available inner-rotor brushless DC motor, with which practical temperature measurements are performed. Additionally, a conventional finned heatsink is parametrically optimized and manufactured to provide context for the TO heatsink. The results of the measurements demonstrate improved absolute thermal performance for the TO heatsink, illustrating the possible benefits of using this technology in conjunction with AM in the field of electrical machines.

## II. METHODOLOGY

### A. Problem Formulation

The goal of the proposed thermal solution is to maximize the thrust-to-weight ratio of the propulsion drive at a given temperature increase. To provide context for the results, the topology optimized heatsink  $HS_{TO}$  is compared to a conventional parametrically optimized finned design  $HS_{PO}$ . Both heatsinks are additively manufactured using SLM and the performance of each is experimentally verified.

The motor under question is a commercially available inner-rotor brushless DC motor [13], the shaft of which is directly attached to a 12x4.5 propeller (Fig. 1). The heatsink is placed directly on the stator outer surface, covering the entire stack length. The relevant performance and geometrical parameters of the drive are presented in Fig. 2 and Table I. The thrust of the drive  $T$  (N) is directly measured (in the case where there is no heatsink on the motor), while the motor heat losses  $Q$  (W) are calculated according to the measured phase winding resistance.

This work was supported by the Estonian Research Council grant (PRG-1827).



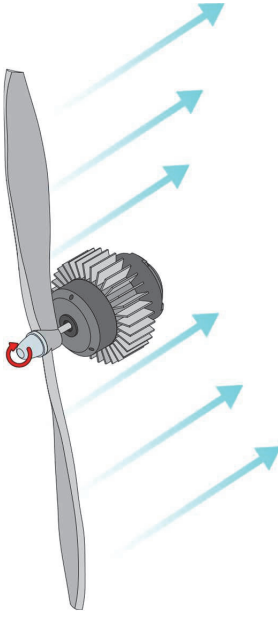


Fig. 1. Visual description of the proposed drive and cooling solution.

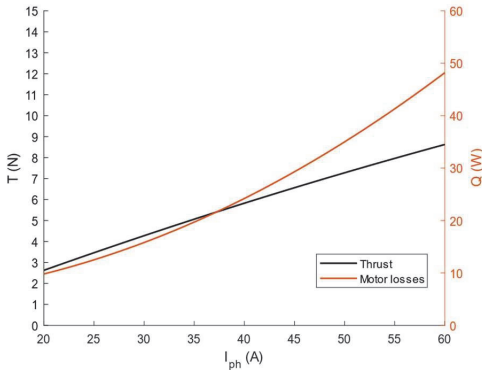


Fig. 2. Performance parameters of the drive.

TABLE I. MAIN PARAMETERS OF THE DRIVE

Parameter	Value
Number of rotor poles	2
Motor outer diameter	34.3 mm
Stator stack length	17 mm
Motor mass	167 g
Phase resistance $R_{ph}$	0.004 $\Omega$
Propeller radius $r_{prop}$	15.1 mm

As shown in Fig. 2, the relationship between thrust and phase current is approximately linear in the measured range, meaning that the goal can simply be defined in terms of improving the maximum allowable current of the motor. In most practical cases, the maximum phase current is limited by cooling, making it a function of the motor's thermal resistance  $R_{TH}$  and a given temperature rise  $\Delta T$ . In terms of design

variables, the weight of the drive  $W$  (N) depends on the volume  $V_{HS}$  and specific density of the heatsink. By defining the heatsink material and a specific temperature rise, an optimization problem for the cooling system is formed:

$$\text{maximize: } \frac{T}{W} = \frac{f(R_{HS})}{f(V_{HS})} \quad (1)$$

### B. Parametric Optimization model

The parametrically optimized heatsink is modelled and manufactured to provide a fair comparison for the TO heatsink. The design variables of this heatsink are the number of fins  $n_{fin}$ , the thickness of the fin  $d_{fin}$  (mm), and the length of the fin  $L_{fin}$  (mm). The specific values for these variables are found via parametric optimization in the 3D non-isothermal CFD model (Fig. 3). During the optimization process, the phase current in the model is set at  $I_{ph} = 60$  A, which results in a thrust of  $T = 8.4$  N for the drive.

The model built in COMSOL Multiphysics consists of a solid 1 mm thick cylindrical base with radially attached rectangular fins. The surrounding air volume is modelled significantly larger than the heatsink and the flow is modelled as laminar and incompressible, with no-slip conditions on the relevant walls. The overall size of the mathematical model is reduced by utilizing rotational symmetry, which significantly increases the density of the  $\sim 3 \cdot 10^6$  element mesh.

The heat generated by the motor is modelled as a boundary heat flux condition imposed on the internal wall of the heatsink base. The value for the total heat flux at any current is calculated using the temperature dependent copper losses and a fixed core loss of 5 W (estimated value). At loads close to the operating point, the core losses of the 2-pole motor become less relevant, justifying the fixed value. The total heat flux is therefore  $Q = 3 \cdot I_{ph}^2 \cdot R_{ph}(\Delta T) + 5$ .

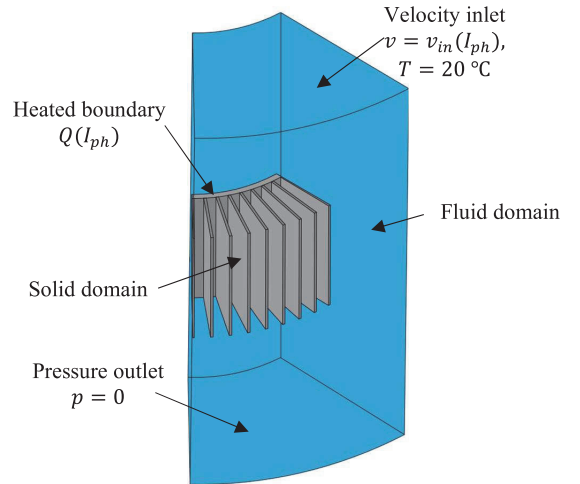


Fig. 3. The non-isothermal CFD model of  $HS_{po}$ .

The airflow created by the propeller is modelled as a uniform inlet velocity of magnitude  $v_{in}$  and an outlet at ambient pressure. The value for  $v_{in}$  is the exit velocity of air, derived from the propeller thrust equation [14] in the case of a 0 m/s inlet velocity:

$$v_{in} = \sqrt{\frac{2T}{\rho_{air} \cdot \pi r_{prop}^2}} \quad (2)$$

where  $\rho_{air}$  is the density of air at 20 °C.

The mass of the drive consists of the motor and the heatsink, which is calculated for each iteration by multiplying the volume of the heatsink with the density of the solid material  $\rho_{Al} = 2.67 \text{ g / (cm}^3\text{)}$  [15]. The thermal performance of the heatsink is defined by the average temperature increase of the heatsink inner surface  $A_{HS}$ , which is limited to 10 °C in the PO model (the corresponding temperature increase in the end-winding is substantially higher due to the relatively high thermal resistances in the system). The parametric optimization problem is thus characterized as following:

$$\text{minimize: } V_{HS} = f(L_{fin}, d_{fin}, n_{fin}) \quad (3)$$

$$\text{subject to: } 2 < L_{Fin} < 30 \text{ mm}$$

$$0.5 < d_{Fin} < 2 \text{ mm}$$

$$2 < n_{Fin} < 100$$

$$\frac{1}{A_H} \int \Delta T \cdot dA_H \leq 10 \text{ K}$$

### C. Topology Optimization model

The TO model presented in Fig. 4 is based on free and porous media flow - a method that has previously been successfully implemented in literature [16], [17]. In this case the fluid is modelled as (approximately) fully permeable, and the heatsink as an effectively impermeable material (porosity is set equal to 1 in both cases). The airflow in the model is otherwise set up analogously to the PO case and the parametrically optimized  $L_{fin}$  value is used to define the TO design space.

The optimization of the heatsink geometry is carried out using the density-based model where each region in the TO design space is described by a continuous density variable  $\theta = 0 \dots 1$ , with 0 representing a completely fluid and 1 an entirely solid material. The intermediate values, therefore, represent an in-between material with a proportional mixture of parameters. To end up with a physically meaningful and manufacturable result, it is necessary to converge the design space into (as close as possible) purely  $\theta = 0$  and  $\theta = 1$  regions. This is aided by penalizing the intermediate density values using the SIMP method:

$$f_{TO}(\theta) = f_{min} + \theta^p \cdot (f_{max} - f_{min}) \quad (4)$$

where  $p = 3$  is the SIMP penalization exponent.

The material parameters, for which the SIMP interpolation is applied, are thermal conductivity ( $\lambda_{air} = 0.03$  and  $\lambda_{Al} = 150 \text{ W / (m} \cdot \text{K)}$  [18]), specific heat capacity ( $C_{air} = 1$  and  $C_{Al} = 0.95 \text{ J / (g} \cdot \text{K)}$  [19]), density, and impermeability ( $P_{air} = 10^7$  and  $P_{Al} = 10^{11} \text{ m}^{-2}$ ). The appropriate values for the impermeability limits are determined manually to ensure the mathematical convergence of the model. All other parameters are taken as the conventional values for air.

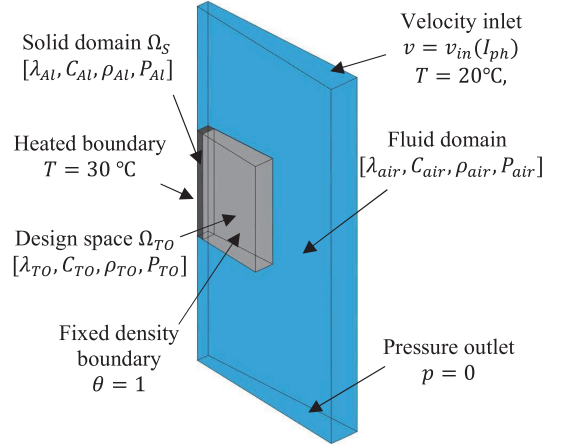


Fig. 4. The non-isothermal CFD model of  $HS_{TO}$ .

The TO model takes the  $L_{HS}$  value from the PO model with the goal of maximizing the thermal performance of the heatsink at the same  $I_{ph}$  (and therefore  $v_{in}$ ) value. In this case, the weight of the heatsink is not directly considered although it is limited by the maximum allowed average density of the design domain.

The TO model also utilizes radial symmetry for a reduced model size, although, in this case, only half of a single fin is modelled, as this is the smallest section required to fully define the characteristic geometry of the heatsink. By imposing a fixed density of  $\theta = 1$  on the mirrored boundary, and dimensioning the sector based on  $n_{fin}$ , the model is biased towards creating a finned structure similar to the  $HS_{PO}$  case. However, in the TO case, the shape of the fin can be any arbitrary shape and is not bound to a predefined list of parameters. It is found that imposing this boundary condition on the model helps the TO algorithm converge on a more effective result.

The thermal loading of the model is somewhat altered from the PO model with heat flux boundary being substituted for a constant temperature boundary at 10 °C. This does not alter the physical characteristics of the model, but it greatly improves convergence and the performance of the final result.

The performance of each solution is calculated using the objective function  $f_O$ , which sums the total domain heat flux in the base of the heatsink (5), essentially calculating the thermal resistance of the heatsink. The resulting optimized geometry is therefore one which can transfer the largest amount of heat from the heatsink inner surface. The proportion of the solid fraction is limited by the average density of the domain space  $\theta_a$ , which is set to 0.4 in this case. The topology optimization problem is thus characterized as:

$$\text{maximize: } f_O = \int_{\Omega_S} \mathbf{q} \cdot dV_S \quad (5)$$

$$\text{subject to: } \theta_a = \frac{1}{V_D} \int_{\Omega_{TO}} \theta \cdot dV_D \leq 0.4$$

$$0 \leq \theta \leq 1$$



The minimum element size inside the design domain is controlled by introducing a Helmholtz filtering radius (0.45 mm), and the optimization problem is solved using the MMA method. The maximum mesh element size in the design space is limited to 0.4 mm, which results in a mesh with approximately  $10^5$  elements. The relatively coarse mesh means that the model can be run on a modern consumer CPU with a total solution time of  $\sim 24$  h for the roughly 80 iterations.

### III. EXPERIMENTAL PROCEDURE

#### A. Modelling Results

Parametrically optimizing the conventional design results in a heatsink with 32 fins, each with a thickness of 0.73 mm and a length of 9.6 mm, which sets the outer diameter of the heatsink at 55.2 mm. The modelled average temperature rise in the case of  $I_{ph} = 60$  A is 11.8 °C (Fig. 5a). The mass and thermal resistance of the heatsink is 16 g and 0.24 K/W respectively.

The output of the TO model shown in Fig. 6a is a continuous space of  $\theta$  values, which can be used to define a solid geometry (Fig. 6b) by imposing a minimum density  $\theta_{min}$  value. This defines the boundary between the solid and non-solid material, which in this case is set to 0.4 (meaning that any region with  $\theta \geq 0.4$  is defined as a solid). The modelled average temperature rise in the case of  $I_{ph} = 60$  A is 7.7 °C (Fig. 5b). While the TO heatsink has the same outer diameter and fin number as the PO model, its mass and thermal resistance values are 32 g and 0.16 K/W respectively.

Adjusting the value of  $\theta_{min}$  determines the specific output geometry, meaning that a similar mass to the PO model can be achieved in the model. However, limiting the solid volume via increasing  $\theta_{min}$  results in a solid body with extremely thin walls, posing a manufacturing challenge. Therefore, a value of  $\theta_{min} = 0.4$  is used for the prototype.

The TO heatsink design incorporates semi-open channels that redirect the airflow radially away from the heatsink base, as shown by the velocity arrow plot in Fig. 7. Creating radial airflow is opposed to conventional design, where the aerodynamic resistance in the axial direction is usually minimized. Even though the change in flow direction can be detrimental, the added surface area (and possibly the disruption of the boundary layer) seems to be overall beneficial to the thermal performance. Fig. 8 shows the formation of these channel over the course of the iterations. It should be noted that similar channels tend to appear across different models using other variables, suggesting a true utility in the design. Therefore, incorporating similar ideas in conventional designs should be considered.

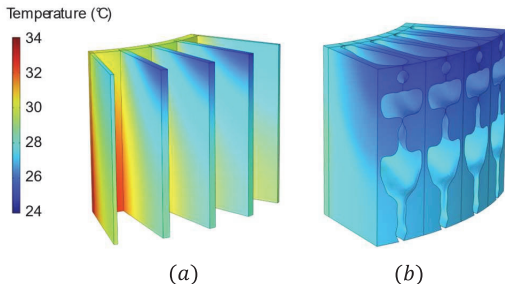


Fig. 5. Temperature distributions of  $HS_{PO}$  (a) and  $HS_{TO}$  (b) sectors,

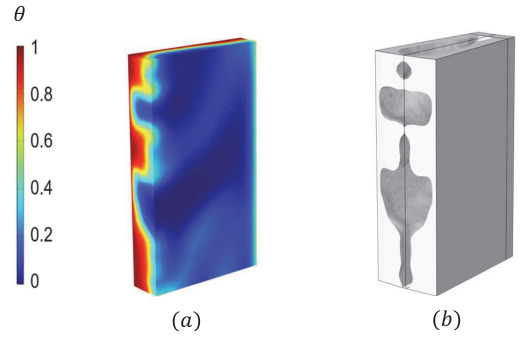


Fig. 6. Material volume factor distributions of and  $HS_{TO}$  (a), and the solid geometry of a single  $HS_{TO}$  sector (b).

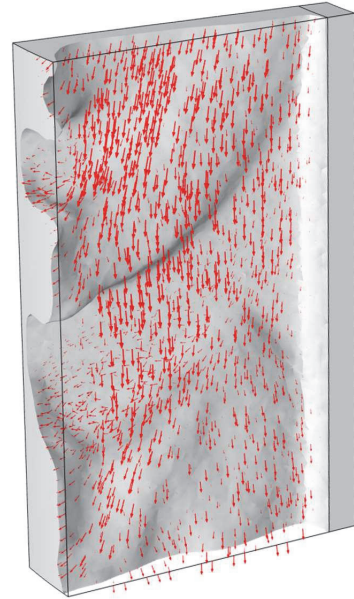


Fig. 7. Airflow distribution in the  $HS_{TO}$  fin gap.

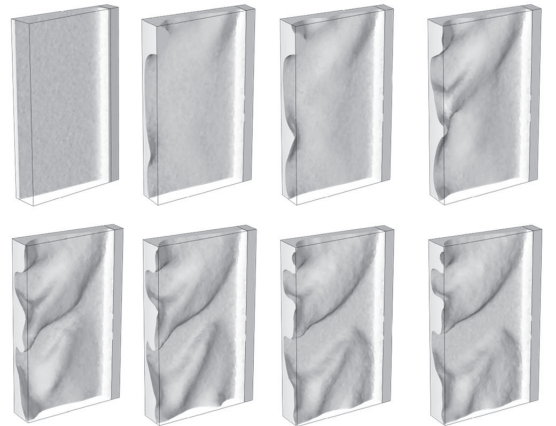


Fig. 8. Evolution of the  $HS_{TO}$  design iterations.

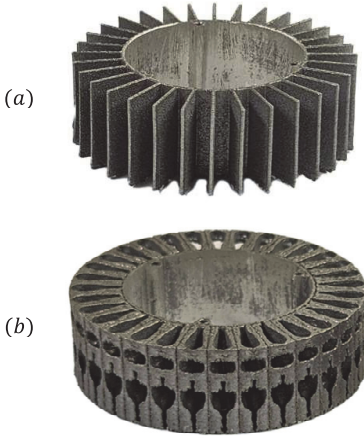


Fig. 9. AM Prototypes for  $HS_{PO}$  (a) and  $HS_{TO}$  (b).

### B. Additively Manufactured Prototypes

Prototypes of the heatsink models are produced via SLM from AlSi10Mg using the SLM Solutions 280 2.0 metal 3D printer. The specific material was chosen for its relatively high thermal conductivity compared to other SLM-manufacturable materials. The as-built parts are heat-treated at 300 °C for 2h to improve the material's thermal properties. The masses of the AM  $HS_{PO}$  and  $HS_{TO}$  samples presented in Figs. 9a and 9b are 9.5 and 25 g respectively; the difference from the models most likely arises from subtle dimensional differences. Both prototypes suffer from minor warping and edge imperfections, although the overall geometry is sufficiently representative of the models.

### C. Load Testing

During the load testing, the heatsinks are press fitted on the stator with thermal compound applied on the mating surfaces. The motor is supplied with a constant  $I_{ph}$  (measured via current clamps) and the thrust created by the propeller is measured using a thrust stand [20]. Steady-state temperatures (determined using a precision data logger) for each current level are measured with a PT1000 sensor thermally bonded to the stator end-windings on the backside of the motor, shielded from direct airflow. The measurement setup for the  $HS_{TO}$  case is presented in Fig. 10.

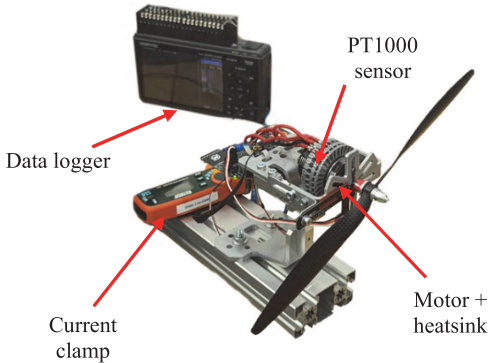


Fig. 10. Measurement setup for the  $HS_{TO}$  case.

## IV. RESULTS AND DISCUSSION

Measurements results for the PO and TO heatsinks presented in Fig. 11 show that the TO heatsink clearly outperforms the PO counterpart in absolute terms by achieving a lower temperature at every current level. At the target current of  $I_{ph} = 60$  A, the TO heatsink resulted in an approximately 4 °C lower end-winding temperature than the PO heatsink, leading to a 0.08 K/W reduction in total thermal resistance.

Fixing the maximum end-winding temperature rise to a set value of  $\Delta T = 60$  °C (chosen arbitrarily for comparison purposes) makes it possible to calculate the thrust-to-weight ratio of the systems by interpolating the maximum phase current. In the case of  $HS_{PO}$ , the maximum temperature rise is reached at a phase current of 49.8 A and 7.2 N of thrust. The mass of the drive is found by adding the masses of the heatsink and the motor, resulting in a combined weight of 1.7 N ( $g = 9.81 \text{ m/s}^2$ ). The thrust-to-weight ratio is therefore 4.2. The maximum phase current for  $HS_{TO}$  is 51.4 A, which produces a thrust of 7.4 N. The weight of the TO drive is 1.9 N, resulting in a thrust-to-weight ratio of 3.9, which is a 7.1 % decrease compared to the PO heatsink.

The impact of increased thermal performance for the heatsink is somewhat dulled by the various thermal resistances (i.e. the winding insulation material) in the motor. The total internal contact resistance  $R_0$  can be estimated by subtracting the simulated heatsink thermal resistance from the practical results, which yields an approximate value of 1.5 K/W, compared to the 0.24 and 0.16 K/W for the  $HS_{PO}$  and  $HS_{TO}$  respectively. Therefore, most of the system's thermal resistance at the specified operating point is caused by  $R_0$ , meaning that the winding temperature is essentially insensitive to the heatsink geometry.

The significantly reduced thermal resistance of the TO heatsink could be applied more effectively if used to cool a motor with lower  $R_0$ , such as one utilizing direct-conductor cooling. Additionally, the mass of  $HS_{TO}$  could be reduced by increasing the value of  $\theta_{min}$ , although in this specific case, that approach results in non-manufacturable models. Finally, in a less weight-dependent application, the improved thermal performance of the TO heatsink would yield a larger overall benefit.

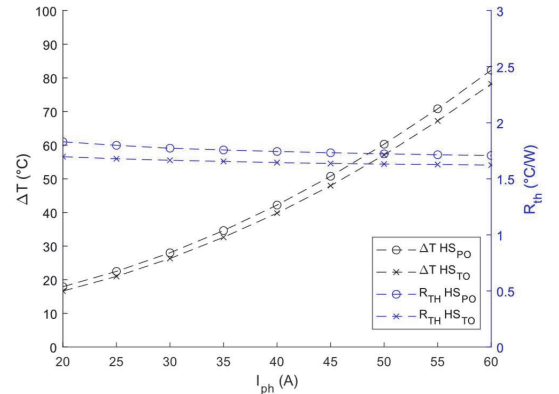


Fig. 11. Measured temperature rises and the corresponding thermal resistance values for both heatsinks.

## V. CONCLUSIONS

Topology optimization can be used in conjunction with additive manufacturing to produce heatsinks with significantly improved performance. In this paper, the synergy between TO and AM was applied on an electric propulsion drive, improving its cooling performance, albeit without benefits to the overall thrust-to-weight ratio. The TO heatsink provided a 33 % reduction in thermal resistance compared to the conventional parametrically optimized case while increasing the weight of the drive by 11 %.

Two impactful steps can be taken in future work. Firstly, applying the TO heatsink on a system with low internal thermal resistance will result in a larger impact in the effective performance gain. Secondly, the optimization process can be taken further in several ways, such as optimizing for the fluid flow in addition to temperature (multi-objective TO), incorporating turbulence in the fluid simulation, and reducing the amount of boundary conditions to give more freedom to the optimization algorithm. This can be done in conjunction with more effective manipulation of the resulting geometry, and improved manufacturing capabilities, so that an effective and light-weight solution could be successfully manufactured.

## REFERENCES

- [1] "Large electric machines for aircraft electric propulsion - Zhang - 2018 - IET Electric Power Applications - Wiley Online Library." Accessed: Feb. 22, 2024. [Online]. Available: <https://ietresearch.onlinelibrary.wiley.com/doi/10.1049/iet-epa.2017.0639>
- [2] A. Credo, G. Fabri, M. Villani, and M. Popescu, "Adopting the Topology Optimization in the Design of High-Speed Synchronous Reluctance Motors for Electric Vehicles," *IEEE Trans. Ind. Appl.*, vol. 56, no. 5, pp. 5429–5438, Sep. 2020, doi: 10.1109/TIA.2020.3007366.
- [3] M. Garibaldi, C. Gerada, I. Ashcroft, and R. Hague, "Free-Form Design of Electrical Machine Rotor Cores for Production Using Additive Manufacturing," *J. Mech. Des.*, vol. 141, no. 071401, Mar. 2019, doi: 10.1115/1.4042621.
- [4] C. Huber et al., "Topology optimized and 3D printed polymer-bonded permanent magnets for a predefined external field," *J. Appl. Phys.*, vol. 122, no. 5, p. 053904, Aug. 2017, doi: 10.1063/1.4997441.
- [5] T. Cheri  re et al., "Multi-material topology optimization using Wachspress interpolations for designing a 3-phase electrical machine stator," *Struct. Multidiscip. Optim.*, vol. 65, no. 12, p. 352, Nov. 2022, doi: 10.1007/s00158-022-03460-1.
- [6] Y. S. See, J. Y. Ho, K. C. Leong, and T. N. Wong, "Experimental investigation of a topology-optimized phase change heat sink optimized for natural convection," *Appl. Energy*, vol. 314, p. 118984, May 2022, doi: 10.1016/j.apenergy.2022.118984.
- [7] E. M. Dede, S. N. Joshi, and F. Zhou, "Topology Optimization, Additive Layer Manufacturing, and Experimental Testing of an Air-Cooled Heat Sink," *J. Mech. Des.*, vol. 137, no. 11, p. 111403, Nov. 2015, doi: 10.1115/1.4030989.
- [8] D. Mart  nez-Maradiaga, A. Damonte, A. Manzo, J. H. K. Haertel, and K. Engelbrecht, "Design and testing of topology optimized heat sinks for a tablet," *Int. J. Heat Mass Transf.*, vol. 142, p. 118429, Oct. 2019, doi: 10.1016/j.ijheatmasstransfer.2019.07.079.
- [9] H. Tiismus, A. Kallaste, T. Vaimann, and A. Rass  lkin, "State of the art of additively manufactured electromagnetic materials for topology optimized electrical machines," *Addit. Manuf.*, vol. 55, p. 102778, Jul. 2022, doi: 10.1016/j.addma.2022.102778.
- [10] J. Ja  imovi   et al., "Net Shape 3D Printed NdFeB Permanent Magnet," *Adv. Eng. Mater.*, vol. 19, no. 8, p. 1700098, 2017, doi: 10.1002/adem.201700098.
- [11] N. Simpson, S. P. Munagala, A. Catania, F. Derguti, and P. H. Mellor, "Functionally Graded Electrical Windings Enabled by Additive Manufacturing," in 2022 International Conference on Electrical Machines (ICEM), Sep. 2022, pp. 1477–1483. doi: 10.1109/ICEM51905.2022.9910912.
- [12] M. Sarap, A. Kallaste, P. Shams Ghahfarokhi, H. Tiismus, and T. Vaimann, "Utilization of Additive Manufacturing in the Thermal Design of Electrical Machines: A Review," *Machines*, vol. 10, no. 4, Art. no. 4, Apr. 2022, doi: 10.3390/machines10040251.
- [13] H. N. America, "XERUN V10 Motor G3 - Modified (3.5-10.5T)," HOBBYWING North America. Accessed: Feb. 26, 2024. [Online]. Available: <https://www.hobbywingdirect.com/products/xerun-v10-g3-motors>
- [14] "Propeller Thrust," Glenn Research Center | NASA. Accessed: Feb. 20, 2024. [Online]. Available: <https://www1.grc.nasa.gov/beginners-guide-to-aeronautics/propeller-thrust/>
- [15] N. Limbasiya, A. Jain, H. Soni, V. Wankhede, G. Kroleczyk, and P. Sahlot, "A comprehensive review on the effect of process parameters and post-process treatments on microstructure and mechanical properties of selective laser melting of AlSi10Mg," *J. Mater. Res. Technol.*, vol. 21, pp. 1141–1176, Nov. 2022, doi: 10.1016/j.jmrt.2022.09.092.
- [16] J. Alexandersen, O. Sigmund, and N. Aage, "Large scale three-dimensional topology optimisation of heat sinks cooled by natural convection," *Int. J. Heat Mass Transf.*, vol. 100, pp. 876–891, Sep. 2016, doi: 10.1016/j.ijheatmasstransfer.2016.05.013.
- [17] X. Dong and X. Liu, "Multi-objective optimal design of microchannel cooling heat sink using topology optimization method," *Numer. Heat Transf. Part Appl.*, vol. 77, no. 1, pp. 90–104, Jan. 2020, doi: 10.1080/10407782.2019.1682872.
- [18] M. Sarap, A. Kallaste, P. S. Ghahfarokhi, H. Tiismus, and T. Vaimann, "The Effect of Build Direction on the Thermal Conductivity of Additively Manufactured AlSi10Mg and Silicon-steel Samples," in 2022 International Conference on Electrical Machines (ICEM), Sep. 2022, pp. 538–543. doi: 10.1109/ICEM51905.2022.9910944.
- [19] E. C. Silva, J. A. Candiango, S. J. Rodrigues,   . M. Sampaio, and A. J. Pontes, "Hybrid Manufacturing of Aluminium Parts Combining Additive and Conventional Technologies—Mechanical and Thermal Properties," *J. Manuf. Mater. Process.*, vol. 6, no. 2, Art. no. 2, Apr. 2022, doi: 10.3390/jmmp6020040.
- [20] T. Robotics, "Series 1585: Drone Thrust Stand," Tyto Robotics. Accessed: Feb. 20, 2024. [Online]. Available: <https://www.tytorobotics.com/pages/series-1580-1585>

# Curriculum vitae

## Personal data

Name:	Martin Sarap
Date of birth:	03.02.1996
Place of birth:	Kuressaare
Citizenship:	Estonia

## Contact data

E-mail:	martin.sarap1@taltech.ee
---------	--------------------------

## Education

2021–2025	PhD, Tallinn University of Technology, Department of Electrical Power Engineering and Mechatronics
2018–2021	MSc, Tallinn University of Technology, Department of Electrical Power Engineering and Mechatronics
2015–2018	BSc, Tallinn University of Technology, Department of Electrical Power Engineering and Mechatronics
2012–2015	High school, Pääsküla Gymnasium

## Language competence

Estonian	Native
English	Fluent

## Professional employment

2021–	Early-Stage Researcher, Tallinn University of Technology, Department of Electrical Power Engineering and Mechatronics
-------	---

## Elulookirjeldus

### Isikuandmed

Nimi:	Martin Sarap
Sünniaeg:	03.02.1996
Sünnikoht:	Kuressaare
Kodakondsus:	Eesti

### Kontaktandmed

E-post:	martin.sarap1@taltech.ee
---------	--------------------------

### Hariduskäik

2021–2025	PhD, Tallinna Tehnikaülikool, Elektroenergeetika ja mehhatroonika instituut
2018–2021	MSc, Tallinna Tehnikaülikool, Elektroenergeetika ja mehhatroonika instituut
2015–2018	BSc, Tallinna Tehnikaülikool, Elektroenergeetika ja mehhatroonika instituut
2012–2015	Keskharidus, Pääsküla Gümnaasium

### Keelteoskus

Eesti keel	Emakeel
Inglise keel	Kõrgtase

### Teenistuskäik

2021–	Doktorant-nooremteadur, Tallinna Tehnikaülikool, Elektroenergeetika ja mehhatroonika instituut
-------	--

ISSN 2585-6901 (PDF)  
ISBN 978-9916-80-342-4 (PDF)